

AD-A053 392

HONEYWELL RADIATION CENTER LEXINGTON MASS

HIRIS REFLIGHT. (U)

APR 77 C BOHNE, L HARKLESS, E DUNBAR

HRC-77-3-3

DNA-4337F

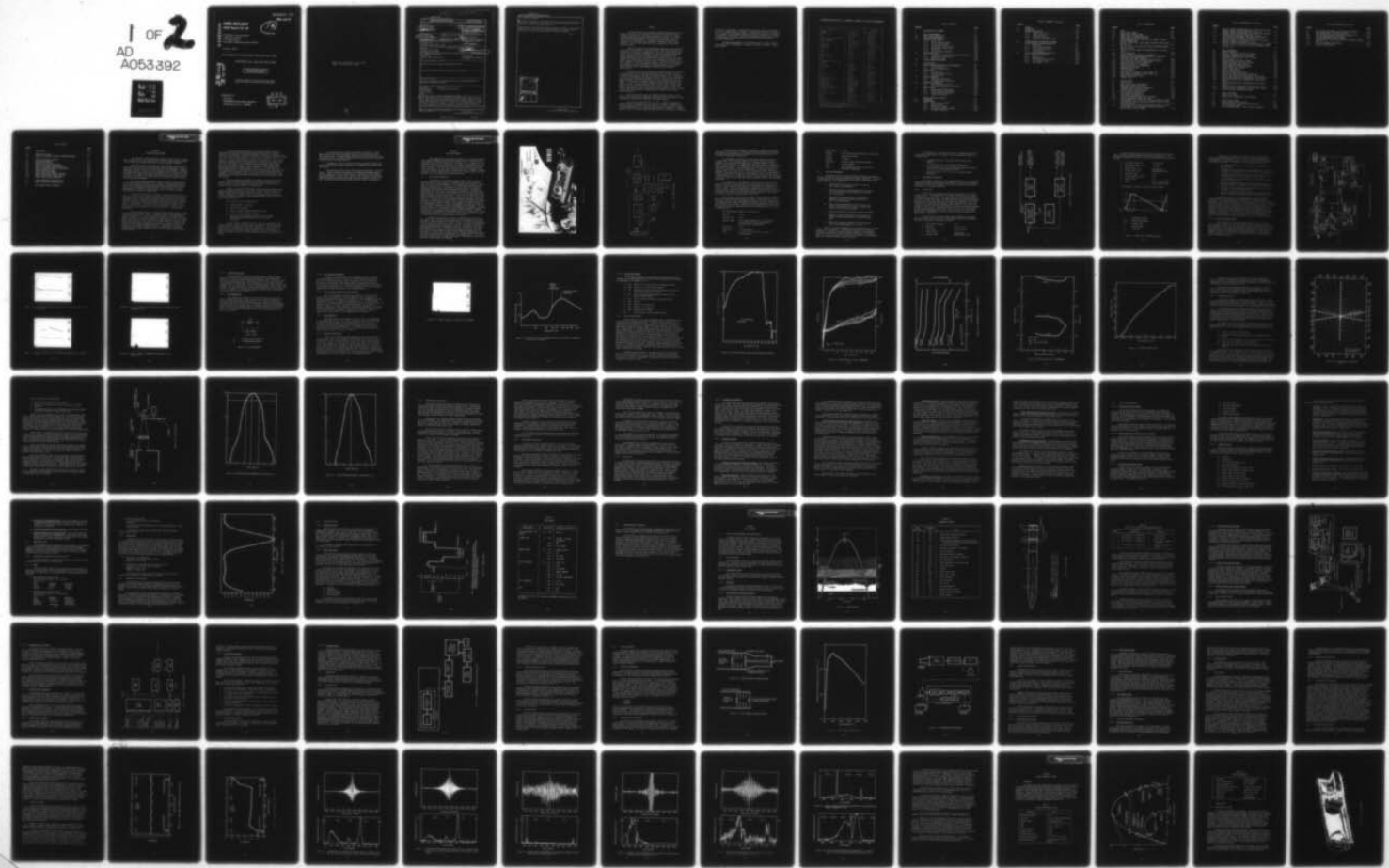
F/G 17/5

UNCLASSIFIED

DNA001-73-C-0164

NL

1 OF 2  
AD  
A053392



I OF  
AD  
A053392



AD-E300 173

DNA 4337F

**AD A 053392**    **HIRIS REFLIGHT**  
**HAES Report No. 65**

12  
1/86

Honeywell Incorporated  
Radiation Center  
2 Forbes Road  
Lexington, Massachusetts 02173

10 April 1977

Final Report for Period May 1973—February 1977

CONTRACT No. DNA 001-73-C-0164

APPROVED FOR PUBLIC RELEASE;  
DISTRIBUTION UNLIMITED.

AD NO.  
300 FILE COPY

THIS WORK SPONSORED BY THE DEFENSE NUCLEAR AGENCY  
UNDER RDT&E RMSS CODE B322074462 L25AAXYX63238 H2590D.

Prepared for  
Director  
DEFENSE NUCLEAR AGENCY  
Washington, D. C. 20305



Destroy this report when it is no longer  
needed. Do not return to sender.



(14) HRC-77-3-3, DNA-HAES-65

UNCLASSIFIED

SECURITY CLASSIFICATION OF THIS PAGE (When Data Entered)

REPORT DOCUMENTATION PAGE		READ INSTRUCTIONS BEFORE COMPLETING FORM
1. REPORT NUMBER DNA 4337F	2. GOVT ACCESSION NO.	3. RECIPIENT'S CATALOG NUMBER
4. TITLE (and Subtitle) HIRIS REFLIGHT HALS Report No. 65	9	
7. AUTHOR(S) Carl Bohne, (HRC) Lloyd Harkless (HRC) Elton Dunbar	18 DNA, SBIE	15
9. PERFORMING ORGANIZATION NAME AND ADDRESS Honeywell Incorporated, Radiation Center 2 Forbes Road Lexington, Massachusetts 02173	19 4337F AD-E399	13 NEW Subtask L25AAXYX632-38
11. CONTROLLING OFFICE NAME AND ADDRESS Director Defense Nuclear Agency Washington, D.C. 20305	17 X632	12. REPORT DATE 10 Apr 1977
14. MONITORING AGENCY NAME & ADDRESS (if different from Controlling Office) AF Geophysics Laboratory Hanscom AFB Bedford, Massachusetts 01731	11 13. NUMBER OF PAGES 184 (12) 178p	
16. DISTRIBUTION STATEMENT (of this Report)	Approved for public release; distribution unlimited.	
17. DISTRIBUTION STATEMENT (of the abstract entered in Block 20, if different from Report)		
18. SUPPLEMENTARY NOTES This work sponsored by the Defense Nuclear Agency under RDT&E RMSS Code B322074462 L25AAXYX63238 H2590D.		
19. KEY WORDS (Continue on reverse side if necessary and identify by block number) Cryogenic Spectra Interferometer Low Background Calibration Spectrometer Rocket Payload Aurora		
20. ABSTRACT (Continue on reverse side if necessary and identify by block number) This report describes the refurbishment and design modification of the cryogenic High Resolution Interferometer Spectrometer (HIRIS), previously developed under Contract DNA 001-72-C-0193, and its successful flight on a rocket probe from Poker Flats, Alaska, on 1 April 1977. A Sergeant booster carried the 900-lb payload to an apogee of 126 km. The HIRIS, operating with an internal temperature near 10 K, obtained 150 spectral scans of aurora, earth, and earth limb between cover opening at 88 km on the upleg and cover closing	Dover	

DD FORM 1 JAN 73 1473 EDITION OF 1 NOV 65 IS OBSOLETE

UNCLASSIFIED

SECURITY CLASSIFICATION OF THIS PAGE (When Data Entered)

404 486

JOB

UNCLASSIFIED

SECURITY CLASSIFICATION OF THIS PAGE(When Data Entered)

20. ABSTRACT (Continued)

At 62 km on the downleg. Good signal-to-noise telemetry was received during the flight. Recovery of the payload was successfully accomplished and the HIRIS is in excellent operating condition.

Also covered in the report are feasibility design activities for an improved spatial and spectral performance interferometer and radiometer, and the development of supporting low background calibration equipment.

A

ACCESSION for	
NTIS	White Section <input checked="" type="checkbox"/>
DDC	Buff Section <input type="checkbox"/>
UNANNOUNCED	<input type="checkbox"/>
JUSTIFICATION	
-----	
BY	
DISTRIBUTION/AVAILABILITY CODES	
Dist.	AVAIL and/or SPECIAL
A	

UNCLASSIFIED

SECURITY CLASSIFICATION OF THIS PAGE(When Data Entered)

## PREFACE

The High Altitude Effects Simulation (HAES) Program sponsored by the Defense Nuclear Agency since the early 1970 time period, comprises several groupings of separate, but interrelated technical activities, e.g., ICECAP (Infrared Chemistry Experiments--Coordinated Auroral Program). Each of the latter have the common objective of providing information ascertained as essential for the development and validation of predictive computer codes designed for use with high priority DoD radar, communications, and optical defensive systems.

Since the inception of the HAES Program, significant achievements and results have been described in reports published by DNA, participating service laboratories, and supportive organizations. In order to provide greater visibility for such information and enhance its timely applications, significant reports published since early calendar 1974 shall be identified with an assigned HAES serial number and the appropriate activity acronym (e.g., bibliography of all HAES reports issued prior to and subsequent to HAES Report No.1, dated 5 February 1974 entitled, "Rocket Launch of an SWIR Spectrometer into an Aurora (ICECAP 72)," AFCRL Environmental Research Paper No. 466, is maintained and available on request from DASIAC, DoD Nuclear Information and Analysis Center, 816 State Street, Santa Barbara, California 93102, Telephone (805) 965-0551.

This report, which is the final report under DNA Contract 001-73-C-0164, is the sixty-fifth report in the HAES series and covers technical activities performed during the period from May, 1973 through February, 1977. The report describes the refurbishment and design modification of the cryogenic High Resolution Interferometer Spectrometer (HIRIS), previously developed under Contract DNA001-72-C-0193, and its successful flight on a rocket probe from Poker Flats, Alaska, on 1 April 1976. A Sergeant booster carries the 900-lb payload to an apogee of 126 km. The HIRIS, spectral scans of aurora, earth, and earth limb between cover opening at 88 km on the upleg and cover closing at 62 km on the downleg. Good signal-to-noise telemetry was received during the flight. Recovery of the payload was successfully accomplished and the HIRIS is in excellent operating condition.

Also covered in the report are feasibility design activities for an improved spatial and spectral performance interferometer and radiometer, and the development of supporting low background calibration equipment

The contract was administered by Lt. Cdr. C. Thomas, DNA COR, with technical direction provided by Dr. A.T. Stair, Jr., of AFGL. Additional key technical support was received from AFGL personnel E. McKenna in mission control and payload integration, and J. Rogers in data reduction. Idealab Inc. provided valuable support in cryogenic slide development and the contribution of J. Pritchard

is especially acknowledged. Interferometer system design support was received from Mr. I. Coleman of Bartlett Systems. Contributions to focal plane technology by G. Frodsham of Electrodynamics Laboratory, Utah State University, to payload integration by R. Morin and L. O'Connor of Northeastern University and to launch site operations by N. Brown and his crew from the University of Alaska are gratefully acknowledged.

The HRC Program Manager was W. Williamson, with key technical contributions provided by H. Blackwell, D. Servaes, R. Sullivan, E. Dunbar, T. Morris and D. Miller.

**CONVERSION FACTORS FOR U.S. CUSTOMARY TO METRIC (SI) UNITS OF MEASUREMENT**

To Convert From	To	Multiply By
angstrom	meters (m)	1.000 000 X E -10
atmosphere (normal)	kilo pascal (kPa)	1.013 25 X E +2
bar	kilo pascal (kPa)	1.000 000 X E +2
barn	meter <sup>2</sup> (m <sup>2</sup> )	1.000 000 X E -28
British thermal unit (thermochemical)	joule (J)	1.054 350 X E +3
calorie (thermochemical)	joule (J)	4.184 000
cal (thermochemical)/cm <sup>2</sup>	mega joule/m <sup>2</sup> (MJ/m <sup>2</sup> )	4.184 000 X E -2
curie	giga becquerel (GBq)*	3.700 000 X E +1
degree (angle)	radian (rad)	1.745 329 X E -2
degree Fahrenheit	degree kelvin (K)	$\frac{t_K}{t_F} = (t^{\circ} F + 459.67)/1.8$
electron volt	joule (J)	1.602 19 X E -19
erg	joule (J)	1.000 000 X E -7
erg/second	watt (W)	1.000 000 X E -7
foot	meter (m)	3.048 000 X E -1
foot-pound-force	joule (J)	1.355 818
gallon (U.S. liquid)	meter <sup>3</sup> (m <sup>3</sup> )	3.785 412 X E -3
inch	meter (m)	2.540 000 X E -2
jerk	joule (J)	1.000 000 X E +9
joule/kilogram (J/kg) (radiation dose absorbed)	Gray (Gy)**	1.000 000
kilotons	terajoules	4.183
kip (1000 lbf)	newton (N)	4,448 222 X E +3
kip/inch <sup>2</sup> (ksi)	kilo pascal (kPa)	6.894 757 X E +3
ktap	newton-second/m <sup>2</sup> (N-s/m <sup>2</sup> )	1.000 000 X E +2
micron	meter (m)	1.000 000 X E -6
mil	meter (m)	2.540 000 X E -5
mile (international)	meter (m)	1.609 344 X E +3
ounce	kilogram (kg)	2.834 952 X E -2
pound-force (lbf avoirdupois)	newton (N)	4,448 222
pound-force inch	newton-meter (N·m)	1.129 848 X E -1
pound-force/inch	newton/meter (N/m)	1.751 268 X E +2
pound-force/foot <sup>2</sup>	kilo pascal (kPa)	4.788 026 X E -2
pound-force/inch <sup>2</sup> (psi)	kilo pascal (kPa)	6.894 757
pound-mass (lbm avoirdupois)	kilogram (kg)	4.535 924 X E -1
pound-mass-foot <sup>2</sup> (moment of inertia)	kilogram-meter <sup>2</sup> (kg·m <sup>2</sup> )	4.214 011 X E -2
pound-mass/foot <sup>3</sup>	kilogram/meter <sup>3</sup> (kg/m <sup>3</sup> )	1.601 846 X E +1
rad (radiation dose absorbed)	Gray (Gy)**	1.000 000 X E -2
roentgen	coulomb/kilogram (C/kg)	2.579 760 X E -4
shake	second (s)	1.000 000 X E -8
slug	kilogram (kg)	1.459 390 X E +1
torr (mm Hg, 0° C)	kilo pascal (kPa)	1.333 22 X E -1

\*The becquerel (Bq) is the SI unit of radioactivity; 1 Bq = 1 event/s.

\*\*The Gray (Gy) is the SI unit of absorbed radiation.

A more complete listing of conversions may be found in "Metric Practice Guide E 380-74," American Society for Testing and Materials.

TABLE OF CONTENTS

<u>SECTION</u>		<u>PAGE</u>
1	INTRODUCTION AND SUMMARY . . . . .	1-1
2	HIRIS REFURBISHMENT . . . . .	2-1
2.1	HIRIS SYSTEM DESCRIPTION . . . . .	2-1
2.2	TASKS AND REQUIREMENTS . . . . .	2-5
2.3	ENGINEERING AND REDESIGN . . . . .	2-6
	2.3.1 Mirror Servo . . . . .	2-6
	2.3.2 Detector Refurbishment . . . . .	2-17
	2.3.3 Straylight Rejection . . . . .	2-23
	2.3.4 Monochromatic Light Source . . . . .	2-29
	2.3.5 Misalignment Compensation . . . . .	2-30
	2.3.6 Electronics . . . . .	2-31
	2.3.7 Ground Support Equipment . . . . .	2-36
2.4	DEVELOPMENT TESTS . . . . .	2-39
	2.4.1 Monochromatic Reference Source Qualification . . . . .	2-39
	2.4.2 Beamsplitter Qualification . . . . .	2-40
	2.4.3 Electronics Tests . . . . .	2-42
2.5	ACCOMPLISHMENT AND RESULTS . . . . .	2-45
3	HIRIS REFLIGHT . . . . .	3-1
3.1	FLIGHT SYSTEM DESCRIPTION AND CONFIGURATION . . . . .	3-1
	3.1.1 Payload Elements . . . . .	3-1
	3.1.2 Ground Support System . . . . .	3-6
3.2	SYSTEM TESTS . . . . .	3-11
	3.2.1 Vibration Test . . . . .	3-11
	3.2.2 Flight Preparation Tests . . . . .	3-13
	3.2.3 Prelaunch Tests . . . . .	3-13
3.3	HIRIS CALIBRATION . . . . .	3-14
	3.3.1 Preflight Measurements . . . . .	3-14
	3.3.2 Calibration Data Processing . . . . .	3-14
3.4	LAUNCH SITE OPERATIONS . . . . .	3-18
	3.4.1 Field Checkout Activities . . . . .	3-18
	3.4.2 Prelaunch Preparation and Checkout . . . . .	3-19
3.5	HIRIS REFLIGHT . . . . .	3-20
	3.5.1 Launch Auroral Conditions . . . . .	3-21
	3.5.2 Vehicle/Payload Performance . . . . .	3-21
	3.5.3 Interferometer Performance . . . . .	3-21
	3.5.4 Flight Data Summary . . . . .	3-22
4	SPHIRIS FEASIBILITY DESIGN . . . . .	4-1
4.1	BACKGROUND . . . . .	4-1
4.2	SYSTEM DESIGN . . . . .	4-3
	4.2.1 Comparison with HIRIS . . . . .	4-3
	4.2.2 Optical System . . . . .	4-6
	4.2.3 Electronics System . . . . .	4-10
	4.2.4 Vacuum and Cryogenic Systems . . . . .	4-23
	4.2.5 In-Flight Calibrator . . . . .	4-30

TABLE OF CONTENTS (continued)

<u>SECTION</u>		<u>PAGE</u>
5	SPARAD . . . . .	5-1
5.1	BACKGROUND . . . . .	5-1
5.2	SPARAD CONFIGURATION . . . . .	5-1
	5.2.1 General Description . . . . .	5-1
	5.2.2 System Design . . . . .	5-2
	5.2.3 Electronics Design. . . . .	5-6
	5.2.4 Vacuum and Cryogenic Design . . . . .	5-9
6	GROUND TEST AND CALIBRATION EQUIPMENT. . . . .	6-1
6.1	LOW BACKGROUND CALIBRATION FACILITY . . . . .	6-1
	6.1.1 Background . . . . .	6-1
	6.1.2 Tasks and Requirements. . . . .	6-2
	6.1.3 Design and Engineering. . . . .	6-3
	6.1.4 Test Program . . . . .	6-13
	6.1.5 Accomplishments and Results . . . . .	6-22
6.2	FIELD PORTABLE MONOCHROMATOR . . . . .	6-26
	6.2.1 Source . . . . .	6-26
	6.2.2 Monochromator . . . . .	6-26
	6.2.3 Wavelength Control Chassis. . . . .	6-27
	6.2.4 Power Output Chassis. . . . .	6-31
	6.2.5 Power Supply . . . . .	6-32

LIST OF ILLUSTRATIONS

<u>FIGURE</u>	<u>PAGE</u>
2.1 HIRIS . . . . .	2-2
2.2 HIRIS BLOCK DIAGRAM . . . . .	2-3
2.3 MIRROR SERVO BLOCK DIAGRAM . . . . .	2-7
2.4 SWEEP OUTPUT TO MIRROR DRIVE COIL . . . . .	2-8
2.5 MIRROR SERVO SIMPLIFIED SCHEMATIC . . . . .	2-10
2.6 SWEEP GENERATOR OUTPUT (TOP) AND COIL CURRENT (BOTTOM) BEFORE OPTIMIZATION . . . . .	2-11
2.7 PLL INT. OUTPUT (TOP), BOIL CURRENT (BOTTOM) AFTER ADJUST- MENT OF R19 . . . . .	2-11
2.8 PLL INT. OUTPUT (TOP) AND STEP VOLTAGE DISTURBANCE BEFORE REDUCTION OF R26 . . . . .	2-12
2.9 SAME AS FIGURE 2.8 AFTER R26 WAS REDUCED TO 5 kΩ (FROM 10 kΩ) . . . . .	2-12
2.10 LEAD COMPENSATION . . . . .	2-13
2.11 SAME AS FIGURE 2.9 AFTER C47 WAS REMOVED . . . . .	2-15
2.12 VARIATION OF FRINGE-FREQUENCY JITTER AS A FUNCTION OF BANDPASS FILTER CENTER FREQUENCY . . . . .	2-16
2.13 HIRIS REFLIGHT SIGNAL DETECTOR SPECTRAL RESPONSE . . . . .	2-18
2.14 SIGNAL AND NOISE VS BIAS, TEMPERATURE . . . . .	2-19
2.15 RESPONSIVITY AND D* VS FREQUENCY . . . . .	2-20
2.16 SIGNAL NOISE AND D* VS TEMPERATURE . . . . .	2-21
2.17 DETECTOR DYNAMIC RANGE . . . . .	2-22
2.18 HEMISPHERICAL MAP . . . . .	2-24
2.19 IFOV TEST SETUP . . . . .	2-26
2.20 HIRIS RELATIVE RESPONSE VS FIELD ANGLE ( $\theta_x$ ) . . . . .	2-27
2.21 HIRIS RELATIVE RESPONSE VS FIELD ANGLE ( $\theta_y$ ) . . . . .	2-28
2.22 BEAMPLITTER CHARACTERISTIC . . . . .	2-41
2.23 THERMAL PROFILE . . . . .	2-43
3.1 MISSION PROFILE . . . . .	3-2
3.2 HIRIS PAYLOAD . . . . .	3-4
3.3 POKER FLATS LAUNCH CONFIGURATION . . . . .	3-7
3.4 EXPERIMENT CONTROL AND MONITOR . . . . .	3-9
3.5 LABORATORY AND PREFLIGHT CONFIGURATION . . . . .	3-12
3.6 EXTENDED SOURCE CALIBRATION SETUP . . . . .	3-15
3.7 POINT SOURCE CALIBRATION SETUP . . . . .	3-15
3.8 HIRIS SPECTRAL RESPONSIVITY . . . . .	3-16
3.9 CALIBRATION DATA REDUCTION . . . . .	3-17
3.10 FOCAL PLANE TEMPERATURES DURING THE FLIGHT . . . . .	3-23
3.11 BAFFLE TEMPERATURES DURING THE FLIGHT . . . . .	3-24
3.12 INTERFEROGRAM (TOP FIGURE) AND SPECTRUM (BOTTOM) OF INTERNAL BLACKBODY AND LED CALIBRATION SOURCES OBTAINED DURING PREFLIGHT CHECKOUT . . . . .	3-25
3.13 INTERFEROGRAM (TOP FIGURE) AND SPECTRUM (BOTTOM) OF INTERNAL BLACKBODY AND LED CALIBRATION SOURCES OBTAINED IN FLIGHT PRIOR TO COVER OPENING . . . . .	3-26

LIST OF ILLUSTRATIONS (continued)

<u>FIGURE</u>	<u>PAGE</u>
3.14 VERTICAL VIEWING INTERFEROGRAM (TOP FIGURE) AND SPECTRUM (BOTTOM) DURING THE UPLEG TRAJECTORY AT 102 km . . . . .	3-27
3.15 DOWNWARD VIEWING INTERFEROGRAM (TOP FIGURE) AND SPECTRUM (BOTTOM) DURING THE UPLEG TRAJECTORY AT 88 km . . . . .	3-28
3.16 LIMB VIEWING INTERFEROGRAM (TOP FIGURE) AND SPECTRUM (BOTTOM) DURING THE DOWNLEG TRAJECTORY AT 101 km . . . . .	3-29
3.17 VERTICAL VIEWING HIGH RESOLUTION SPECTRUM OF CO <sub>2</sub> BANDS DURING THE DOWNLEG TRAJECTORY AT 76 km . . . . .	3-30
3.18 VERTICAL VIEWING HIGH RESOLUTION SPECTRUM OF O <sub>3</sub> ( $\nu_1$ BAND) AT 1042 cm <sup>-1</sup> (9.6 micrometers) DURING THE DOWNLEG TRAJEC- TORY AT 76 km . . . . .	3-30
4.1 SPIRE TRAJECTORY . . . . .	4-2
4.2 SPHIRIS INSTRUMENT . . . . .	4-4
4.3 SPHIRIS OPTICAL AND ELECTRONICS SYSTEMS . . . . .	4-5
4.4 OVERVIEW OF SPHIRIS OPTICS, SCHEMATIC . . . . .	4-7
4.5 MICHELSON INTERFEROMETER OPTICS SCHEMATIC . . . . .	4-8
4.6 DETECTOR OPTICS . . . . .	4-8
4.7 SIGNAL CHANNEL FUNCTIONAL DIAGRAM . . . . .	4-14
4.8 REFERENCE CHANNEL FUNCTIONAL DIAGRAM . . . . .	4-16
4.9 MIRROR SERVO FUNCTIONAL DIAGRAM . . . . .	4-18
4.10 TIMING GENERATOR FUNCTIONAL DIAGRAM . . . . .	4-19
4.11 FLIGHT SYSTEM DATA INTERFACE . . . . .	4-22
4.12 SPHIRIS DEWAR CABLING . . . . .	4-24
4.13 SPHIRIS SYSTEM CABLING . . . . .	4-25
4.14 SPHIRIS OFF-SENSOR ELECTRONICS . . . . .	4-26
4.15 SPHIRIS RADIATION-SHIELD-DOOR TEMPERATURE . . . . .	4-32
4.16 SPHIRIS HOLD TIME AND MASS-FLOW RATE VS SUN ANGLE . . . . .	4-34
4.17 SPHIRIS RADIATION-SHIELD TEMPERATURES, NIGHT MISSION . . . . .	4-35
4.18 SPHIRIS RADIATION-SHIELD TEMPERATURES, DAY MISSION (CASE 1) . . . . .	4-36
4.19 SPHIRIS RADIATION-SHIELD TEMPERATURES, DAY MISSION (CASE 2) . . . . .	4-37
4.20 RADIATION-SHIELD TEMPERATURE VS MISSION TIME (CASE 1) . . . . .	4-38
4.21 RADIATION-SHIELD TEMPERATURE VS MISSION TIME (CASE 2) . . . . .	4-39
4.22 SPHIRIS INFLIGHT CALIBRATION SOURCES . . . . .	4-40
5.1 SPARAD INSTRUMENT . . . . .	5-3
5.2 SPARAD FOCAL PLANE . . . . .	5-4
5.3 SPARAD FLIGHT ELECTRONICS, BLOCK DIAGRAM . . . . .	5-7
6.1 LBCF OPTICAL SYSTEM . . . . .	6-5
6.2 SOURCE ASSEMBLY BLOCK DIAGRAM . . . . .	6-7
6.3 RADIANCE STABILITY VS TEMPERATURE STABILITY . . . . .	6-9
6.4 LBCF INTEGRATING SPHERE . . . . .	6-10
6.5 LBCF BLACKBODY SOURCE: OUTPUT SPATIAL UNIFORMITY . . . . .	6-14

LIST OF ILLUSTRATIONS (continued)

<u>FIGURE</u>		<u>PAGE</u>
6.6	LBCF INTEGRATING SPHERE: OUTPUT SPATIAL UNIFORMITY . . . . .	6-15
6.7	INTEGRATING SPHERE - SPECTRAL RESPONSE . . . . .	6-16
6.8	LBCF INTEGRATING SPHERE RADIANCE VS APERTURE SIZE . . . . .	6-18
6.9	SCATTER PERFORMANCE OF LECF MIRRORS . . . . .	6-19
6.10	LBCF COLLIMATION/ALIGNMENT TECHNIQUE . . . . .	6-21
6.11	INTERFEROGRAM OF LBCF OPTICAL TRAIN AT CRYOGENIC TEMPERA- TURES . . . . .	6-23
6.12	HS-2 SPECTROMETER INSTALLATION . . . . .	6-24
6.13	VERTICAL FIELD PROFILE . . . . .	6-25

LIST OF TABLES

<u>TABLE</u>		<u>PAGE</u>
2.1	TEST POINTS . . . . .	2-44
3.1	SEQUENCE OF EVENTS . . . . .	3-3
3.2	FLIGHT SYSTEM POWER FOR HIRIS EXPERIMENT SYSTEM . . . . .	3-5
4.1	SPHIRIS FEASIBILITY DESIGN . . . . .	4-1
4.2	MISSION REQUIREMENTS . . . . .	4-3
4.3	TELESCOPE OPTICAL DATA . . . . .	4-9
4.4	RELAY OPTICS SURFACE PARAMETERS . . . . .	4-11
4.5	SPHIRIS ELECTRICAL CHARACTERISTICS . . . . .	4-12
4.6	SPHIRIS ELECTRONICS DESIGN REQUIREMENTS . . . . .	4-13
4.7	SPHIRIS COMMAND SIGNALS . . . . .	4-23
4.8	SPHIRIS HEAT LOAD SUMMARY . . . . .	4-29
4.9	SPHIRIS FOCAL-PLANE THERMAL ANALYSIS . . . . .	4-31
4.10	SPHIRIS LASER-DIODE THERMAL ANALYSIS . . . . .	4-31
4.11	SPHIRIS HELIUM WEIGHT BREAKDOWN . . . . .	4-33
5.1	SPARAD PERFORMANCE CHARACTERISTICS . . . . .	5-5
5.2	SPARAD ELECTRICAL CHARACTERISTICS . . . . .	5-8
6.1	TEST SENSORS DESIGN PARAMETERS . . . . .	6-4

## SECTION 1

### INTRODUCTION AND SUMMARY

The objective of this program was to develop flight sensors for measurements in support of the High Altitude Effects Simulation (HAES) program conducted by the Defense Nuclear Agency through the Air Force Geophysics Laboratory.

The High Altitude Effects Simulation (HAES) program is a DNA effort to obtain indirectly information on the reaction of the upper atmosphere to nuclear explosives. Because of the ban on nuclear testing in the atmosphere, a number of experiments are being carried out in the laboratory and in the field to determine the parameters that will characterize the environment and its reactions in a suitable model. This model and its predictive computer codes will be used to assess and evaluate the operation of critical DOD radar and optical infrared systems in nuclear disturbed environments.

One of the on-going measurements programs (ICECAP) is being conducted in the polar disturbed atmosphere. Its objective is to investigate ionization and excitation mechanisms and mechanisms and chemical processes leading to both short- and long-wavelength infrared emissions in an auroral display. Field measurements are coordinated utilizing rocket, balloon, aircraft, and ground-based observation platforms as appropriate.

Visible and infrared auroral emissions of the upper atmosphere are produced by the interaction of energetic electrons and protons with ionospheric molecular constituents. DNA has supported instrumentation development and conducted experiments to acquire geophysical information associated with auroral phenomena as support material for computer simulations of high altitude, nuclear, radiation effects. IR measurements of an auroral event were successfully made in situ from a sounding rocket at altitudes of 70 to 200 kilometers. Spectral resolution was limited to ten wave numbers in the spectral range of 7 to 24 micrometers (Reference 1).

Under a separate contract, the HIRIS instrument (High Resolution Infrared Spectrometer) was developed. HIRIS is a cryogenic Michelson interferometer, with a spectral resolution of  $2 \text{ cm}^{-1}$  over a spectral region of 5 to 22 micrometers, a spatial resolution of 2.5 degrees, operating at temperature near 10K. This instrument was successfully flown and recovered in an engineering test flight on a Black Brant rocket from Poker Flats, Alaska in early 1974. Results of the test flight indicated that performance upgrading would be required in certain areas in order to meet all required HAES measurement objectives. Consequently, the specific objectives of this program included efforts to refurbish HIRIS, incorporating those modifications deemed necessary by the flight test experience and to support a HIRIS reflight.

The HAES measurement objectives also dictated the need for spectral measurements with improved spatial resolution and improved off-axis rejection relative to the capability of the HIRIS instrument. Consequently, experiment objectives were defined by DNA and AFGL for a Spectral Spatial Infra-Red Experiment (SPIRE), to consist of a rocketborne payload with three primary instruments. One of these would be an extended capability HIRIS modified by the addition of a high rejection telescope to provide high off-axis rejection and an improved spatial resolution of 4.4 mr (0.25 degree). This instrument would be the SPHIRIS, Spatial High Resolution Infrared Spectrometer. A second instrument, SPARAD, Spatial Radiometer, would provide even higher spatial resolution, 0.5 mr (0.03 degree) in a fixed spectral region. A third instrument, the Circular Variable Filter Spectrometer would provide both spatial and spectral resolution intermediate between SPHIRIS and SPARAD. The CVF radiometer was to be provided by Utah State University under separate contract; SPHIRIS and SPARAD efforts were part of the HRC program under this contract.

Complete development of SPHIRIS was contingent on successful operation of HIRIS. While the HIRIS engineering test flight was successful, there was no data collection and complete end-to-end operation of HIRIS, including data collection and data reduction, remained to be demonstrated.

Pending a successful HIRIS reflight, efforts under this program towards SPHIRIS and SPARAD were limited to conducting a detailed feasibility design of SPHIRIS through a detailed design review, and feasibility design of SPARAD. In addition, development of certain critical ground calibration and test equipment, to meet the combined requirements of HIRIS, SPHIRIS, SPARAD, and the CVF Spectrometer was a contract objective.

Thus the major contract objectives were:

- Refurbish HIRIS for reflight.
- Support HIRIS reflight.
- Conduct a detailed SPHIRIS feasibility design.
- Conduct a SPARAD feasibility design.
- Develop the Low Background Calibration Facility (LBCF) and Field Portable Monochromator for use with SPIRE instruments.

All major contract objectives were met. HIRIS was refurbished, incorporating a number of design modifications and improvements. It was successfully flown at Poker Flats, Alaska on 1 April 1976, collecting 150 spectral scans of auroral activity, zodiacal light, earth limb emission and earth emission. The flight data has been reduced and is being analyzed by AFGL. The HIRIS was successfully recovered, returned to HRC and successfully operated in laboratory conditions.

The SPARAD feasibility design was completed, resulting in a design meeting spatial resolution requirements within an outline satisfying launch vehicle constraints. A detailed SPHIRIS feasibility design was completed, including certain critical subassembly development and tests to demonstrate feasibility. A detailed design review was conducted.

Development of the LBCF and Field Portable Monochromator hardware was completed with the LBCF tested to demonstrate its capability to calibrate SPIRE type sensors.

The remaining sections of this report describe the details of the above efforts. Section 2 describes the details of the HIRIS refurbishment covering analyses, design, and test activities; Section 3 summarizes the HIRIS reflight and provides samples of typical data; Sections 4 and 5 describe the SPHIRIS and SPARAD configurations resulting from their respective feasibility design activities. The final section describes the LBCF and Field Portable Monochromator.

SECTION 2  
HIRIS REFURBISHMENT

HIRIS, High Resolution Infrared Spectrometer, is a cryogenic Michelson interferometer developed under DNA contract DNA001-72-C-0193, and flown in an engineering test flight in February 1974 (see Figure 2.1). A complete and comprehensive description of the instrument, its design, development and test, the test flight, and recommendations are given in the final report to that contract effort, reference 2. In this report, the discussion will concentrate on post flight refurbishment and tests and the reflight activities; a summary instrument description and test flight results are also given to provide a basis for understanding of the refurbishment and reflight activities.

2.1 HIRIS SYSTEM DESCRIPTION

A block diagram of the HIRIS reflight system is shown in Figure 2.2. The HIRIS instrument is a Michelson interferometer which scans the spectral region from 455 to 2500 wavenumbers (4 to 22 micrometers) and produces a double-sided interferogram every 1.36 seconds. The entire optical system including detector, collecting optics, interferometer cube and baffles is operated at approximately 10K through cooling with supercritical helium. This method of operation provides conditions of low background radiation for the arsenic doped silicon detector. The optical system consists of an f/1 all-reflecting system having four gold-coated A-2 steel mirrors. The detector is located in the focal plane to define a resultant field of view of 45 mr. The effective system aperture is 2.54 cm with a series of knife-edge forebaffles to provide out-of-field rejection. A window made of barium fluoride 1-cm thick is mounted in the baffles to attenuate the instrument response at 15 micrometers and longer wavelengths. The interferometer consists of a base, slide assembly, and fixed and moving mirrors, all made of hardened A-2 steel for homogeneous thermal response. The beam splitter consists of 0.4 micrometer (optical thickness) of germanium deposited on a 1-cm thick slab of polished polycrystalline potassium chloride. A similar uncoated slab is sandwiched with the beamsplitter to act as a compensator. These crystals are spring-mounted in a hardened A-2 steel mount specifically designed to accommodate thermal and vibration loads on the crystals.

The ball bearing slide is driven by a speaker type voice coil motor. The primary input to the motor servo amplifier is a ramp generator which causes the motor to drive the slide and scan mirror slowly 0.5 cm toward the beamsplitter for 1.26 second then return in 0.1 second. An LVDT is mounted on the instrument slide and provides position feedback for the servo. An auxiliary (reference) interferometer coupled to the instrument slide scans the outputs of an outboard He-Ne laser which is coupled into the Dewar through a fiber optic light guide. This auxiliary interferometer provides velocity feedback information for the mirror servo. Alternate zero crossings from the reference interferometer output are used to define the signal interferometer data sampling points. The output of the signal interferometer is sampled approximately 17,000 times per scan and converted to a digital signal for telemetry.

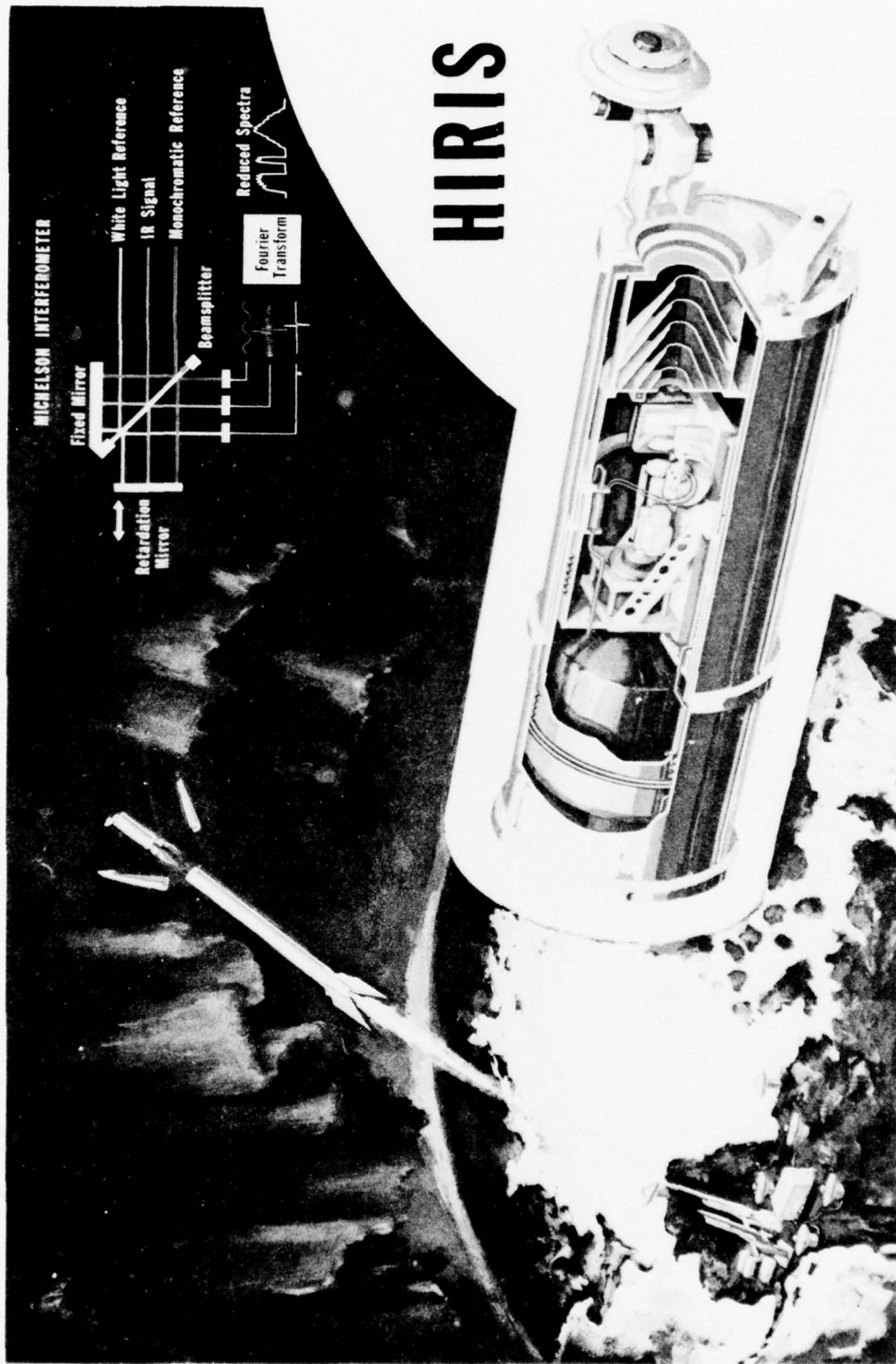


Figure 2.1 HIRIS

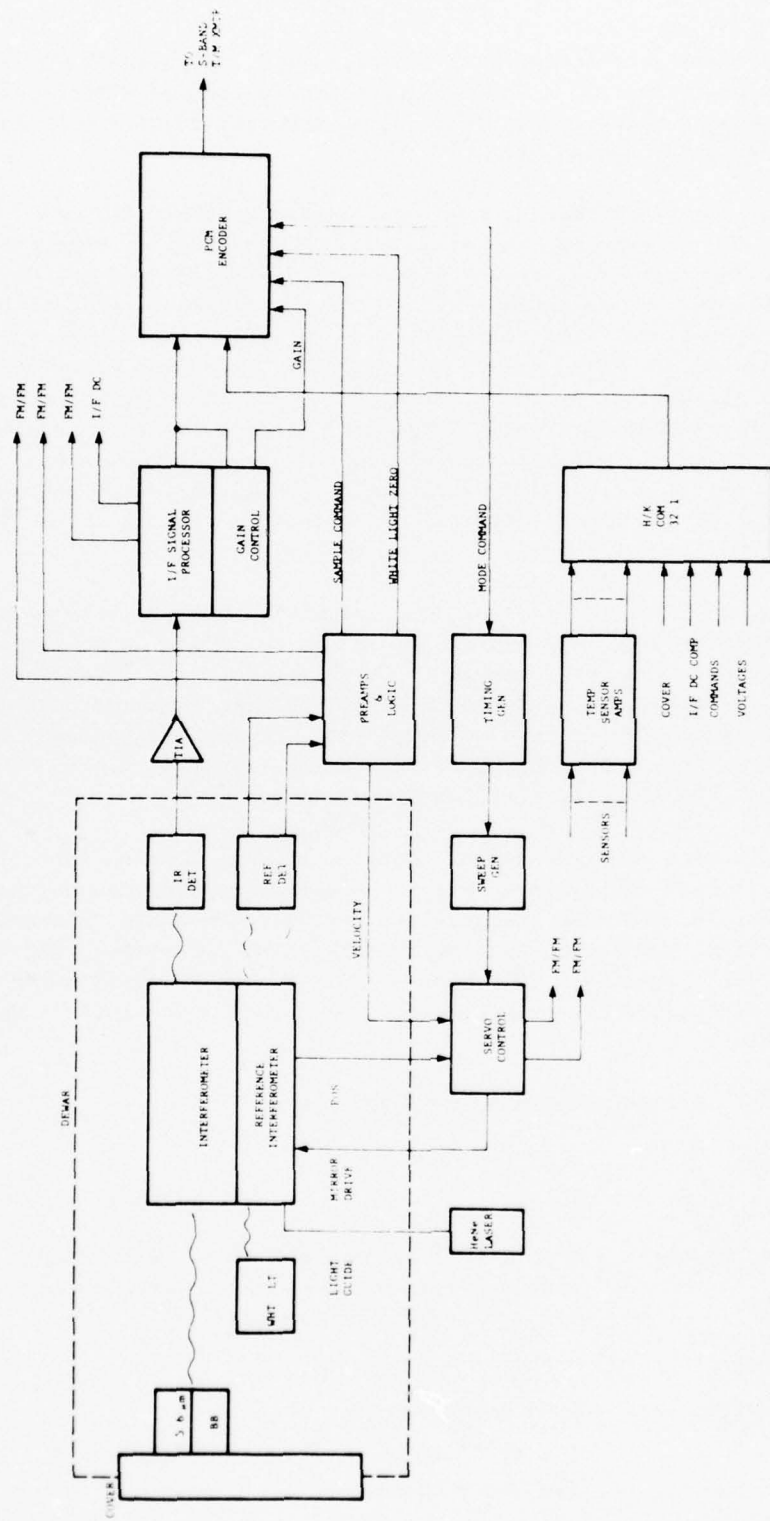


Figure 2.2 HIRIS BLOCK DIAGRAM

A second auxiliary (reference) interferometer, coupled to the instrument slide, scans the output of a white light source contained within the dewar. This auxiliary interferometer output defines the zero retardation position of the signal interferometer moving mirror.

The subassembly containing the three interferometers is housed in a cryogenic dewar. The instrument chamber is evacuated to prevent frosting of the optics at the extremely low temperatures. The dewar includes a 10-liter tank for liquid helium, and is capable of 4½ hours hold-time under conditions of normal prelaunch operations. The instrument is provided with a cold calibration cover which is opened and closed during the flight. Cover open actuation is set for a nominal altitude of 82 km following nose cone ejection, allowing the instrument to be fully open by 87 km. Cover reclosure is set for a nominal 60 km altitude on the down leg to allow for data acquisition below the auroral region. A small blackbody source at 160K and a  $1786 \text{ cm}^{-1}$  (5.6 micrometers) InSb LED mounted on the cover permit pre- and post-data taking calibration checks on the instrument performance.

The bottom plate on the dewar has a vacuum connector, fill and vent connectors for liquid helium transfer lines, and hermetic seal electrical connectors. A He-Ne laser and power supply are also mounted in a pressure box on the bottom plate. The laser is maintained at atmospheric pressure during the flight to prevent arcing in the high voltage supply at high altitudes. The laser is coupled to the reference interferometer inside the dewar with a fiber optic light guide, encased in a sealed stainless steel tube.

The instrument electronics box contains plug-in modules for: instrument scan timing, mirror servo, reference processor, signal processor, gain control, power conversion, blackbody temperature control, LED drive, command logic, housekeeping function signal conditioning, housekeeping commutator, and PCM encoder. The PCM encoder contains a 2048-word by 16-bit buffer memory which allows the interleaving of data, synchronizing codes and housekeeping data in each output telemetry frame.

The HIRIS reflight system characteristics are:

Aperture:	2.54 cm
Field of View:	45 mr
Spectral Range:	455 to 2500 wavenumbers (4 to 22 micrometers) with attenuation by a BaF <sub>2</sub> window below $667 \text{ cm}^{-1}$ (above 15 micrometers)
Resolution:	$2 \text{ cm}^{-1}$
Scan Period:	1.36 seconds/scan
NESR:	$5 \times 10^{-12} \text{ W/cm}^{+2} \text{ sr}^{+1} \text{ cm}^{-1}$ at $1000 \text{ cm}^{-1}$ (10 micrometers)

Dynamic Range:  $1 \times 10^4$   
Detector: Si:As (10K operating temperature, 8 volts bias)  
Cryogen: Supercritical helium  
Capacity: 10 liters  
Hold Time: 4½ hours (normal prelaunch activities)  
Size: 15-inch diameter  
Output: PCM - Signal data (233,472 bits/s) plus experiment housekeeping

## 2.2 TASKS AND REQUIREMENTS

An analysis of the data from the HIRIS first flight was performed to evaluate the HIRIS performance and identify performance limitations. As a result of this analysis, the following redesign tasks, aimed at improving the HIRIS system performance, were identified.

- Redesign the mirror servo to provide a 0.5-cm scan and to improve its performance.
- Investigate the signal interferometer detector to identify and eliminate the spiking observed in the HIRIS first flight system.
- Investigate the straylight source to identify and eliminate the constant irradiance observed in the HIRIS first flight system.
- Assess alternate monochromatic light sources for the reference interferometer to identify a reliable light source for the HIRIS reflight system.
- Redesign the beamsplitter coatings to improve throughput.
- Redesign the signal interferometer optics alignment to eliminate cryogenic misalignment in the HIRIS reflight system.
- Redesign the external electronics to reduce electronic noise, improving performance and reliability.

Results of the above redesigns were to be incorporated into the HIRIS as part of the refurbishment. In addition, modifications to the GSE were required to 1) provide an electronics checkout console at the blockhouse, 2) upgrade the existing electronics checkout console used at the telemetry sight, 3) provide a DR-11A interface to permit co-addition of interferometric data, and 4) upgrade the PDP-11 computer software.

A test program, to evaluate and/or qualify the changes incorporated in the HIRIS reflight system, was required. The test program consisted of the following tasks:

- A qualification test of the He-Ne laser and fiber optics assembly.
- A qualification test of the redesigned beamsplitter.
- A qualification test of the misalignment compensation technique and a test of the redesigned mirror slide.
- Functional thermal cycle tests of the repackaged external electronics.

## 2.3 ENGINEERING AND REDESIGN

The studies, development and/or redesign performed on the mirror servo, interferometer detector, stray source, monochromatic light source, misalignment compensation, piezoelectric alignment device, external electronics, and GSE are discussed in the following paragraphs.

### 2.3.1 Mirror Servo

The mirror servo controls the sweep and flyback motion of the interferometer mirror. The required motion is a smooth, linear scan over a distance of approximately 0.5 cm, followed by a rapid flyback to the starting position for maximum scanning efficiency. This sawtoothed motion must occur approximately once per 1.4 second. The control of mirror motion is accomplished with a stable ramp generator and feedback information from two external sources. Positional feedback from a linear position transducer (LVDT) connected to the mirror slide is used to locate the start and stop positions of the slide and provide reasonable linearity in sweep motion. Additionally, during the data scan, an optically derived 13-kHz fringe signal from a laser source is used for accurate velocity feedback data. The functional elements of the mirror servo are shown in the block diagram of Figure 2.3.

In order to meet the signal interferometer performance requirements the mirror starting point, sweep rate, sweep length, flyback time and settling time after flyback must be controlled as follows:

● Starting Point Accuracy	$\pm 2\%$
● Sweep Rate	$0.55 \text{ cm/s} \pm 1\%$
● Sweep Length	$0.505 \pm 0.005 \text{ cm}$
● Flyback Time }	Combined time
● Settling Time }	approximately 160 ms

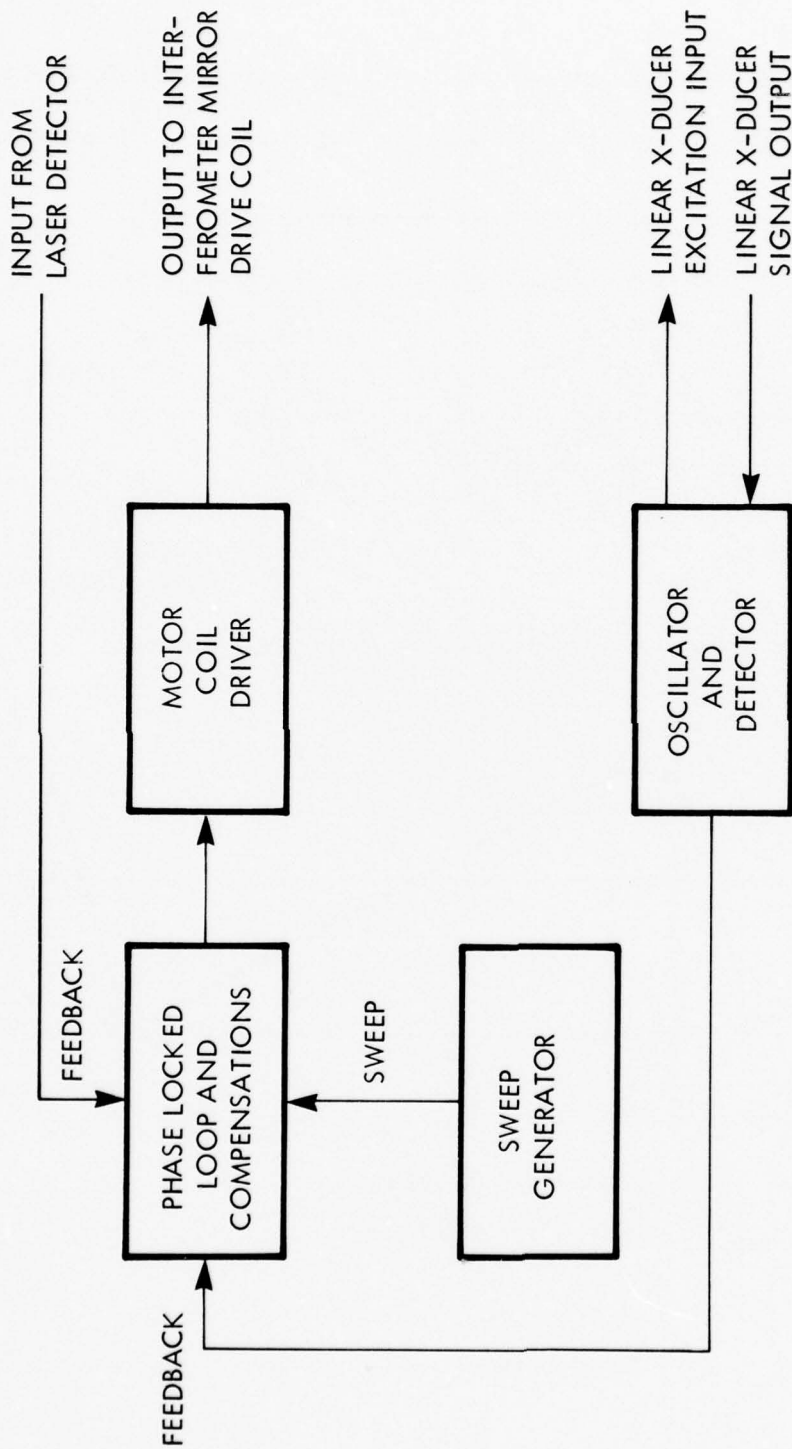
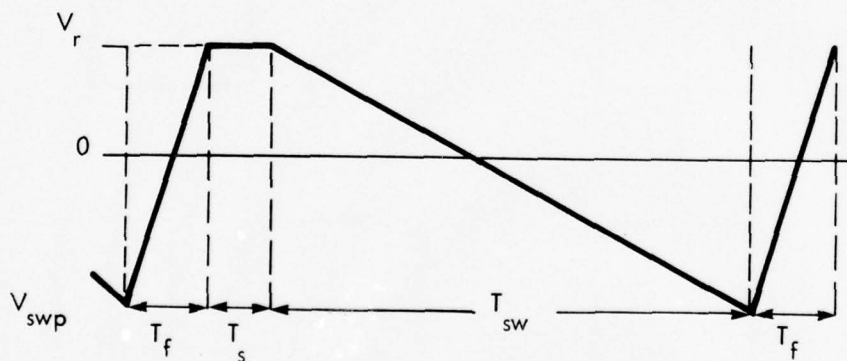


Figure 2.3 MIRROR SERVO BLOCK DIAGRAM

The sweep voltage required at the input to the mirror drive motor in order to provide the specified mirror motion is shown in Figure 2.4. The performance requirements associated with the sweep voltage to the mirror drive coil are:

• Slide Rest Voltage, $V_r$	$+7 \text{ volts} \pm 10\%$
• Peak Sweep voltage, $V_{swp}$	-13 volts
• Flyback Time, $T_f$	{ Combined time
• Settling Time, $T_s^*$	approximately 160 ms
• Sweep Time, $T_{sw}^*$	1.24 s
• Voltage Stability, 0-60°C	$\pm 1\%$
• Sweep Linearity	$\pm 1\%$
• Timing	0 - 4 V Logic FB + $\overline{\text{FB}}$ (FB to start flyback)

\* Determined by (external) timing of FB logic command.



- |           |                      |
|-----------|----------------------|
| $V_r$     | = SLIDE REST VOLTAGE |
| $V_{swp}$ | = PEAK SWEEP VOLTAGE |
| $T_f$     | = FLYBACK TIME       |
| $T_s$     | = SETTLING TIME      |
| $T_{sw}$  | = SWEEP TIME         |

Figure 2.4 SWEEP OUTPUT TO MIRROR DRIVE COIL

A redesign for optimization of the mirror servo was undertaken to provide the above defined mirror motion. A set of oscilloscope photographs corresponding to those shown for the mirror servo control circuits in the HIRIS Design Report were taken. An analysis of these photographs showed that:

- 1) The fringes were as good as or better than those shown in the design report.
- 2) The phase lock loop (PLL) error was approximately 200 mV pk-pk as compared to approximately 40 mV pk-pk shown in the design report.
- 3) Performance without laser input appeared similar (PPL error and PLL integrated error) to that shown in the design report.
- 4) Initial transient in the fringes appeared to be better than that shown in the design report.
- 5) The linear transducer oscillator source was much improved and showed no distortion as compared to that shown in the design report.
- 6) The mirror was not operating in the center portion of the linear transducer as shown in the design report.
- 7) All other performance characteristics were very similar to that shown in the design report when allowing for the different timing.

Following the comparison of the performance of the servo with the original design, a development effort was undertaken to optimize the servo performance. The development effort consisted of an analysis of the performance improvements which could be obtained by: improving the motor coil driver, increasing the PLL loop gain, using lead compensation in the PLL compensation amplifier output, increasing the PLL bandwidth, removing the PLL compensation amplifier output capacitor, increasing the sweep amplitude and making circuit adjustments to compensate for servo errors. The details and results of the development effort are discussed in paragraphs 2.3.1.1 through 2.3.1.7 and the resulting servo redesign is summarized in paragraph 2.3.1.8. The simplified mirror servo schematic of Figure 2.5 shows the circuit components referred to in the following paragraphs.

#### 2.3.1.1 Motor Coil Driver Circuit

It was apparent from the oscilloscope photograph of the coil drive current, shown in Figure 2.6, that the response of the coil driver loop was somewhat underdamped. The current loop gain was reduced by lowering the value of feedback resistor R19 in the operational amplifier. The reduction in the value of the feedback resistor to 60 K-ohms  $\pm$  5% improved the damping and provided a faster response as shown by the oscilloscope photograph of Figure 2.7. The improved response of the motor coil driver circuit permits the use of a wider bandwidth in the PLL compensation amplifier.

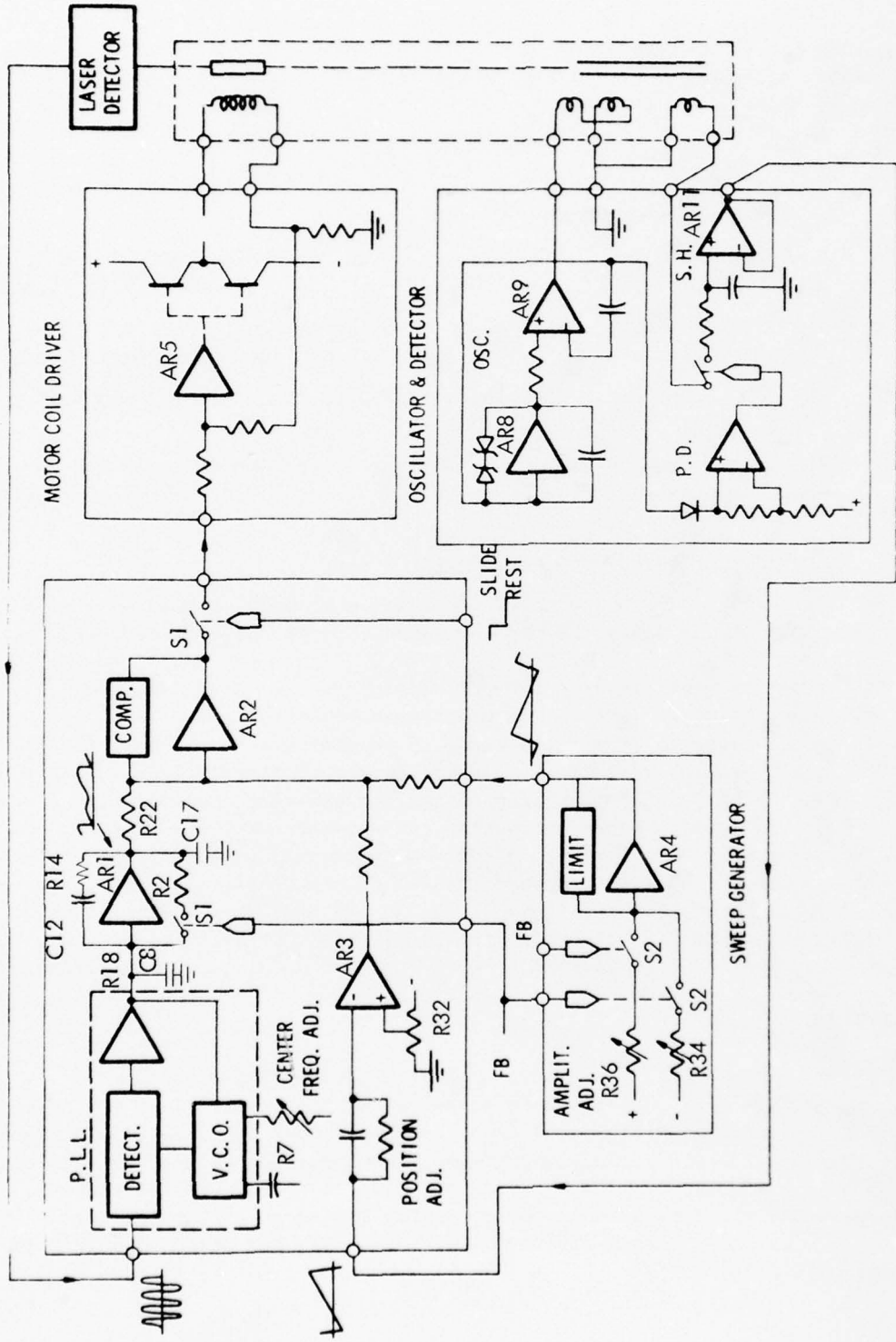


Figure 2.5 MIRROR SERVO SIMPLIFIED SCHEMATIC

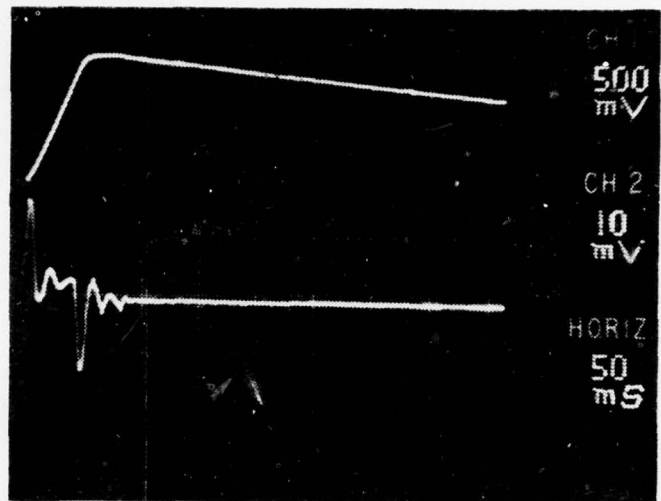


Figure 2.6 SWEEP GENERATOR OUTPUT (TOP) AND COIL CURRENT (BOTTOM) BEFORE  
OPTIMIZATION

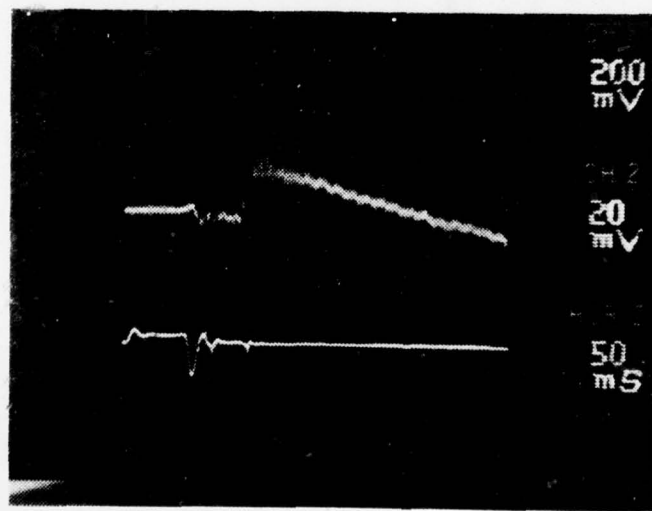


Figure 2.7 PLL INT. OUTPUT (TOP), COIL CURRENT (BOTTOM) AFTER ADJUSTMENT  
OF R19

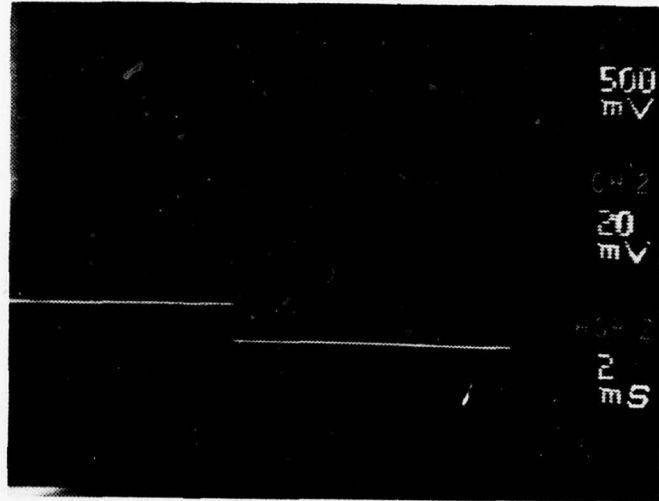


Figure 2.8 PLL INT. OUTPUT (TOP) AND STEP VOLTAGE DISTURBANCE BEFORE REDUCTION OF R26

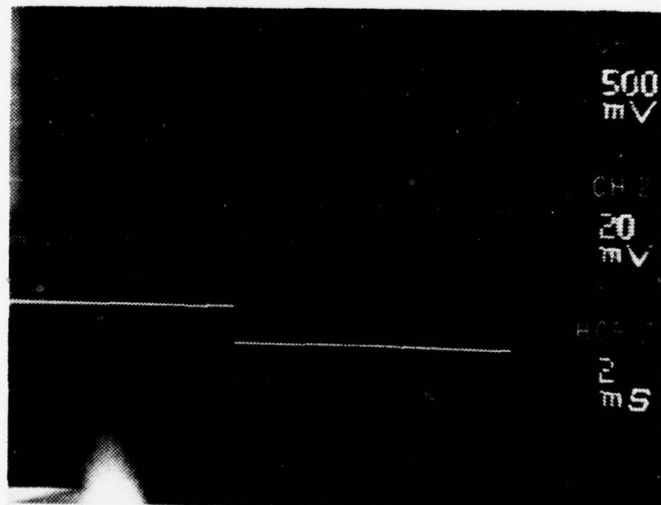


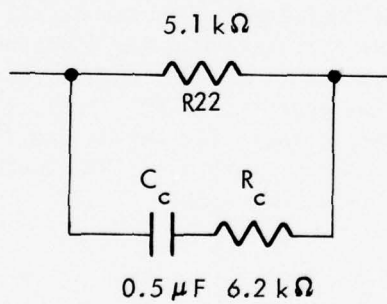
Figure 2.9 SAME AS FIGURE 2.8 AFTER R26 WAS REDUCED TO 5 k $\Omega$  (FROM 10 k $\Omega$ )

### 2.3.1.2 Phase Lock Loop Gain

The step response of the PLL loop was obtained by inserting a small step current into pin 2 of the summation amplifier, AR-3, and measuring the response at the output of the PPL compensation amplifier, AR-1. The input current step function was obtained from a source consisting of a 16 millivolt step into a series resistor of 100 K-ohms. The resulting step response, shown in Figure 2.8, indicated that the loop gain was too low, as characterized by a fast rise and a long overshoot. The gain was doubled by reducing the summing amplifier input resistor, R-22, to 5.1 K-ohms  $\pm$  5%. The improved response of the PLL loop resulting from the increased gain is shown in Figure 2.9.

### 2.3.1.3 Lead Compensation

Lead compensation consisting of a series RC network was added across the PLL compensation amplifier output resistor, R22, as shown in Figure 2.10. The effect of the added lead compensation was to widen the servo bandwidth and a noticeable reduction of the PLL error was observed. However, no lead compensation was included in the redesign servo as a subsequent development involving the removal of the slew rate limiting capacitor C17 (see paragraph 2.3.1.5) at the output of the PLL compensation amplifier showed that the lead compensation network was not required.



$C_c$  = COMPENSATION CAPACITOR  
 $R_c$  = COMPENSATION RESISTOR

Figure 2.10 LEAD COMPENSATION

#### 2.3.1.4 PLL Bandwidth Improvement

An attempt to increase the PLL servo bandwidth was made by reducing the value of the capacitor C8 at the input to the PLL compensation amplifier, AR-1, and by further reducing the value of the resistor, R22, in series with the input of that amplifier. This change resulted in a significant increase in the noise at the output of the PLL compensation amplifier, AR-1, and occasional sweep failures were observed. As a result, no adjustment in the value of either capacitor C8 or resistor R22 was made in the optimized design.

#### 2.3.1.5 PLL Compensation Amplifier Output Capacitor

The PLL compensation amplifier output capacitor C17 serves to limit the slew rate of that amplifier. The step response of the PLL compensation amplifier was measured with capacitor C17 removed and a PLL compensation amplifier output resistor R22, of 5.1 K-ohms (see paragraph 2.3.1.2). An oscilloscope photograph of the results obtained by removing capacitor C17 is shown in Figure 2.11. Analysis of Figure 2.11 shows no significant change from the data shown in Figure 2.9, except for a slight increase in the frequency components of the noise. Additional measurements of PLL error, sweep stability and sweep reliability showed that capacitor C17 was not required for proper servo operation. Therefore, capacitor C17 has been deleted in the redesigned servo electronics.

#### 2.3.1.6 Sweep Amplitude

The sweep amplitude was increased to obtain a full 0.5-cm displacement of the interferometer mirror. The increase in sweep amplitude was accomplished by reducing the sweep frequency at the timing generator. As a result of increasing the sweep amplitude, the operational amplifier, AR-5, in the motor coil driver saturated at the negative end. The saturation of amplifier AR-5 was corrected by changing zener diode CR12 to a 1N5241B thereby increasing the sweep voltage limit from -6.2 volts to -13 volts.

#### 2.3.1.7 Sources of Servo Error

Prior to the previously described adjustments there were three major sources of servo error: 1) an excessive transient when the PLL took over control, 2) nonlinearity of the linear transducer, and 3) jitter due to rolling friction of the mirror support. Of these sources of error, the rolling friction appeared to be the more significant. However, the initial sweep speed error could cause loss of sweep track if the adjustment of sweep bias was incorrect. The variation of the error believed to be introduced by the rolling friction with frequency was measured by the use of an adjustable bandpass filter. The result of these measurements is shown in the plot of Figure 2.12. The measurements were taken by switching the bandpass filter to equal values of high and low-pass frequencies.

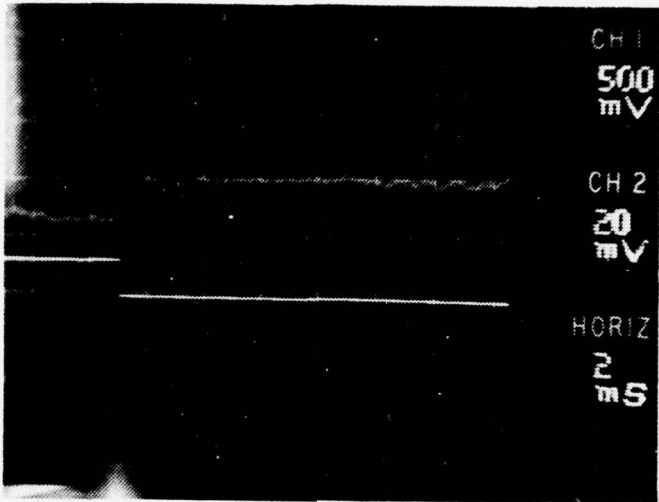


Figure 2.11 SAME AS FIGURE 2.9 AFTER C47 WAS REMOVED.

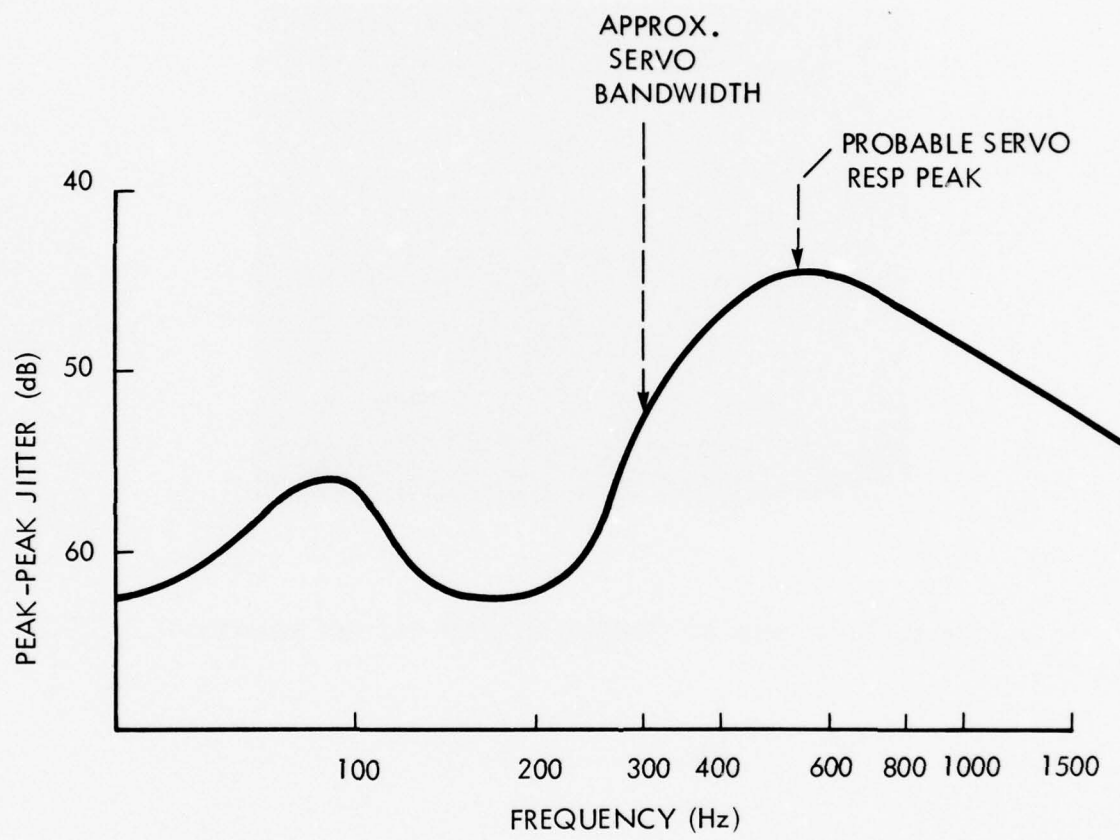


Figure 2.12 VARIATION OF FRINGE-FREQUENCY JITTER AS A FUNCTION OF BANDPASS FILTER CENTER FREQUENCY

### 2.3.1.8 Incorporated Changes

The following components and potentiometers were changed, selected or adjusted, in the redesigned servo as a result of the development effort described in paragraphs 4.3.1.1 through 4.3.1.7:

- 1) R35: Selected for a flyback time of approximately 160 ms
- 2) R36: Selected for correct fringe frequency
- 3) R7: Selected for correct PLL integrator output in absence of laser (range going from 0 to -15 V)
- 4) R6: Set for a free-running frequency (no laser) equal to desired fringe frequency
- 5) R32: Set for correction position of white light pulse
- 6) C17: Deleted
- 7) R19: Changed to 60 K-ohms  $\pm$  5%
- 8) R22: Changed to 5.1 K-ohms  $\pm$  5%
- 9) CR12: Changed to type 1N5241B
- 10) - Timing generator output frequency reduced

### 2.3.2 Detector Refurbishment

A major objective of the HIRIS refurbishment was to improve sensitivity by eliminating or reducing noise produced by detector spiking observed in the calibration and first HIRIS flight data. To achieve this objective, the original flight detector was subjected to a comprehensive test program in an attempt to characterize the detector spiking problem. Tests were conducted both at HRC and NELC. Results showed 1) that the spiking characteristic was sensitive to background, bias and temperature, 2) spiking was observed at all background levels, increasing dramatically at high backgrounds with lower bias levels, and 3) that detector resistance did not decrease abruptly at high bias voltage indicating that the detector was not "breaking down" in the traditional manner. The conclusion was that spiking could only be reduced or eliminated by replacing the existing detectors with detectors selected for low spiking. The detector specification was revised and the primary and backup HIRIS focal planes were sent to the detector supplier, Rockwell International, for detector replacement. Detector material selection was made by RI to minimize spiking within the detector bias limits while meeting all other performance specifications. Excellent results were obtained; the new detectors showed a total absence of spiking.

Performance characteristics of the detector flown in the refurbished HIRIS are given in Figures 2.13 to 2.17. Spectral response half power points were 10 to 24 micrometers, with the detector being nearly flat with wavelength, near the peak, from 18 to 23 micrometers, as shown in the spectral response curve of Figure 2.13, measured at NELC.

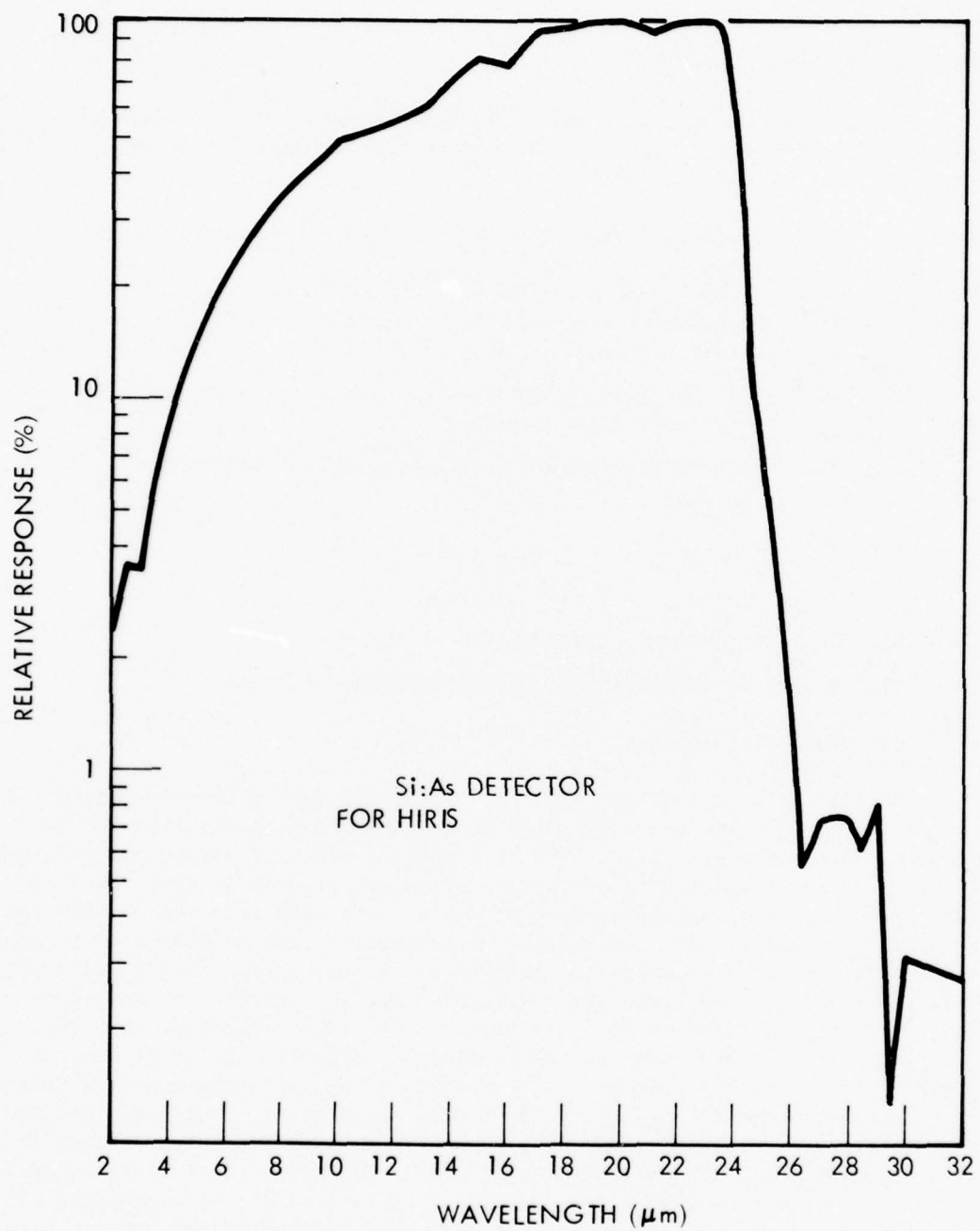


Figure 2.13 HIRIS REFLIGHT SIGNAL DETECTOR SPECTRAL RESPONSE

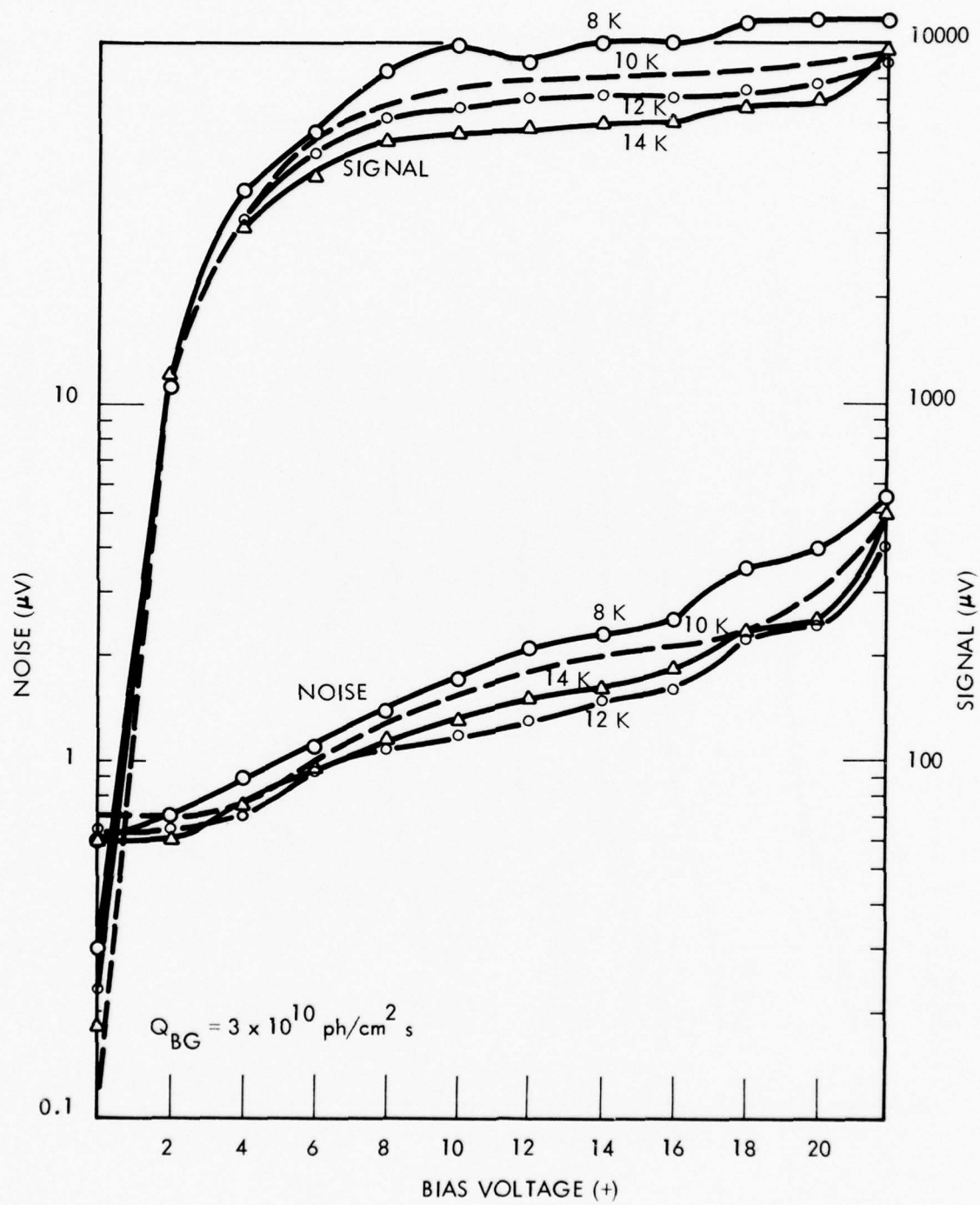


Figure 2.14 SIGNAL AND NOISE VS BIAS, TEMPERATURE

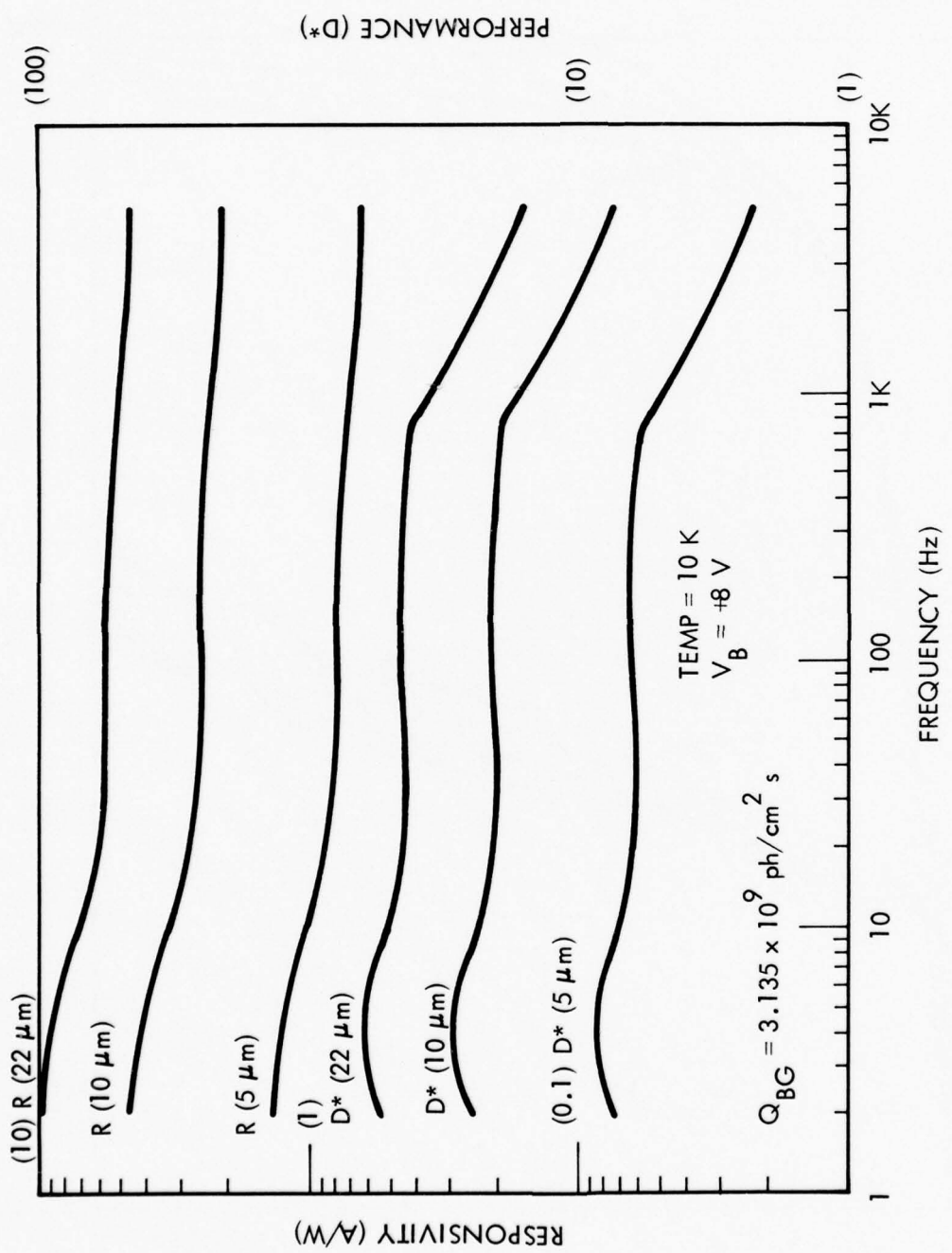


Figure 2.15 RESPONSIVITY AND  $D^*$  VS FREQUENCY

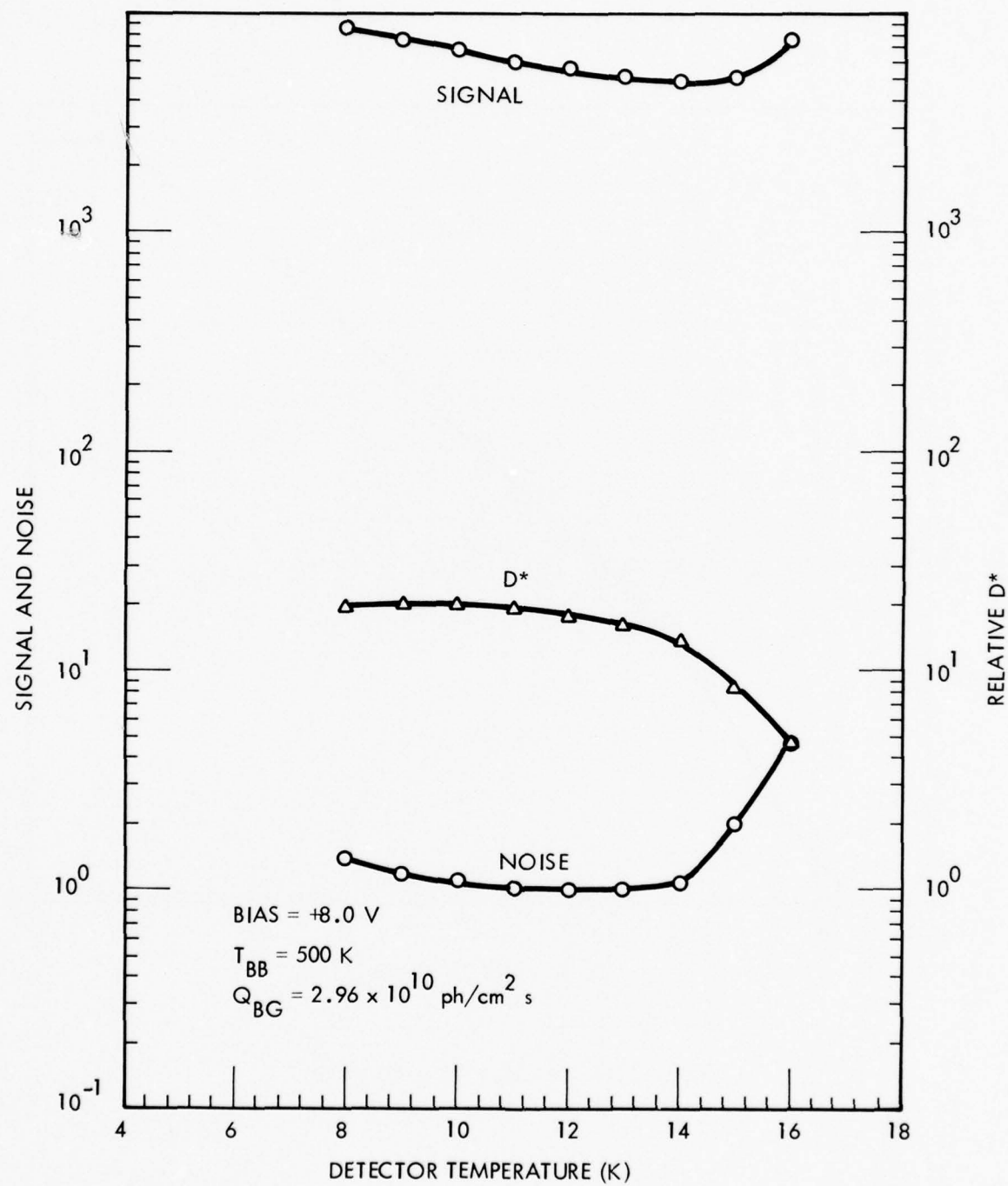


Figure 2.16 SIGNAL NOISE AND D\* VS TEMPERATURE

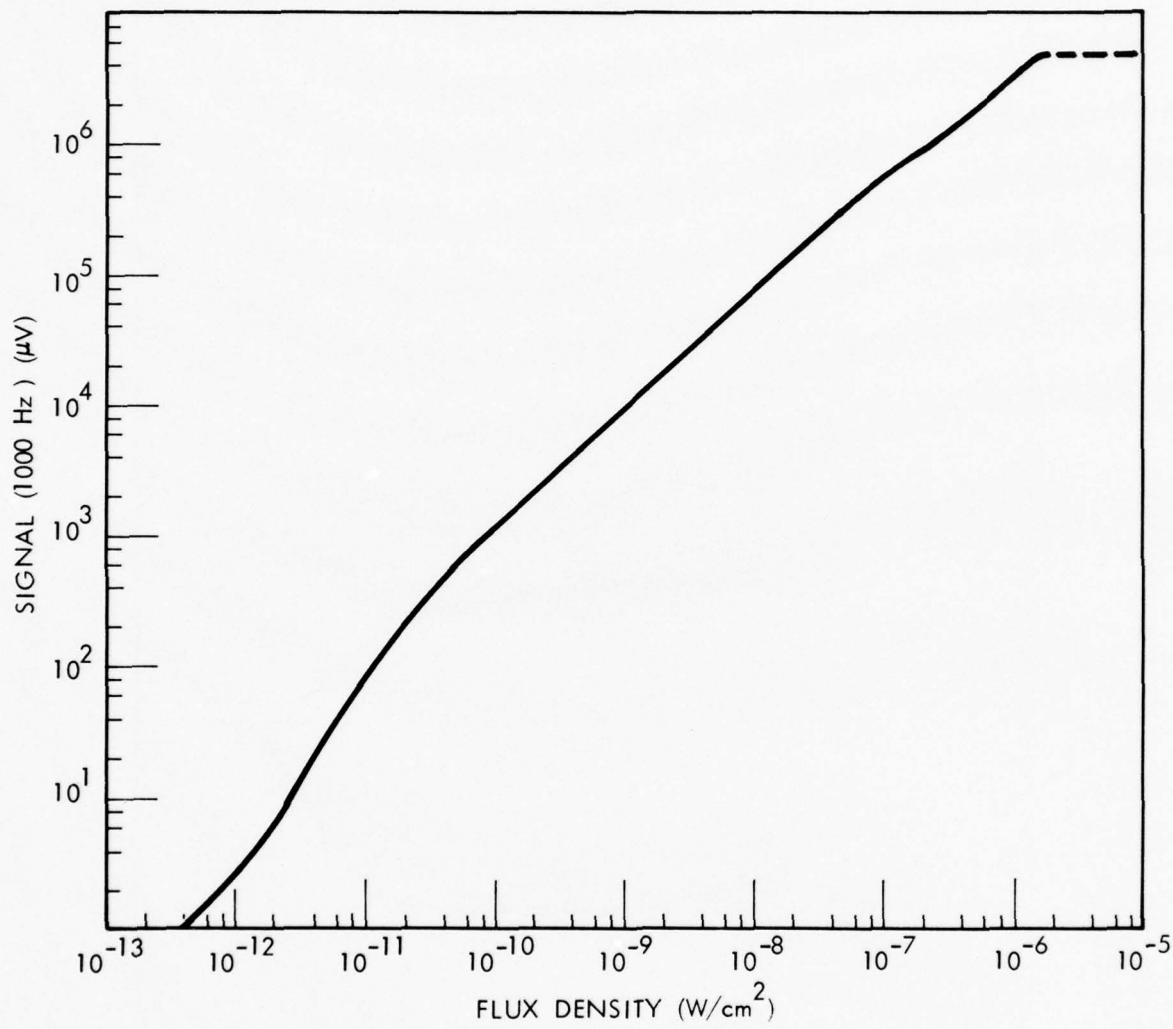


Figure 2.17 DETECTOR DYNAMIC RANGE

Signal and noise versus bias voltage for different temperatures is given in Figure 2.14, from which an optimum bias of 8 volts was determined. Responsivity and  $D^*$  versus frequency for three wavelengths is given in Figure 2.15, which shows a  $D^*$  break frequency of  $\approx 1$  kHz.

Optimum detector operating temperature was determined to be 10 K, as shown by Figure 2.16, with  $D^*$  relatively flat over the temperature range of 8 K to 12 K. The detector exhibited a dynamic range of better than 6 orders of magnitude as shown by results given in Figure 2.17.

### 2.3.3 Straylight Rejection

Analyses were conducted to determine modifications required to improve straylight rejection performance and to eliminate sources of constant irradiance observed in the initial flight data. The source of constant irradiance was analyzed using both computer modeling and measurement of the interferometer characteristics.

The computer analysis of the HIRIS interferometer was accomplished using a model of the interferometer optical system and the General Unwanted Energy Rejection Analysis Program (GUERAP) developed by the Honeywell Aerospace Division for the Space and Missile Systems Organization of the Air Force. GUERAP is able to efficiently and accurately calculate the off-axis rejection characteristics of a given optical system or baffle and evaluate the effect of both internal and external emission energy on infrared systems.

The computer analysis revealed that the tenth scan light emitting diode (LED) and the baffles would scatter radiation from the cover mechanism into the interferometer field of view. The recommendations resulting from this study were to:

- 1) Change to an optical baffle design
- 2) Reposition the tenth scan LED outside the interferometer field of view
- 3) Modify the door mechanism so that it cannot radiate into the baffle
- 4) Polish the cover mechanism to reduce emissions
- 5) Improve the beam splitter substrate and compensator surface and materials.

Measurements of the interferometer optical system were made to obtain a hemispherical response map. During this test, all interferometer surfaces which are optically exposed to the atmosphere during flight were irradiated by collimated visible light using a twelve-inch collimator with a one-inch central obscuration. The relative system response as a function of incident angle was measured using two azimuth scans and one scan across the blackbody controller and photometer. The resulting data were used to prepare the hemispherical map shown in Figure 2.18.

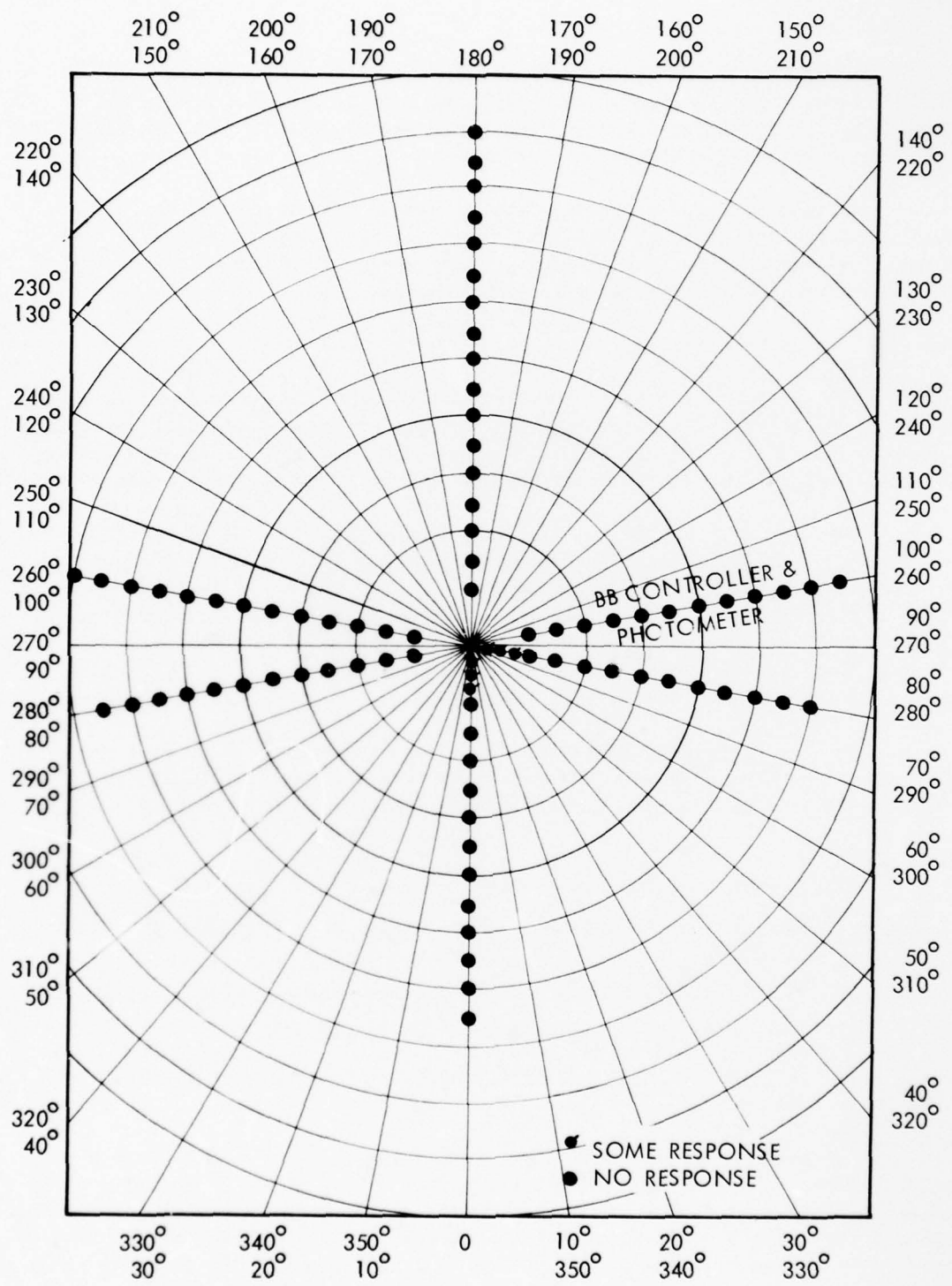


Figure 2.18 HEMISPHERICAL RESPONSE MAP

The results of this test showed that:

- 1) No off-axis scattering sources were found.
- 2) Reflections from the MLI were observed external to the HIRIS baffles.
- 3) The beamsplitter white light transmission was considerably higher than expected (possibly as high as 20 percent).

Another series of measurements made to obtain the interferometer field of view using the test setup are shown in Figure 2.19. In this test the HIRIS aperture was illuminated using a two-inch collimating lens. The pinhole light source in the focal plane of the collimating lens was translated in both X and Y directions and the interferometer response versus source displacement was measured. The results of this test are summarized in Figures 2.20 and 2.21 which show the interferometer relative response as a function of field angle in the X and Y planes, respectively. From this data it can be seen that the interferometer response at 3.2 degrees off-axis is down approximately  $10^{-4}$  from the on-axis response.

A third series of measurements were made to obtain the stray signals due to mirror slide vibration at frequencies within the processing electronics bandpass. In this test the interferometer was illuminated with light from a helium-neon laser and the interferogram data was monitored through a variable bandpass electronic filter. An examination of interferogram data obtained indicated that there was no measurable noise due to mirror slide vibration.

Based on the results of previously discussed measurements and computer studies, a new baffle was designed and built and the door mechanism was modified. The new baffle assembly is an optical baffle with sharp edges in contrast to the original aerodynamic baffle. The door mechanism was cut down to prevent its emissions from reaching the baffles.

Tests were conducted to verify that the redesigned baffle and modified door mechanism performed as predicted. A photographic test of the redesigned baffle was performed. In this test, a high intensity light source was located at the detector position using fiber optics. The path of this source was photographically observed at each baffle position. A photograph test was also performed to demonstrate that no radiation from the door reached the detector. The results of these tests confirmed that the objectives of the redesign had been attained.

The HIRIS reflight provided further proof that the constant irradiance had been eliminated by the redesigned baffle and modified door mechanism because no unexplained signals were observed.

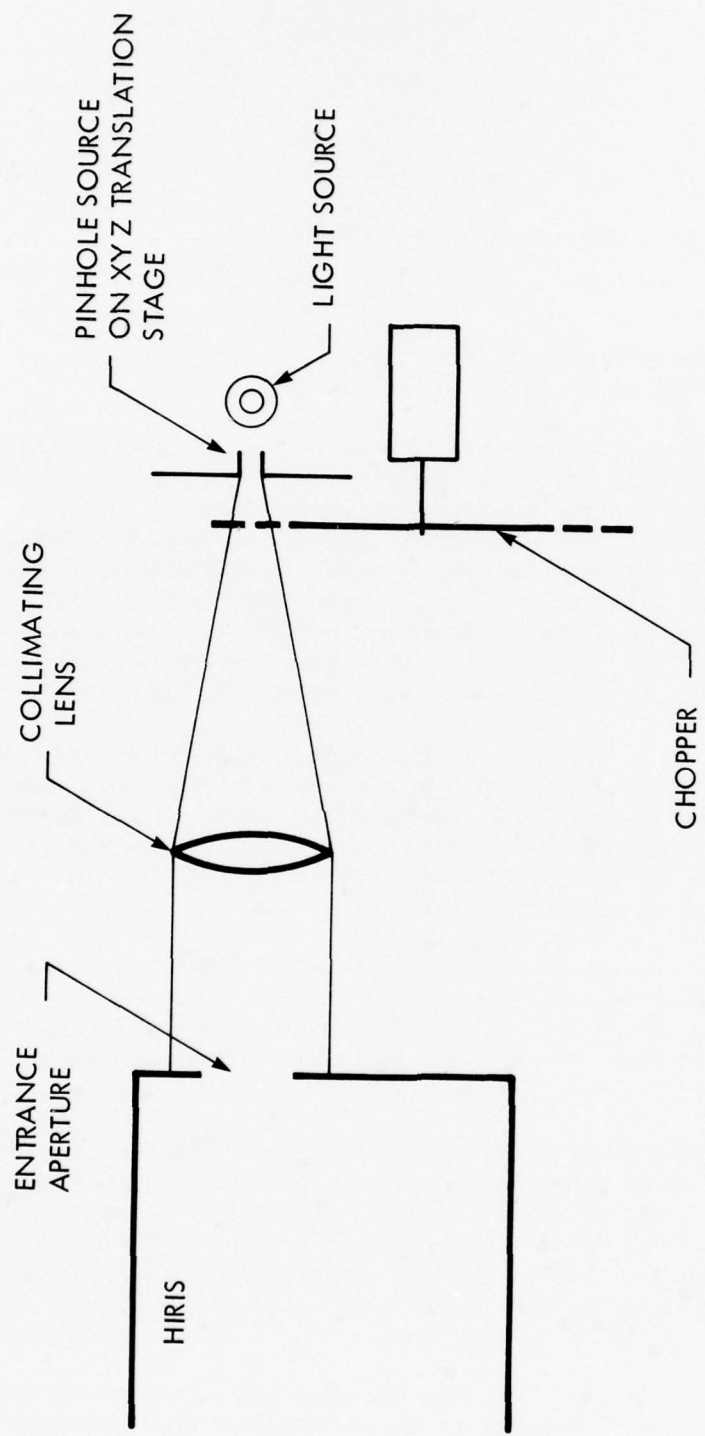


Figure 2.19 IFOV TEST SETUP

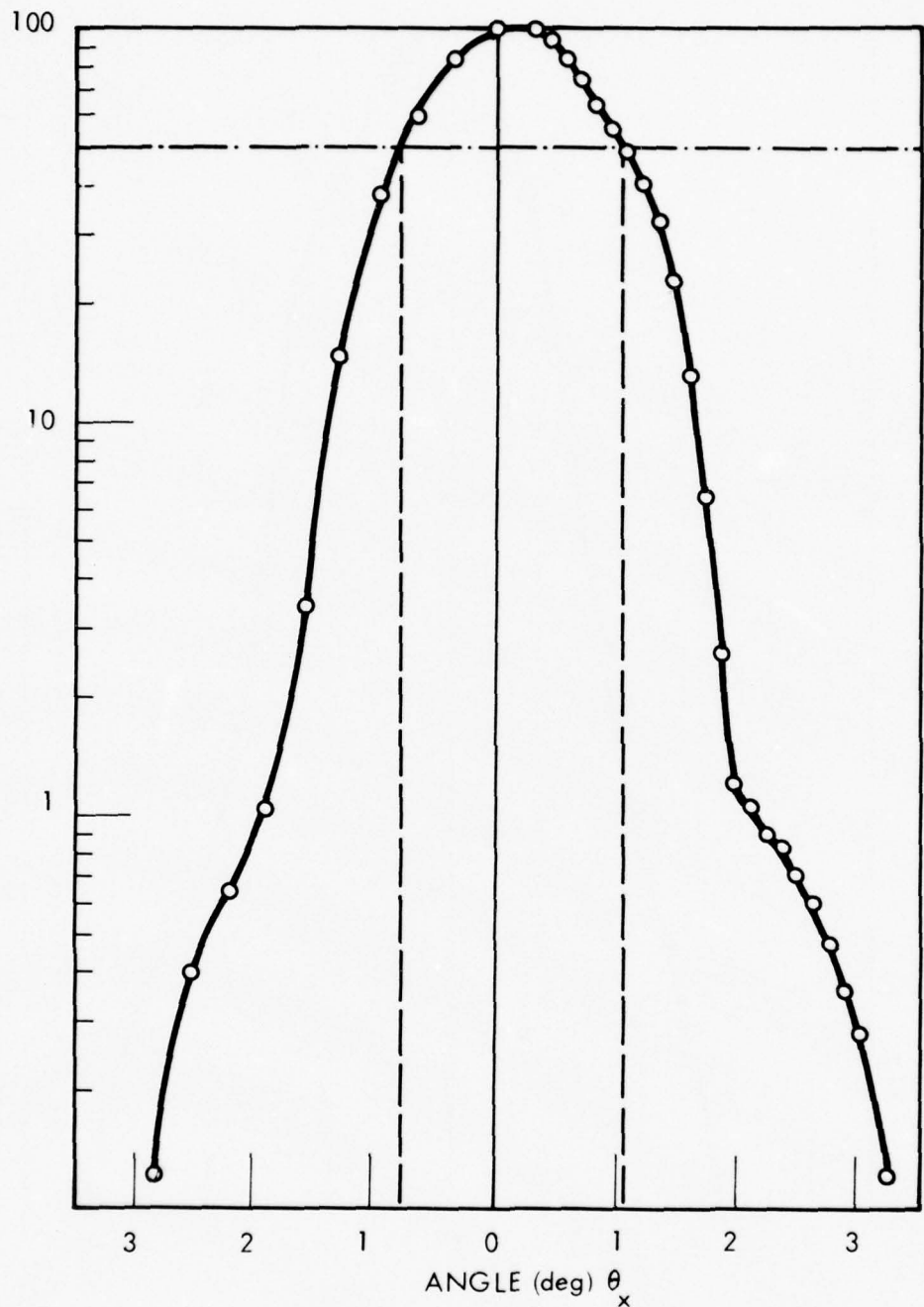


Figure 2.20 HIRIS RELATIVE RESPONSE VS FIELD ANGLE ( $\theta_x$ )

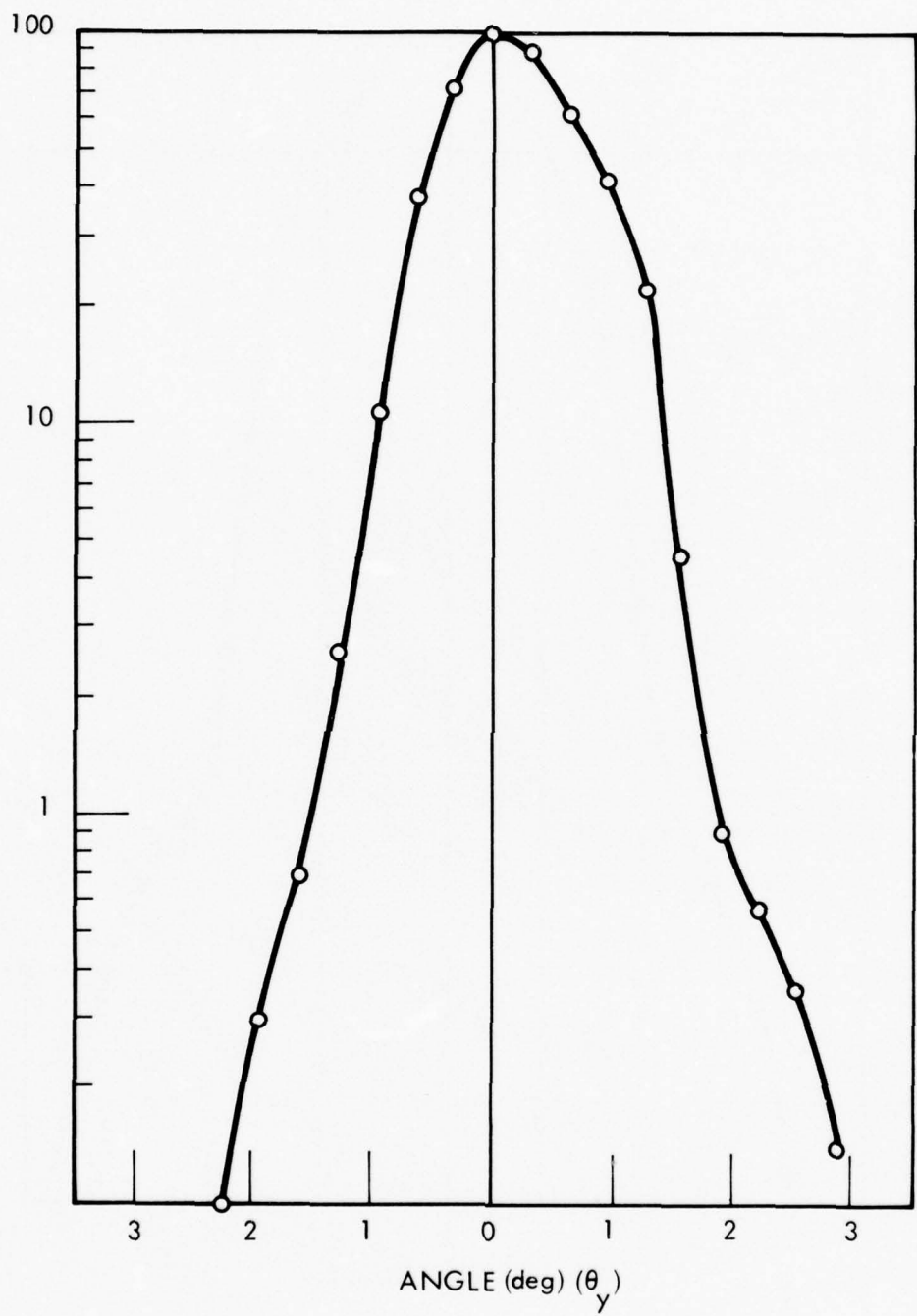


Figure 2.21 HIRIS RELATIVE RESPONSE VS FIELD ANGLE ( $\theta_y$ )

#### 2.3.4 Monochromatic Light Source

The reference interferometer which provides the mirror position and velocity information requires a monochromatic reference source. Traditionally, a helium-neon laser or a single spectral line obtained by filtering the output from a gas discharge tube has been used as the monochromatic reference source. Since the reference interferometer shares the slide and cryogenic environment with the signal interferometer, the reference source must be contained in a photon tight container and must function at cryogenic temperatures.

The development of a gallium arsenide lasing diode for the reference source was undertaken. The lasing diode proved adequate in coherence and intensity and a means of shielding its output from the signal interferometer was developed. However, the lasing diode was found to be unreliable at cryogenic temperatures because it failed after several cold cycles.

Parallel approaches were initiated to obtain a suitable reference source. One approach involved the search for a suitable gas discharge tube. The other approach involved the development of fiber optics which would permit operation of a laser source external to the cryogenic environment.

A study to select the most appropriate gas discharge tube resulted in selection of neon lamps. A sample of various neon lamps was obtained and the starting voltage and currents were measured at 10 K. Several neon lamps, including types NE-2 and NE-67, were found to have satisfactory cold starting characteristics and currents. The starting of the neon lamps at temperatures below the liquid temperature (28 K) of neon is made possible by ions generated by the small amount of radioactive substance contained in the lamps. Spectral filtering of the lamp output is required to obtain the required single spectral line source from the large number of strong, widely separated lines emitted by neon. Cryogenic (10 K) spectral filters operating in the visible spectrum had not been developed by the community of filter vendors. Experiments with candidate filters failed to produce a filter with an acceptable spectral transmission which could withstand the cryogenic environment. The filtered gas discharge tube approach to a monochromatic reference source was, therefore, rejected.

In a parallel effort, a technique and design developed at AFGL was investigated. This technique used an external HeNe laser fed to the interferometer section through a light pipe encased in a protective steel tube. The light pipe/steel tube functioned as a feedthrough to transmit the laser energy through a bulkhead interface. This technique had been proven in room ambient conditions at AFGL. Tests conducted at HRC showed that the light pipe/steel tube could withstand cryogenic temperatures. In performing these tests the fiber optics were folded in half and a portion immersed repeatedly in liquid helium without exhibiting any observable change in optics properties.

Based on the promising results of the test performed on the sample fiber optics, development of a fiber optic light pipe to satisfy the HIRIS reference interferometer requirements was undertaken. Several sources of the glass fiber and steel tubing required to fabricate the fiber optics were investigated and samples were obtained. Photon tight fiber optics assemblies were fabricated from the glass fiber and steel tubing. The difference in the expansion of the glass fibers, steel tubing, and bonding material caused some difficulty in fabricating a tube encased fiber optics which would withstand temperature cycling from room ambient to cryogenic temperatures without delaminating. However, methods and materials were developed which resulted in a satisfactory bond between the glass fiber and steel tubing.

A number of helium-neon lasers and laser power supplies of different manufacture were investigated to identify those which best satisfied the HIRIS requirements. A Spectra physics laser and a Crestronics power supply were selected. HRC made minor modification in the mounting of the laser tube in its housing to provide improved resistance to shock and vibration.

A dry nitrogen filled pressurized container was designed and fabricated to house the laser and power supply as necessary to prevent arcing of the high voltage during flight.

#### 2.3.5 Misalignment Compensation

A requirement for the refurbished HIRIS was to demonstrate improved cryogenic operating temperature alignment stability. Means were to be incorporated that would provide proper interferometer section optical alignment at the operating temperatures near 10 K considering that assembly and initial alignment operations were performed in laboratory ambient temperatures near 300 K.

Both active and passive alignment techniques were investigated. The active technique was based on piezoelectric devices to provide a remotely controlled adjustment of fixed mirror position. This would allow active alignment of the optics at cryogenic operating temperature to eliminate nonrepeatable cooldown misalignments. The passive technique was based on incorporating structural modifications which would result in repeatable cooldown alignment shifts. These shifts could then be compensated in the initial warm alignment to achieve the desired cryogenic alignment.

Both techniques demonstrated successful alignment capability. A piezoelectric mirror alignment device was designed, fabricated, and tested at the sub-assembly level. Tests at 10 K showed that the fixed mirror could be controlled to provide  $\pm 10$  fringes of adjustment with an applied voltage of  $\pm 400$  volts. The range of adjustment could be increased by redesigning the device using closer spaced piezoelectric stacks with thinner wafers and higher applied voltages. However, the passive technique, described below, was also successful, was felt to be a lower risk approach, and was, therefore, incorporated into the refurbished HIRIS.

Improvements in alignment stability were felt to be most likely obtained in the V-cube, which provided the mount for the beam splitter and fixed mirror, and in the retardation mirror mount. Results of a computer analysis of the V-cube showed that the design was not stable over the 300 K to 10 K temperature range. It was found that thermally induced stresses distorted the beamsplitter and affected the fixed mirror alignment.

The V-cube was replaced with a delta cube designed to provide improved stability over the 300 K to 10 K temperature range. A delta cube was fabricated and checked for stability when subjected to a cold cycle test. The newly designed delta cube proved to have superior stability over the required temperature range.

The design of the retardation mirror was also analyzed for stability. The analysis showed that the shaft used to attach the retardation mirror to the slide would bend from the pressure of the retaining set screws. Changes in the bending of this shaft with changes in temperature would cause misalignment of the retardation mirror. A cold test of the retardation mirror mount confirmed the misalignment predicted by the analysis.

The retardation mirror and its attachment to the slide were redesigned to minimize instability with changing temperature. The redesigned retardation mirror was fabricated and subjected to a cold test. The results of the cold test proved the new design to be stable.

The redesigned optical system was assembled and the interferometer was checked for alignment stability when subjected to a cold cycle test. The tests showed a consistent change of alignment of twenty fringes over the temperature range from 300 K to 10 K. The interferometer was realigned to obtain twenty fringes at room temperature and the cold cycle test was repeated. The results of the test showed adequate interferometer alignment at the 10 K operating temperature after several cold cycles.

#### 2.3.6 Electronics

The "off-sensor" electronics hard-wired circuit boards were reconfigured to printed circuit boards to permit repackaging the entire "off-sensor" electronics in a manner which ensured reduced electronic noise levels and improved reliability. The redesign resulted in three discrete packages consisting of a transimpedance amplifier (TIA) assembly, a power regulator and an electronics module. The TIA assembly contains a power filter board and an amplifier board. The electronics module contains: two piggyback modules, a blackbody controller and commutator, a PCM encoder module, a gain switching logic and white light delay board, a timing generator board, a mirror servo board, a temperature monitor board, a reference interferometer (laser and white light) processor board, a signal interferometer processor board, a housekeeping electronics package, and a bus bar assembly.

### 2.3.6.1 Transimpedance Amplifier

The transimpedance amplifier (TIA) design was modified to reduce front-end electronic noise. This was accomplished by replacing the detector bias-battery assembly and associated wiring harness with a highly-filtered and regulated dc supply on the TIA board. This bias supply readily permitted the use of an optimum bias to reduce detector spiking. The signal interferometer dc component was removed from the input of the TIA to permit further log amplification of the dc component on the signal interferometer processor board while establishing only an ac feedback path to the detector MOSFET preamplifier in the dewar. Since initial damping adjustment of the TIA was no longer necessary, the circuit was removed. Preamplifier gain was selected prior to flight by means of a switch on the TIA which selected one of two MOSFET load resistors on the focal plane while grounding the other.

Additional noise reduction was achieved by the design and installation of a dc power supply filter board which filtered the preregulated +18 V and -20 Vdc power to the TIA power regulator integrated circuit. The filter uses a trifilar-wound choke for improved frequency response. The signal interferometer single-ended ac output amplifier, an LM101A, was replaced with two, low-noise OP-05 amplifiers in a balanced output configuration to obtain better common-mode noise rejection.

### 2.3.6.2 Electronics Module

In order to reduce system noise and improve reliability, the entire "off-sensor" electronics assembly was repackaged in a module configuration utilizing photo-etched and shielded printed circuit boards, a prefabricated power bus and ground-plane, assignment of high-noise level (digital) circuits and low noise level (signal processing) circuits to separate specific areas. Signal shielding and terminations were also given a high priority in the repackaging design. With additional digital noise sources reduced by using low-power TTL and Schottky TTL circuits the overall electronics crosstalk and EMI susceptibility were sufficiently reduced to ensure a  $\pm 1$  LSB (600 microvolt) system noise level in the signal interferometer data channel.

Blackbody Controller and Commutator Assembly - The blackbody controller electronics required no redesign. A chassis was designed to accommodate the controller and commutator with their associated wiring harness. The commutator was repaired and operationally checked against the requirements. The wiring harness was designed to accommodate thirty-two parallel channels of housekeeping (i.e., temperatures, critical voltages, and command responses) for redundancy.

Pulse Code Modulation - Both the flight and flight spare pulse code modulation (PCM) encoder crystal-controlled oscillators were modified to reduce the non-return to zero (NRZ) output bit-rate by one-half. The NRZ telemetry output amplifier was modified to: 1) increase output, with one adjustment potentiometer added to set the required transmitter deviation and 2) set the pre-modulation filter at 0.7 x bit-rate (187 kHz).

The sample/hold circuit was modified to increase the sample period from 5 microseconds to 7 microseconds to allow more time to settle on each data sample, and the time between samples was accordingly increased from 39 to 78 microseconds. Since the encoder power supply operated synchronously (to reduce non-coherent noise levels) with the original 26 kHz data sampling rate, the power supply was also modified to operate at the 13 kHz sample rate.

The signal interferometer simulator and PCM decommutator was modified to be compatible with the new scan and mode commands of 1.26 and 0.14 seconds, respectively. The PCM encoder was tested and qualified with the flight transmitter.

Gain Switching Logic and White Light Delay Board - Additional logic was incorporated into the gain switching logic and white light delay board design to provide a 4-sample count delay circuit. In addition, the previous 54 series logic was replaced wherever possible with 54L series logic to reduce logic current spikes. White-light delays up to 16,000 counts are possible with a presetable, programmable up-down delay counter. The nominal delay was 7583 counts between occurrences of white-light and signal interferometer zero retardation during preflight checks.

Gain-switching can be enabled or the system locked in either low (X1) or high (X16) gain. Functionally, gain switching is enabled by the occurrence of the reference white-light. White-light status is delayed to occur simultaneously with the signal interferometer zero-retardation. If the signal interferometer absolute peak level exceeds the predetermined signal processor comparator threshold the processor gain switching amplifier output must be reduced (low gain) to ensure an input to the PCM Encoder A/D converter of less than  $\pm 5$  V until the signal level again falls below the threshold. Since the interferogram is usually symmetrical, an up/down counter is first preset to a count of 128 when the threshold is exceeded, then counts up until the occurrence of the delayed white-light status reverses direction (zero retardation) whereupon it counts down to "zero," returning the signal interferometer signal processor amplifier to a high gain mode. The programmable preset count of 128 allows for slightly nonsymmetrical interferograms.

The 4-count delay provides a means of ensuring that the peak interferogram exceeds the threshold for at least 4 data samples before changing to low gain thereby preventing false gain-switching due to noise spikes. In addition, the gain is not allowed to change while data is sampled by utilizing the PCM sample inhibit pulses for counting and control purposes.

The gain state of the signal interferometer signal processor is fed to the PCM Encoder to ensure proper signal level encoding.

Timing Generator Board - The timing generator board design was modified to incorporate an adjustable low-frequency LM101A op-amp oscillator, allowing the selection of 1 to 4 scans-per-second with a constant interferometer mechanical slide velocity of approximately 5.4 millimeters per second. The previous design required the 912-Hz subframe rate from the PCM encoder. This proved to be a large source of in-band noise. To facilitate small adjustments in the duration of timing commands, the mode command and flyback TTL counters and comparator logic were incorporated. Series 54L logic was used to reduce the current noise spiking. Mode and flyback were set nominally to 1.24 and 0.16 seconds, respectively. Previously, these signals were 0.9 and 0.09 second, respectively.

Mirror Servo Board - The mirror servo board design remained basically unchanged except for the summing amplifier lead compensation, a reduction in motor coil driver gain, and additional laser phase lock loop (PLL) output filtering as required for the increased interferometer slide movement and PLL stability to obtain a 1 wavenumber resolution. In addition, a carefully laid out printed circuit board design was incorporated to permit better partitioning, and consequently better isolation of noisy and sensitive circuits, such as the summing amplifier and LVDT excitation.

Temperature Monitor Board - The temperature monitor board was redesigned to provide four new temperature measurements of the electronics assembly, i.e., the TIA, Power Regulator, Electronic Box A, and Electronic Box B. In addition, auxiliary electronics provides for a calibration command (Blackbody +28 V power on/off) and a blackbody thermocouple readout.

A common +1.3687 volt reference is generated using a 1N4582 6.4-volt reference diode and a HA2929 operational amplifier. Four AD521K integrated circuit instrumentation amplifiers compare the common reference to voltages generated by four USI 44211 thermistors in bridge configurations. Each circuit is calibrated to generate a scale factor  $T_C = 18 \text{ V out} - 20 \pm 1 \text{ C}$ , from  $-20 \text{ C}$  to  $+70 \text{ C}$ .

The blackbody chromel-constantan type E thermocouple readout utilizes a  $0^\circ\text{C}$  reference junction (EZT 213-C9-POC) and an AD521K instrumentation amplifier. The range of operation is 30 K to 300 K with a corresponding output of 0 volt to 5.12 volts. The scale factor is nonlinear, but calibrated at well-known reference points ( $\text{LN}_2$ , Freon 13, ice water). The output is processed by the housekeeping PCM commutator and A/D converter. The GSE computer linearizes and displays the values. However, precision measurements of blackbody temperature were made during preflight calibrations utilizing only the thermocouple and a precision thermocouple bridge setup.

Reference Processor Boards - The design of the reference processor boards was modified to produce a D/A sample pulse at every other laser fringe zero-crossing instead of every crossing, reducing the signal interferometer data sample rate from 26 kHz to 12 kHz. A spare reference detector bias supply was eliminated. Before

flight, the 13-kHz test oscillator circuit was removed to eliminate possible interference between the laser and this source. These circuit simplifications along with the utilization of 54L series logic aided in the reduction of overall system noise. Only the gain select and the sample command output filters were changed to accommodate new signal levels and the 54L series logic.

Signal Interferometer Signal Processor Board - The signal interferometer signal processor board design was modified in order to remove and relocate the TIA external to the electronics assembly to reduce in-band noise.

The signal interferometer dc component, which is removed at the TIA level, is processed by a three-decade dc scaling amplifier with three (3) outputs. These three outputs are further processed (8-bit accuracy) by the housekeeping commutator, extending the resolution of the previous design from 20 to 2.0 millivolts over a limited dynamic range of inputs.

The previous design of the 4-pole signal interferometer data bandpass filter was modified to form two series, 4-pole, low-pass filters. The first section cutoff frequency is approximately 5700 Hz, and the second section cutoff frequency is approximately 6600 Hz. The design of the gain switch amplifier and threshold comparators remained unchanged.

Housekeeping Electronics Package - The housekeeping electronics package was disassembled and the subassemblies retrofitted with a new wiring harness and frame to conform to new electronics box mechanical and electrical layout. Emphasis was placed on reducing noise on signal and power leads to and from the package by improved shielding and routing of all power from the power bus bar assembly.

The command logic section of the housekeeping was modified to cause the blackbody and LED calibration sources to turn-on approximately 75 milliseconds after a command is given. Removal of the command signal will cause the sources to turn off. In addition, the open-cover and close-cover command logic was modified to allow immediate opening and closing of the cover upon command. The opening command was interlocked with a barometric pressure switch during flight as a safeguard against opening the cover at low altitude.

Bus Bar - A potted, laminated, bus bar assembly was designed to permit low impedance distribution of the +15 Vdc, -15 Vdc, +23 Vdc, and +5 Vdc power. The +5 Vdc and +23 Vdc busses are isolated from the more sensitive +15 Vdc and -15 Vdc busses by two ground planes which are terminated to chassis ground. Distribution of power is by means of tabs along the bus bar assembly at the exact location of the boards. No daisy chaining of power was permitted, except where required in the housekeeping package.

### 2.3.7      Ground Support Equipment

#### 2.3.7.1    Electronics Checkout Console

The electronics checkout console was upgraded to accommodate the added monitors and PCM modifications in the refurbished HIRIS. Additional electronics were incorporated to provide read-out of the additional temperature monitors. The PCM decommutator bit synchronizer was modified to accommodate the slower NRZ bit rate of 267 MHz. The test point cable and connectors were modified to interface with the redesigned test and flight cable harnesses. A 5-volt power supply was also replaced.

The upgraded electronics checkout console was utilized at the telemetry site to provide data to the PDP-11 computer via the PCM down link, receivers, tape recorders and decommutator. A new electronics console, described below, was designed for use in the blockhouse.

#### 2.3.7.2    Computer/Electronics Checkout Console Interface

The interface between the PDP-11 computer and the electronics checkout console was modified to provide for real-time co-addition of the signal interferometer output data. The modification was accomplished by the incorporation of a DR-11A interface, providing a real-time co-addition interface logic board, in addition to the original DR-11B interface. This modification permitted a pre-determined number (up to 512) of real-time co-additions of the interferometric data to be commanded from the computer console as well as providing for the normal operation of the HIRIS system.

The real-time co-addition of the interferometric data provides an increase in signal to noise ratio of  $\sqrt{n}$ , where n = number of scans co-added. The improved signal to noise ratio in the interferometric data permits the calibration of the signal interferometer at very low internal blackbody temperatures.

#### 2.3.7.3    Blockhouse Electronics Console

A second electronics console was designed for use in the blockhouse to provide command and status via the payload umbilical connector. This electronics console provides only: test points for selected housekeeping voltages, external power control, and command and status functions. In the blockhouse electronics console, commands are controlled by toggle switches and the status of the received command is displayed by a light emitting diode (LED) located above the toggle switch. The commands provided are:

- 1) Slide Lock On/Off
- 2) Slide Lock Inhibit/Ready
- 3) Slide Rest On/Off
- 4) Calibrate On/Off
- 5) Command Enable/Disable

The command enable/disable switch permitted the other four (4) commands to be enabled during the HRC experiment checkout portion of the launch sequence and to be disabled prior to launch to allow the payload timer/sequencer to be checked out and subsequently actuated at launch time. The slide lock inhibit/ready command permitted HRC checkout of the interferometer by overriding the slide lock function of the payload timer. No cover open and close commands were provided in the blockhouse console because those commands are used only during cover testing at HRC and at the Poker Flats preparation areas.

The blockhouse electronics console provides control of the vent heater, the power regulator and the housekeeping functions. The vent heater control permits vent heater power to be applied until an external heater power supply can be connected during liquid helium filling. Vent heater power can be applied with all other system power shut down to permit safe venting of the gas.

#### 2.3.7.4 Computer Software

The computer software was modified to accommodate the interferogram co-addition, DR-11A interface, and other system changes associated with the HIRIS redesign. The current software, as modified for the HIRIS reflight, provides twelve operator selectable options. These options are:

- 1) Take Data
- 2) Retrieve Data
- 3) Take 30 Interferograms in a Row
- 4) Real Time Co-Addition
- 5) Transfer Interferogram from Tape to Disk
- 6) Transfer Interferogram from Disk to Tape
- 7) Transfer Sums from Tape to Disk
- 8) Transfer Sums from Disk to Tape
- 9) Transfer Flight Recorder to DEC Tape
- 10) Process Data from Flight DEC Tape
- 11) Transfer Co-Addition from Disk to DEC Tape
- 12) Strip Housekeeping Data from Flight Tape

A brief description of the function of each of the twelve options is provided in the following paragraphs:

1. Take Data - This routine enables the operator to record a scan of data onto tape or a disk. It contains all the subroutines for displaying an interferogram in its entirety or in pieces, and for modifying and apodizing the interferogram. The interferogram can be Fourier transformed and the resulting spectra displayed or the values of the spectra printed in tabular form.
2. Retrieve Data - This routine enables the operator to transfer selected, previously recorded data from disk or tape into computer memory. It contains all the subroutines for displaying an interferogram in its entirety or in pieces, and for modifying and apodizing the interferogram. The interferogram can be Fourier transformed and the resulting spectra displayed or the values printed in tabular form.
3. Take 30 Interferograms in a Row - This routine enables the operator to record every fourth sequential scan on disk. It was prepared for laboratory use in observing a dynamic situation and provides for recording 30 distinct, numbered interferograms in four minutes.
4. Real Time Co-Addition - This routine enables the operator to record data from the DR-11A interface. It permits any preselected number of scans to be added together. It records 16,000 points following the start strobe initiated by the white-light pulse. Fourteen bits of interferogram data are recorded for each point.
5. Transfer Interferogram from Tape to Disk - This routine enables the operator to transfer interferogram data from tape to disk via the computer memory.
6. Transfer Interferogram from Disk to Tape - This routine enables the operator to transfer interferogram data from disk to tape via the computer memory.
7. Transfer Sums from Tape to Disk - This routine is no longer used.
8. Transfer Sums from Disk to Tape - This routine is no longer used.
9. Transfer Flight Recorder to DEC Tape - This routine enables the operator to transfer interferogram data from the flight tape to DEC tape via the decommutator and computer memory. Seven interferograms and housekeeping data are recorded on each DEC tape. No housekeeping data is transferred during the scan mirror flyback.

10. Process Data from Flight DEC Tape - This routine enables the operator to process the flight data recorded on DEC tape using option 9. The flight data is unpacked and written on either a disk or DEC tape at the option of the operator.
11. Transfer Co-Addition from Disk to DEC Tape - This routine is not used.
12. Strip Housekeeping Data from Flight Tape - This routine enables the operator to transfer all housekeeping data with interferogram identification number from the flight tape to a single disk. It facilitates tabulation of the flight housekeeping records.

#### 2.4 DEVELOPMENT TESTS

The developmental and/or qualification tests performed at the subsystem level on the laser, fiber optics, beamsplitter, mirror slide, misalignment compensation technique, and electronics module are discussed in the following paragraphs. System level tests performed in a partial or complete integrated payload package are described in Section 3.

##### 2.4.1 Monochromatic Reference Source Qualification

The major components of the reference source were separately subjected to vibration qualification, as described below.

###### 2.4.1.1 Laser

The Spectra Physics laser and the Crestronics laser power supply were qualified to the test levels of AFGL Specification No. 75-1. The laser and its power supply were subjected to the following levels of vibration and shock while operating:

- 1) Sine Vibration Z axis and X axis  
Ref. AFGL Specification No. 75-1, Tech Data  
Section 2.3.1.

<u>Freq.</u>	<u>Amplitude</u>	<u>Sweep Rate</u>
5-14 Hz	0.05 D.A.	2 oct/min
14-2 kHz	$\pm 5$ g	2 oct/min

- 2) Random Vibration Z axis and X axis  
Ref. AFGL Specification No. 75-1, Tech Data  
Section 2.3.2.

<u>Freq.</u>	<u>Amplitude</u>	<u>Sweep Rate</u>
0-100 Hz	+6 dB/octave	$0-0.056 G^2/Hz$
100-1000 Hz	-	$0.056 G^2/Hz$
1000-2 kHz	-6 dB/octave	$0.056 G^2/Hz-0$

- 3) Shock Z axis and X axis  
Ref. AFGL Specification No. 75-1 Tech Data  
Section 3.1

50 g peak amplitude sawtoothed pulse of 6 millisecond duration. Three tests each axis.

No variations in laser output or power supply input were observed during or after the test.

#### 2.4.1.2 Fiber Optics

A length of fiber optics encased in a stainless steel tube was subjected to vibration tests while one end was maintained at room temperature and the other end was maintained at approximately 10 K. The length of the fiber optics assembly was 54 inches with two 180-degree bends of one-half inch radius. The first bend was located six inches from one end of the fiber optics assembly and the second bend was located five inches from the first bend. The straight end of the assembly was mounted on the vibration fixture and the bent end of the assembly was mounted in a fixture which permitted it to be cooled to 10 K. The straight end was subjected to a sine sweep and random vibration per the following schedule:

- 1) Both ends at room temperature  
Sine sweep, 5 g, 14 Hz to 2 kHz, 2 oct/min  
Random, 8.5 g rms, 2 min
- 2) Straight end at room temperature and bent end at 10 K  
Sine sweep, 5 g, 14 Hz to 2 kHz, 2 oct/min  
Random, 8.5 g rms, 1 min  
Random, 8.5 g rms, 2 min

The integrity of the fiber optics was verified after each period of vibration and no degradation in performance was observed.

#### 2.4.2 Beamsplitter Qualification

The beamsplitter used in the refurbished HIRIS system was fabricated and tested to HRC specification 22934ES01. The beamsplitter substrate of hot pressed KCl was obtained from Cooke Optical Company and polished by Janos Optical Company. The Ge coating was applied at HRC under the supervision of Bartlett Systems.

The qualification test of the beamsplitter consisted of: 1) Measurement of the reflectance and transmittance spectra of the beamsplitter at 45 degrees incidence to the coated surface and the determination of the optical thickness of the coating at room temperature, and 2) repeating the test at 10 K and determining the temperature dependence of the optical thickness of the coating. The results of the qualification tests showed the flight beamsplitter optical properties to be within 5 percent of the theoretical values given in Figure 2.22.

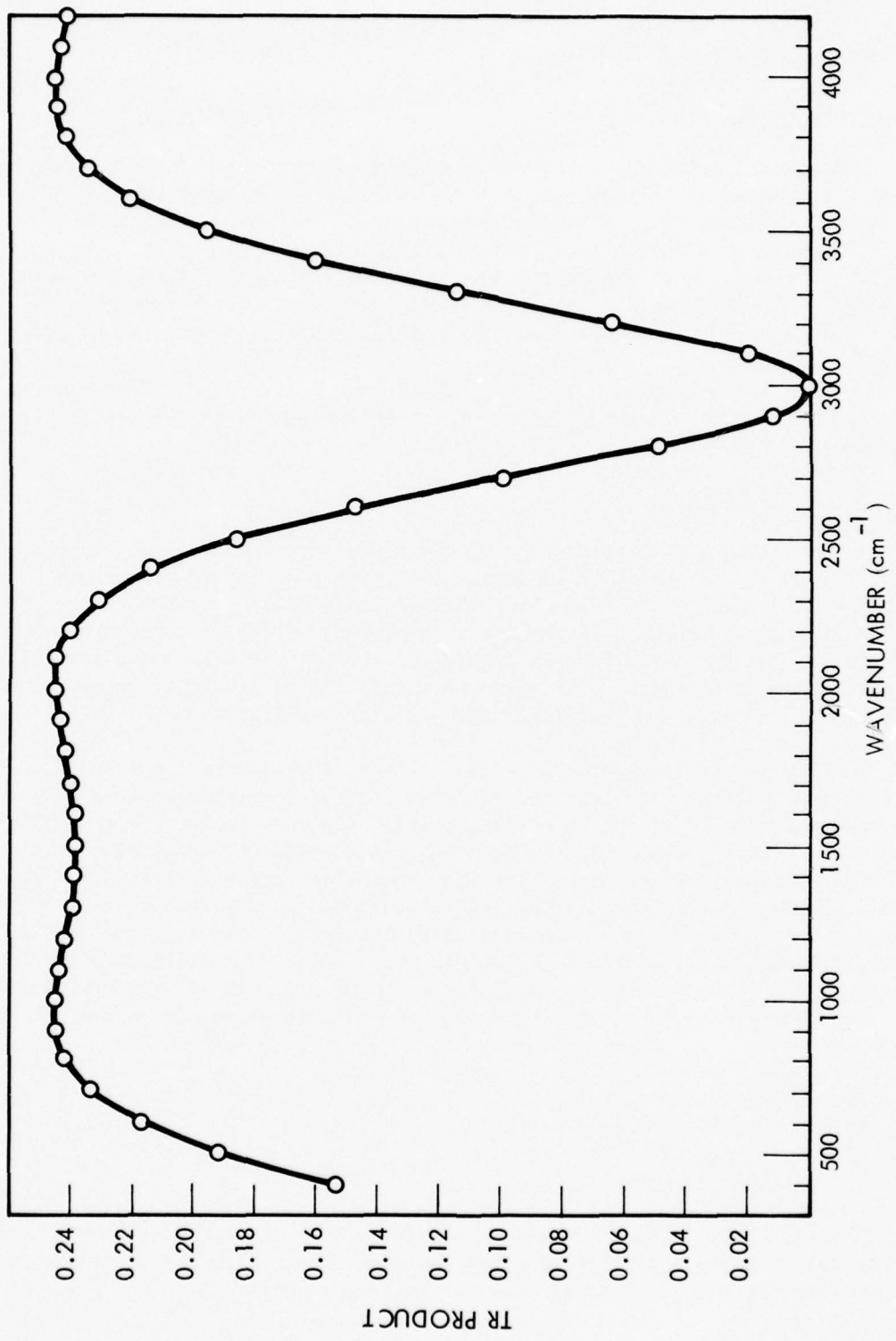


Figure 2.22 BEAMSPLITTER CHARACTERISTIC

### 2.4.3 Electronics Tests

#### 2.4.3.1 Board Level Tests

Functional tests were performed on the redesigned electronics module printed circuit boards A6, A7, A8, A9, A11 and A12 and on the redesigned transimpedance amplifier (TIA) printed circuit board. The tests were performed both on the breadboard circuit boards and on the flight circuit boards. The test consisted of functional and performance measurements made at high, low and nominal supply voltages. In addition, the timing generator circuit board, A7, was tested for output waveform and frequency stability over the temperature range of -20°C to +70°C.

The results of the board level tests showed that the objectives of the redesign had been satisfied.

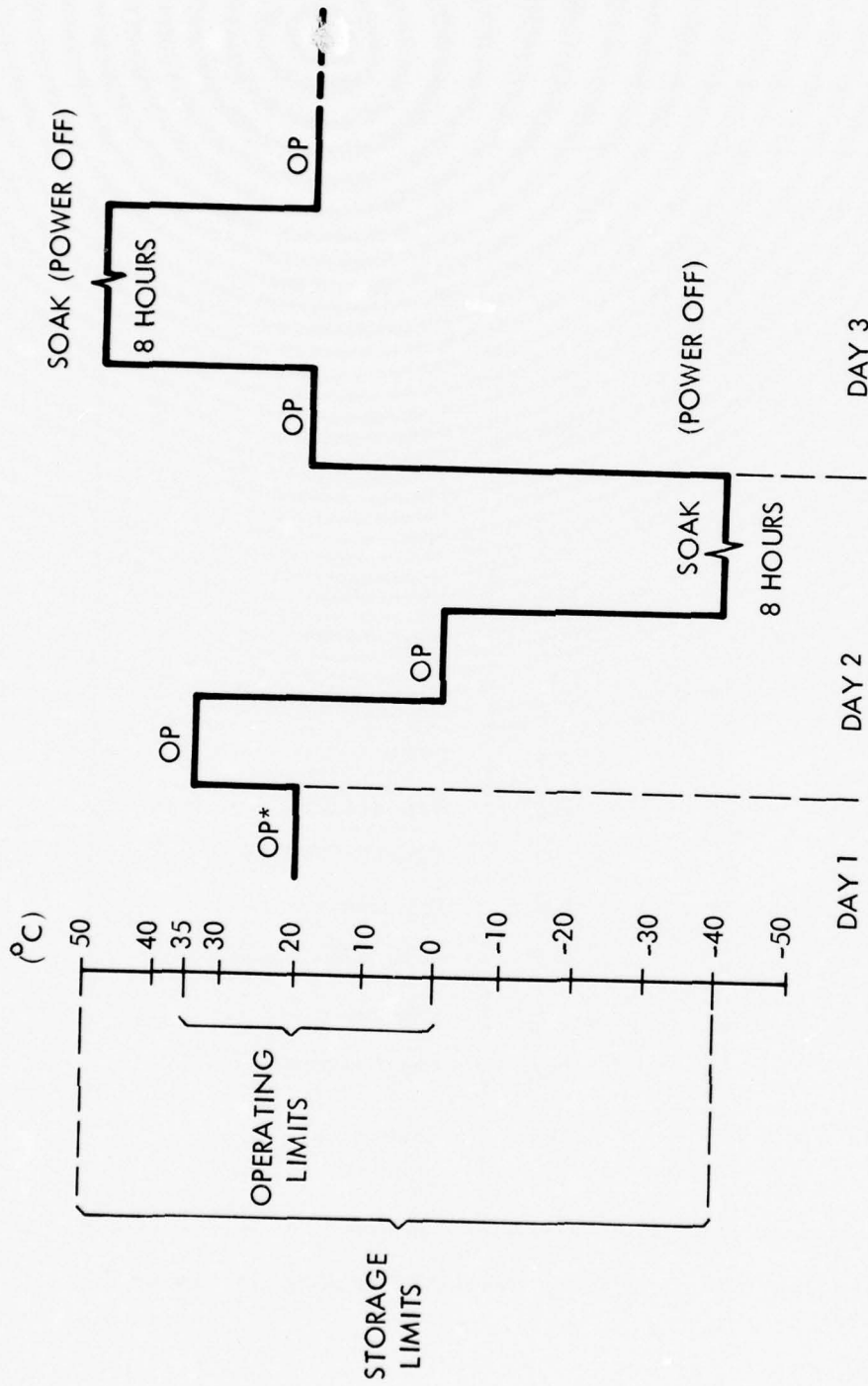
#### 2.4.3.2 Module Level Tests

A test plan was prepared defining the tests required to verify the performance of the redesigned transimpedance amplifier and electronics module under extremes of ground and flight environmental temperatures, in accordance with the requirements stated in Sections 9.1 and 9.2 of ICD-200-1. The thermal profile used for the tests is shown in Figure 2.23. The test plan was also designed to provide the test data which would serve as a baseline during integration and preflight vibration tests and preflight checkout at Poker Flats.

The flight circuit boards were installed in the electronics module and an operating temperature cycle test was performed on the electronics module and the transimpedance amplifier flight circuit board. The necessary input signals and output loads for the electronics module and transimpedance amplifier were provided by a cold HIRIS Dewar. Both the GSE command and control console and the launch (blockhouse) command and control console were used during the test to verify the integrated operation of the system including the GSE. The system test points identified in Table 2.1 were brought out of the test chamber for test purposes and to provide the baseline data for system testing prior to total payload/booster integration. The results of the tests verified the satisfactory performance of:

- 1) Commands
- 2) Housekeeping
- 3) Servo and timing
- 4) Reference channels
- 5) Signal channels

The housekeeping signals were verified via both the computer and GSE. The signal channel was verified using light emitting diode (LED) and blackbody sources and computer real-time co-addition of the signal data.



\* OP = OPERATING ELECTRONICS (POWER ON) SOAK PERIOD IS DETERMINED BY ELECTRONICS BOX TEMPERATURE READOUTS WITH BACKUP CHAMBER THERMOMETER.

Figure 2.23 THERMAL PROFILE

Table 2.1  
TEST POINTS

BOARD/MODULE	TEST POINT	FUNCTION OR CABLE ID
GAIN SWITCHING & W/L DELAY:	A6 - TP6	DEL W/L
TIMING GEN:	A7 - TP3	MC (100 Driving impedance)
	- TP5	FB
	- OVB	OVB, TIMING
MIRROR SERVO:	A8 - TP6	XDUCER (BOWTIE)
	- TP1	PLL
	- TP4	VEL. ERR.
	- OVA	OVA, SERVO
REF. PROCESSOR:	A11 - TP1	LASER, TIA
	- TP5	BIAS
	- TP6	W/L STATUS
	- TP7	SAMPLE COMMAND
	- TP8	W/L TIA
	- OVB	OVB, REF. PROCESSOR
SIG. PROCESSOR:	- TP2	I/F AC
	- OVA	OVA, SIGNAL
TIA:	- TP3	BIAS
	- TP7	RET.

In addition, the W/L "ON" Leads were available externally via an ON/OFF Switch.

## 2.5 ACCOMPLISHMENT AND RESULTS

The performance of the HIRIS system was upgraded by modification of the mirror servo, optical baffles, door mechanism, monochromatic light source, beam splitter, V-cube, retardation mirror, external electronics and GSE.

The mirror servo was modified to increase the scan to 0.5 cm and to improve its response, gain and damping characteristics. The optical baffles and door mechanism were redesigned to eliminate the stray source of constant irradiance. The monochromatic light source was changed from a laser diode to a helium-neon laser and fiber optics assembly to provide improved reliability. The beamsplitter was modified to provide improved performance of the interferometer optics. The V-cube and retardation mirror mechanical assemblies were redesigned to provide improved stability of the interferometer optics. The external electronics were repackaged to improve reliability and reduce electronic noise. The GSE was redesigned to provide for the real-time, co-addition of the interferograms. A blockhouse electronics console was also added to the set of GSE to provide consoles at both the blockhouse and telemetry site.

### SECTION 3

#### HIRIS REFLIGHT

##### 3.1 FLIGHT SYSTEM DESCRIPTION AND CONFIGURATION

The HIRIS reflight system, as described in paragraph 2.1.1 of this report, was integrated with the other systems comprising the payload and GSE by the payload integrator, Northeastern University. An unguided, solid-propellant, rocket motor (Sergeant) lifted the approximately 900-pound payload plus ballast to an apogee of 130 km. Launch was from a standard, MRL20K, rail launcher at the Poker Flats Research Range. Launch elevation was approximately 82 degrees from the horizontal. Figure 3.1 shows the mission profile, and Table 3.1 lists the sequence of flight events by elapsed mission time and payload altitude. The following paragraphs describe the overall reflight system by payload equipments and systems and the ground support system.

###### 3.1.1 Payload Elements

The HIRIS payload, Figure 3.2, includes the following elements from the nose cone aft: ejectable nose cone, photometer (not shown), service module and telemetry antenna, attitude control system (ACS), recovery and turnaround system, and first separation and  $\Delta$  velocity system.

###### 3.1.1.1 Ejectable Nose Cone

The forward portion of the 3.0:1 split ogive is ejected horizontally as a two-piece clam shell. Pyrotechnic actuators and mechanical springs eject each clam-shell half, horizontally, from the payload to expose the HIRIS instrument aperture (covered).

###### 3.1.1.2 Photometer

A Model PM-2 Photometer (Utah State University) mounts on the upper end of the HIRIS instrument to measure the  $3194 \text{ \AA}$   $N_2^+$  auroral activity. It has a field of view of 45 milliradians which is coaligned with the interferometer.

###### 3.1.1.3 Service Module and Telemetry Antenna

The service module contains all payload-support and housekeeping electronics. Major subsystems are: the HIRIS electronics box (see paragraph 4.3.8), flight system power, telemetry subsystem, flight timers, tracking subsystems, recovery location aid, magnetometer and accelerometer, and umbilical connectors. Batteries are employed as primary flight-system power during flight for the experiment and other payload functions. Table 3.2 lists the batteries and their capacities and functions for the HIRIS experiment system. All four batteries are Marathon sealed Nicad.

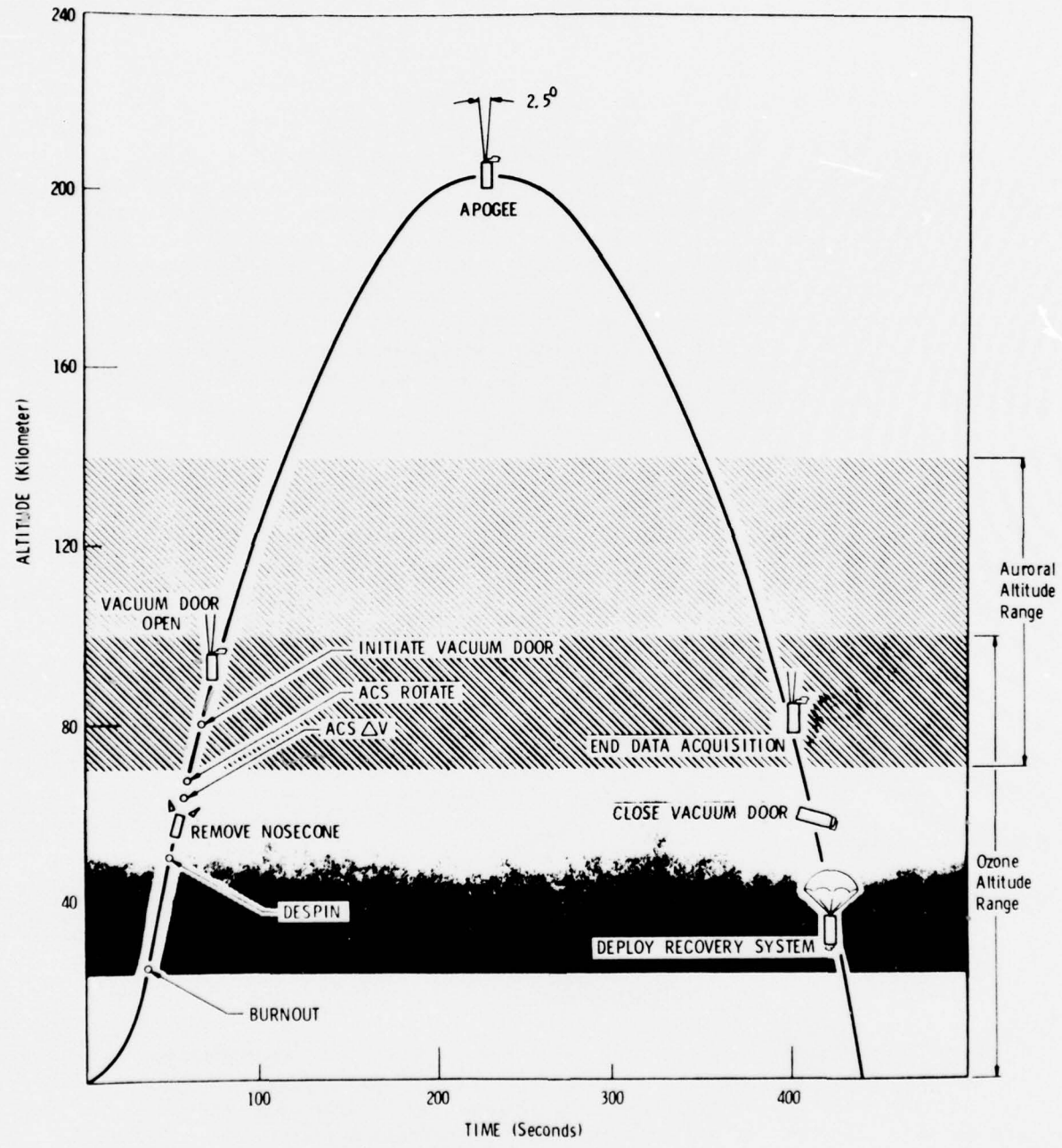
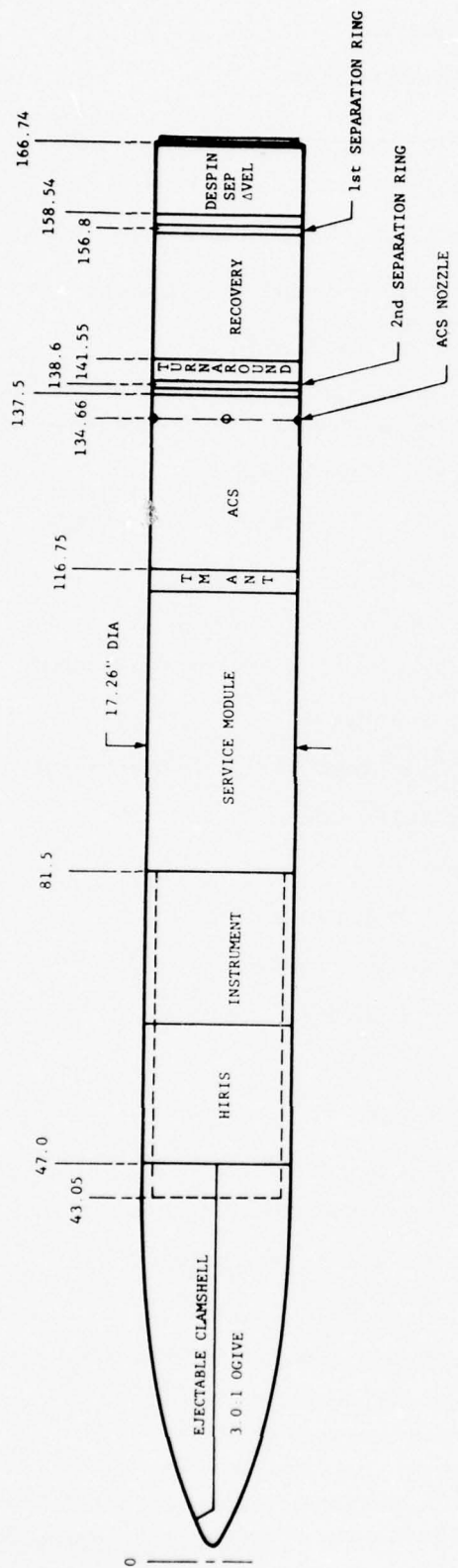


Figure 3.1 MISSION PROFILE

Table 3.1  
SEQUENCE OF EVENTS

TIME (Seconds)	ALTITUDE (km)	EVENT
36	29.8	Rocket Motor (Vehicle) Burnout
51	49.5	Vehicle/Payload Despin
54	53.1	Vehicle/Payload Separation & ACS Activation to hold 66 degrees of Forward Pitch Angle
56	55.5	Activate Vehicle Retro
63	63.6	ACS Erects Payload to 90 degrees
68	69.1	Eject Nose Cone
69	70.1	Activate Payload $\Delta$ Velocity
77	78.3	Deactivate ACS & Remove Slide Lock
78	79.3	Start Calibrate
83	84.1	Stop Calibrate & Start Cover Open
89	89.5	Cover Fully Open
181	130	Apogee
304	60.8	Start Cover Close
310	53.7	Cover Fully Closed
311	52.5	Start Calibrate
316	46.3	Stop Calibrate
317	45.0	Lock Slide
380	15.2	Recovery Beacon On
480	6.1	Deploy Recovery System
620	3.0	Deploy Turnaround System
800	---	Payload Impact



CONDITION	WEIGHT LBS	C OF G IN	RMOI SLUG FT <sup>2</sup>	PMOI SLUG FT <sup>2</sup>	ACS ARM FT
ALL UP PAYLOAD	800	94.4	6.4	24.7	
BALLAST					
AFTER 1st SEPARATION	740	88.9	5.9	18.9	3.81
AFTER CLAMSHELL EJECTION	690	92.7	5.5	15.2	3.50

Figure 3.2 HIRIS PAYLOAD

Table 3.2  
FLIGHT SYSTEM POWER FOR HIRIS EXPERIMENT SYSTEM

ITEM	DESCRIPTION	FUNCTION
1	+28 V Battery, 2.3 ampere hour	Power Regulator
2	-28 V Battery, 1.2 ampere hour	Power Regulator
3	+28 V Battery, 1.2 ampere hour	PCM Encoder, Blackbody, and Laser
4	+28 V Battery, 2.3 ampere hour	Vent Heater and Cover Drive

A two-link, S-band, telemetry subsystem is employed. The PCM encoder output at 233,472 bits per second is transmitted on a PCM link, and all other data functions are transmitted on an FM/FM link. Both transmitters feed a single modular antenna which is the next element after the service module.

Three Northeastern University Model-50 digital programmers supply all in-flight timed functions. The flight timers initiate commands to the HIRIS during flight; these commands are: open cover, close cover, slide rest, slide lock, and calibrate. The timers are started at liftoff by disconnect of the payload umbilical cable.

Two independent tracking systems are employed, a radar and a tone-range system. Ground radar interrogates an S-band radar transponder on board which transmits a coded reply through a pair of antennas, enabling the radar to maintain a continuous lock on the payload. A UHF FM receiver receives tone signals on 430 MHz through another pair of antennas and returns the tone information on the FM/FM link to the tracking system where a computer converts relative phase information to slant range. Slant range can then be combined with azimuth and elevation data from the tracking radar to obtain positional data.

The flight programmer activates a P-band transmitter operating on 242 MHz while the payload is descending on the parachute. The recovery helicopter is equipped by AFGL with receivers and directional antennas to home on this signal. A special lithium battery operates this transmitter for a minimum of 50 hours at -60 F.

A magnetometer monitors payload aspect and spin rate, and a linear accelerometer ( $\pm 25$  g) monitors payload acceleration. The service module has three, recessed, umbilical connectors which permit connecting payload elements to the blockhouse. One line in the umbilical cable connects the HIRIS instrument to the experiment control console; the other two lines connect other payload elements to the payload control console(s).

#### 3.1.1.4 Attitude Control System (ACS)

A three-axis inertial platform provides pitch, yaw, and roll attitude data referenced from an uncaged attitude prior to launch. Maneuvers are pre-programmed and initiated from the flight timers in the service module. Two pitch, two yaw, and four roll nozzles maneuver the payload. A 430-cubic-inch nitrogen receiver, pressurized to 3600 lb/in.<sup>2</sup>, supplies the thrusting medium through a regulator. The ACS will hold roll at less than 90 degrees within  $\pm$  5 degrees and pitch and yaw within  $\pm$  3 degrees of that programmed. Payload attitude is transmitted on the FM/FM telemetry link.

The canister also incorporates a delta-velocity system which increases forward velocity of the payload after ejection of the nose cone. Nitrogen gas contained in a 320-cubic-inch spherical vessel at 3600 lb/in.<sup>2</sup> exhausts through three nozzles, spaced 120 degrees, thrusting 30 degrees off the vertical. The  $\Delta V$  command from the flight timer initiates a squib valve between the vessel and nozzle manifold. The gas exhausts in approximately eight seconds, imparting a minimum 150-pound-second impulse to the payload and increasing its velocity by about 10 feet/second. Both  $\Delta V$  and ACS vessel pressures are monitored through telemetry.

#### 3.1.1.5 Recovery and Turnaround System

In order to recover the experiment, a four-stage decelerator, consisting of a reefed 8.5-foot-diameter main parachute, is employed. Barometric switches actuate this system at 20,000 feet altitude, initiating the sequence. Barometric switches also actuate a payload turnaround system at 8,000 feet. Actuating a manacle ring on the forward end of the recovery module separates the recovery canister from the rest of the payload. An external hinged rod that is attached to this canister and to a point forward of the payload center of gravity then becomes the only connecting member between the payload and the parachute. Because the hinged attachment point is forward of the payload C.G., an aft-end impact occurs, sparing the HIRIS sensor direct impact damage.

#### 3.1.1.6 First Separation and $\Delta$ Velocity System

This housing contains mechanical flight programmers which deploy a "Yo-Yo" despin mechanism and actuate a manacle-ring separation clamp. Compression springs add an increment of velocity along the flight path to the separated payload.

### 3.1.2 Ground Support System

Ground equipment (see Figure 3.3) to support the HIRIS payload includes: an experiment control console, port-control equipment, a payload control console, user trailer equipment, a vacuum pumping station, and cryogenic support. Shorting plugs and standard oscilloscopes and test meters are also required.

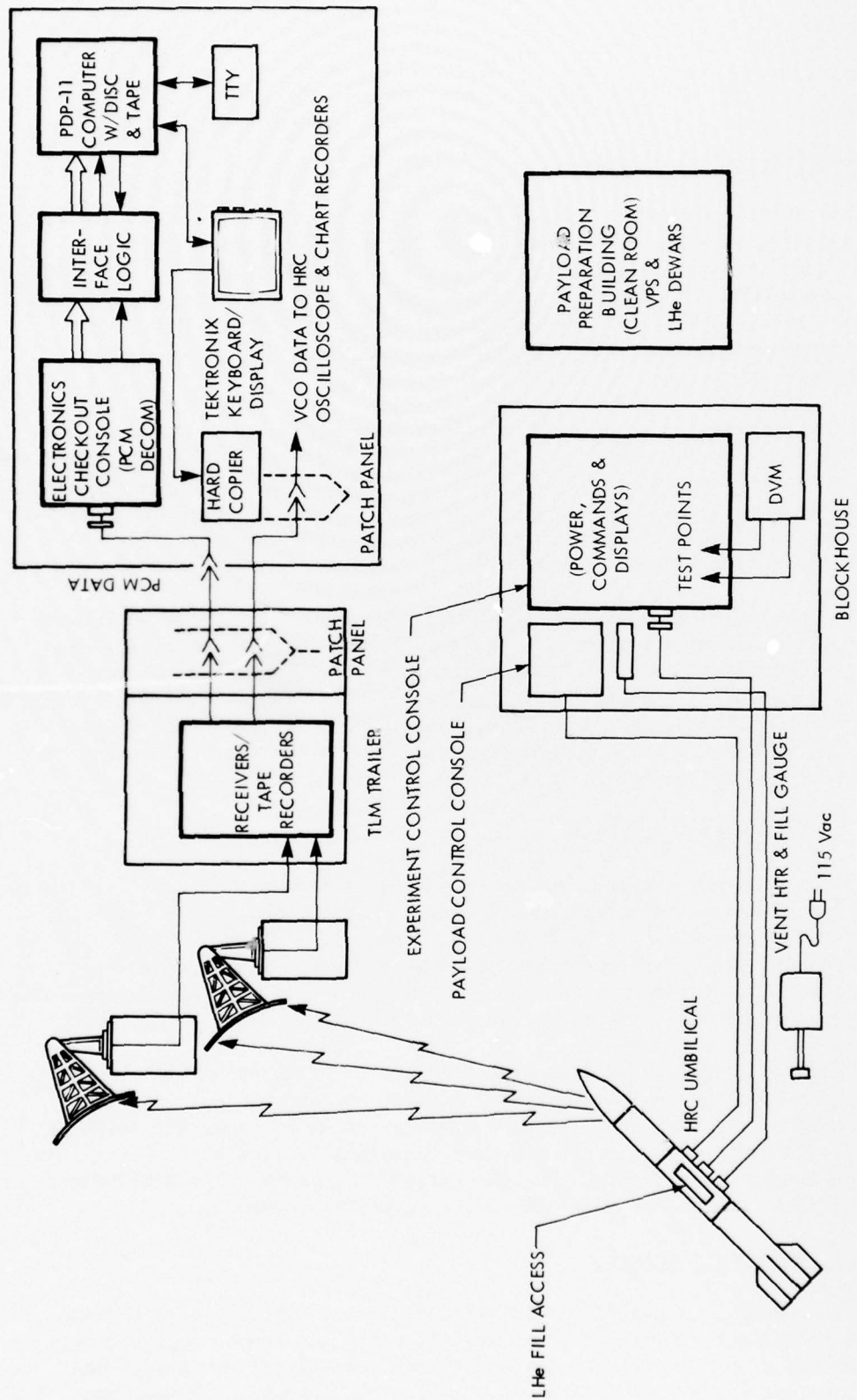


Figure 3.3 POKER FLATS LAUNCH CONFIGURATION

### 3.1.2.1 Experiment Control Console

This console connects to the HIRIS electronics box with a test cable or through an adapter to the umbilical cable. The console contains: power supplies for the instrument electronics in the nonflight mode, command switches and status indicators, a matrix selector switch to monitor selected housekeeping functions on a built-in DVM, a PCM decommutator, and a digital interface unit to connect the decommutator to the PDP-11 computer. Figure 3.4 is a block diagram of experiment control.

Prior to installing the payload on the launch pad, the experiment control console is connected to the experiment by the test cable. Any of the H/K functions may be monitored, the I/F slide may be operated, the cover may be opened and closed (if the dewar is warm and not evacuated), and calibration sources on the cover may be operated (if the dewar is evacuated and cold). The PCM encoder output is available and connected directly to the PCM decommutator and thence to the computer.

When the payload is on the launch pad, the functions of the experiment control console are divided between the range blockhouse and the user trailer. This console still provides at the blockhouse: ground power in the nonflight mode, command and status, and H/K monitoring on the DVM. The rest of the functions principally the PCM decommutator and computer interface, are performed by the electronics checkout console and interface logic unit in the user trailer at the receiving end of the telemetering link.

### 3.1.2.2 Portable Control Equipment

Cold helium gas venting from the dewar has a tendency to cool the vent; water vapor in the ambient air freezes and can block the vent. To prevent this, a heater installed in the vent with a thermistor controls its temperature. When the instrument has power, the vent heater is also powered. However, if the instrument is to be shut down for more than a few minutes, it is necessary to plug a portable power supply and controller into the back of the dewar.

The interferometer slide is free to slide back and forth between its stops when the instrument has no power. To prevent damage when the instrument is moved, a portable battery and control box are provided to power the slide and hold it against a stop. The control box contains six 12-volt storage batteries and a current limiter that controls the current to 0.8 ampere. The HIRIS instrument must not be transported unless this box is connected and operating.

### 3.1.2.3 Payload Control Console

This console, connected to the service module, allows monitoring and operation of the flight timers, ACS, and the telemetry and beacon systems. It also has provisions for controlling the power transfer relays that switch the payload to internal battery power and for checking and charging the payload

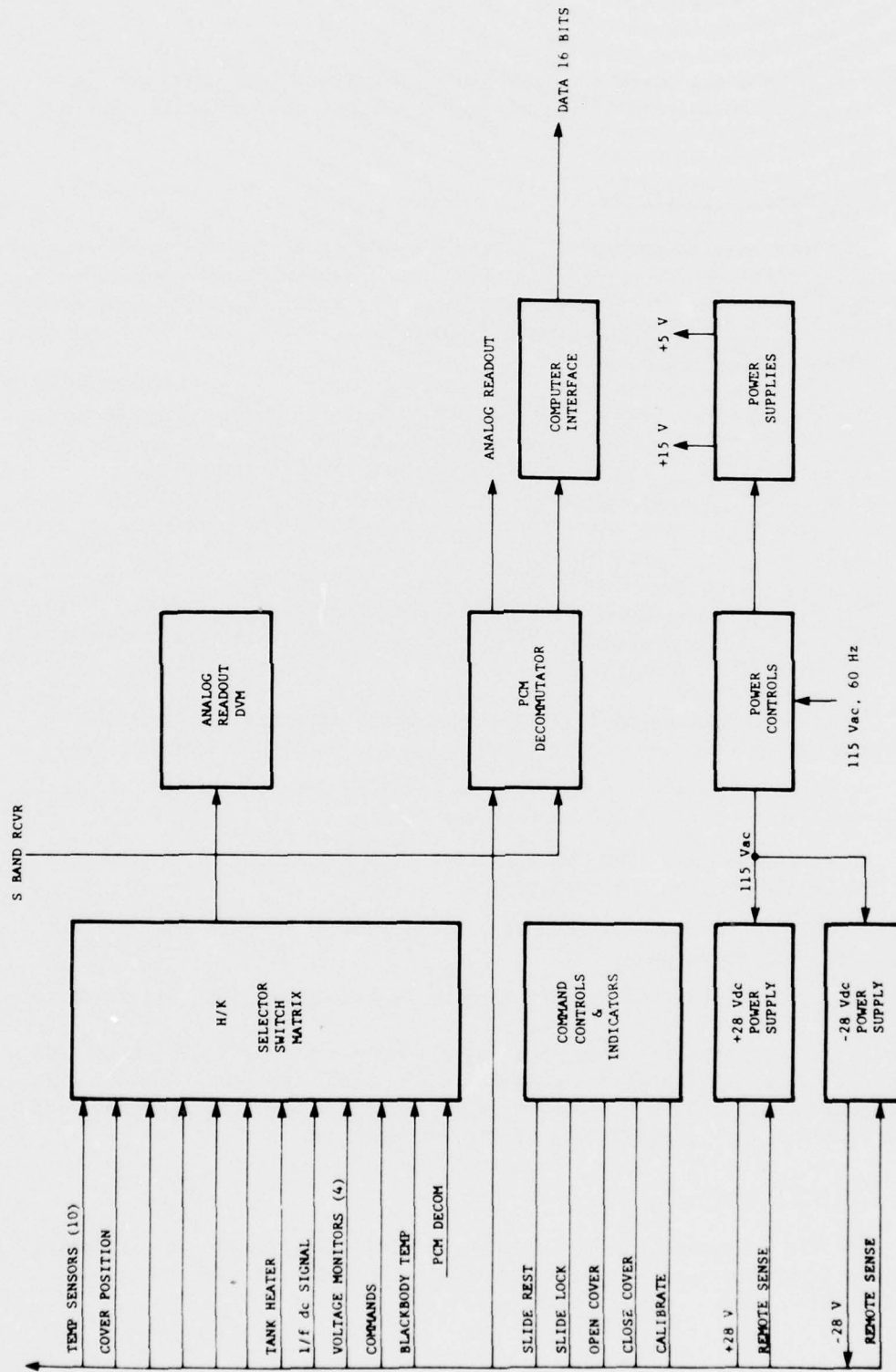


Figure 3.4 EXPERIMENT CONTROL AND MONITOR

batteries. An S-band telemetry receiver and tone filter bank, which can be connected to a high-speed multichannel recorder, permit monitoring the FM/FM telemetry channels.

#### 3.1.2.4 User Trailer Equipment

The user trailer houses all of the GSE for receiving and processing telemetered PCM data. These equipments are: the electronics checkout console, interface logic unit, PDP-11 computer with discs and tape, the experiment status terminal (TTY), a Tektronix keyboard-and-display unit, a Tektronix hard copier, oscilloscope and chart recorders.

The electronics checkout console is utilized primarily for PCM decommutation. The PCM decommutator is connected to the output of an S-band telemetry receiver tuned to the PCM link frequency. The interface logic interfaces the console to the computer. The TTY and keyboard and display unit are readout devices, and the hard copier makes a permanent paper record of the display.

The DEC PDP-11 Computer is equipped with 28 K of core memory, a direct memory access unit, three interface cards, a dual DECTAPE unit, and a flexible disc unit. Programs are available:

- a. To print housekeeping data in either octal directly from the H/K A/D converter or converted to voltages and scaled to temperatures;
- b. To store in core or on the disc and plot an interferogram, the output of a single scan of the instrument;
- c. To co-add in real time corresponding points of successive scans and store and or plot the result;
- d. To convert an interferogram into a spectrum plot using fast Fourier transform techniques;
- e. To modify the spectrum plots with an instrument calibration function.

It is possible to select portions of the various plots and blow them up for greater detail. Scales are automatically calculated and printed on the labeled coordinates. During the flight, telemetry data was recorded on a wide-band tape recorder for later data reduction and analysis.

#### 3.1.2.5 Vacuum Pumping Station

The VPS evacuates the HIRIS dewar, periodically cleans up outgassing, and monitors dewar pressure. It contains a roughing pump, a turbo-molecular pump, a diffusion pump, and an ion gauge.

### 3.1.2.6 Cryogenic Support

Portable liquid-helium storage dewars of 100-liter capacity are used to fill the experiment dewar. The dewar tank requires about 150 liters for initial cooldown and thereafter requires about 80 liters per 24 hours of system operation. Helium is transferred through a flexible double-wall line between the storage dewar and the instrument tank; the space between the line walls is evacuated. A second double-wall line carries the vented cold gas away from the experiment. These lines are terminated at one end with male mini-bayonet fittings, which mate with the female fittings on the HIRIS dewar. The other end of the transfer lines are standard storage-tank couplings. The tank in the instrument dewar has a liquid-helium (superconducting) level sensor. An external instrument is connected to the helium level sensor during fill operations which indicates when the tank is full.

## 3.2 SYSTEM TESTS

The HIRIS reflight system was subjected to vibration tests, flight preparation tests and prelaunch tests as part of the payload. A discussion of the vibration tests, flight preparation tests and prelaunch tests as they pertain to the HIRIS reflight system is provided in the following paragraphs.

### 3.2.1 Vibration Test

The HIRIS system was integrated into the payload in the HRC laboratory by Northeastern University. The HIRIS system was cooled down and its performance measured and found to be in agreement with the baseline data. The test configuration is shown in Figure 3.5. The payload, with the HIRIS system cooled down, was then moved to AFGL for vibration tests.

Vibration tests were conducted at AFGL with the HIRIS integrated into the payload package. The test configuration is shown in Figure 3.5. The vibration test consisted of a simulation of the vertical vibration environment encountered by the payload during powered flight. The vibration test was performed by AFGL using a vibration environment defined by the payload integrator, Northeastern University. Since the slide lock in the HIRIS system is engaged throughout powered flight, it was engaged during the vibration test and the system operated in a nonscanning, nondata taking mode. The output of the He-Ne laser reference interferometer and the output of the linear transducer were monitored on an oscilloscope throughout the vibration test to obtain a measure of slide motion. The HIRIS system housekeeping data was telemetered and recorded using Northeastern University's R.F. down link and a receiver/recorder. The oscilloscope data showed that the slide did not move off the end bumper during vibration test. The recorded housekeeping data was compared with the baseline data and found to be normal.

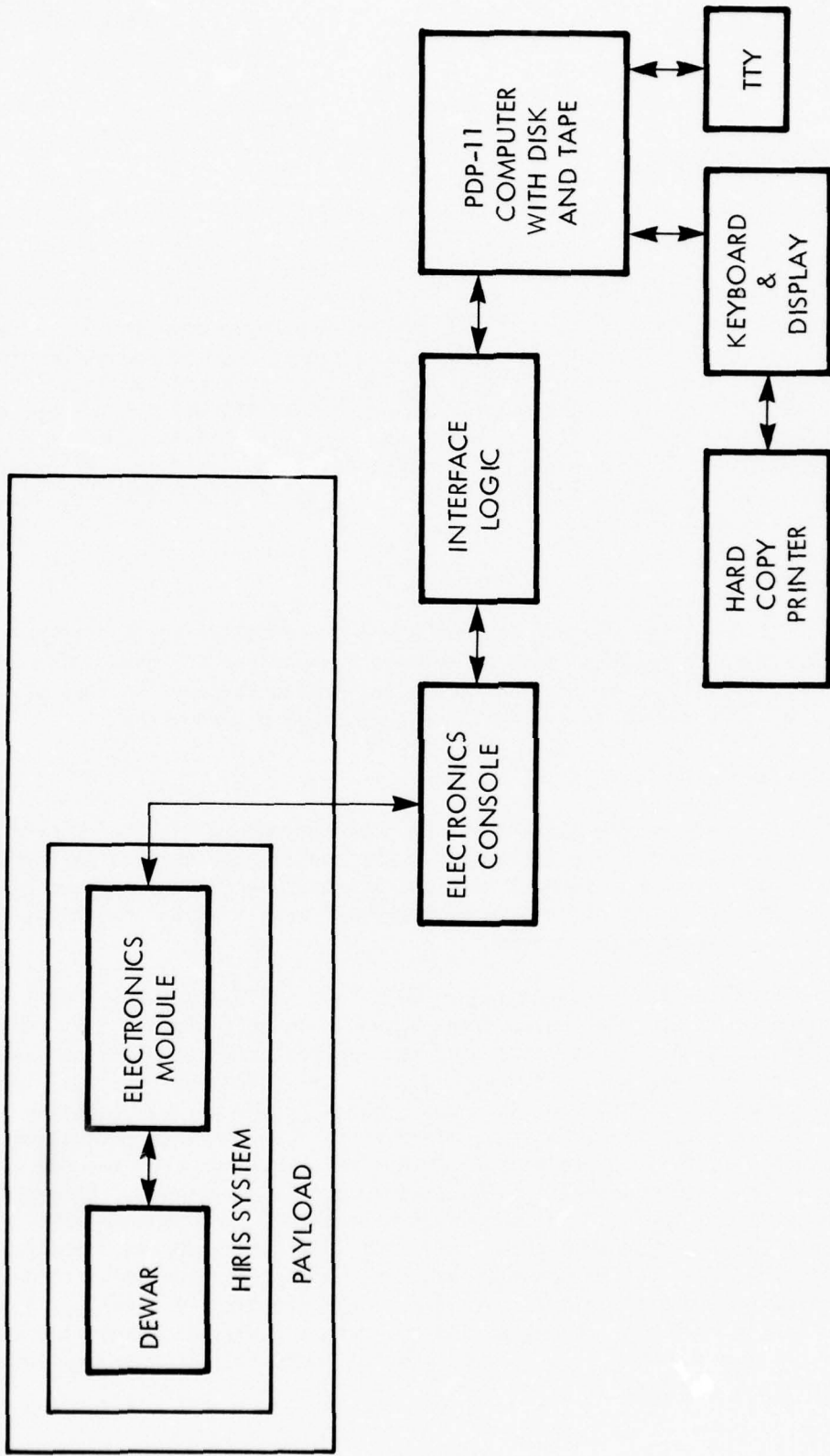


Figure 3.5 LABORATORY AND PREFLIGHT CONFIGURATION

Following the vibration tests, the HIRIS system was returned to HRC for post vibration test. During the post vibration test it was found that the He-Ne laser reference interferometer output amplitude had decreased. Investigation showed that the decrease in output amplitude resulted from a misalignment of the fiber optics and lens assembly caused by the relief of stresses in the fiber optics tube and lens mount. Although the reduction in reference interferometer output was not sufficient to significantly affect the system performance, the lens and fiber optics were realigned. All other system and housekeeping data obtained during the post vibration tests agreed with the baseline data indicating that no other degradation in system performance had occurred during the vibration test.

### 3.2.2 Flight Preparation Tests

The HIRIS was mated with the nose cone and Northeastern University's payload support electronics and tested in the flight preparation area at Poker Flats. A pre-cooldown test was performed on the electronics and the data obtained was found to be in agreement with the ambient temperature baseline data. The HIRIS system was then cooled down and a test of the entire system performed using both the blackbody and LED sources. A comparison of the data obtained during the test with the baseline data indicated that the system was normal. The preflight test configuration is shown in Figure 3.5.

Following the above HIRIS system tests, sequence checks of Northeastern University's flight programmer/sequencer and telemetry systems were performed. The HIRIS system was operated (with the door mechanism disabled to protect the interferometer) in support of these non-HIRIS systems tests. Subsequent to the flight programmer/sequencer and telemetry tests, the HIRIS system received a final calibration, discussed in paragraph 3.3.

The HIRIS system was then tested in a vertical orientation to assess the performance of the interferometer when subjected to the 1-g load imposed by the launch configuration. As expected, the mirror servo performance was marginal and it was decided that the HIRIS performance on the pad would be assessed prior to erection of the missile.

### 3.2.3 Prelaunch Tests

The HIRIS system underwent cleaning and final assembly with the payload and was moved to the launch site where it was mated with the Sergeant booster. The launch configuration is shown in Figure 3.3. Horizontal and vertical performance checks were made using both the external power from the HIRIS electronics console in the blockhouse and internal power from the flight batteries in the payload. The HIRIS system operation was controlled via the HIRIS electronics console in the blockhouse. The HIRIS system status and performance data was obtained via the umbilical and the HIRIS electronics console in the blockhouse and via the telemetry link and the HIRIS GSE including the PDP-11 computer at the telemetry site.

### 3.3 HIRIS CALIBRATION

Preflight calibration of the HIRIS was performed using the AFGL bolt-on calibrator and the internal HIRIS blackbody source, the intention being to perform a comprehensive post flight calibration using the LBCF when the LBCF became available. The sources available for the preflight measurements provided the capability for calibrating the instrument spectral responsivity, but not for field-of-view mapping, which was scheduled for post-flight measurements. Post flight calibration measurements will be performed under a separate contract and will be reported separately.

#### 3.3.1 Preflight Measurements

Since the HIRIS mission involves measuring extended mission sources, the quantity of interest is the source radiance, expressed in units of watts/ $\text{cm}^2 \text{sr cm}^{-1}$ . The ideal method of calibration using an extended blackbody filling the HIRIS field of view was employed, as shown schematically in Figure 3.6.

However, the extremely high sensitivity of the HIRIS instrument precluded the use of source temperatures greater than 100 K, to avoid system saturation. This restriction limited the availability of extended source data to the 600 to 1000 wavenumber range. To obtain data out to 2500 wavenumbers, the HIRIS cover-mounted blackbody was utilized. Some runs included lithium fluoride or sapphire blocking filters to avoid saturation, as shown in Figure 3.7. This allowed source temperatures as high as 300 K, which produced adequate signal out to 2500 wavenumbers. The geometric effect of using a "point source" blackbody was determined by using data near 1000 wavenumbers. In this region signal was available from both the extended source and the point source. The geometrical factor G was determined from the relation:

$$G = \frac{V_p(1000)}{V_E(1000)}$$

where  $V_p$  and  $V_E$  are the Fourier transformed computer voltages for the point source and extended source respectively, normalized by the respective Planck function radiances. Instrument spectral responsivities obtained with the point source were divided by G to produce the equivalent extended source radiance responsivity. The HIRIS spectral responsivity function is plotted in Figure 3.8.

#### 3.3.2 Calibration Data Processing

The basic flow of calibration data is shown in Figure 3.9. The output of the HIRIS A/D converter/PCM encoder was decommutated and transmitted to the PDP-11 computer. The data were stored on the PDP-11 disk. Data quality was assessed by retrieving stored data and performing Fourier transforms on the PDP-11. In cases where the signal to noise ratio of a single interferogram was inadequate,

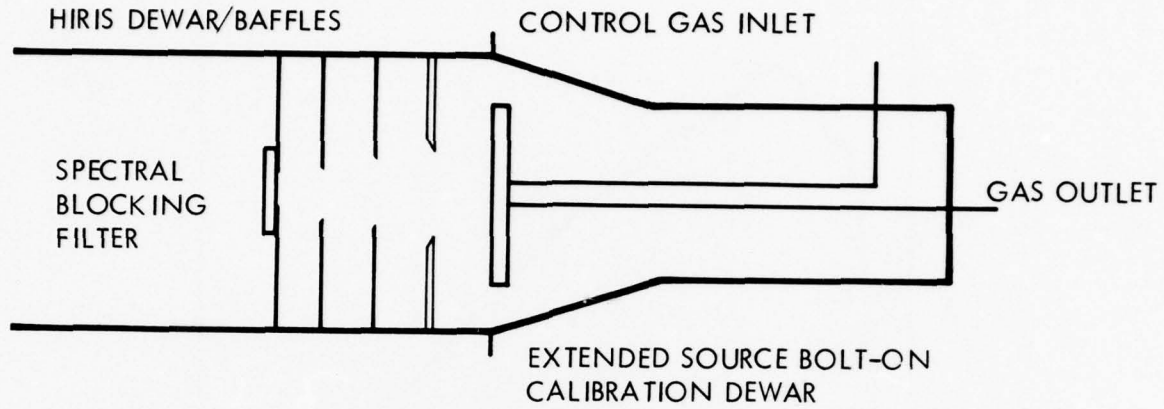


Figure 3.6 EXTENDED SOURCE CALIBRATION SETUP

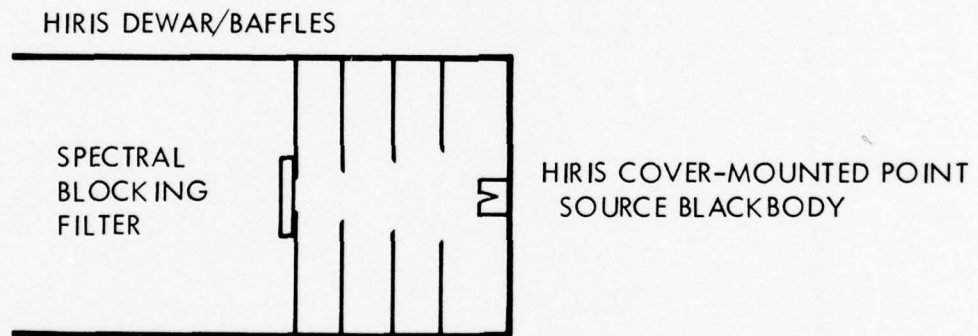


Figure 3.7 POINT SOURCE CALIBRATION SETUP

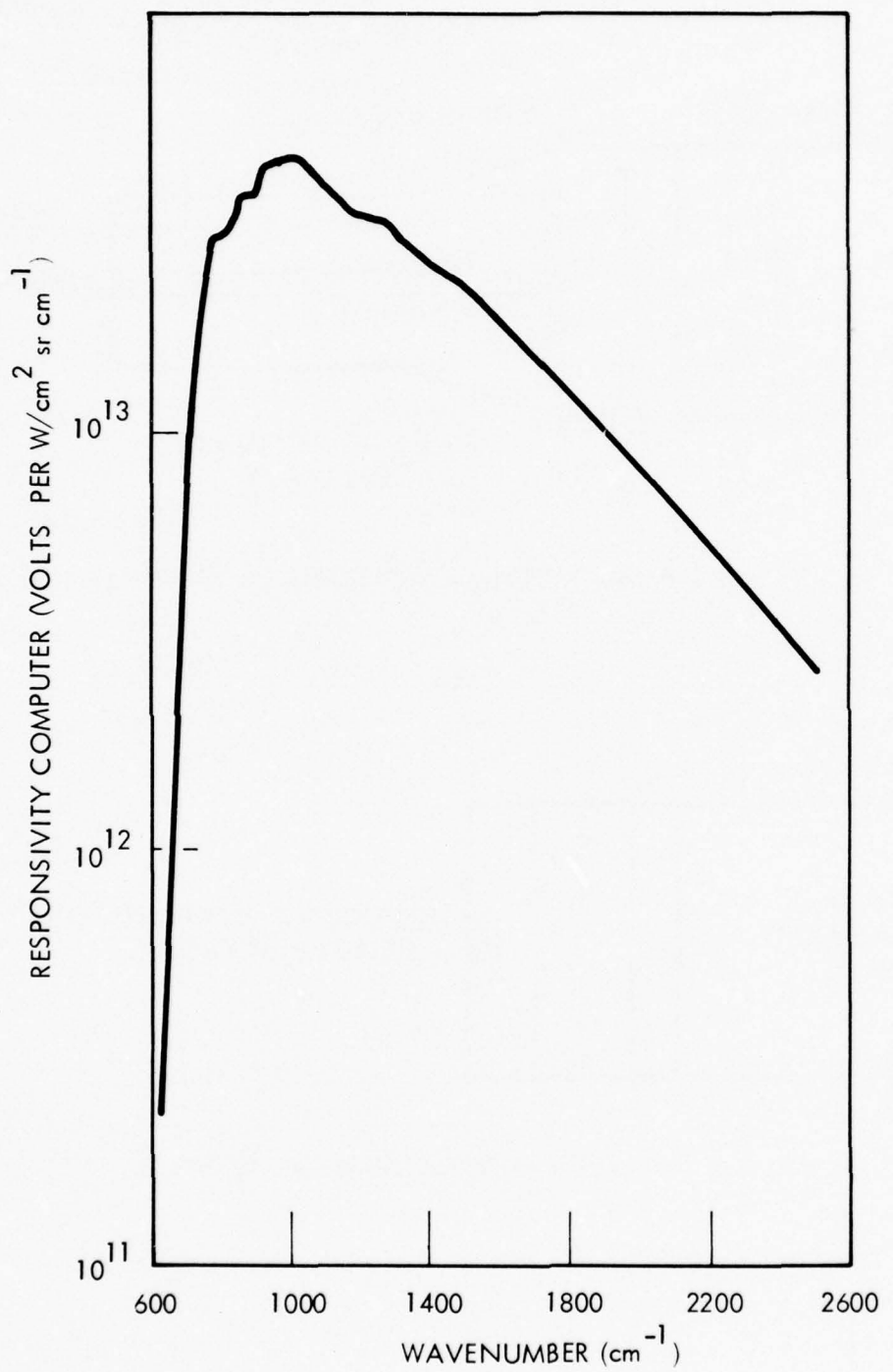


Figure 3.8 HIRIS SPECTRAL RESPONSIVITY

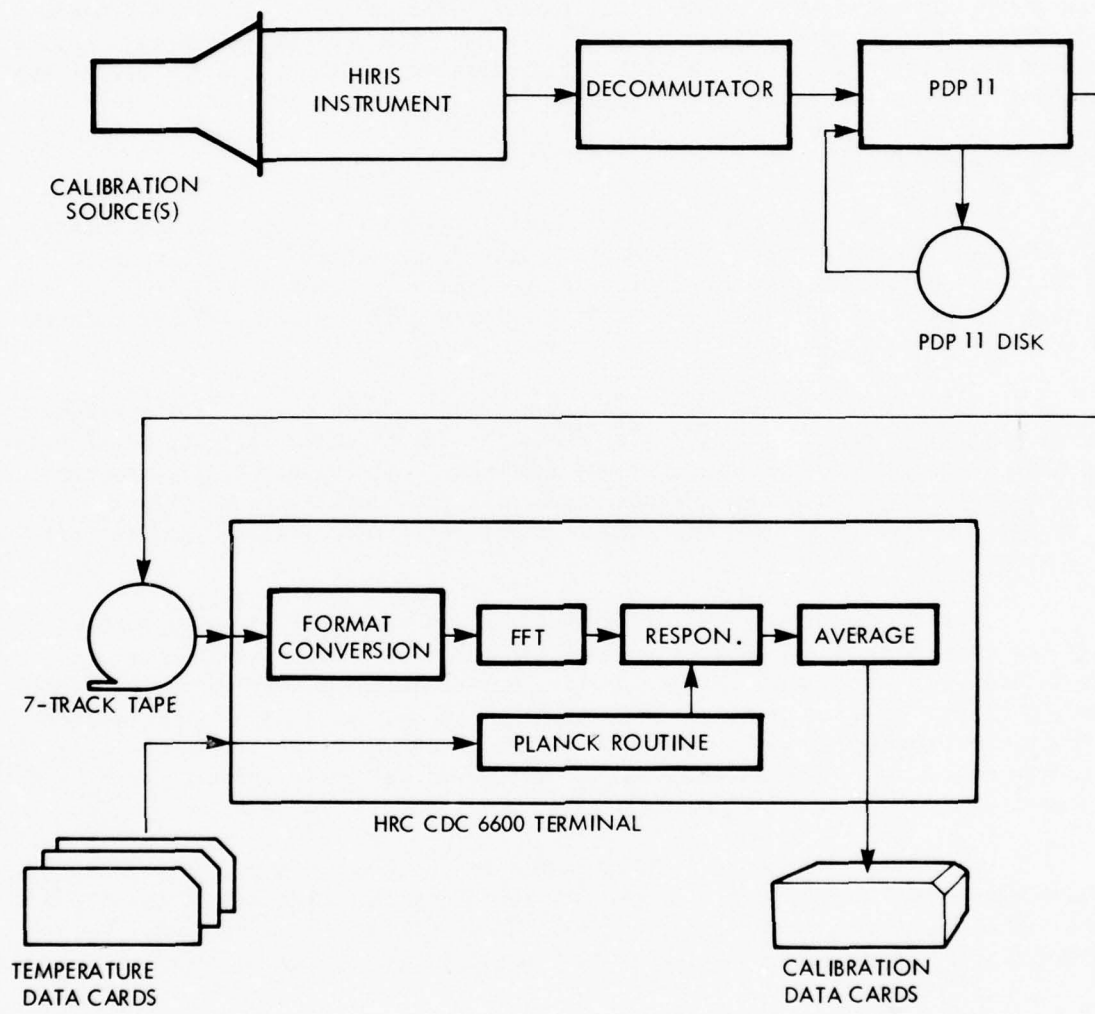


Figure 3.9 CALIBRATION DATA REDUCTION

coherent addition of many interferograms was performed in real time. For some source temperatures, it was necessary to co-add up to 512 scans to produce adequate signal to noise. Selected interferograms were transcribed to 7 track tape for inclusion in the CDC 6600 responsivity data file. Format conversion was performed followed by Fourier transformation and responsivity determination. Source temperatures were input from cards. The geometrical factor is stored with the program code since it is an invariant of the calibration. The average of several responsivity determinations was performed and the results were punched on cards for use by the flight data reduction software on the AFGL computer.

### 3.4 LAUNCH SITE OPERATIONS

Preparation for flight covers the activities from the time field service personnel and equipment were on the launch site until launch. Prior to their arrival, a document entitled "HIRIS Field Operations Procedures Manual" was prepared by HRC<sup>3</sup>. This manual served as the basic guidance for field procedures during this period.

In the field environment, it was not possible to protect the instrument in conventional clean room conditions. Under these circumstances, the dewar cover was kept closed except when the unit was returned to the clean facility in the payload preparation building. Standard cleaning procedures were applied to the instrument exterior prior to the opening of the cover and access to the interior of the module.

Standard laboratory-safety precautions were adhered to while working with the equipment in the payload preparation building. While working in the launch area, personnel took care to avoid: using equipment that generates static charges in the vicinity of the solid-propellant rocket; working at the launcher without the cognizance of blockhouse personnel; and smoking in the launch area. A specified set of safety precautions was observed whenever personnel were handling cryogenic substances or equipments.

The basic philosophy of maintenance in the field was to replace failed subsystems at the board level. A complete set of spare boards was at the field site, and some spare parts for field repair of boards were also on hand. Failed subsystems were repaired in the laboratory area of the payload preparation building.

#### 3.4.1 Field Checkout Activities

##### 3.4.1.1 Preliminary On-Site Tasks

Upon receipt of the payload in Alaska, the first task was to verify that the current from the slide-lock battery was 0.8 ampere. This meant that the slide was not loose during shipment from HRC to the Poker Flats test range. Next, the payload was uncrated and installed on the payload dolly in a payload preparation area. The GSE was uncrated and arrayed around the dolly for convenient access. The slide-lock battery was disconnected and recharged.

#### **3.4.1.2 Dewar Shorting Plugs**

The MOSFET transistors in the signal and reference preamplifiers of the HIRIS instrument are susceptible to damage by static electricity. To minimize the possibility of damage, the connectors on the dewar for these two signal cables have been fitted with parallel connectors and shorting plugs. These plugs are installed when the system is powered down before disconnecting their associated cables. They are removed after cables have been reconnected and before power is applied. When testing the detector assembly in the dewar, all test equipment was grounded to the dewar, and the operator wore a wrist strap which was also grounded to the dewar.

#### **3.4.1.3 Warm System Checks**

The laboratory and preflight configuration of Figure 3.5 was set up in a work area of the payload preparation building, and the precooldown tests were conducted. Baseline checks were performed on the HIRIS instrument and other payload elements and systems from their controlling consoles. The computer system was baseline checked with the software. Then, the payload was moved into the clean room of the payload preparation building for dewar cover checks. The cover was first opened and closed from GSE commands and then from flight-timer commands; cover-position voltage and time data was monitored and recorded. After these cover open/close checks, the payload and GSE were moved from the clean room to the original work area.

#### **3.4.1.4 Cold System Checks**

The vacuum pumping station was connected to the dewar, and it was evacuated and subsequently cooled down. A test of the HIRIS flight system was conducted and some adjustments were made. All data was measured and recorded, including scope photos and hard copies of interferograms and transfers. The output of FM/FM telemetry channels was recorded. All five commands were exercised from the electronics checkout console, and then the flight-timer sequence was operated. After checking the hard-wiring and switch settings in the electronics box, all batteries were charged, the portable slide-lock controller was engaged, and all sections of the payload were reinstalled. Final calibration was completed in accordance with paragraph 3.3. The portable vent-heater control unit was connected to keep the instrument cold.

### **3.4.2 Prelaunch Preparation and Checkout**

#### **3.4.2.1 Launch Configuration**

The launch configuration of Figure 3.3 was established. A wideband tape recorder was connected to the telemetry receiver in the telemetry trailer. The experiment control console, payload control equipment, power supplies, and the umbilical cables were patched to the mini-blockhouse near the launch pad.

With the slide-lock battery control on, the assembled payload was moved to the launch pad and joined to the Sergeant rocket motor and installed on the launching rail. A liquid-helium storage dewar and transfer lines were set up on the pad along with ACS nitrogen-charging equipment for topping off tanks. The portable vent-heater controller was connected.

#### 3.4.2.2 Vertical Checks

An integral part of the countdown was the vertical checks. These checks verified that the equipment was ready for launch. The countdown was restarted, thereafter, when members of the flight director's team in a nearby visual and radiometric observatory advised that auroral conditions were optimum for launch.

#### 3.5 HIRIS REFLIGHT

The HIRIS reflight was successfully launched from Poker Flats, Alaska, on 1 April 1976 at 08:05:20:034. The rocket engine carried the 900-pound payload to an apogee of approximately 126 km. A total of 171 spectral scans was obtained with 150 of these being taken between the cover opening at 88 km on the upleg and closing at 62 km on the downleg. Good signal-to-noise telemetry was received throughout the flight. Recovery of the payload was successfully accomplished, and post-flight operation indicated that the instrument was in excellent condition.

The payload penetrated an area of class II aurora which had been predosed by a class III+ aurora on the upleg and a class II+ aurora on the downleg. The Chatinika incoherent backscatter radar, operated by Stanford Research Institute, reported electron densities of over  $10^{16}$  cm<sup>-3</sup> during the entire time of data taking. The onboard photometer did not obtain information on the emission at 3914 Å within the interferometer's field of view. However, complete documentation of the auroral conditions is available through the comprehensive ground-based data obtained by the University of Alaska. The attitude control system did not attain the planned vertical attitude stabilization, and the payload pitched at the rate of 10.5 degrees/second. These maneuvers in no way affected interferometer performance, but resulted in its field of view scanning across the sky; periodically looking vertically, through the earth limb, and down at the earth.

The interferometer seems to have worked extremely well throughout all phases of the flight; therefore, excellent first-of-its-kind data were obtained not only during the vertical viewing time, but at all other aspects as well. Emission spectra of the atmospheric species CO<sub>2</sub> at 2325 cm<sup>-1</sup> (4.3 micrometers) and 667 cm<sup>-1</sup> (15 micrometers), O<sub>3</sub> at 1042 cm<sup>-1</sup> (9.6 micrometers), and NO at 1786 cm<sup>-1</sup> (5.6 micrometers) were obtained with a resolution of two wavenumbers. Further analysis of the data was required before statements could be made about the observation of auroral produced emission of the fundamental band of NO<sup>+</sup> in the 2325 cm<sup>-1</sup> (4.3 micrometers) region. There may be some spectral features in the 870-1100 cm<sup>-1</sup> (9.1-11.5 micrometers) region near apogee. Unidentified bands were observed in this region by previous ICECAP LWIR CVF flights.

Successful recovery of the HIRIS sensor and its excellent performance during this flight makes it a good choice to be incorporated in future payloads for measurement of high-resolution spectra of infrared emissions from a highly-dosed atmosphere.

### 3.5.1 Launch Auroral Conditions

Auroral conditions at the time that launch of the HIRIS payload was committed were that of a bright class III+ breakup with a surge coming from the east. This is confirmed by the ground-based (Utah State University) scanning-photometer data of reference 4. The breakup continued with increasing brightness until approximately 50 seconds after launch when the aurora weakened and moved south. The payload penetrated a class II aurora on the upleg and a class II+ aurora during the downleg. The Chatinika incoherent backscatter radar reported electron densities of over  $10^6 \text{ cm}^{-3}$  during the entire data-taking time. Excellent ground-based observation of the auroral conditions during the flight were obtained by the University of Alaska at both Poker Flats and Fort Yukon.

### 3.5.2 Vehicle/Payload Performance

The Sergeant motor performed well as did most payload functions, including vehicle/payload separation, delta velocity, nose cone ejection, cover opening and closing, payload turnaround, and parachute deployment. The ACS performed the despin function and erected the payload to the vertical as programmed. At this point, an erroneous third command was received, causing the payload to tumble (pitch over) at the rate of 10.5 degrees/second. Further testing of the ACS was needed to determine if this command was self-generated within the ACS or was caused by a stray electrical pulse which acted as a command function. Payload tumbling in no way affected interferometer performance; however, an extensive data-reduction effort was required to correlate instrument pointing angles, auroral activity in the field of view, atmospheric slant paths, and time-dependent interferograms. Projection of the auroral activity through the instrument line-of-sight had to be obtained from the ground-based data taken at Poker Flats and Fort Yukon, because the onboard photometer appears not to have obtained any data on the emission at 3914 Å. The payload experienced some buffeting on the downleg after cover closing, but the turnaround/recovery system performed well with no apparent anomalies. Other than the expected cover-heating effects (several damaged wires), the HIRIS instrument was in excellent condition. The payload was located and recovered intact on the same day and was returned to HRC for post-flight operation and calibration; it demonstrated comparable performance with pre-flight conditions. Minimal repair or rework would be necessary for the HIRIS instrument to become flightworthy again for future missions.

### 3.5.3 Interferometer Performance

The cover performed flawlessly. All parameters of the instrument specifications were met or exceeded. A review of the flight telemetry tapes

indicated no data dropouts throughout the flight. The reduced flight spectra shows the instrument yielded better than the expected  $2 \text{ cm}^{-1}$  spectral resolution. Flight calibration indicated that no degradation in sensitivity was experienced from preflight calibrations, where the NESR was measured to be approximately  $5 \times 10^{-12} \text{ watts/cm}^2 \text{ sr cm}^{-1}$  at  $1000 \text{ cm}^{-1}$  (10 micrometers). The system noise level during flight was comparable to preflight levels ( $\pm 1 \text{ mV}$ ). Inflight pre and post-data-taking calibrations met expectations. All I/F timing sequences and housekeeping measurements worked properly.

Focal plane temperature and baffle temperature were monitored during flight; Figures 3.10 and 3.11 show these temperatures as a function of time after launch with cover opening starting at 84.2 seconds (83 km) and cover closing complete at 295.5 seconds (62 km). Focal plane temperature was maintained within a half degree Kelvin. The small oscillations seen in Figure 3.10 correspond to the vehicle pitching rate and are most likely due to the focal plane viewing the warm earth. Similar effects can be seen in the baffle temperature (Figure 3.11) it rose about 8 K during cover opening and then slowly decayed until atmospheric heating below 90 km caused it to rise again. All temperatures were well within acceptable tolerances for instrument operation during the entire flight.

### 3.5.4 Flight Data Summary

A total of 171 spectral scans were obtained during the flight of which 150 were viewing outside the instrument between cover opening and closing. Because of payload tumbling, six complete revolutions were experienced during those 150 scans. Each revolution consisted of about 12 spectra above the horizon, 2 spectra of the earth limb, and 12 spectra of the earth itself. Before cover opening, 5 background and 4 calibration scans were obtained. Three scans before and after data taking occurred during cover operation and are not useful. Four calibrations were observed after cover closing, but atmospheric buffeting of the payload makes their usefulness doubtful.

Complete and detailed data reduction is a continuing activity being carried out under a separate contract, DNA 001-76-C-0302. Portions of the data recorded during the flight are presented here in Figures 3.12 through 3.18.

In Figures 3.12 through 3.16, the top plot is the normalized interferogram which represents the actual output of the interferometer. Only the central 1000 sample points (out of the approximately 17,000 samples obtained) are shown. The bottom plot is the IR spectrum obtained by performing a fast Fourier transform on the interferogram shown in the top plot. The spectrum plots are normalized and are not corrected for instrument response. This means that there are no absolute radiance values and that the heights of the emission features, relative to one another, will change when calibration is applied during final data reduction.

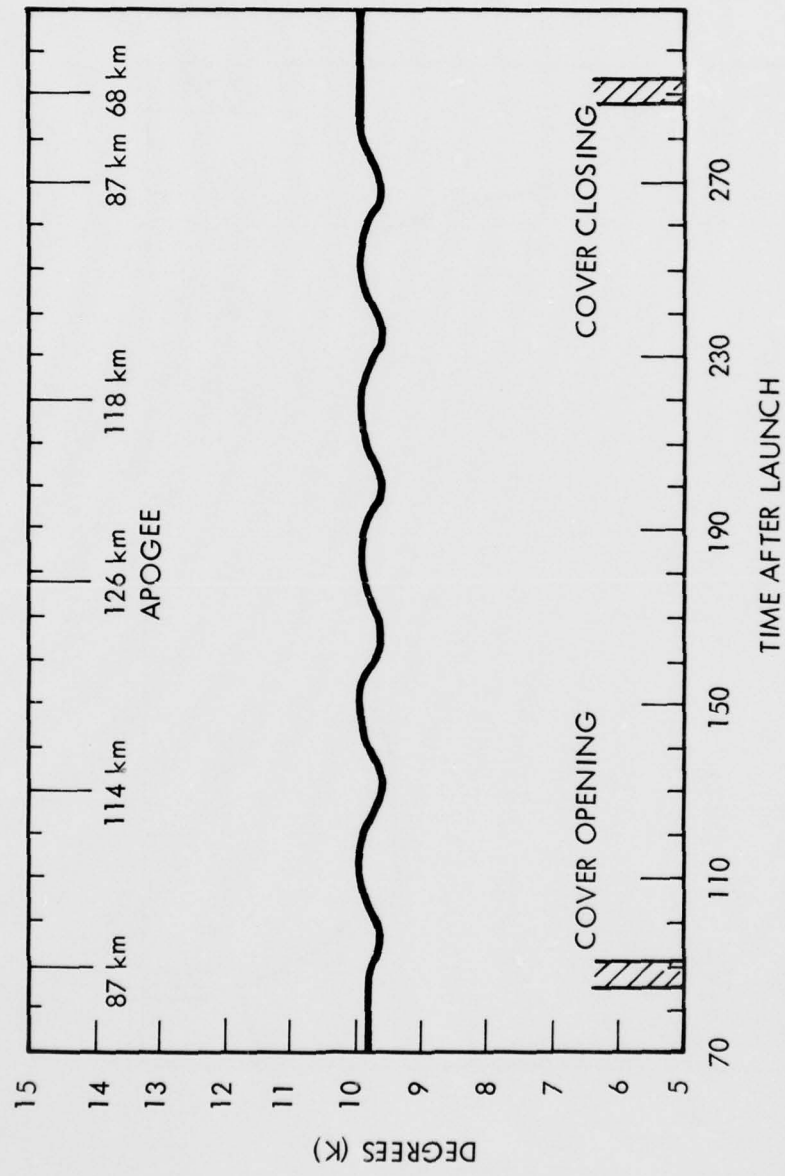


Figure 3.10 FOCAL PLANE TEMPERATURES DURING THE FLIGHT

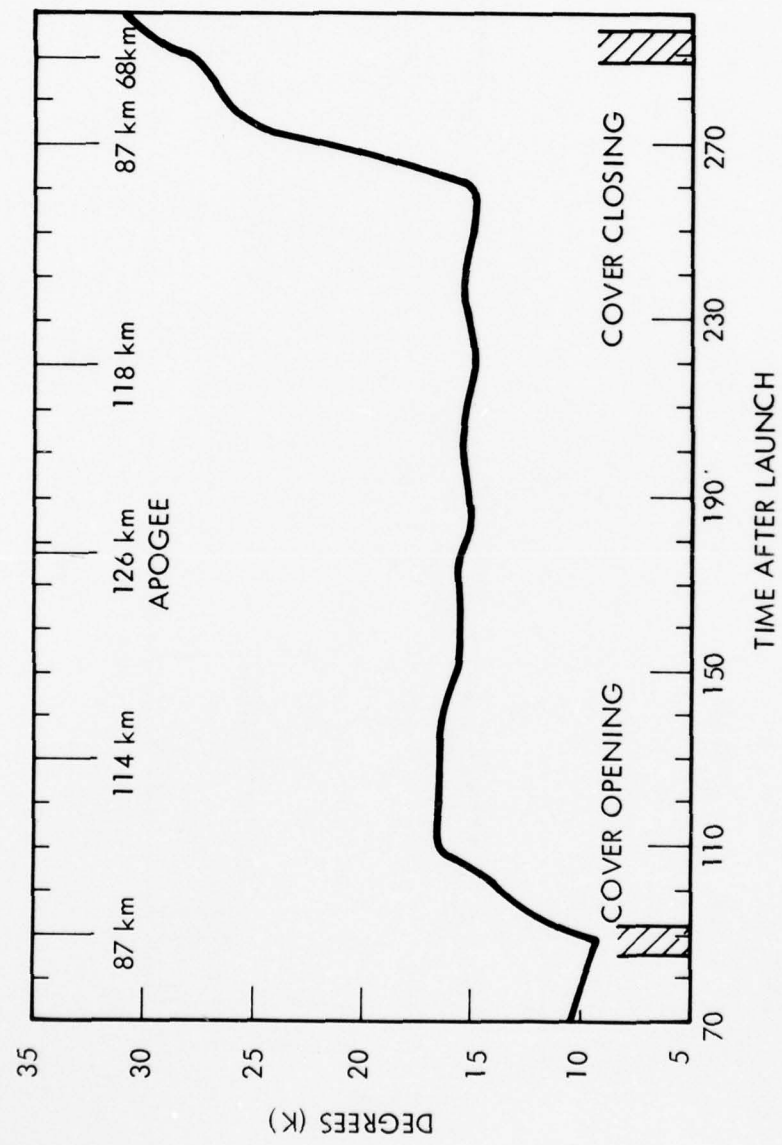


Figure 3.11 BAFFLE TEMPERATURES DURING THE FLIGHT

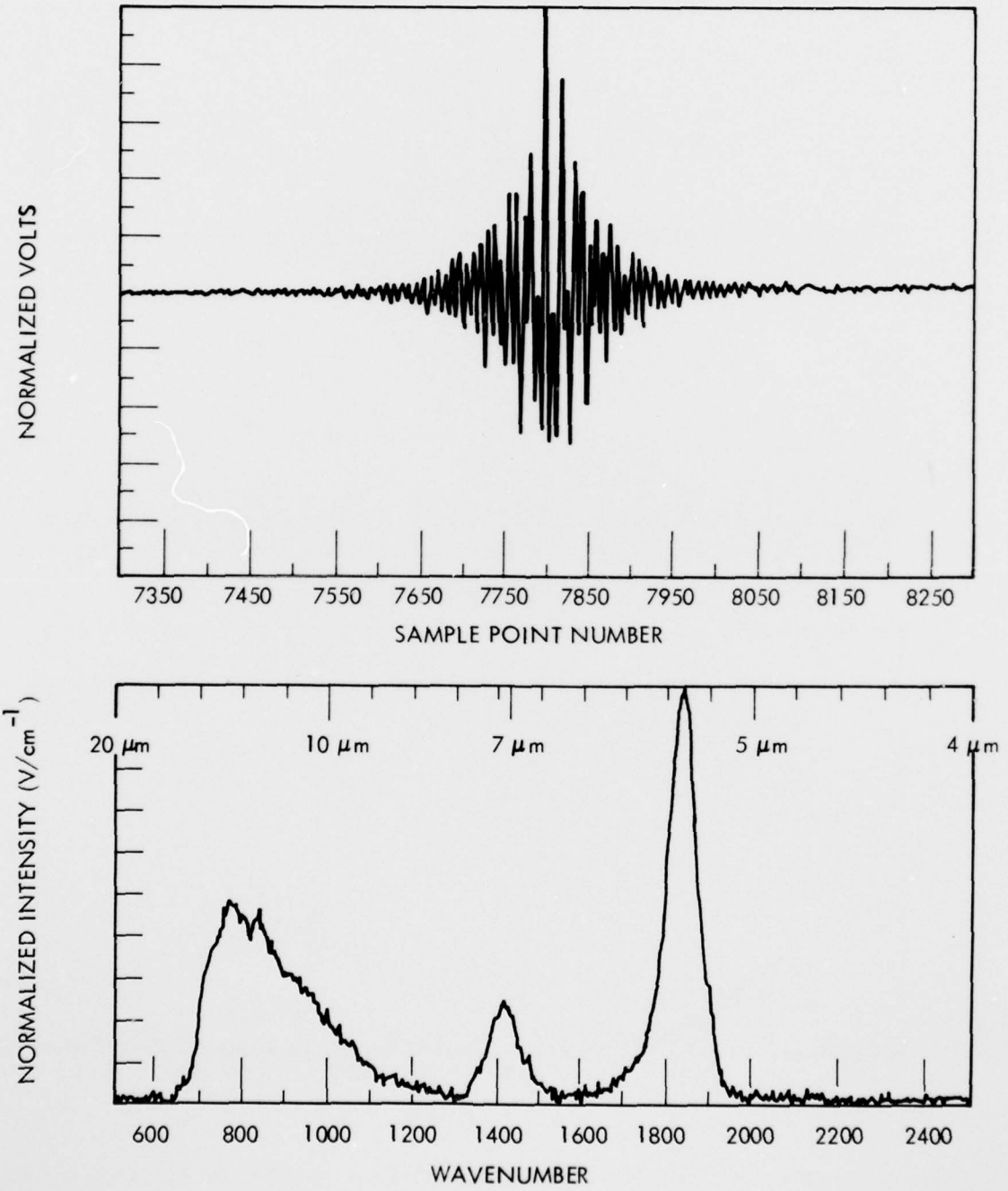


Figure 3.12 INTERFEROGRAM (TOP FIGURE) AND SPECTRUM (BOTTOM) OF INTERNAL BLACK-BODY AND LED CALIBRATION SOURCES OBTAINED DURING PREFLIGHT CHECKOUT

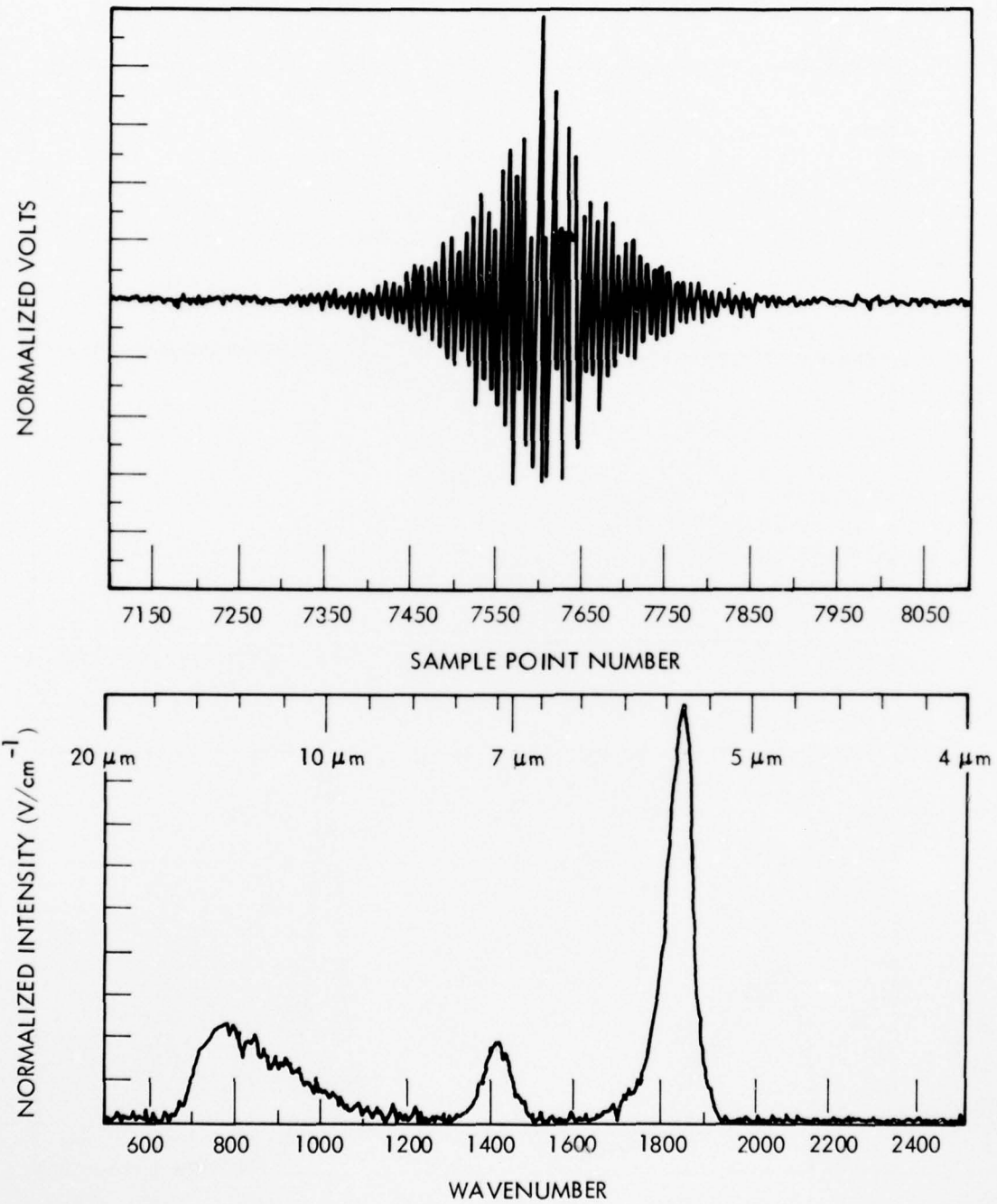


Figure 3.13 INTERFEROGRAM (TOP FIGURE) AND SPECTRUM (BOTTOM) OF INTERNAL BLACKBODY AND LED CALIBRATION SOURCES OBTAINED IN FLIGHT PRIOR TO COVER OPENING

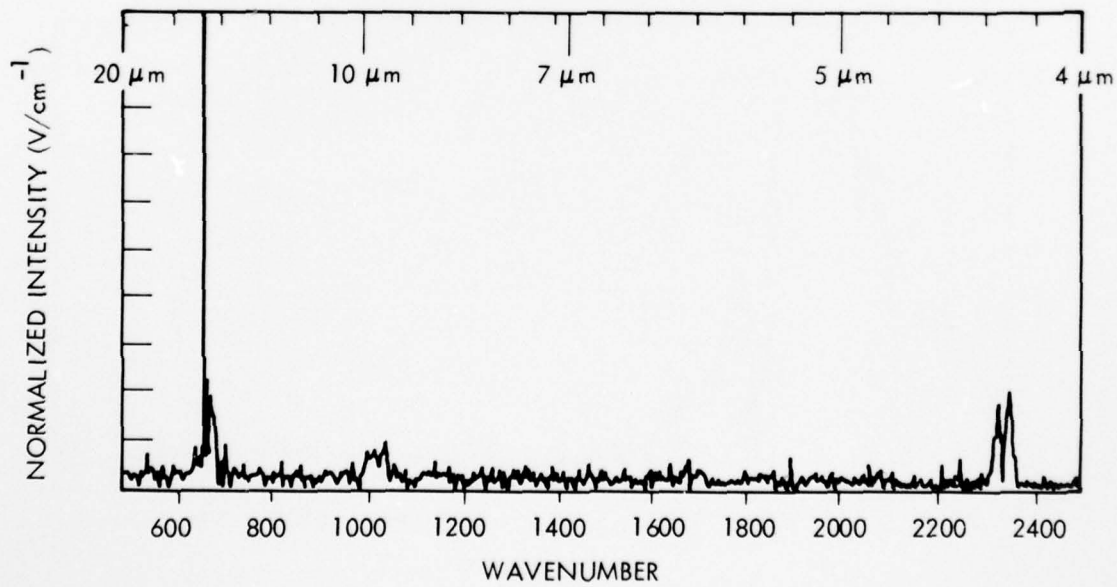
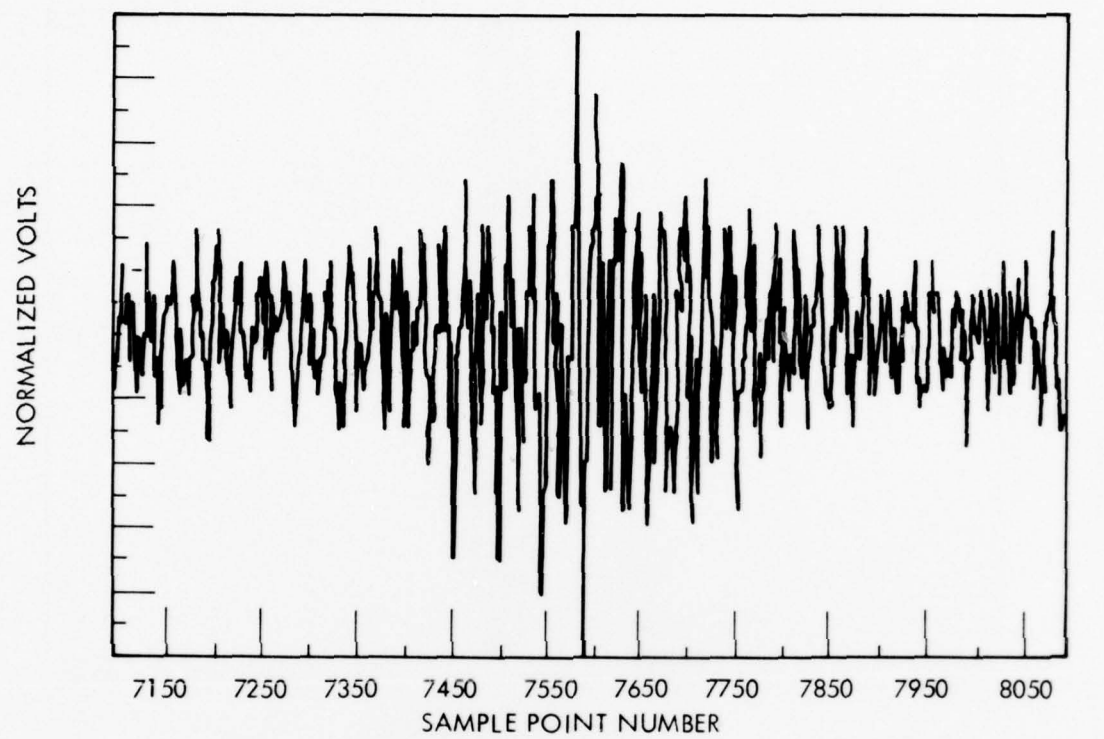


Figure 3.14 VERTICAL VIEWING INTERFEROGRAM (TOP FIGURE) AND SPECTRUM (BOTTOM) DURING THE UPLEG TRAJECTORY AT 102 km

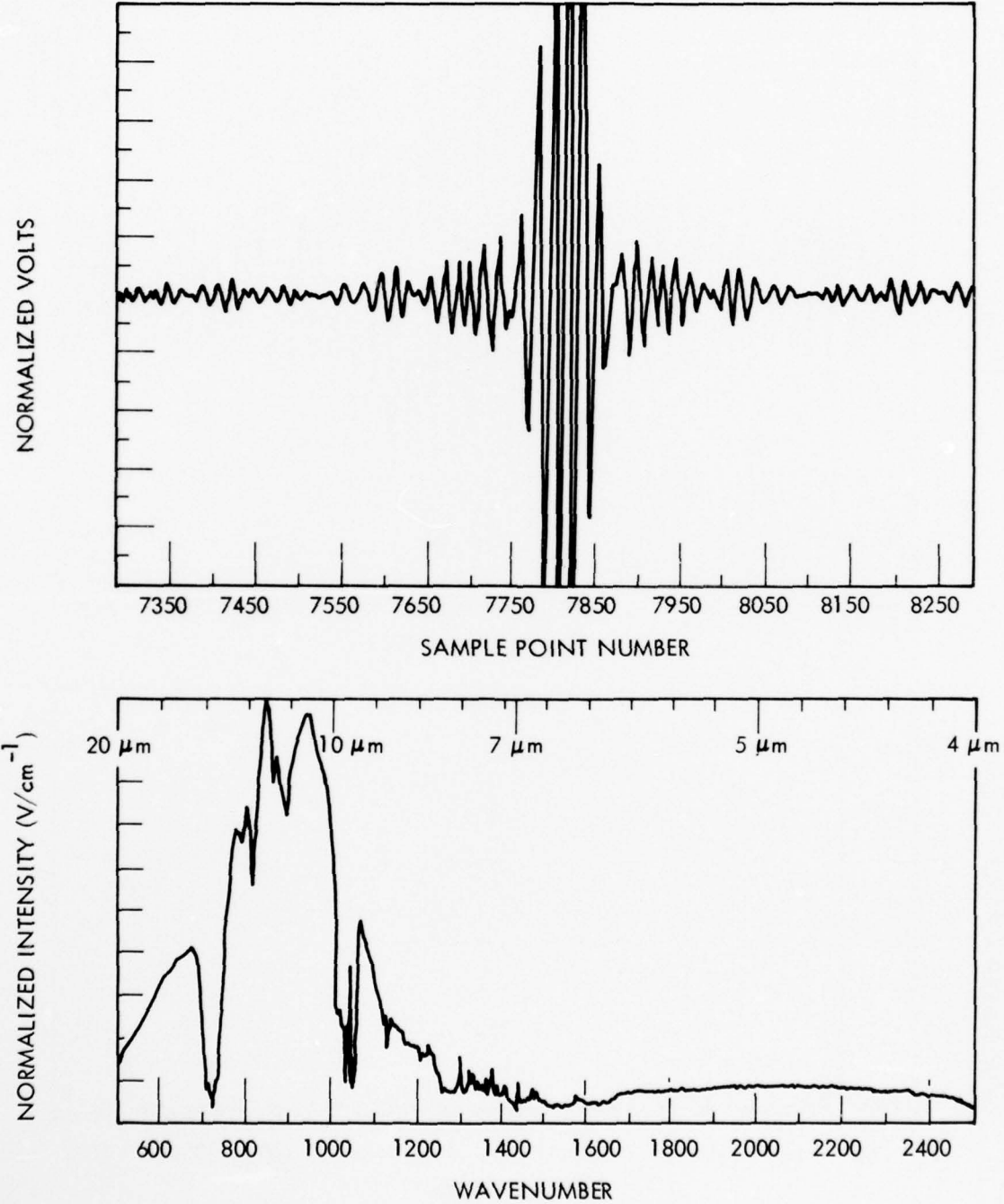


Figure 3.15 DOWNWARD VIEWING INTERFEROMGRAM (TOP FIGURE) AND SPECTRUM (BOTTOM) DURING THE UPLEG TRAJECTORY AT 88 km

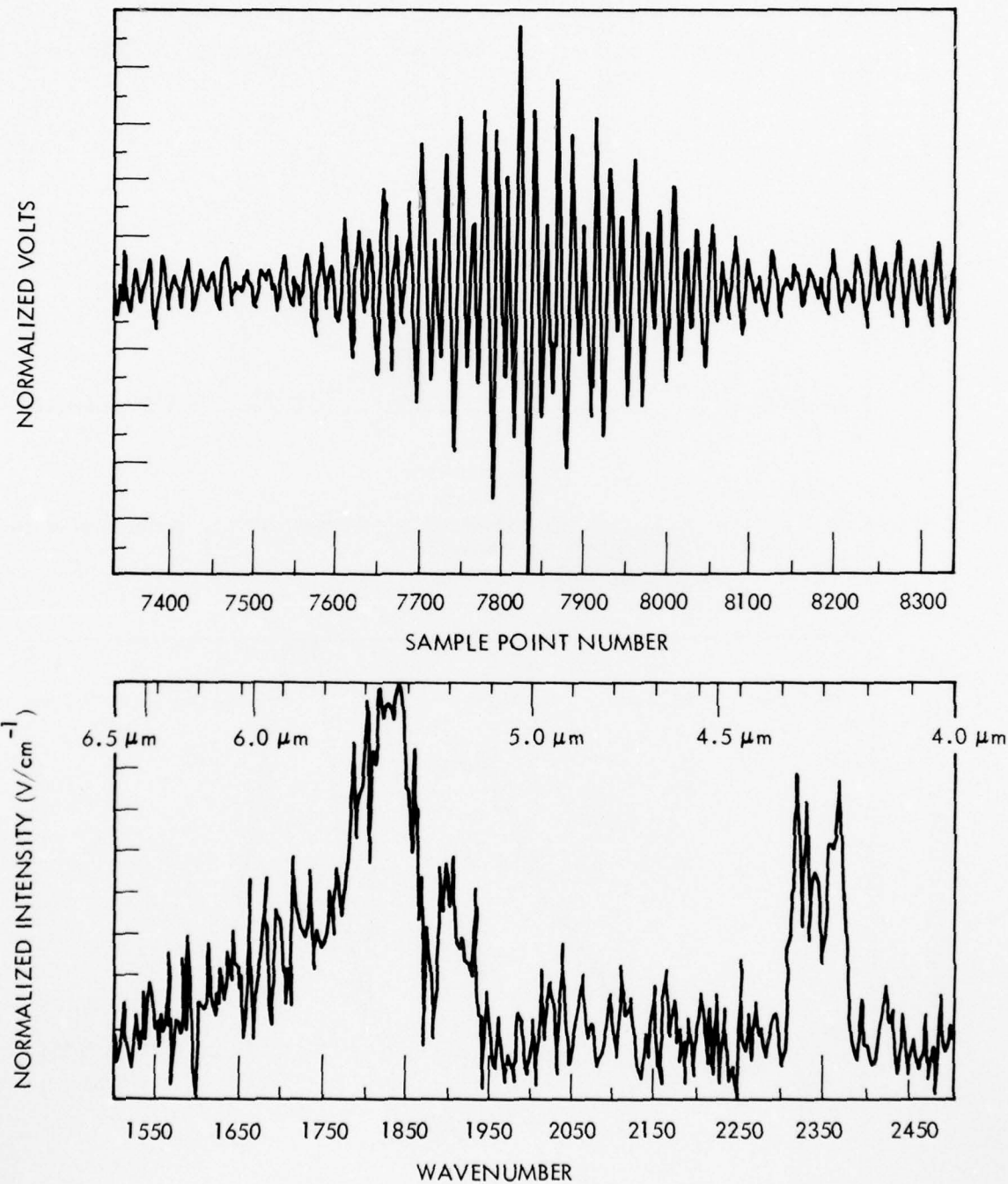


Figure 3.16 LIMB VIEWING INTERFEROGRAM (TOP FIGURE) AND SPECTRUM (BOTTOM) DURING THE DOWNLEG TRAJECTORY AT 101 km

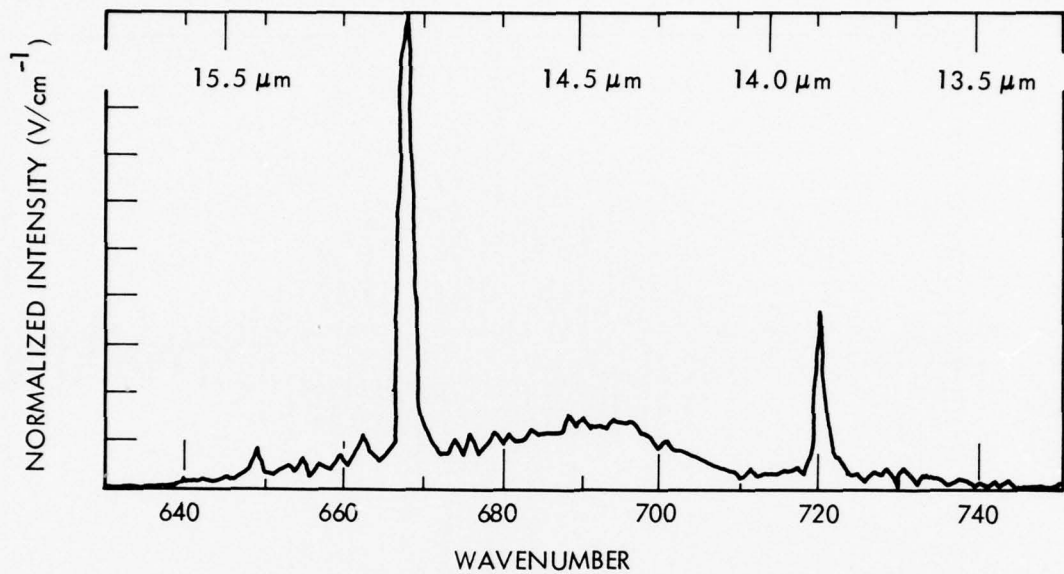


Figure 3.17 VERTICAL VIEWING HIGH RESOLUTION SPECTRUM OF  $\text{CO}_2$  BANDS DURING THE DOWNLEG TRAJECTORY AT 76 km

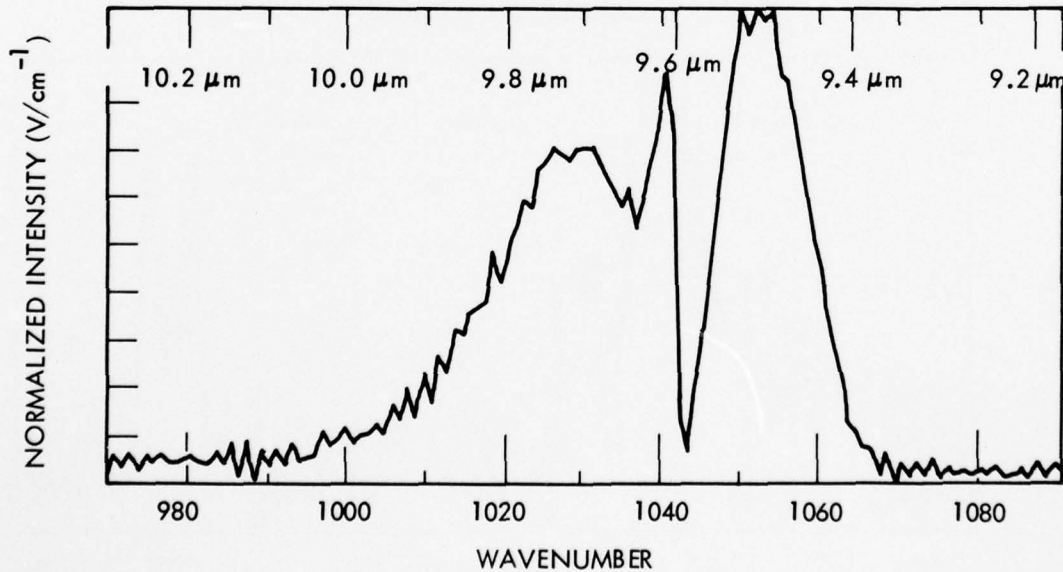


Figure 3.18 VERTICAL VIEWING HIGH RESOLUTION SPECTRUM OF  $\text{O}_3$  ( $\nu_3$  BAND) AT  $1042 \text{ cm}^{-1}$  (9.6  $\mu\text{m}$ ) DURING THE DOWNLEG TRAJECTORY AT 76 km.

The first data shown are for the internal calibration sources (blackbody and LED) as obtained during prelaunch checkout (Figure 3.12) and in flight before cover opening (Figure 3.13). Comparison of these two spectra show the spectral features to be the same. The difference in amplitude of the blackbody emission at  $800 \text{ cm}^{-1}$  (12.5 micrometers) results from a not unexpected difference in blackbody temperature. These internal blackbody and LED spectra are not used for absolute calibration, but rather as a measure of overall performance by the interferometer. In this case, they indicate that forces exerted on the instrument during launch did not affect operation or sensitivity.

The first vertical-looking scan at 102 km is shown in Figure 3.14. The features seen are  $\text{CO}_2$  at  $667 \text{ cm}^{-1}$  (15 micrometers) and  $2225 \text{ cm}^{-1}$  (4.3 micrometers) and  $\text{O}_3$  at  $1042 \text{ cm}^{-1}$  (9.6 micrometers).

A spectrum recorded while viewing down from 88 km, Figure 3.15, shows that the center of the interferogram signal is clipped. While data reduction efforts may be able to approximate the true central peaks, the spectrum shown has no correction applied. The results of the distorted center will not affect the resolution or high-frequency spectrum, but will introduce a low-frequency background which is evident between  $1600$  and  $2500 \text{ cm}^{-1}$  (4.0 to 6.25 micrometers). Featured are spectra of the earth blackbody along with absorption features  $667 \text{ cm}^{-1}$  (15 micrometers)  $\text{CO}_2$ ,  $1042 \text{ cm}^{-1}$  (9.6 micrometers)  $\text{O}_3$ , and 1250 to  $1667 \text{ cm}^{-1}$  (6 to 8 micrometers)  $\text{H}_2\text{O}$ .

The spectrum between  $1500$  and  $2500 \text{ cm}^{-1}$  (4.0-6.7 micrometers) viewing just above the earth horizon from 101 km is shown in Figure 3.16.

Figures 3.17 and 3.18 demonstrate the spectral resolution that was achieved; these figures are expanded plots of the vertical-viewing emission spectra of  $667 \text{ cm}^{-1}$  (15 micrometers)  $\text{CO}_2$  and  $1042 \text{ cm}^{-1}$  (9.6 micrometers)  $\text{O}_3$  at 76 km. The vertical-viewing emission spectra at  $667 \text{ cm}^{-1}$  (15 micrometers) and  $1042 \text{ cm}^{-1}$  (9.6 micrometers) (which are predictably independent of auroral conditions) are essentially the same on the upleg and downleg, indicating no degradation in instrument performance during flight. The rate of fall-off of  $667 \text{ cm}^{-1}$  (15 micrometers)  $\text{CO}_2$  emission as a function of altitude also appears to be consistent with that measured by the previous LWIR CVF flights.

While final data reduction and analysis remain to be completed, results indicate that the data obtained were excellent as a result of the first successful flight of a high resolution cryogenic interferometer.

SECTION 4  
SPHIRIS FEASIBILITY DESIGN

4.1 BACKGROUND

The SPHIRIS instrument configuration was defined to meet the objectives of obtaining combined high spatial and spectral resolution with high off-axis rejection to meet measurement requirements of the DNA/AFGL HAES program. The approach to the configuration was to interface two developed areas of critical technology, cryogenic interferometry from the HIRIS program and cryogenic high off-axis rejection telescopes from the ELS (Earth Limb Sensor) program, into a single sensor meeting the design goals of Table 4.1. The instrument would be flown in an experiment similar to the AFGL SPIRE experiment, as illustrated in Figure 4.1, meeting the mission requirements of Table 4.2.

Table 4.1  
SPHIRIS SYSTEM DESIGN GOALS

Parameter	Value
Spectral Resolution	$2 \text{ cm}^{-1}$
Scan Rate	1 double sided interferogram/s
Spectral Range	4 to 18 micrometers
NESR	$2 \times 10^{-11} \text{ W/cm}^2 \text{ sr cm}^{-1}$ @ 5 $\mu\text{m}$
FOV	4.36 mr x 4.36 mr
Entrance Aperture	10 Inch
Dynamic Range	$2 \times 10^4$
Wavelength Precision	$0.5 \text{ cm}^{-1}$
Point Source Rejection	$4.5 \times 10^{-10}$ @ 1° Off Axis
Operating Geometry	100 km Tangent Ht @ 250 km Altitude

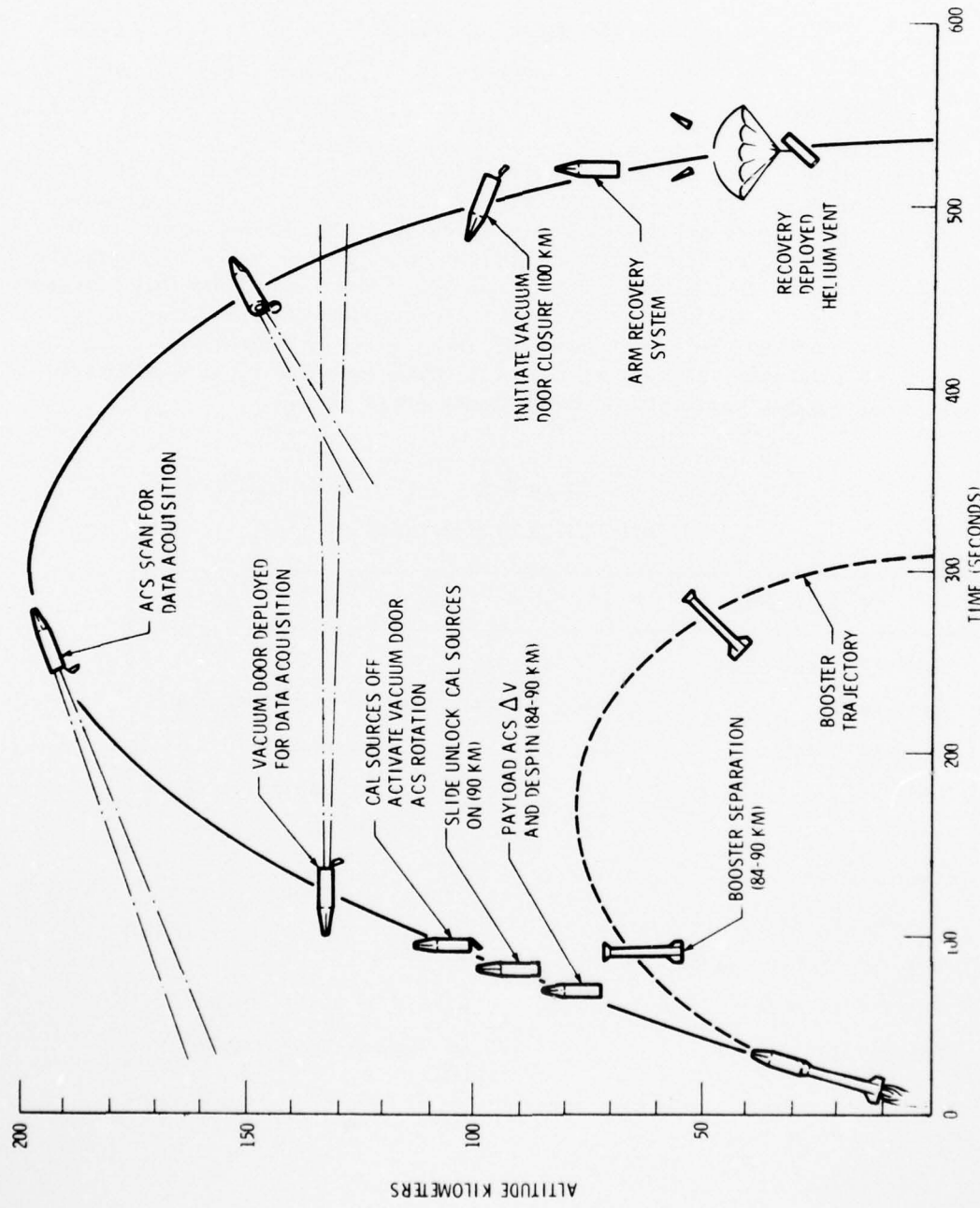


Figure 4.1 SPIRE TRAJECTORY

Table 4.2  
MISSION REQUIREMENTS

Experiment	Earth Limb/Exceed
Booster Compatability	Castor/Sargent/?
Data Acquisition Alt	130 - 200 km
Sensor Hold Time (Vertical)	5.5 Hrs + 400 s Mission
Sensor C/O (Vertical)	Internal Cal Sources
Sensor Size	20" Dia x 75" Long
Sensor Wt	< 450 Pounds
Trajectory	Sounding Rocket

#### 4.2 SYSTEM DESIGN

##### 4.2.1 Comparison with HIRIS

The SPHIRIS instrument is a spectrometer, the principal functional component of which is the interferometer assembly. The dewar module, electronics package, and GSE comprise the first-order breakdown of equipment. The cryogenic dewar houses the interferometer assembly, telescope and baffle chamber, and cryogenic tank (see Figure 4.2); its other functional elements are its vacuum cover and cover-drive mechanism, in-flight calibrator, and multilayered insulation. The electronics package contains all airborne electronics outside of the dewar. The Vacuum Pumping Station (VPS), ground liquid-helium supply, receivers, checkout console, and computer system broadly comprise the ground support equipment and would be modified HIRIS equipment.

Optical, electronics, and vacuum/cryogenic system comprise the first-order system breakdown. The interferometer assembly is the heart of the optical system which extends throughout the telescope and baffle chamber and includes the in-flight calibrator (see Figure 4.3). The electronics system will be discussed under the following groups: signal channel, reference channels, mirror servo, housekeeping, and experiment interface. The vacuum and cryogenics system covers: the dewar, its insulation, the cryogenic tank for liquid helium, its cooling system, and the evacuation system.

The purpose of the SPHIRIS experiment is to combine the ELS telescope with the HIRIS interferometer (I/F) assembly. The telescope increases off-axis rejection of input signals to the I/F and narrows its Field of View (FOV).

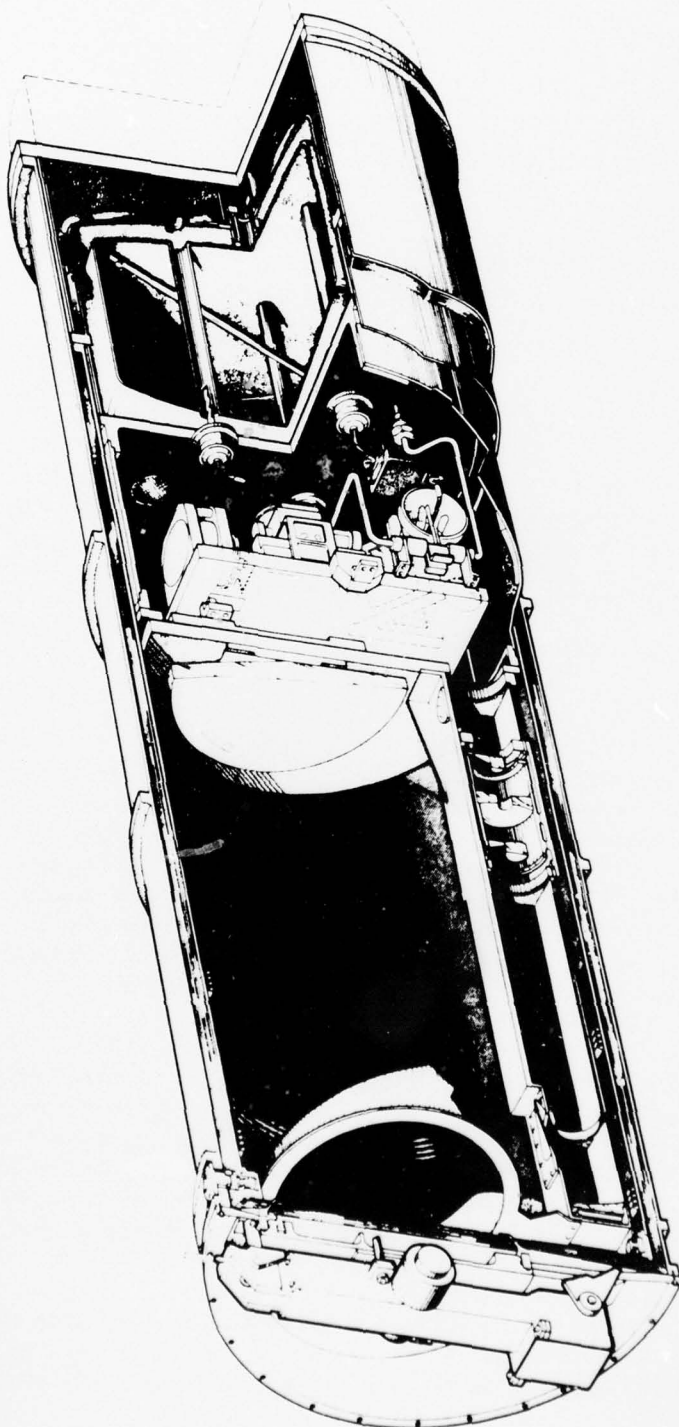


Figure 4.2 SPHIRIS INSTRUMENT

AD-A053 392

HONEYWELL RADIATION CENTER LEXINGTON MASS

F/G 17/5

HIRIS REFLIGHT. (U)

APR 77 C BOHNE, L HARKLESS, E DUNBAR

DNA001-73-C-0164

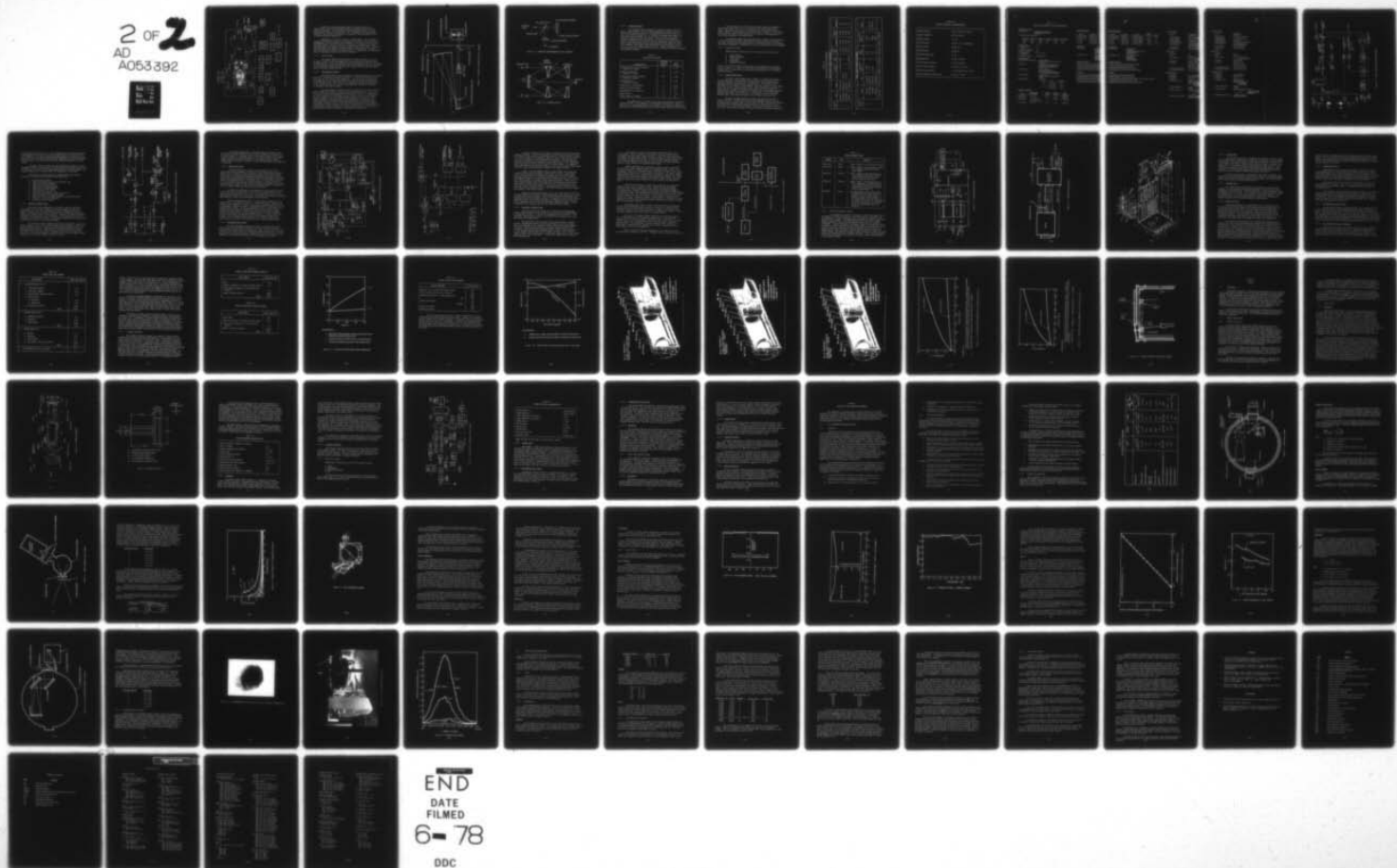
UNCLASSIFIED

HRC-77-3-3

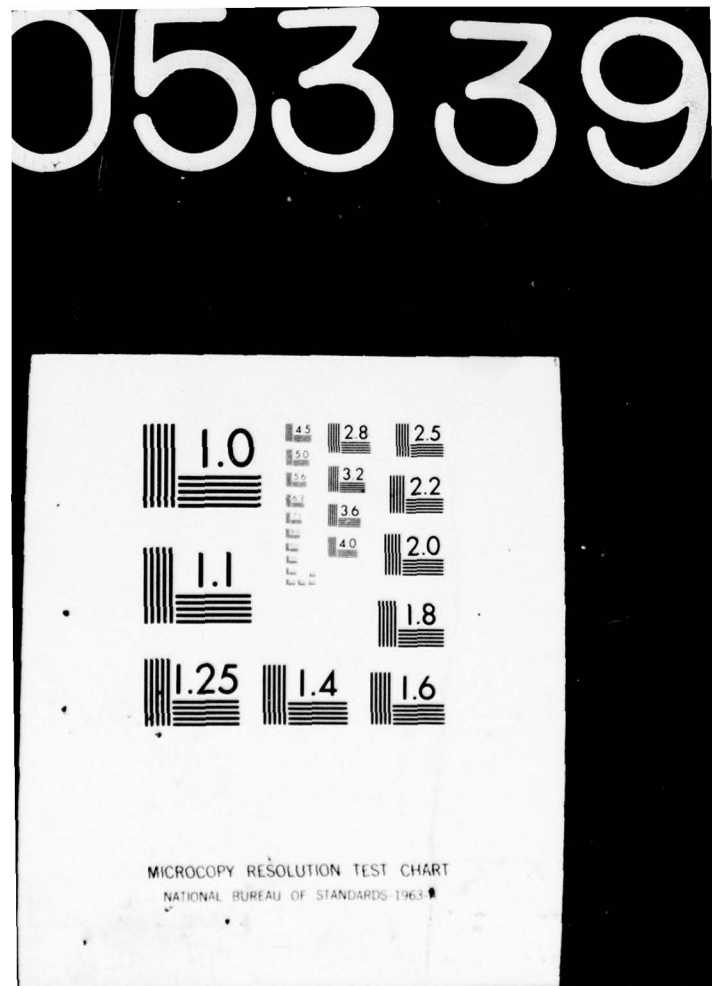
DNA-4337F

NL

2 OF 2  
AD  
A053392



END  
DATE  
FILED  
6-78  
DDC



MICROCOPY RESOLUTION TEST CHART  
NATIONAL BUREAU OF STANDARDS-1963

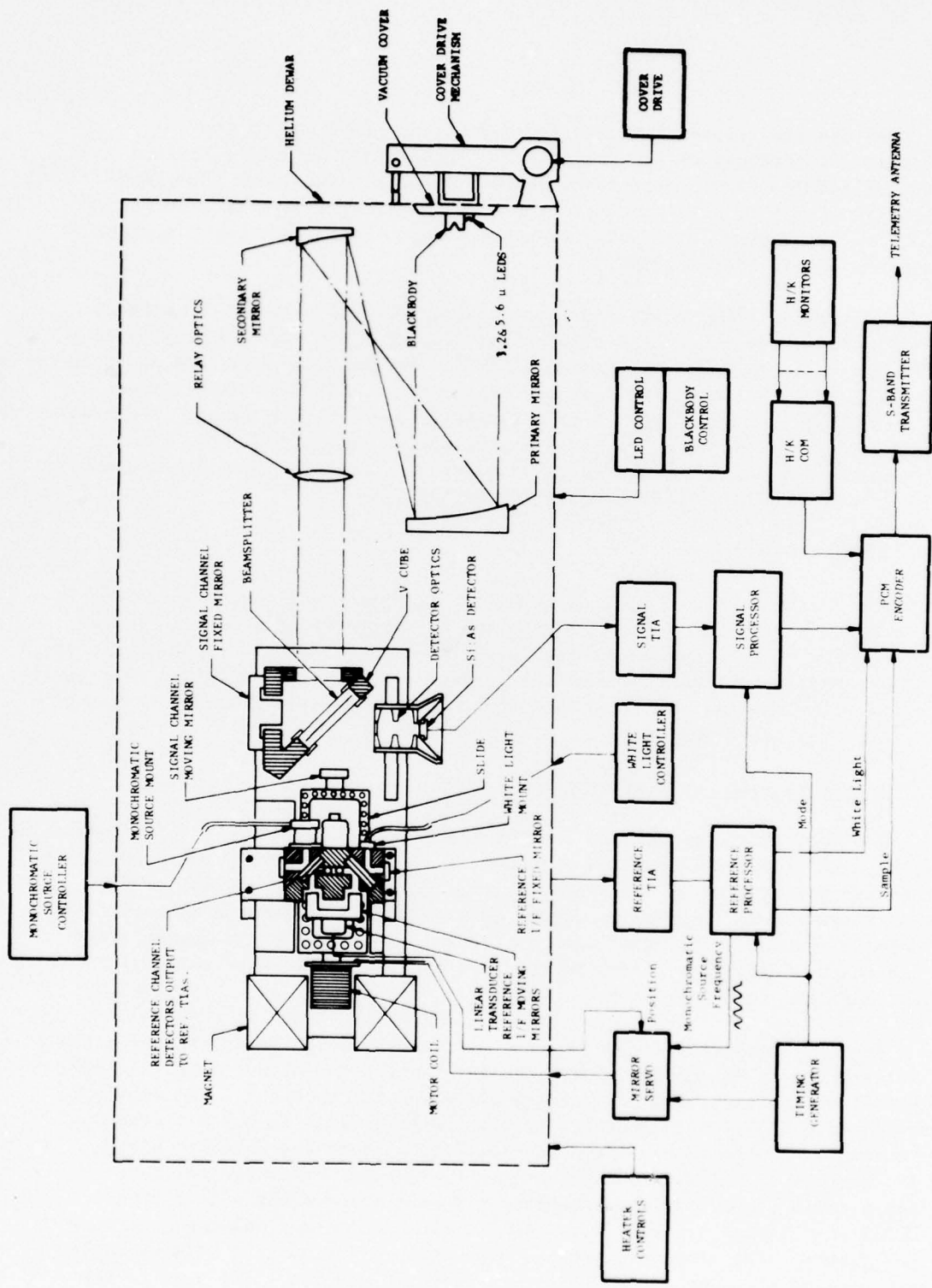


Figure 4.3 SPHIBIS OPTICAL AND ELECTRONICS SYSTEMS

Besides the telescope assembly added to the front end of the interferometer, functional differences between the SPHIRIS and HIRIS instruments are negligible. Both instruments measure spatially-resolved, IR, atmospheric spectra from 5 to 22 micrometers. The I/F assemblies are functionally identical, and instrument sensitivity is not changed. Both instruments operate at the same cryogenic temperatures.

Differences occur mostly in size and configuration. The I/F assembly is mounted horizontally, along the cylindrical axis of HIRIS, and vertically or perpendicular to the cylindrical axis of SPHIRIS. Vacuum cover size and position have been changed to match the telescope arrangement, and SPHIRIS has a larger cryogenic tank; these changes result in a larger (longer) helium dewar. Electronics were redesigned to accommodate the SPHIRIS mission and repackaged. The HIRIS in-flight calibrator contains two signal sources: a blackbody and a 5.6-micrometer LED; a 3.2-micrometer LED has been added for SPHIRIS.

#### 4.2.2 Optical System

The complete SPHIRIS optical schematic is shown in Figure 4.4 and can be seen to consist of two major assemblies, the telescope section and the interferometer section. These two assemblies have almost completely different functions, the telescope section providing off-axis rejection and spatial resolution performance; the interferometer section providing spectral coverage and resolution performance. They are discussed separately below.

##### 4.2.2.1 Interferometer Section

The interferometer section employs the conventional Michelson interferometer type optics, graphically illustrated in Figure 4.5. The incident plane wave is split into two plane waves by the beamsplitter. One path is by reflection from the beamsplitter to the fixed plane mirror, M<sub>1</sub>, and back through the beamsplitter to the detector optics. The other path is transmission through the beamsplitter to the retardation mirror, M<sub>2</sub>, back to the beamsplitter and then by reflection to recombine at the detector optics.

The interferometer collecting optics are concentric in an all-reflective system illustrated in Figure 4.6 with a one-inch aperture stop and a small (17%) flat, central obscuration; characteristics are given in Table 4.2. The geometric spot size on axis is 0.2 milliradian, and for the full field is 0.7 milliradian. In this arrangement, the source image becomes defocused at the detector plane (image in Figure 4.6) and irradiates the entire detector. This optical configuration permits a complete dynamic-range calibration over the entire sensor (the SPHIRIS instrument) field of view (FOV) while filling the one-inch aperture of the detector optics. However, point source calibration must be referenced to an extended-source calibration system to obtain accurate results. The size of the exposed detector surface contributes to limiting the sensor's FOV.

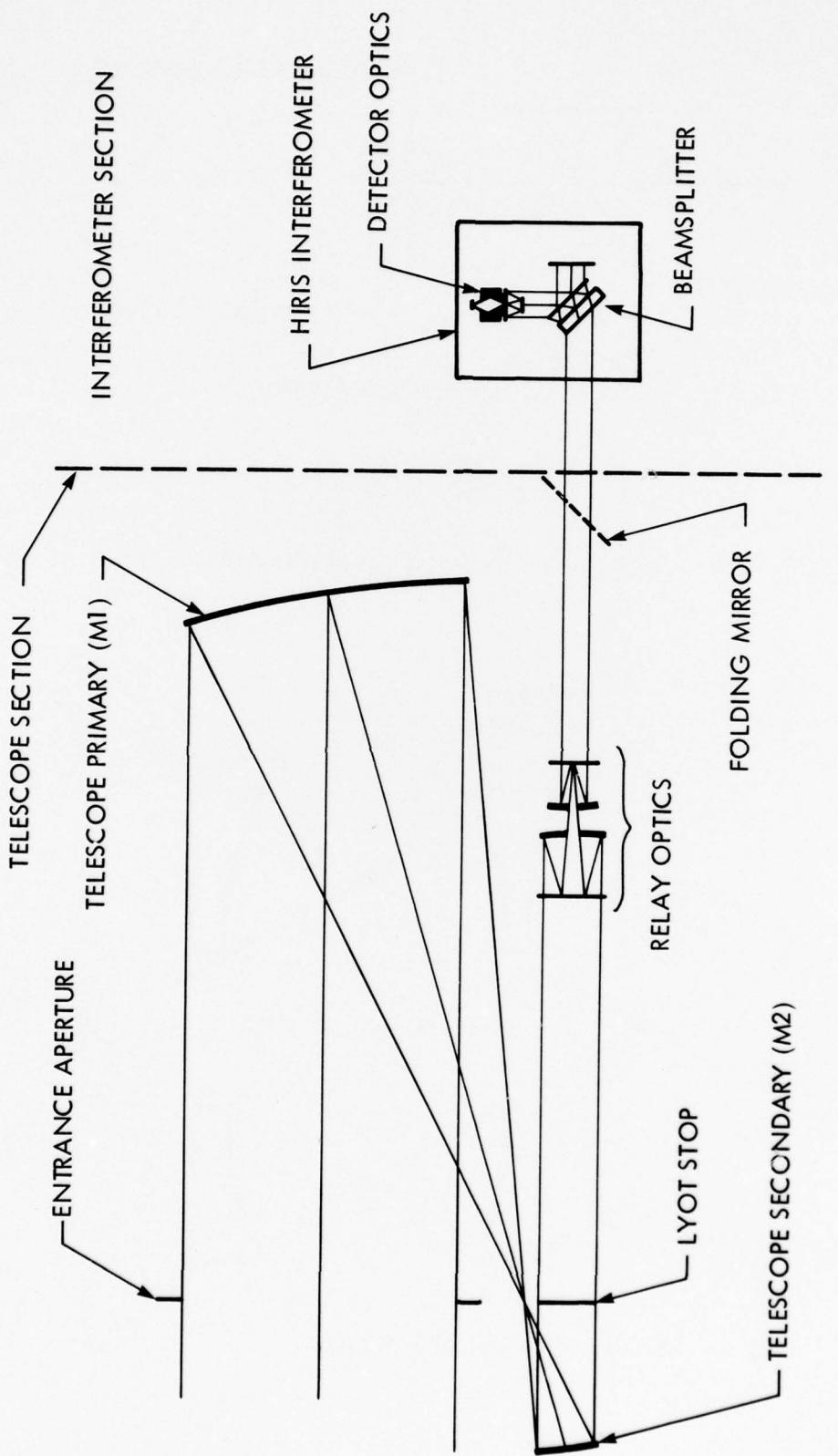


Figure 4.4 OVERVIEW OF SPHIRIS OPTICS, SCHEMATIC

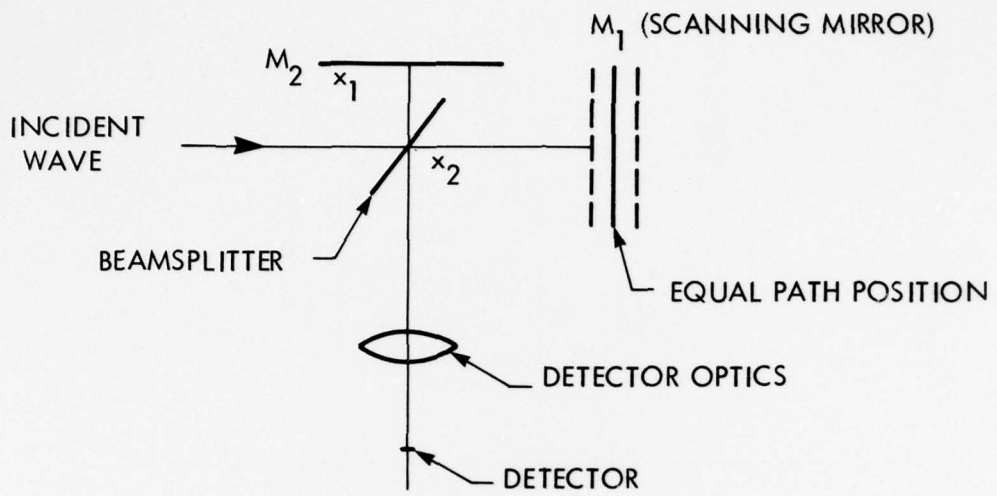


Figure 4.5 MICHELSON INTERFEROMETER OPTICS SCHEMATIC

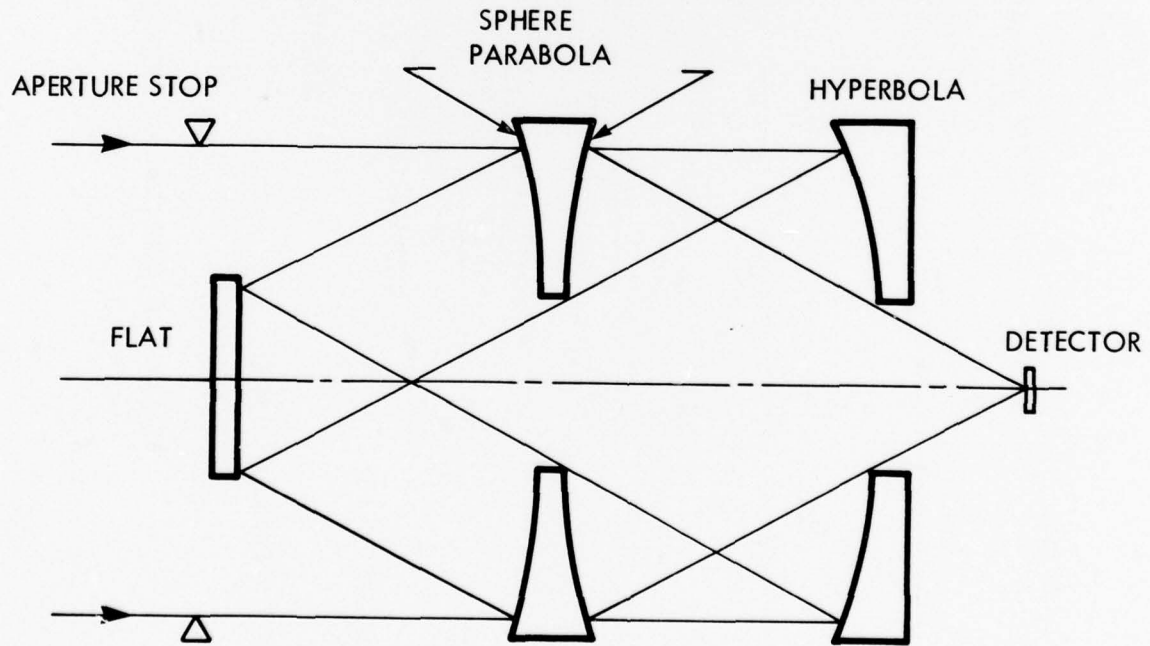


Figure 4.6 DETECTOR OPTICS

#### 4.2.2.2 Telescope Section

The telescope section consists of a rejection telescope and relay optics. Characteristics of each of these assemblies are given in Table 4.3. The rejection telescope consists of two parabolic mirrors (M1 and M2) and a Lyot stop as shown in Figure 4.4. It reduces the incoming beam diameter and images the entrance aperture onto the Lyot stop. The Lyot stop rejects diffracted light from out-of-field source. M1 and M2 of the telescope are reflective aluminum mirrors, surfaced by electroless nickel plating and gold coated. The primary optic (M1) is a ten-inch, low-scatter, spherical mirror with a measured average BRDF (Bidirectional Reflection Distribution Function) of  $2 \times 10^{-5} \cos \theta$  at 1 degree with  $1/\theta^2$  rolloff. Specially-designed mirror mounts eliminate mirror-figure distortion due to mounting and provide maintainable and repeatable alignment.

Table 4.3  
TELESCOPE OPTICAL DATA

CHARACTERISTIC	REJECTION TELESCOPE OPTICS	RELAY OPTICS
Entrance Aperture (clear & usable) (diameter in inches)	10	1.927
Entrance Obscuration (diameter in inches)	0	0.819
Exit Aperture (clear & usable) (diameter in inches)	1.927	0.896
Exit Obscuration (diameter in inches)	0	0.391
Effective FOV (milliradians)	4.3	20.91
Actual FOV (milliradians)	12	20.91
Transmission (% of signal in)	77	65
Magnification	4.8	2.15
Baffle Length to Diameter	3:1	NA

The combination of low-scatter optics and stops minimizes scattered and diffracted energy. Cold alignment of the boresight is repeatable to within one minute of arc. The primary aperture of the sensor is ten inches in diameter, and the effective collecting aperture narrows to eight inches, limited by the Lyot stop.

The relay optics unit has four mirrors which reduces the diameter of the telescope output about 2 to 1; it images the Lyot stop on the detector optics. The relay optics consist of two primary and two secondary mirrors as shown in Figure 4.4 with element characteristics given in Table 4.4. The folding mirror bends the output of the relay optics to focus it on the beamsplitter in the vertical mounting of the interferometer.

The telescope chamber walls have baffling to increase off-axis rejection. At the low vacuum and cryogenic temperatures of flight operation, the baffles also trap stray molecules and other particles in the front section by cryopumping, and prevent cryodeposition contamination of the cold interferometer section elements.

#### 4.2.3 Electronics System

SPHIRIS flight electronics fall into five major functional groups:

- Signal Channel
- Reference Channels
- Mirror Servo
- Housekeeping
- Experiment Interface

Each will be briefly described with reference to the simplified block diagram portion of Figure 4.3. Table 4.5 lists design requirements for the electronics system, Table 4.6 summarizes the main operating characteristics of the SPHIRIS electronics system.

##### 4.2.3.1 Signal Channel Group

This group, shown schematically in Figure 4.7, detects the IR signal from the telescope at the instrument focal plane and provides amplification, filtering, and gain conditioning for the PCM encoder. The signal TIA (trans-impedance amplifier) provides initial amplification; it is located beside the detector on the detector optics assembly. This TIA consists of a cold MOSFET array, that acts as a source follower, which feeds a wide-band operational amplifier with a feedback path through the load resistor for the signal detector. The operational amplifier is mounted on the "magnet end" of the helium dewar to minimize cable length to the focal plane. The output of the TIA operational amplifier goes to the signal processor in the off-sensor electronics box.

The signal processor amplifies, filters, and gain switches an IR signal as follows: the HIGH gain state provides sufficient gain to raise the rms noise level at the TIA output to 3 bits above the LSB of the PCM A/D converter; the LOW gain state amplifies the maximum signal (2.6 V peak-to-peak) to full scale ( $\pm 5$  volts) on the PCM A/D converter. Each mirror scan starts with HIGH gain state, and as signal increases, fixed plus and minus thresholds automatically

Table 4.4  
RELAY OPTICS SURFACE PARAMETERS

RELAY OPTICS SURFACE PARAMETERS						
Surface No.	Name	Type	F.L.	Vertex Radius	Conic Cons.	Clear. Aper. Rad.
1	Primary	Elliptical	--	-6.356	-0.580	1.126
2	Secondary	Spherical	-1.566	--	0.410	0.95
3	Secondary	Spherical	0.545	--	0.196	0.95
4	Primary	Elliptical	--	3.746	-0.55687	0.915

RELAY OPTICS SURFACE TOLERANCES						
Surface No.	Name	Type	Axial Sep. +(in.)	Tilt +(deg)	Off Center +(in.)	Figure
1	Primary	Elliptical	0.039	0.29	0.003	2 $\lambda$
2	Secondary	Spherical	0.35	1.5	0.7	+ 0.137 in.
3	Secondary	Spherical	0.10	1.0	0.006	+ 0.839 in.
4	Primary	Elliptical	$\infty$	0.5	0.003	5 $\lambda$

Criteria: On-Axis Blur  $\leq$  0.0006 in. diameter at detector (nominal 0.00456)

Table 4.5  
SPHIRIS ELECTRICAL CHARACTERISTICS

Signal Detector	Si:As, 0.045-inch square
Signal Bandwidth	650 to 2750 Hz
Dynamic Range	$2 \times 10^4$
A/D Conversion	14 bits, two's complement
PCM Bit Rate	466,944 Hz
PCM Word Rate	29,184 Hz
PCM Data-Frame Rate	9.2 Hz
Sampling Rate	26 kHz (nominal)
Laser Fringe Frequency	13 kHz (nominal)
Mirror Scan Frequency	One scan per second
Mirror Scan Velocity	5.5 millimeters per second
Linear Transducer Excitation	9 kHz at 4 volts

Table 4.6  
SPHIRIS ELECTRONICS DESIGN REQUIREMENTS

MIRROR SERVO AND TIMING

- MASTER CLOCK INDEPENDENT, LOW FREQUENCY OSCILLATOR, PROGRAMMABLE FOR 3 FREQUENCIES

OSC. FREQ. SCAN TIME FLYBACK TIME SCAN RATE SCAN EFF. SCAN LENGTH

100 Hz	0.900 s	0.100 s	1 per s	0.90	5 mm
200	0.450	0.070	1.9	0.87	2.5
400	0.225	0.045	3.7	0.83	1.25

- SLIDE VELOCITY 5.5 mm/s
- VELOCITY TOLERANCE  $\pm 6\%$  FOR PCM
- STARTING POINT ACCURACY  $\pm 2\%$
- PEAK OUTPUT CURRENT 1 amp
- LINEAR TRANSDUCER EXCITATION 9 kHz AT 4 V pk-pk
- PHASE LOCK LOOP INPUT 12,965 Hz NOMINAL

MISC. HOUSEKEEPING

- TEMPERATURE MONITOR AMPLIFIERS SENSOR CURRENT  $10 \mu A$   
OUTPUT VOLTAGE 0 TO +5 V FOR TEMP RANGE  
13 CHANNELS
- COVER DRIVE LINEAR CONTROL DRIVING 40 oz-in. dc  
TORQUE MOTOR, FOR 15 SECOND OPEN/  
CLOSE PERIODS. TACH FEEDBACK FOR  
CONSTANT SPEED.
- COMMAND LOGIC SWITCH CLOSURE INPUT  
LOGIC LOW OUTPUT COMMAND  
FUNCTIONS: OPEN COVER, CLOSE COVER,  
SLIDE REST, SLIDE LOCK, CALIBRATE
- H/K COMMUTATOR 64 INPUTS, 1 POLE  
912 SAMPLES/SECOND CLOCKED FROM PCM  
ENCODER
- POWER REGULATOR IC REGULATORS

INPUT	OUTPUT	REGULATION
+28 V	+5 V @ 1.5 A	$\pm 2\%$
	+15 V @ 1.0 A	$\pm 1\%$
	+18 V @ 0.8 A	$\pm 1\%$
-28 V	-15 V @ 0.6 A	$\pm 1\%$
	-20 V @ 0.8 A	$\pm 1\%$

TEMPERATURE CONTROLLERS

NAME	CONTROL TEMP AND TOLERANCE	POWER CAPABILITY	HEATER RESISTANCE	TEMP SENSOR
• LASER DIODE	$10^\circ K \pm 0.25^\circ K$	0.8 W	50 ohms	THERMISTOR
• FOCAL PLANE	$10^\circ K \pm 0.5^\circ K$	0.15 W	50 ohms	THERMISTOR
• TANK HEATER	$< 29^\circ K$ CAGE, REAR	5 W	90 ohms	GaAs DIODES
	$< 70^\circ K$ RAD SHIELD, REAR			
• VENT HEATER	$300^\circ K \pm 10^\circ K$	150 W	5 ohms	THERMISTOR

EMITTER POWER SOURCES

EMITTER	LOCATION
• TUNGSTEN BULB	REFERENCE I/F
• GaAs LASER DIODE	REFERENCE I/F
• $5.6 \mu$ LED	10th SCAN CAL.
• $5.6 \mu$ LED	FRONT COVER
• $3.2 \mu$ LED	FRONT COVER

TELEMETRY DATA

- PCM ENCODER 466,944 Hz B  
16 BIT WORD
- 32 WORDS PER
- 64 WORDS PER
- NRZ-L FORM
- VCO INPUTS,  $\pm 2.5$  V SIGNAL INTL.  
LASER FRINGE
- WHITE LIGHT MIRROR POSITION  
DRIVE MOTOR

HARDENING PROTECTION

- CRITICALLY DAMPED TIA FOR IMPROVED TRANS.
- CLAMP AT TIA OUTPUT FOR LARGE GAMMA PULSE
- FOUR COUNTS BEFORE INITIATING GAIN SWITC.
- DEWAR CAPABILITY FOR EXPANSION TO QUAD

PACKAGING

- SIGNAL CHANNEL TIA ON REAR PLATE OF DEWEY
- REFERENCE PREAMPS AT AUXILIARY INTERFEROM.
- ISOLATED CABLES AND ROUTING FOR SIGNAL,
- BLACKBODY CONTROL AND MONITOR ON FRONT
- REMAINDER AS PLUG-IN PC BOARDS IN ONE OR

## EMITTER POWER SOURCES

EMITTER	LOCATION	TYPE SUPPLY	NOMINAL OUTPUT	STABILITY
• TUNGSTEN BULB	REFERENCE I/F	CONSTANT VOLTAGE	5 V	+ 5%
• GaAs LASER DIODE	REFERENCE I/F	CONSTANT CURRENT	100 mA, adj	+ 1%
• 5.6 $\mu$ LED	10th SCAN CAL.	CONSTANT CURRENT	100 mA	+ 1%
• 5.6 $\mu$ LED	FRONT COVER	CONSTANT CURRENT	100 mA	+ 1%
• 3.2 $\mu$ LED	FRONT COVER	CONSTANT CURRENT	100 mA	+ 1%

## TELEMETRY DATA

- PCM ENCODER                          466,944 Hz BIT RATE  
16 BIT WORDS  
32 WORDS PER FRAME (1 H/K, 29 DATA)  
64 WORDS PER SUBFRAME  
NRZ-L FORMAT
- VCO INPUTS,  $\pm 2.5$  V                SIGNAL INTERFEROGRAM  
LASER FRINGE  
WHITE LIGHT PULSE  
MIRROR POSITION  
DRIVE MOTOR CURRENT

## HARDENING PROTECTION

- CRITICALLY DAMPED TIA FOR IMPROVED TRANSIENT RESPONSE.
- CLAMP AT TIA OUTPUT FOR LARGE GAMMA PULSES.
- FOUR COUNTS BEFORE INITIATING GAIN SWITCHING.
- DEWAR CAPABILITY FOR EXPANSION TO QUAD DETECTOR ARRAY.

## PACKAGING

- SIGNAL CHANNEL TIA ON REAR PLATE OF DEWAR.
- REFERENCE PREAMPS AT AUXILIARY INTERFEROMETER.
- ISOLATED CABLES AND ROUTING FOR SIGNAL, REFERENCE, AND H/K FUNCTIONS IN DEWAR.
- BLACKBODY CONTROL AND MONITOR ON FRONT COVER.
- REMAINDER AS PLUG-IN PC BOARDS IN ONE OFF-SENSOR PACKAGE.

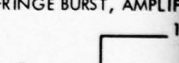
## I/F SIGNAL CHANNEL

- AC GAIN
- DYNAMIC RANGE
- SIGNAL PASSBAND
- CIRCUIT BANDWIDTH
- FILTER CHARACTERISTIC
- GAIN SWITCHING
- A/D CONVERSION
- SAMPLING RATE

## FOCAL PLANE/TIA

- DETECTORS: Si:As
- SIZE:  $0.045 \times 0.045$
- LOAD RESISTORS:  $4 \times 10^8 \Omega$  (SIGNAL CHANNEL)  
 $1 \times 10^{11} \Omega$  (BACKGROUND)
- PREAMPLIFIER: HMUL 2661 MOSFET
- TIA OUTPUT: NOISE  $0.9 \mu V/\sqrt{Hz}$
- BACKGROUND CALIBRATION: MAX SIGNAL 1.3 V PEAK
- DC COMPONENT MONITOR: CIRCUIT BW DC TO  $10,000$   
 $10^9$  TO  $10^{12}$  photons/cm<sup>2</sup>
- BACKGROUNDS: 0.33 V/VOLT AT TIA OUTPUT

## REFERENCE CHANNELS

- DETECTORS SILICON PHOTODIODES
  - PREAMPLIFIERS HMUL 2661 MOSFET
  - TIA OUTPUT 50 mV pk-pk
  - LASER FRINGE SIGNAL 12,965 Hz, NOMINAL AMPLIFY TO 5 V pk-pk  
USED FOR SAMPLE COMMAND SERVO FEEDBACK
  - SAMPLE COMMAND PULSE 25,930 pps  
1  $\mu$ s PULSE
  - WHITE LIGHT SIGNAL FRINGE BURST, AMPLIFIED
  - DELAYED WHITE LIGHT STATUS 0 TO 100 ms, ADJUSTABLE  
USED FOR GAIN SWITCHING
- 

3

#### V/F SIGNAL CHANNEL

• AC GAIN	X64 HIGH STATE X4 LOW STATE
• DYNAMIC RANGE	27,800 PK SIGNAL/RMS NOISE
• SIGNAL PASSBAND	610 Hz (18 $\mu$ ) TO 2750 Hz (4 $\mu$ )
• CIRCUIT BANDWIDTH	160 TO 8800 Hz
• FILTER CHARACTERISTIC	4 POLE BUTTERWORTH, 24 dB/OCTAVE
• GAIN SWITCHING	AUTOMATIC AFTER 4 COUNTS (152 $\mu$ s) ABOVE THRESHOLD
• A/D CONVERSION	14 BITS, BIPOLAR INPUT
• SAMPLING RATE	26 kHz, ASYNCHRONOUS

#### FOCAL PLANE/TIA

• DETECTORS:	Si:As
• SIZE:	0.045 x 0.045
• LOAD RESISTORS:	$4 \times 10^8 \Omega$ (SIGNAL CHANNEL) $1 \times 10^{11} \Omega$ (BACKGROUND SENSOR)
• PREAMPLIFIER:	HMUL 2661 MOSFET
• TIA OUTPUT:	NOISE $0.9 \mu V/\sqrt{Hz}$ MAX SIGNAL 1.3 V PEAK
• BACKGROUND CALIBRATION:	CIRCUIT BW DC TO 10,000 Hz $10^9$ TO $10^{12}$ photons/cm <sup>2</sup> s
• DC COMPONENT MONITOR:	0.33 V/VOLT AT TIA OUTPUT

#### REFERENCE CHANNELS

• DETECTORS	SILICON PHOTODIODES
• PREAMPLIFIERS	HMUL 2661 MOSFET
• TIA OUTPUT	50 mV pk-pk
• LASER FRINGE SIGNAL	12,965 Hz, NOMINAL AMPLIFY TO 5 V pk-pk USED FOR SAMPLE COMMAND SERVO FEEDBACK TELEMETRY VCO
• SAMPLE COMMAND PULSE	25,930 pps 1 $\mu$ s PULSE
• WHITE LIGHT SIGNAL	FRINGE BURST, AMPLIFY TO 5 V pk-pk
• DELAYED WHITE LIGHT STATUS	0 TO 100 ms, ADJUSTABLE USED FOR GAIN SWITCHING

1  
0

LEVEL CHANGE AT ZERO  
RETARDATION USED FOR  
COADDITION

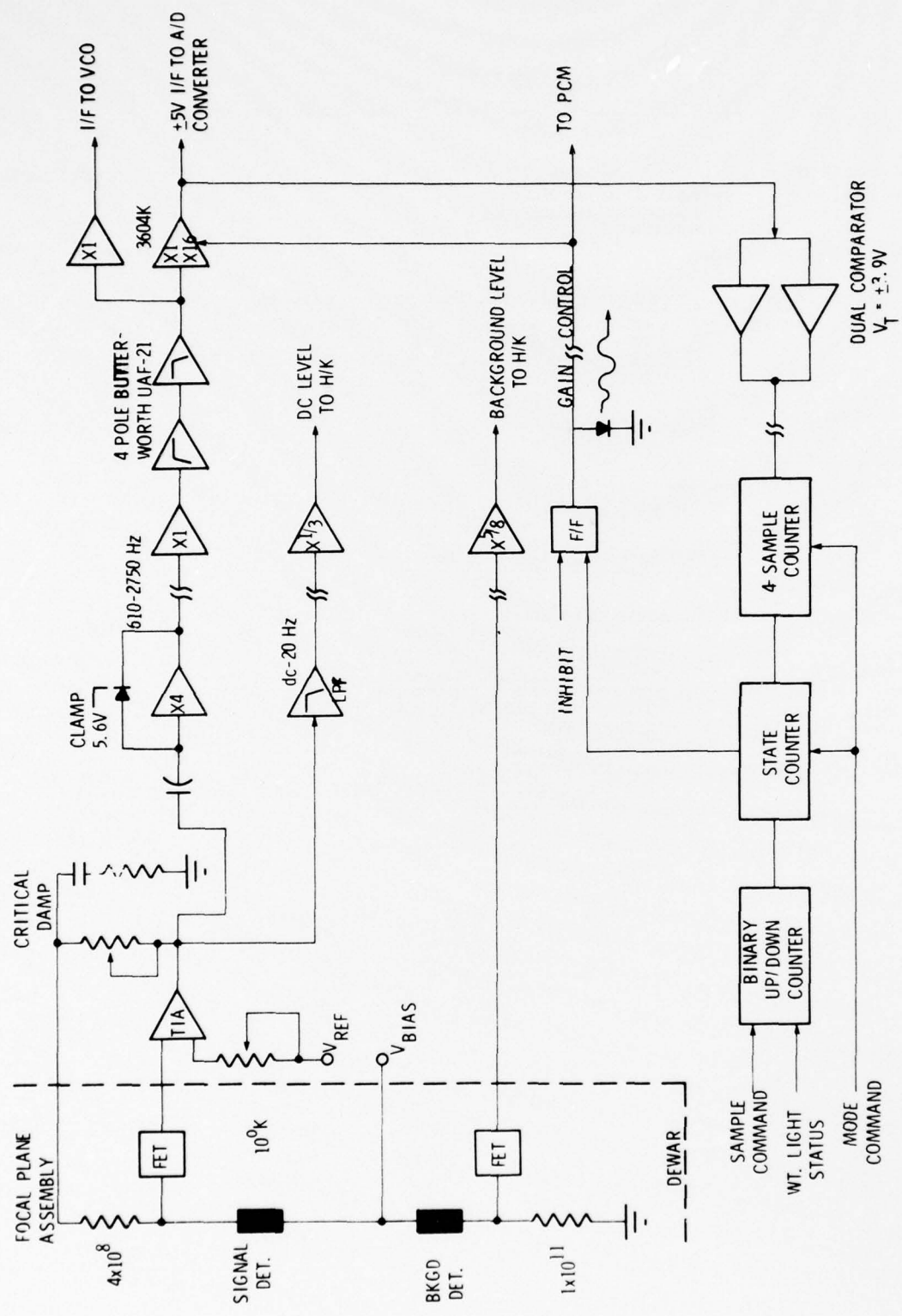


Figure 4.7 SIGNAL CHANNEL FUNCTIONAL DIAGRAM

reduce the gain by a factor of 16. Gain switching logic uses counting techniques to automatically revert back to high gain, symmetrically, on the other side of zero retardation. To prevent false gain switching because of transients or gamma pulse effects, four successive above-threshold comparisons must occur before gain switching occurs. Gain switching is inhibited during data sampling by the PCM encoder.

The signal channel contains low-pass and high-pass filters with cutoff frequencies located four times removed from the upper and lower signal frequencies. The objective is to achieve linear phase response across the signal passband. The processed signal goes to the PCM encoder for transmission to the ground.

This design is patterned after the developed HIRIS signal channel electronics and incorporates the modifications listed below:

- Replaced Si:As detector
- Replaced Butterworth filters with universal type
- Added 4-count gain switching
- Redesigned gain switching logic
- Added critical damping components
- Added clamp for gamma pulses
- Added Trimpot for V<sub>REF</sub> at TIA
- Increased resolution of dc level by factor of 2
- Added H/K readout of background detector
- Added test points, gain state indicator, and operator switch
- Packaged on 3 pc board assemblies
- Moved TIA to rear of dewar

#### 4.2.3.2 Reference Channels Group

This group, shown schematically in Figure 4.8, detects, amplifies, and processes the laser cosine signals from the monochromatic source and the white-light pulse. Two silicon photodiodes on the I/F assembly detect each source. The reference TIAs consist of a MOSFET-source-follower and operational-amplifier arrangement similar to the signal TIA. However, the MOSFET and feedback components are located on the cold I/F assembly, and the operational amplifier is located in the off-sensor package. The outputs of these TIAs go to the reference processor also located in the off-sensor package.

The reference processor amplifies the laser and white-light signals from the two reference TIAs to 5 volts (peak-to-peak) before processing. In the laser channel, fringe crossovers are detected and sample command pulses generated at the crossover rate (26 kHz). These pulses are inhibited during mirror flyback. The analog fringe signal is directed to the mirror servo board for phase-lock loop control. The fringe frequency is nominally 12,965 Hz, and the sample command pulses for A/D conversion nominally occur at 25,930 pps.

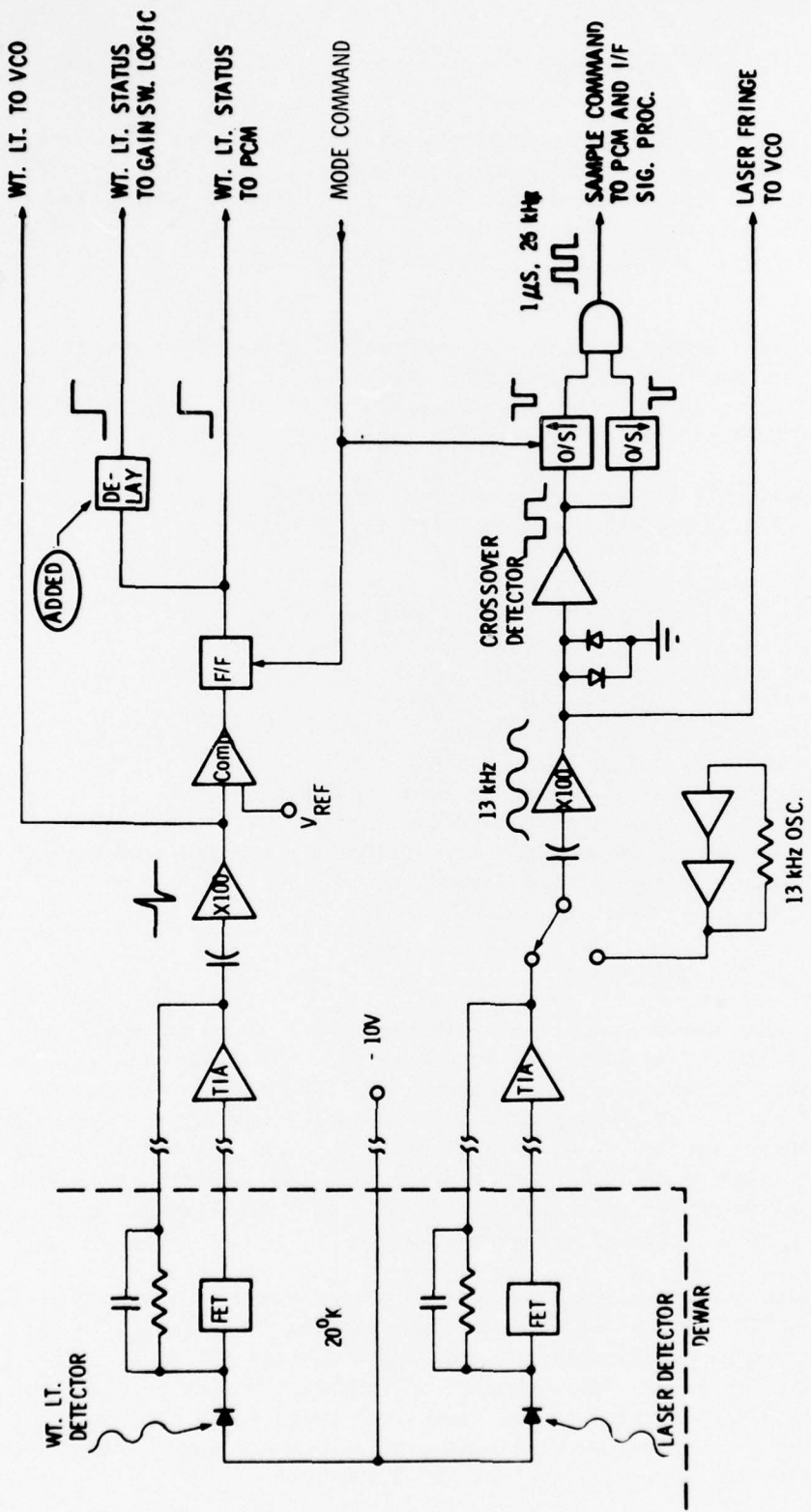


Figure 4.8 REFERENCE CHANNEL FUNCTIONAL DIAGRAM

In the white-light channel, a threshold detector triggers a logic level shift to signify passage of the scan mirror through zero retardation in the white-light I/F. A variable delay circuit allows alignment of this signal to zero retardation in the signal channel. This delayed, white-light, logic signal is used in gain-switch counting. The processed reference signals ("white-light" and "sample" on Figure 4.3) go to the PCM encoder for transmission to the ground.

#### 4.2.3.3 Mirror Servo Group

This group consists of the slide drive mechanism, mirror servo electronics, shown schematically in Figure 4.9, and timing generator, shown in Figure 4.10; it controls the sweep and flyback motion of the interferometer mirror slide. The timing circuit generates the basic scan/flyback waveforms for the mirror servo and the corresponding data/inhibit waveforms for the signal channel and reference channels. The master clock is a free-running oscillator which can be programmed, locally, in discrete steps to provide scan rates of 1 to 4 per second. Logic circuits derive the proper scan commands for the servo and data/inhibit commands for the signal and reference channels. The desired scan is a one-per-second sawtooth with 90% scan efficiency.

A thrust force developed in the speaker-like drive mechanism attached to the slide controls mirror motion. Drive thrust is proportional to drive current from the motor-coil drive circuit. The command signal to this circuit, which keeps the slide moving, is an error signal produced by comparing a sawtoothed sweep-generator signal to two measurements of mirror motion.

The first measurement is made by a linear motion transducer with its primary fed by an excitation oscillator. A sample-hold detector produces a dc signal from the transducer ac output. This signal, representing mirror position, is compensated, inverted, and fed to a summing amplifier for comparison with the sweep-generator command. The second measurement of mirror motion examines velocity linearity, using the monochromatic source (laser fringe) frequency. A phase-lock loop produces a dc error signal which is integrated and summed with the sweep-command and transducer feedback signals. Accurate closed-loop control of mirror velocity during the sweep motion uses both laser-fringe frequency error (resulting from mirror motion) and transducer feedback error, with priority to the first. The transducer, only, controls flyback motion.

#### 4.2.3.4 Housekeeping (H/K) Group

The term housekeeping categorizes a group of diagnostic and control functions that facilitate mission functions and monitor critical parameters of the experiment packages (dewar and electronics). This group controls and monitors temperatures and controls power to internally-generated signal sources. The H/K group consists of strategically-placed temperature sensors (H/K monitors), an H/K commutator, several power controllers, and four temperature controllers.

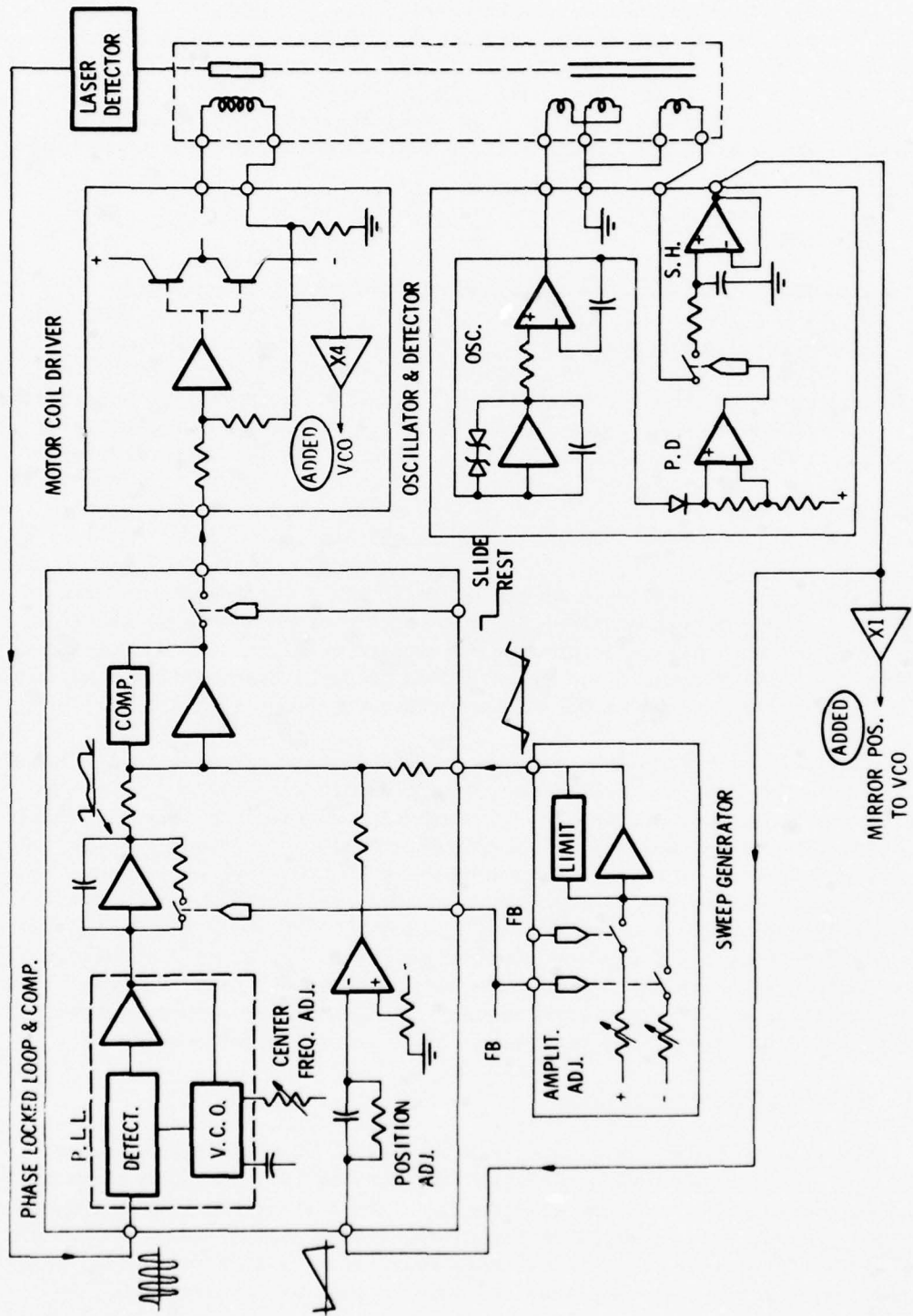


Figure 4.9 MIRROR SERVO FUNCTIONAL DIAGRAM

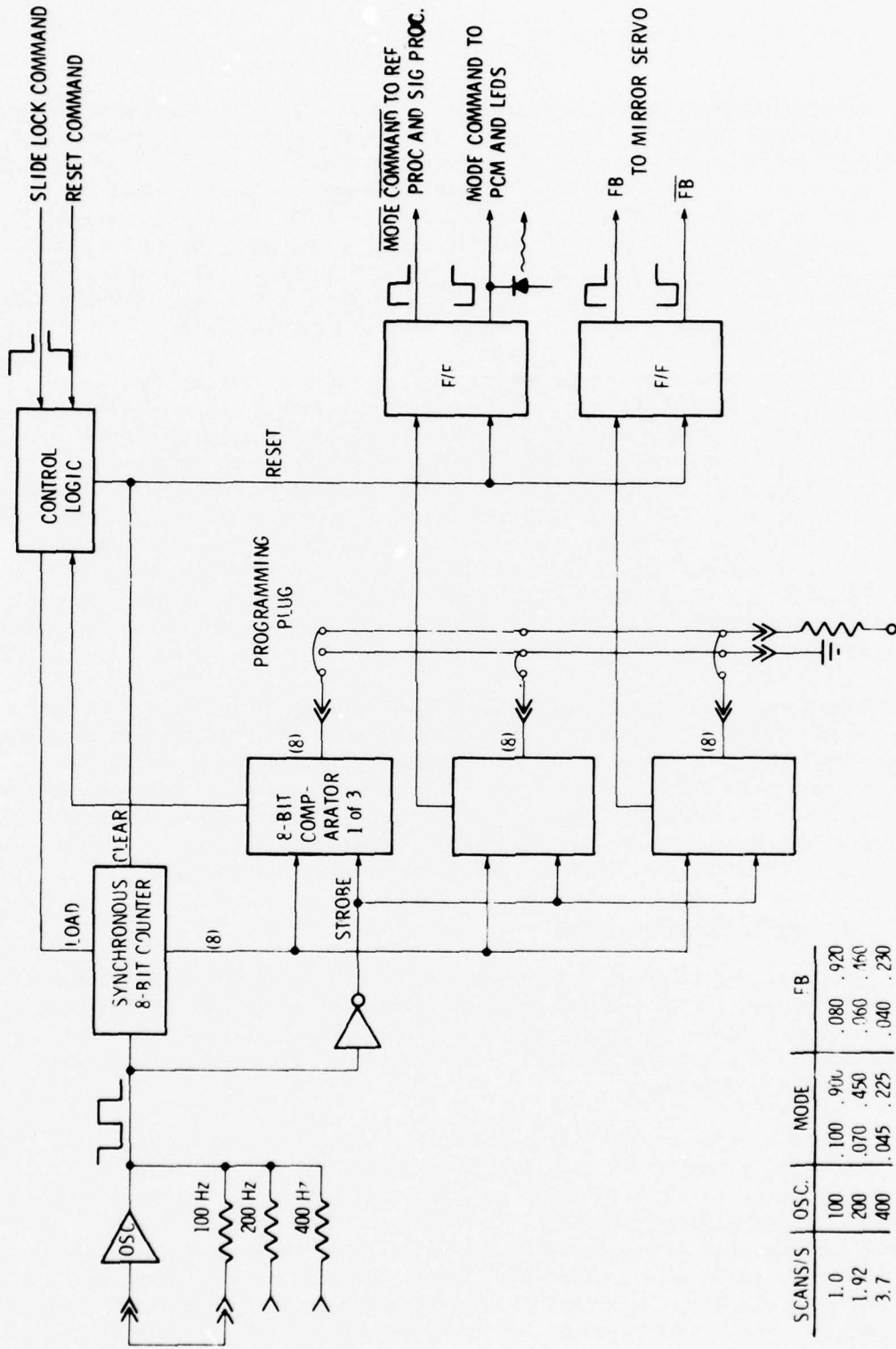


Figure 4.10 TIMING GENERATOR FUNCTIONAL DIAGRAM

Cryogenic temperatures in the dewar are monitored with gallium-arsenide temperature sensors. A precise 10-microampere current passes through each sensor. The resultant voltage drop is amplified and offset in an analog circuit to produce a 0 to +5 Vdc signal in the operating temperature range. These and other H/K monitors (including one in the blackbody) are integrated in the H/K commutator. This single-pole solid-state commutator sequentially scans up to 64 housekeeping signals and connects them to the H/K input of the PCM encoder. The commutator gets incremented once per PCM output frame, so that a new H/K sample always appears in word 3. Thus, each H/K monitor is sampled 14.25 times per second.

Power to the monochromatic source (a laser diode), white light bulb, calibration LEDs, and the blackbody is controlled as follows. An adjustable current source operates the reference laser diode; RC time constants slowly apply and remove current. An adjustable voltage source (0 to +2 V) operates the tungsten filament of the white light bulb. Normal load values are 1.7 volts and 14 mA; operation is continuous unless inhibited manually. Fixed, 100 mA, current source operates the 5.6-micrometer LED located within the front opcls. Mode command and logic control turns this LED on for one complete scan out of every ten scans of the mirror drive. A solid-state circuit, called the blackbody control switch, applies +28 Vdc to the blackbody during a calibrate command; load current is less than one ampere.

Temperature controllers maintain 10 K at the signal detector mount and the monochromatic source mount and "room" temperature at the helium vent; a helium tank heater operates upon demand. The helium tank heater and helium-vent heat exchanger operate from the heater controls. A closed-loop control circuit applies proportional power to the helium tank heater upon demand from either the cold-shield temperature sensor or the radiation-shield temperature sensor. Another closed-loop circuit maintains 300 K at the helium-vent heat exchanger.

#### 4.2.3.5 Experiment Interface Group

This electronics group categorizes the functions in the experiment packages that interface with the GSE prior to launch and those non-HRC elements of the payload in flight. It covers the remaining blocks of Figure 4.3. The experiment interface group consists of the PCM encoder, telemetry, cover drive and control, and command logic.

The PCM encoder receives inputs from the signal channel, reference channels, housekeeping monitors, and other experiment circuits for encoding prior to transmission to the experiment checkout and data-collecting equipment of the GSE. The PCM encoder consists of a sample-and-hold and 14-bit A/D converter for processing analog housekeeping data. The PCM encoder accepts a  $\pm 5$  volt (maximum) analog signal from the signal processor. Upon receiving a sample command, the detected signal is sampled and converted to a 14-bit digital signal in binary "two's complement." An input mode-command signal defines the data sampling period.

From the start of scan, the PCM encoder stores 1440 words in its buffer memory. Words 4 through 32 of the PCM data frame are filled with an alternating zero-one pattern during this period. After 1440 words are written into memory, the data readout begins. Writing and reading cycles continue until the writing is completed at the start of mirror flyback. Reading continues until the buffer memory has been emptied, at which time the flyback data-word pattern is again inserted into the serial NRZ-L output.

SPHIRIS instrument data, collected in flight, is sent to the ground by a two-link, S-band, telemetry system with interfaces shown in Figure 4.11. The digital output of the PCM encoder in the electronics box goes to the S-band transmitter, located in the service module of the payload. PCM output is mostly signal-channel and H/K data. Analog outputs from other circuits of the SPHIRIS experiment (and other payload sources) are transmitted by an FM/FM link. FM/FM analog outputs come from such SPHIRIS sources as the signal channel, reference channels, mirror servo group (position), I/F motor current, and selected H/K data.

The cover-drive circuit, a board in the electronics box, opens and closes the dewar cover in response to input commands (see next paragraph). Sufficient drive current operates the cover motor at the specified opening and closing speed; tachometer feedback will maintain a reasonably constant rate. A microswitch on the cover mechanism indicates fully-open and fully-closed positions and halts drive power. The time from fully closed to fully open (or fully open to fully closed) is a nominal 15 seconds. A potentiometer, connected to the moving arm, provides a continuous reading of cover position. A barometric-switch interlock on the motor power prevents accidental opening during launch or anytime below 50 kilometers of altitude.

The command-logic circuit, a board in the electronics box, generates the five required experiment-command signals in response to a specific switch closure (logic zero) from either the GSE prior to launch or the payload timer in flight. (There can be no ground control of the experiment in flight). Table 4.7 lists these commands, input switch type, and command function.

Any one of the following signals terminates the calibration sequence:  
1) A release (open) by the GSE calibrate-command switch, 2) An open-cover command, and 3) A slide-lock command. One second after a power turn-on, a logic 0-to-1 transition at the command-logic board resets the logic at the timing-generator board. The command-logic circuitry utilizes Schmitt triggers (or equivalent) to regenerate input commands and to provide a reasonable degree of noise immunity on each input-command line.

Overall internal and external interfacing of the SPHIRIS electronics is illustrated in Figures 4.12 and 4.13. Packaging concept is shown in Figure 4.14.

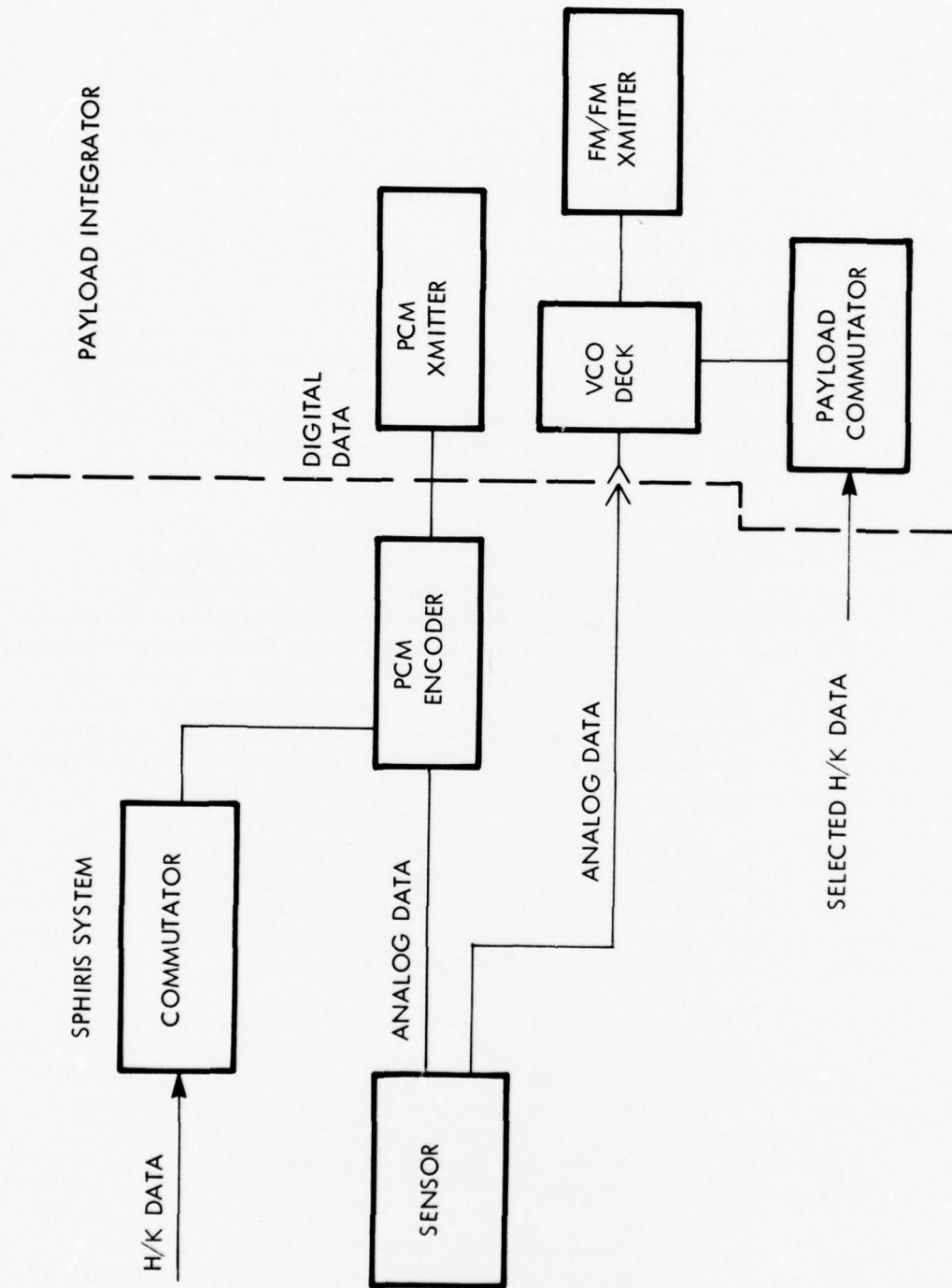


Figure 4.11 FLIGHT SYSTEM DATA INTERFACE

Table 4.7  
SPHIRIS COMMAND SIGNALS

COMMAND	TYPE	FUNCTION
Open Cover	Pulse	Sends a signal to the cover-drive circuit.
Close Cover	Pulse	Sends a signal to the cover-drive circuit (on a separate line from the open-cover signal).
Slide Rest	Duration	Sends a signal to the mirror-servo circuit, continuous with switch closure. In this mode, the servo no longer controls motion of the slide.
Slide Lock	Duration	Sends a signal to the timing-logic circuit, continuous with switch closure. In this mode, the slide is held at the starting point of scan with a control force of approximately 7 g.
Calibrate	Pulse	The command-logic circuit first counts two complete mirror scans (using mode command as a clock pulse); then it applies a signal to the blackbody control switch and the current source for the 5.6-micrometer LED. In this manner, two scans of background are recorded before the calibration sources are turned on.

#### 4.2.4 Vacuum and Cryogenic Systems

It is necessary to create and critically control three aspects of the spectrometer's internal environment: cleanliness, pressure evacuation, and low temperature. Extreme cleanliness makes it possible to maintain low-scatter optics in the instrument. A contamination prevention and control program during manufacture, lab testing, and shipping (clean rooms, etc) achieves cleanliness. A high vacuum within the pressure vessel of the instrument makes it possible to achieve and maintain the required operating temperatures; it also provides a matching, near-space, pressure environment on the ground and in flight when the sensor door opens to permit the spectrometer to perform the SPHIRIS mission. The required in-flight cryogenic temperatures within the sensor reduce photon background below a maximum sensitivity. The following paragraphs describe the vacuum system and the source, flow path, control, and insulation of the cryogenic system.

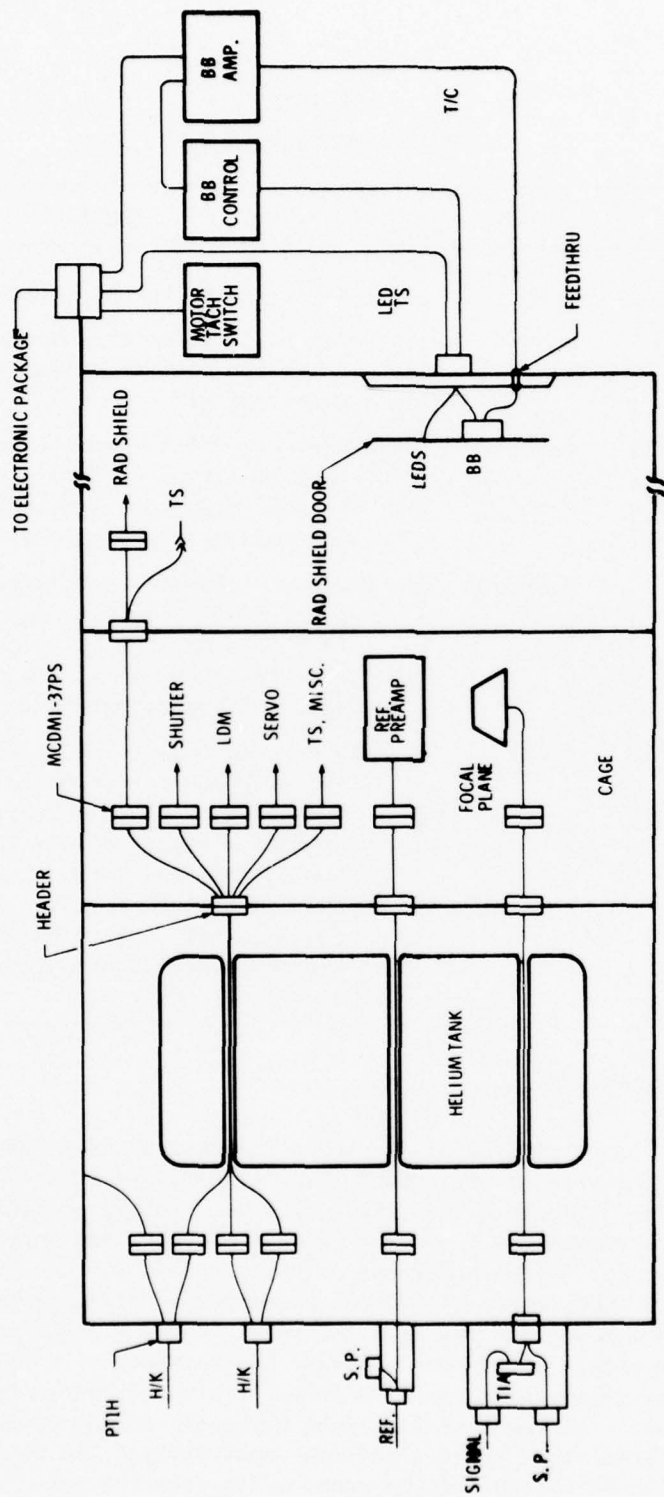


Figure 4.12 SPHIRIS DEWAR CABLING

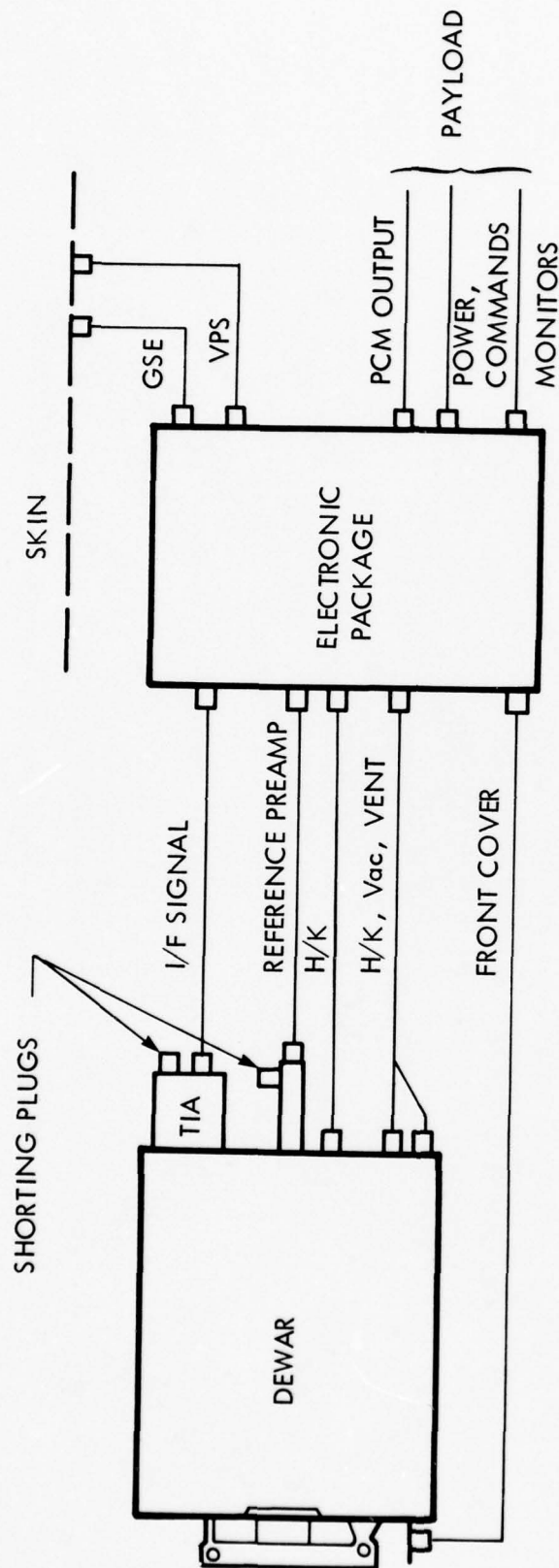
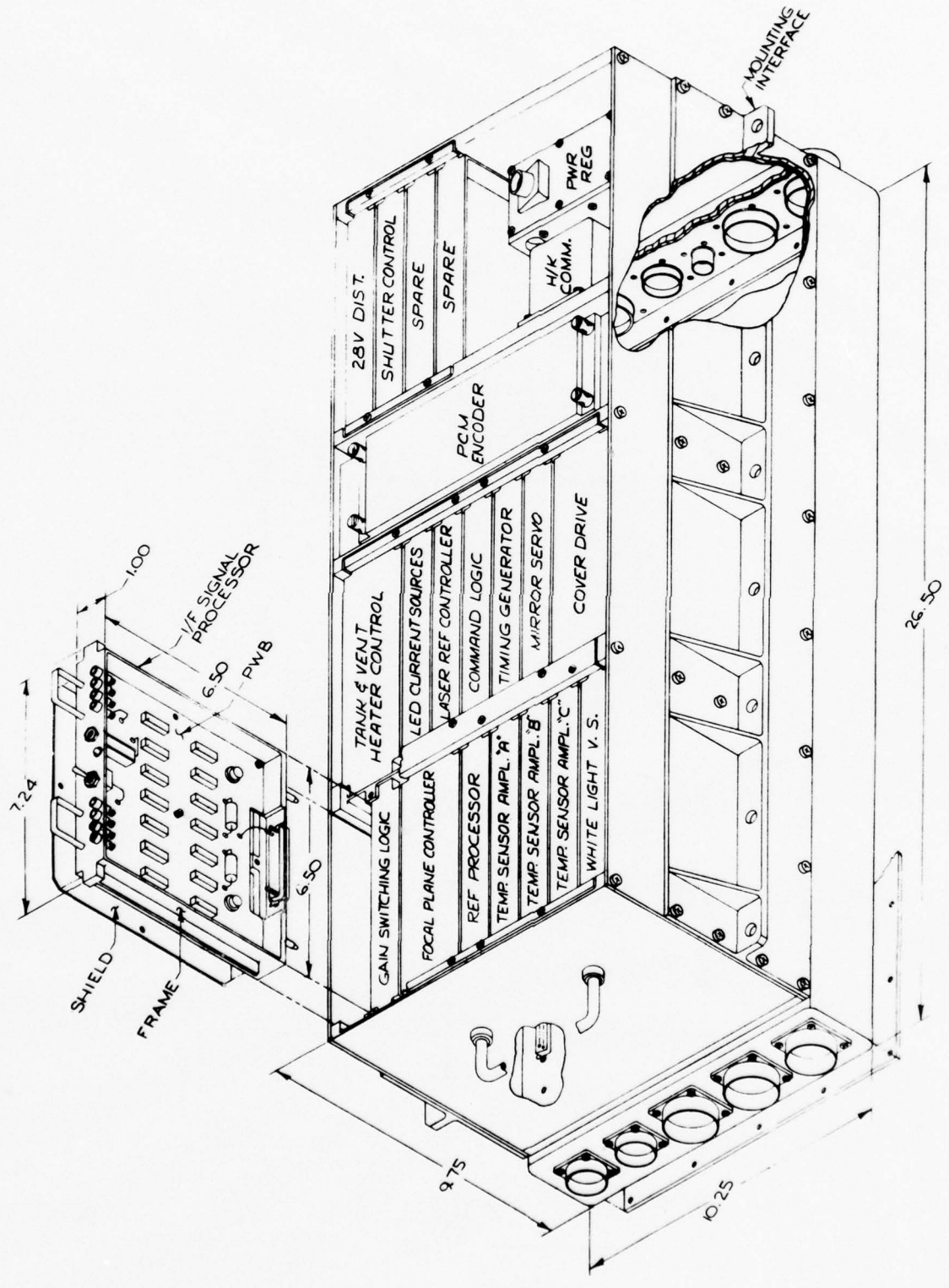


Figure 4.13 SPHIRIS SYSTEM CABLING



4-26

Figure 4.14 SPHIRIS OFF-SENSOR ELECTRONICS

#### 4.2.4.1 Vacuum System

The cryogen storage tank, I/F assembly, and telescope and baffle chamber are contained within a pressure vessel inside the helium dewar. The I/F assembly is enclosed by the radiation shield, and the bulk of the optics is mounted on an optical bench. The pressure vessel provides a rigid structure to contain a high vacuum ( $10^{-4}$  Torr or better) during the ground-hold and flight periods. High vacuum reduces convective heat transfer and eliminates cryodeposits on critical components. A Vacuum Pumping Station evacuates the experiment pressure vessel during an actual or simulated countdown that requires many hours.

The VPS is built around a turbo-molecular pump used for pumpdown prior to cryogen fill; normal procedure is to pump for at least 12 hours before flowing helium. The pressure vessel will maintain the vacuum above the required minimum for at least 8 hours after disconnecting the VPS.

#### 4.2.4.2 Cryogen Source

The cryogen storage tank retains the refrigerant for cooling sensor components to their respective operating temperatures. Liquid helium at three atmospheres is the refrigerant. This helium tank has a liquid-level sensor inside to determine the amount of fill. A tank capacity of 24 liters provides the sensor with cooling for a 7- to 8-hour hold time plus a 400-second flight time. The helium tank in the experiment pressure vessel is filled from a commercially-supplied LHe dewar on the launch pad during the long countdown.

#### 4.2.4.3 Helium Flow Path

Liquid helium changes to a supercritical state in the tank at about 5.5 K, and the supercritical helium flows through four heat-exchanger stages of the spectrometer in a serial path. The first stage of heat exchange takes place at the focal plane of the IR detector. The focal plane is thermally isolated and cooled to 10 K by three flexible straps of pure copper fastened to the heat exchanger. The second stage of heat exchange takes place at the reference source (laser diode) mount; the laser diode is also controlled at 10 K. Both first- and second-stage heat exchangers are copper with copper plates.

The third-stage heat exchanger is internally-finned aluminum tubing clamped to the boom of the optical bench which supports the telescope optics and interferometer. The interferometer is thermally coupled to the optical bench structure by pure copper straps; the bench, telescope optics, and I/F are cooled to 30 K or less. The helium next flows to the fourth-stage, radiation-shield, heat exchanger which is thermally isolated from the pressure vessel by low-conductive supports and multilayered insulation (MLI). This heat exchanger consists of 12 loops of internally-finned aluminum tubing wrapped around the radiation shield; the temperature of the radiation shield is controlled at 70 K. The radiation shield serves as an intermediate thermal stage between the warm environment and the cold

optical system. It absorbs the major heat load coming into the optical system. The use of a radiation shield increases the thermal efficiency of the cryogenic system. When the helium leaves the radiation-shield heat exchanger, it flows outside of the pressure vessel and dewar to be exhausted through the vent heater and vent-pressure relief valve.

#### 4.2.4.4 Temperature Control

The vent heater and the vent heat exchanger are serially connected to the radiation shield. Vent heat warms up the cold cryogen prior to leaving the SPHIRIS system so as to prevent frosting in the rear of the sensor and to prevent the pressure relief valve from freezing in the open position. The heater size is 150 watts. The vent heat exchanger is made of copper with integrally-soldered copper plates; the heater is imbedded in the heat exchanger.

The pressure relief valve at the end of the helium vent line is set for 3 atmospheres of pressure. This valve is a passive device and operates independently of other safety devices. It maintains operating pressure for the cryogen system.

The temperature control system has electronic circuitry (see Figure 4.7) which maintains the proper cryogen flow rate so that the temperatures of the radiation shield and/or optical bench are maintained at or below their maximum for operation. This is accomplished by detecting the temperature of either stage and using this output to drive a heater in the storage tank. Adding heat in the tank increases the mass flow rate.

#### 4.2.4.5 Multilayered Insulation (MLI)

The MLI blanket provides a radiation barrier from the pressure vessel to the radiation shield; it reduces the radiation heat load to the radiation shield. The blanket consists of 20 layers of 1/4-mil crinkled aluminized mylar. Each 1.4-mil layer is perforated to 0.5% of its area for venting. The 20 layers are contained within a 5-mil, aluminized-mylar, semirigid container. This container is sealed except for strategically-located venting points which have a particulate and an activated charcoal filter within them. A section of the MLI blanket forms part of the sensor front cover to insulate the door area when the cover is closed.

#### 4.2.4.6 Heat Loading and Flow Rate Analysis

Table 4.8 gives a summary of the heat loads on the major assemblies of the SPHIRIS dewar from external sources. The temperature requirements for the focal plane and laser diode are 10 ( $\pm 0.5$ ) K with an I/F temperature equal to or less than 30 K. Both the IR detector in the focal plane and the reference source (laser diode) have a heater and temperature sensor for active

Table 4.8  
SPHIRIS HEAT LOAD SUMMARY

HEAT SOURCE	HEAT LOAD (Watts)
1. RADIATION SHIELD (70 K)	
a. Fiberglass Support	2.45
b. Front Ball Support	2.64
c. Multilayered Insulation (MLI)	5.87
d. Penetrations	
1) Radiation	7.40
2) Conduction	3.98
e. Calibration Sources	<u>1.32</u>
TOTAL	23.66
2. OPTICAL BENCH (30 K)	
a. Fiberglass Support	0.42
b. Radiation	0.61
c. Penetrations	<u>0.35</u>
TOTAL	1.38
3. HELIUM TANK (6 K)	
a. Support	0.15
b. Radiation	0.19
c. Penetrations	0.11
d. Tank Heater (10-watt capacity)	<u>1.20</u>
TOTAL	1.65
4. VENT HEATER (150-watt capacity)	78

control. Tables 4.9 and 4.10 give heat loads for these first and second stages of heat exchange. The front door plate (dewar cover) has a requirement to reduce emission from the warm plate to an acceptable level. This is accomplished by applying several layers of MLI on the door plate. The following assumptions are made: emissivity ( $\epsilon$ ) is 0.05 on each side of each layer; there are five layers; the plate temperature is 100 K; and the environmental temperature is 70 K. The above door-plate conditions will result in a temperature at the outer layer of 74 K. Figure 4.15 shows temperature variation during the mission time for two pertinent values of emissivity.

Flow rate is governed primarily by heat load; but flow rate is also a function of external radiation conditions, particularly sun angle during a day mission. To achieve an eight-hour hold time with an approximate flow rate of 0.065 gram per second, which satisfies night mission thermal loading, it requires about 1859 grams of liquid helium which occupies 18 liters of tank volume. Using these figures as a basis, and incorporating a practical safety factor, a tank size of 24.5 liters was decided upon. Table 4.11 lists cryogen allocation by weight. Ullage is cryogen that is not usable because it is too warm; residual represents the tank reserve.

The results of thermal analysis indicate an impact on hold time (or, conversely, increased helium capacity) if sun angles are less than 90 degrees (see Figure 4.16). Furthermore, vent-heater power consumption increases rapidly with solar heating due to increased flow. Figures 4.17 through 4.21 show the results of dewar temperature variations with night and day missions; day missions are most unpredictable and uncontrollable with severe sun loading and produce internal instrument temperatures as much as 20 K higher than the night mission. Since missions were constrained to flights experiencing low sun loading, cryogen tank sizes and cryogen weights given in Table 4.11 were acceptable for SPHIRIS.

#### 4.2.5 In-Flight Calibrator

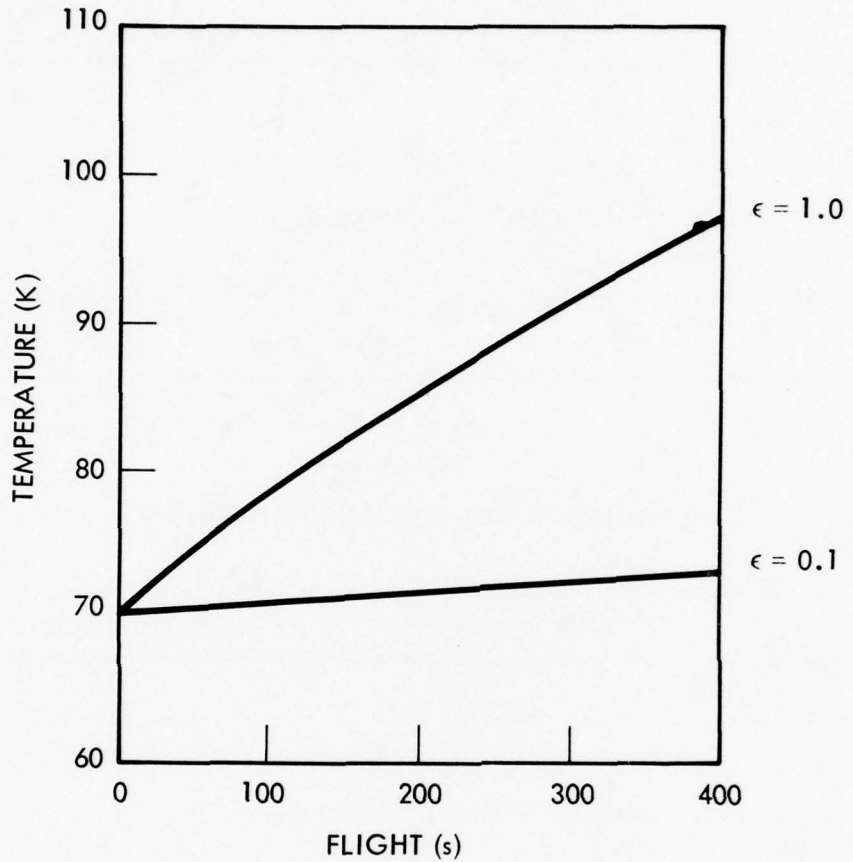
The in-flight calibrator, Figure 4.22, serves as a means of system alignment and sensitivity check in the laboratory, at the launch pad for a go/no-go decision, and during the launch and the flight. This internal calibrator system contains six IR sources: a warm door at 70 K; a point-source blackbody at 300 K in conjunction with a cryogenically-cooled 10.6-micrometer spike filter; a 5.6-micrometer LED; a 3.2-micrometer LED; a 10th-scan 5.6-micrometer LED; and a cold shutter to optically isolate the interferometer from the rejection telescope. Figure 4.3 shows their location on the vacuum door. The blackbody radiates a broad spectrum from 2 to 22 micrometers. The LEDs radiate line spectrums. The 10th-scan LED provides a secondary standard for system sensitivity calibration at every tenth scan of operation. The tenth-scan feature depends on a successful calibration transfer from a known standard source in a low-background chamber.

Table 4.9  
SPHIRIS FOCAL-PLANE THERMAL ANALYSIS

HEAT SOURCE	HEAT LOAD (mW)
Bias	16.0
Support (Isolation = 10-mil Stainless Steel)	47.4
Wires (10-mil Manganin & 10-mil Beryllium Copper)	0.4
Heater (150-mW capacity)	<u>110.0</u>
TOTAL	173.8

Table 4.10  
SPHIRIS LASER-DIODE THERMAL ANALYSIS

HEAT SOURCE	HEAT LOAD (mW)
Laser Diode	150.0
Support (Isolation = 10-mil Stainless Steel)	82.0
Wires (10-mil Manganin & 10-mil Beryllium Copper)	0.3
Heater (1.8-watt capacity)	<u>420.0</u>
TOTAL	652.3



ASSUMPTIONS:

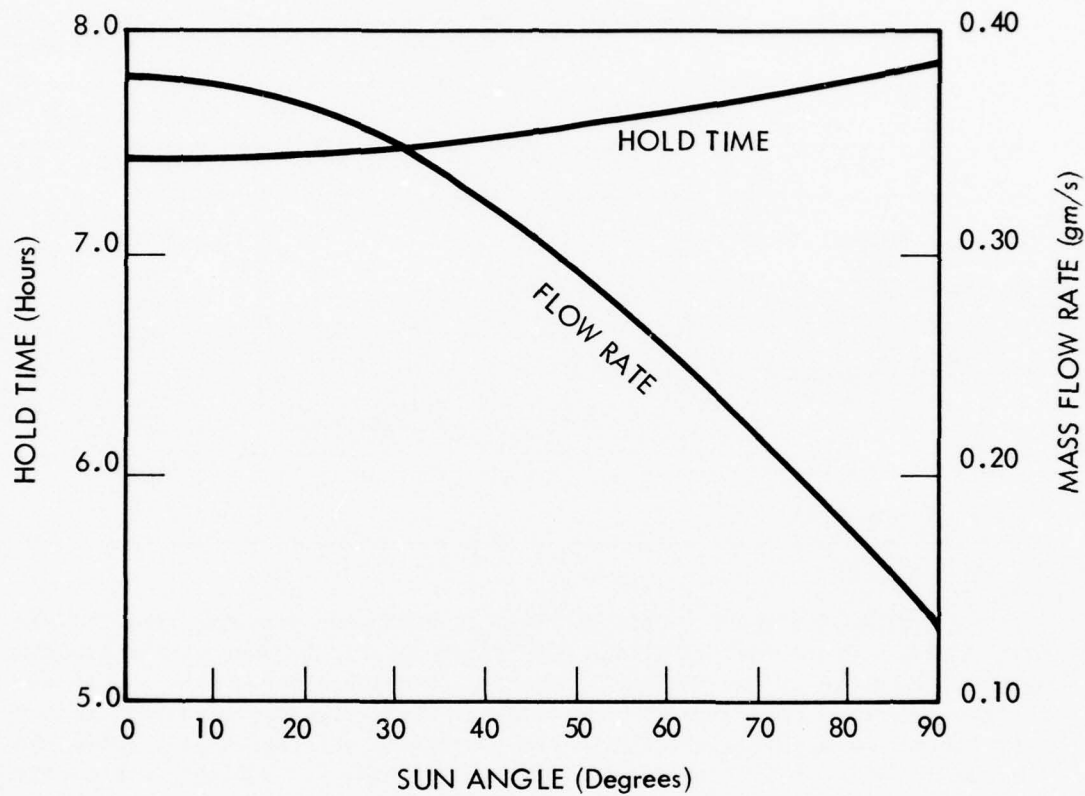
- a. HEATING AND COOLING IS FROM ONE SIDE OF THE RADIATION-SHIELD DOOR ONLY.
- b. EARTH EMISSION IS TYPICAL FOR A NIGHT MISSION.
- c. MATERIAL PROPERTIES CHANGE WITH TEMPERATURE.

Figure 4.15 SPHIRIS RADIATION-SHIELD-DOOR TEMPERATURE

Table 4.11  
SPHIRIS HELIUM WEIGHT BREAKDOWN

DESIGN COMMITMENT	HELIUM (Grams)
Tank Size = 24.5 Liters (97% usable volume)	2970
85% Fill (practical figure for filling)	2520
Ground Hold (8 hours @ 0.065 grams/second)	<u>1859</u>
	NET 661
Flight (400 seconds)	<u>40</u>
	SUBTOTAL 621
Ullage (not usable)	<u>392</u>
Residual (reserve)	229

Since the spectrometer operates at cryogenic temperatures, the six calibrating sources must be within the helium dewar. Because of the broadband spectral coverage by the SPHIRIS instrument, a calibration source should provide spectral emission from 5 to 22 micrometers. Therefore, the blackbody radiator must operate at a sufficiently high temperature to emit spectrally above the instrument NESR without exceeding its dynamic range. To achieve this condition, the blackbody source has been attenuated by reducing its effective aperture to 0.030 inch.



ASSUMPTIONS:

- SPHIRIS USES A HIRIS-TYPE CONTROL SYSTEM OF FLOW RATE.
- RESULTS SHOW THE EFFECT OF EARTH'S ALBEDO PLUS EMISSION.

Figure 4.16 SPHIRIS HOLD TIME AND MASS-FLOW RATE VS SUN ANGLE

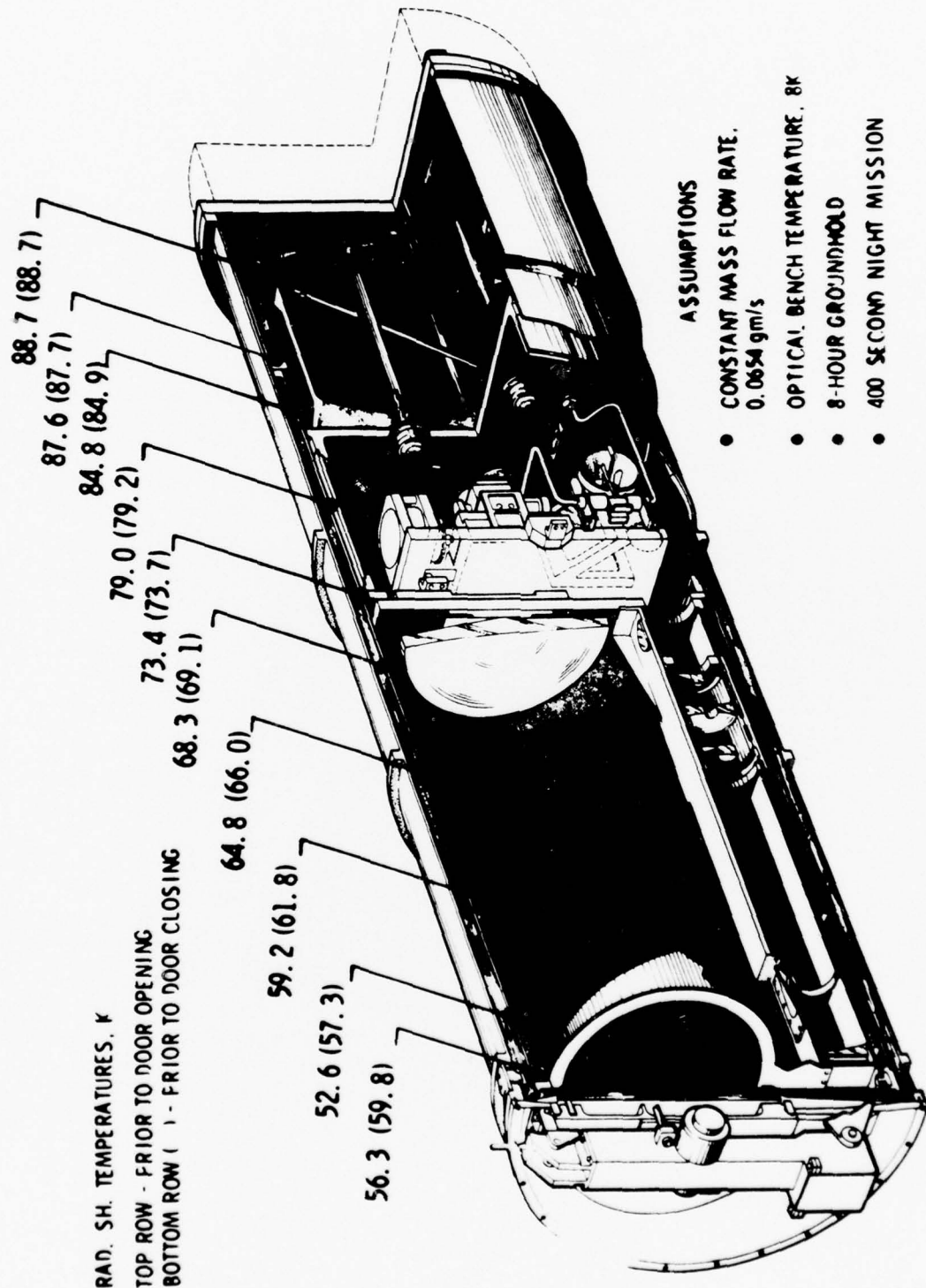


Figure 4.17 SPHIRIS RADIATION-SHIELD TEMPERATURES, NIGHT MISSION

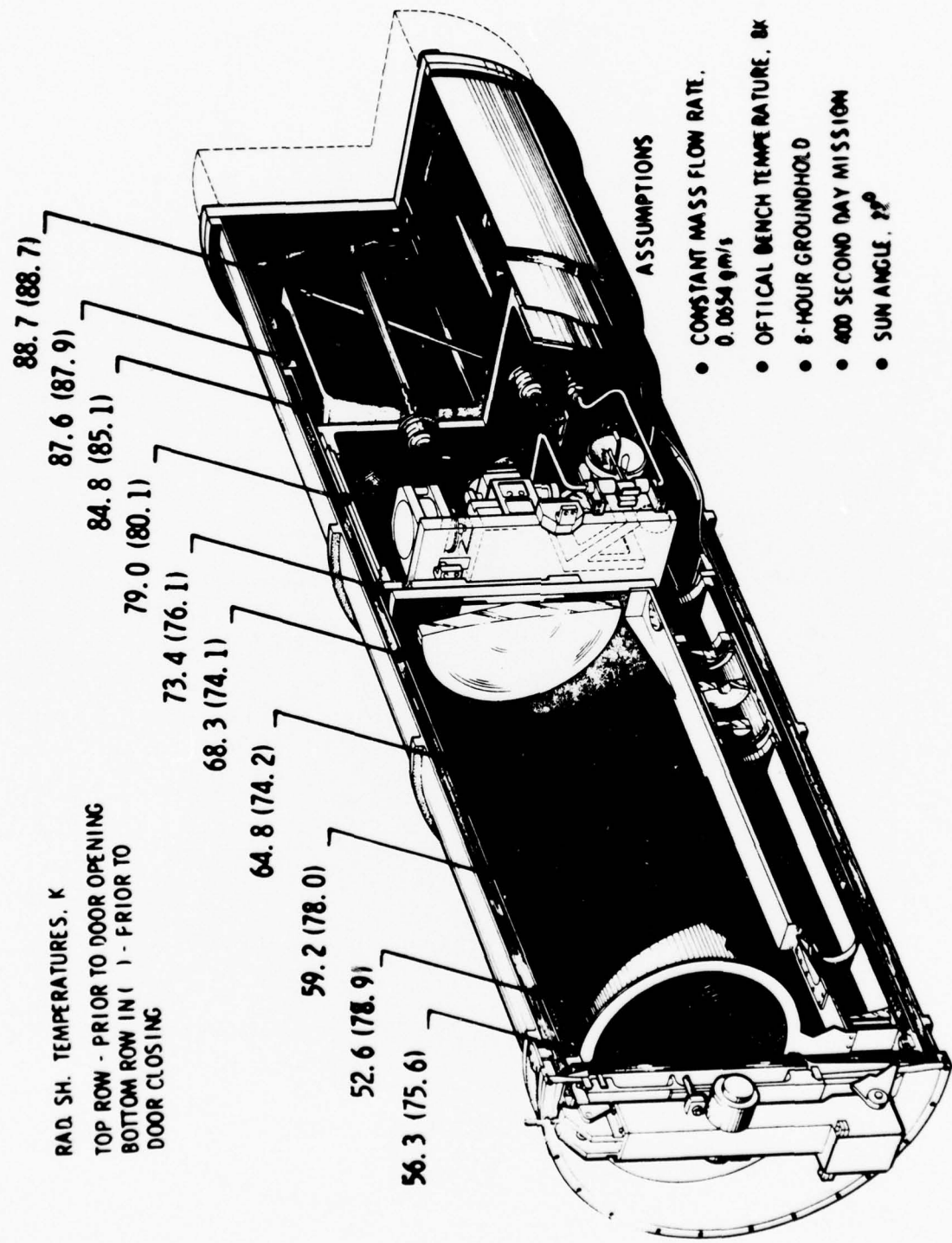


Figure 4.18 SPHERIS RADIATION-SHIELD TEMPERATURES, DAY MISSION (CASE 1)

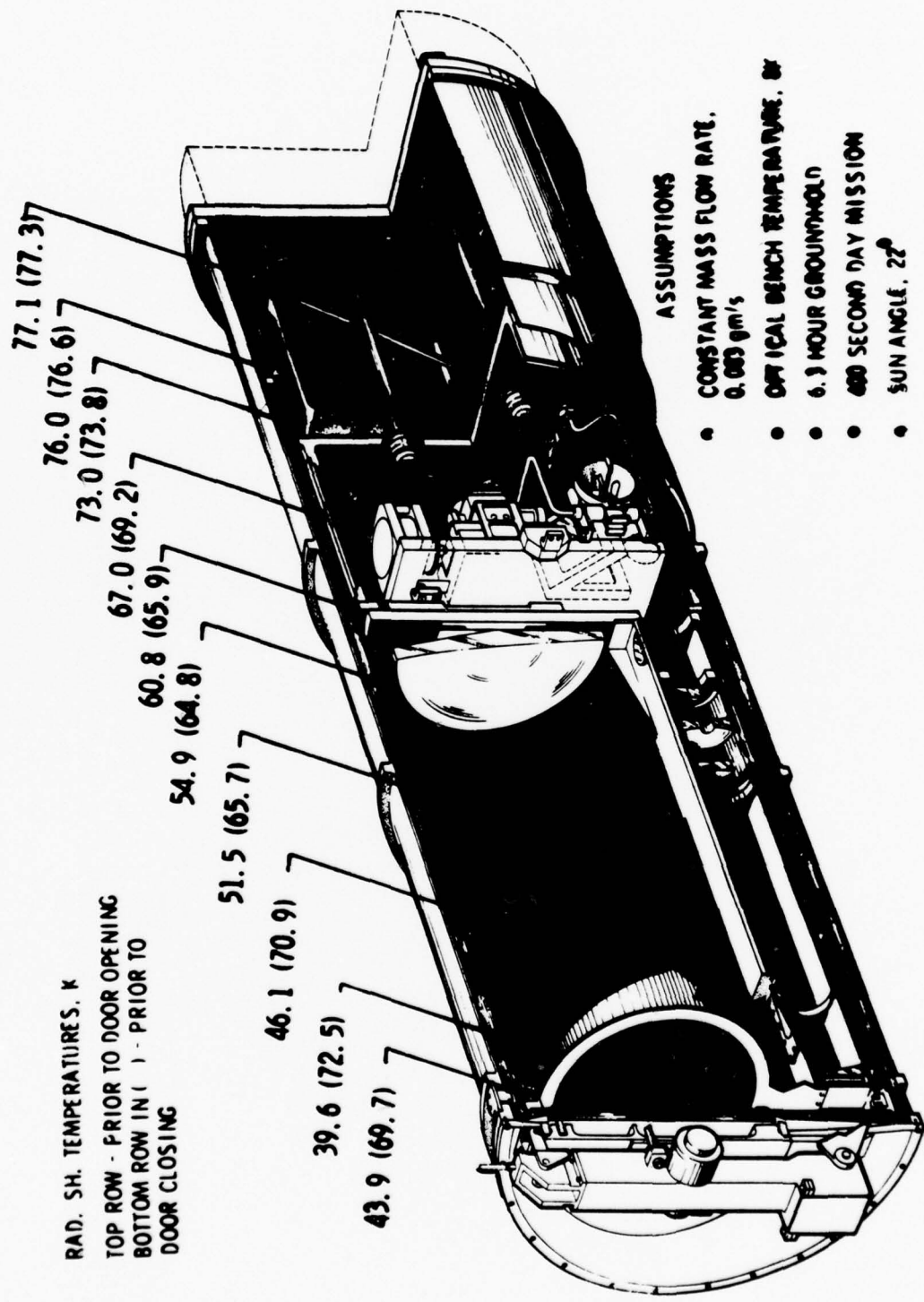
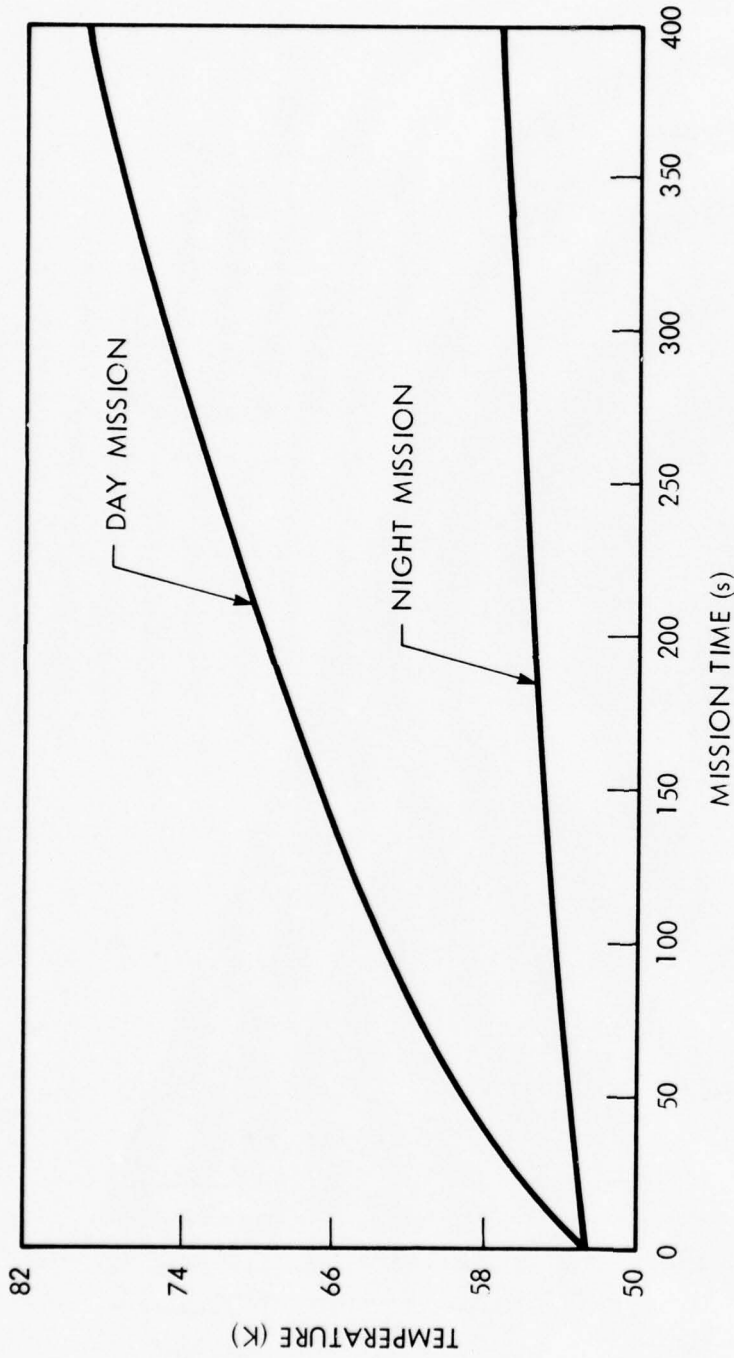


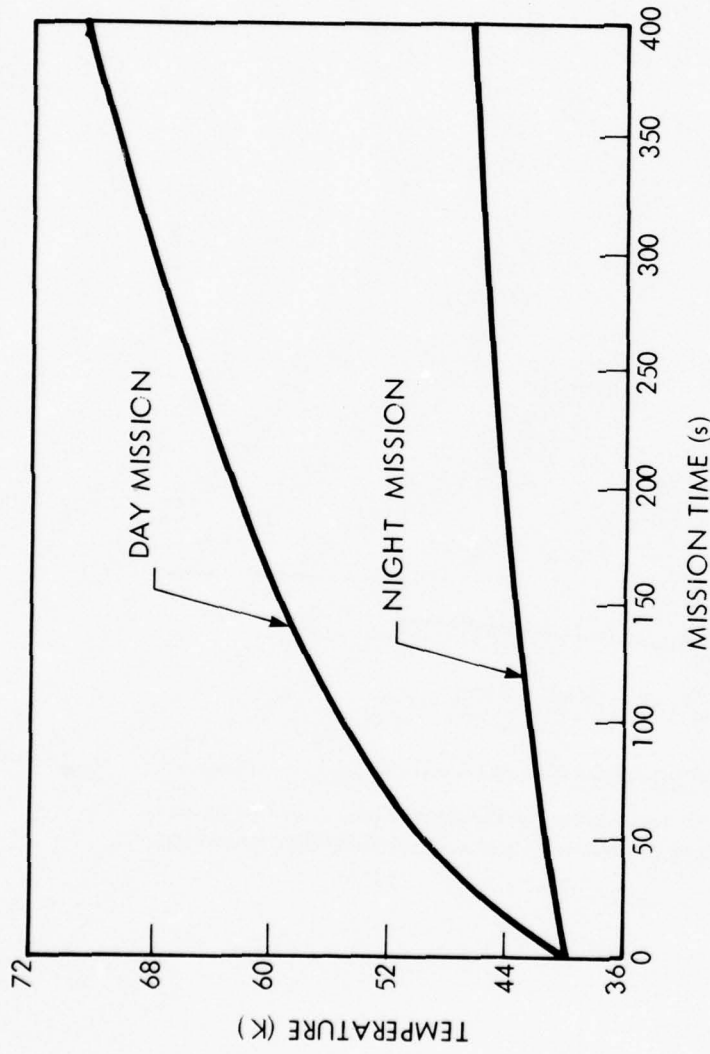
Figure 4.19 SPHIRIS RADIATION-SHIELD TEMPERATURES, DAY MISSION (CASE 2)



#### ASSUMPTIONS:

- CURVES ARE FOR MAXIMUM TEMPERATURE-RESPONSE NODE. (NODES ARE ISOTHERMAL SECTIONS OF THE RADIATION SHIELD, AND THIS IS THE WORST-CASE NODE.)
- MASS FLOW RATE = 0.0654 grams/s; GROUND HOLD TIME = 8 HOURS.

Figure 4.20 RADIATION-SHIELD TEMPERATURE VS MISSION TIME (CASE 1)



#### ASSUMPTIONS:

- a. CURVES ARE FOR MAXIMUM TEMPERATURE-RESPONSE NODE. (NODES ARE ISOTHERMAL SECTIONS OF THE RADIATION SHIELD, AND THIS IS THE WORST-CASE NODE.)
- b. MASS FLOW RATE = 0.083 grams/s; GROUND HOLD TIME = 6.3 HOURS.

Figure 4.21 RADIATION-SHIELD TEMPERATURE VS MISSION TIME (CASE 2)

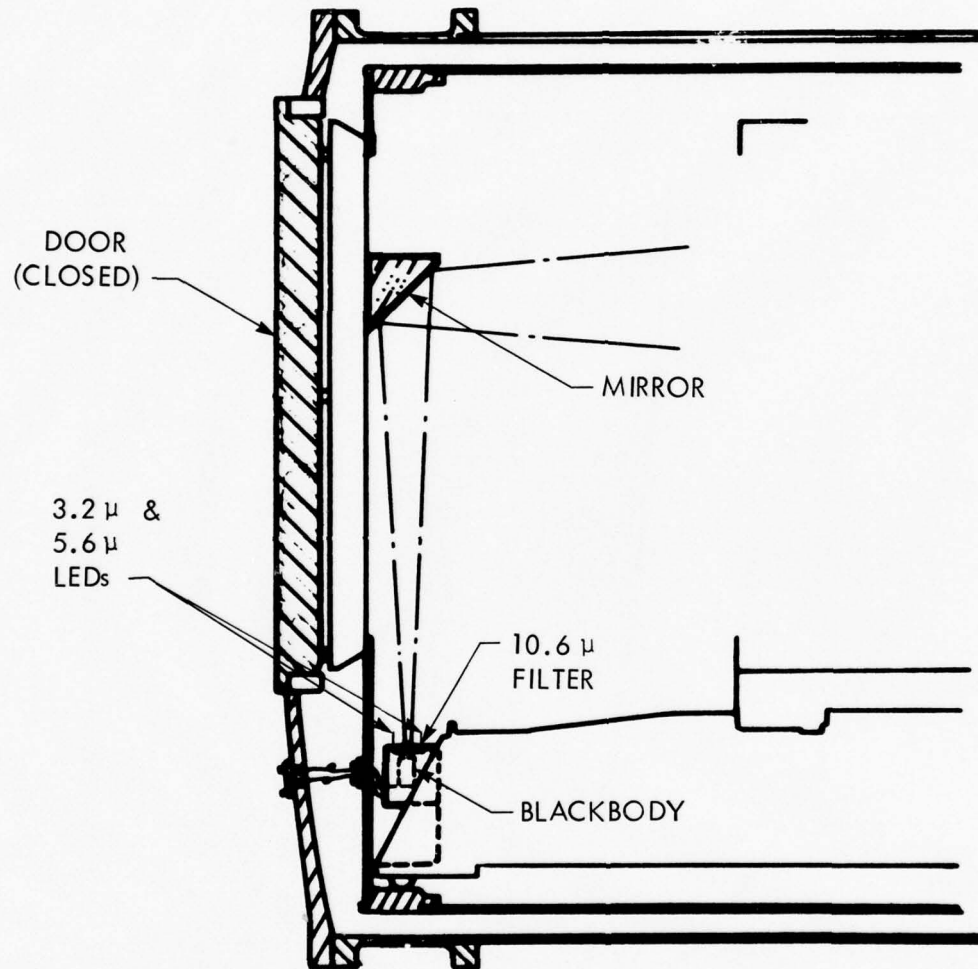


Figure 4.22 SPHIRIS INFLIGHT CALIBRATION SOURCES

## SECTION 5

### SPARAD

#### 5.1 BACKGROUND

Experimental objectives of SPARAD (SPAtial RADiometer) were to supplement those established for SPHIRIS as part of the SPIRE experiment by providing higher spatial resolution measurement of the scanned scene than could be obtained with SPHIRIS. The measurement goal was to spatially resolve 0.5 mrad in the scan direction, as compared to the SPHIRIS resolution of 4.36 mrad. This was to be achieved within the packaging constraints of the payload package and with a noise equivalent spectral radiance comparable to SPHIRIS. These constraints led to SPARAD being a relatively wide band fixed spectral region radiometer in order to obtain acceptable noise levels within the packaging constraints.

The contract objectives were to determine a feasible configuration for SPARAD, define achievable performance characteristics, and generate an instrument design to a preliminary design level. The following paragraphs describe the resulting configuration.

#### 5.2 SPARAD CONFIGURATION

##### 5.2.1 General Description

An optical system, based on the SPHIRIS telescope, was scaled to produce the desired spectral sensitivity and high off-axis rejection. This design optimizes the altitude region from which near-earth measurements can be acquired. A spectral bandpass filter, located in the optical system's collimated beam, defines the spectral region of interest. Two aspheric germanium lenses focus the region at two points in the optical train. This technique provides a location for signal chopping and detector imaging with sufficient physical separation to prevent electromagnetic interference at the detector array. Two signal detectors cover a field of view compatible with the SPHIRIS interferometer (i.e., 0.25 degree) and provide 0.5-milliradian angular resolution along normal axes associated with horizontal and vertical scanning directions.

A full-field, on-board, calibration plate, located on the dewar door, is monitored to serve as a reference for calibration. This plate stays in the temperature region of 90 to 100 K during normal operation. Thus, pre- and post-data-calibration data are available without introducing complicated control electronics.

The size of the sensor and its electronic package is compatible with small payload diameters for future applications, and the entire instrument is a self-contained unit requiring only external power and telemetry.

The cryogenic dewar for the SPARAD radiometer as shown in Figure 5.1 consists of two main sections: the cryogen tank and the radiometer compartment. Access to the radiometer can be obtained by removing the outer vacuum shell and intervening cold shield. The SPARAD design requirement is for a radiometer physically small in size and compatible in performance to the SPHIRIS instrument.

The SPHIRIS high-rejection telescope confines FOV of the instrument to  $4.36 \times 4.36$  milliradians. The reduction in FOV to 0.5 mrad for SPARAD plus the optical loss in the telescope degrades the SPHIRIS Noise Equivalent Spectral Radiance (NESR) to a value of  $3 \times 10^{-10}$  watts/cm<sup>2</sup> sr cm<sup>-1</sup>. For the spectral band of 10 to 12 micrometers, a compatible SPARAD Noise Equivalent Radiance (NER) requirement is  $5 \times 10^{-8}$  watts/cm<sup>2</sup> sr.

### 5.2.2 System Design

#### 5.2.2.1 Radiometer

With an optical f-number of 6 and an effective entrance aperture of one inch, the optical system covers the same FOV as SPHIRIS while maintaining an instantaneous FOV of  $4.36 \times 0.5$  milliradians. Figure 5.2 illustrates a feasible focal plane for SPARAD. The vertical scan rate is confined to one FOV per interferometer scan of 11.8 mrad/s, resulting in a required bandwidth of 1.4 Hz for detector A and 12 Hz for detector B. To cover a tangent height range of 70 km to 150 km from an altitude range of 100 km to 300 km requires a maximum total vertical scan angle of about 10 degrees. The vertical scan takes about 16.5 seconds. Using a horizontal scan rate of 11.8 mrad/s and a horizontal scan angle of 45-degree steps, each segment of horizontal scan takes about 74 seconds. A feasible scan profile, consisting of one vertical and one horizontal scan and repeating 4 times to cover 180 degrees plus one final vertical scan, takes approximately 380 seconds. The scan rate and scan profile are flexible and can be changed to suit mission requirements.

Based on the above horizontal scan rate, the required bandwidth for detector A is about 12 Hz and 1.8 Hz for detector B. For simplicity of design, the radiometer is optically chopped at 45 Hz, and both channels are bandpassed over 24 Hz during all scans. Further signal processing (co-addition, filtering, etc) may be performed on the ground. It should be pointed out that the one-inch effective aperture provides a blur diameter of one milliradian at the detector focal plane. Detector size is matched to the blur for optimum performance. However, since a system resolution of 0.5 mrad is desired in this case, a detector size of 0.5 mrad may be used at a sacrifice of no worse than a factor of 0.5 degradation in NER. With an optical efficiency of 0.5, the system efficiency should be better than 0.25. The achievable D\* performance provides an NER of  $5 \times 10^{-10}$  watts/cm<sup>2</sup> sr for channel A during the vertical scan. The worst NER of  $2 \times 10^{-9}$  occurs in channel B during the horizontal scan.

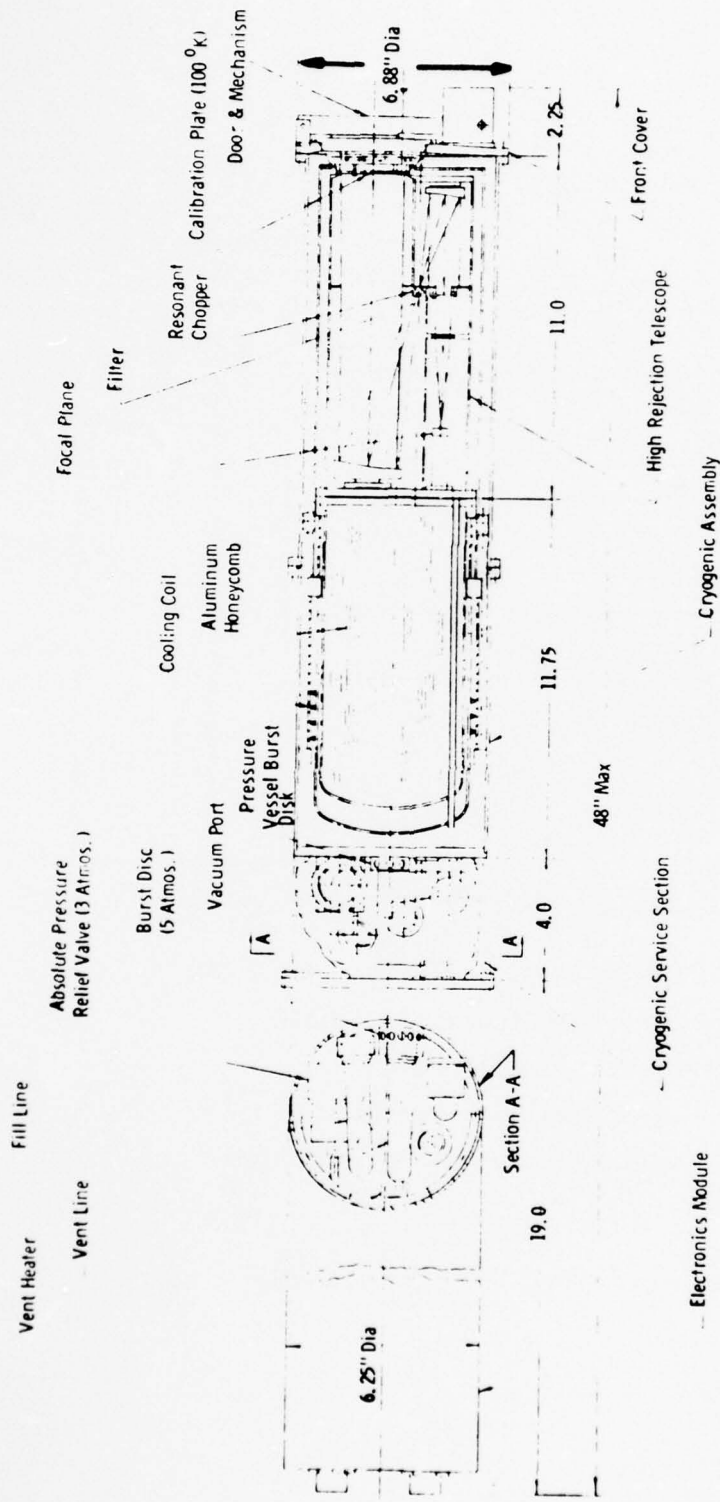
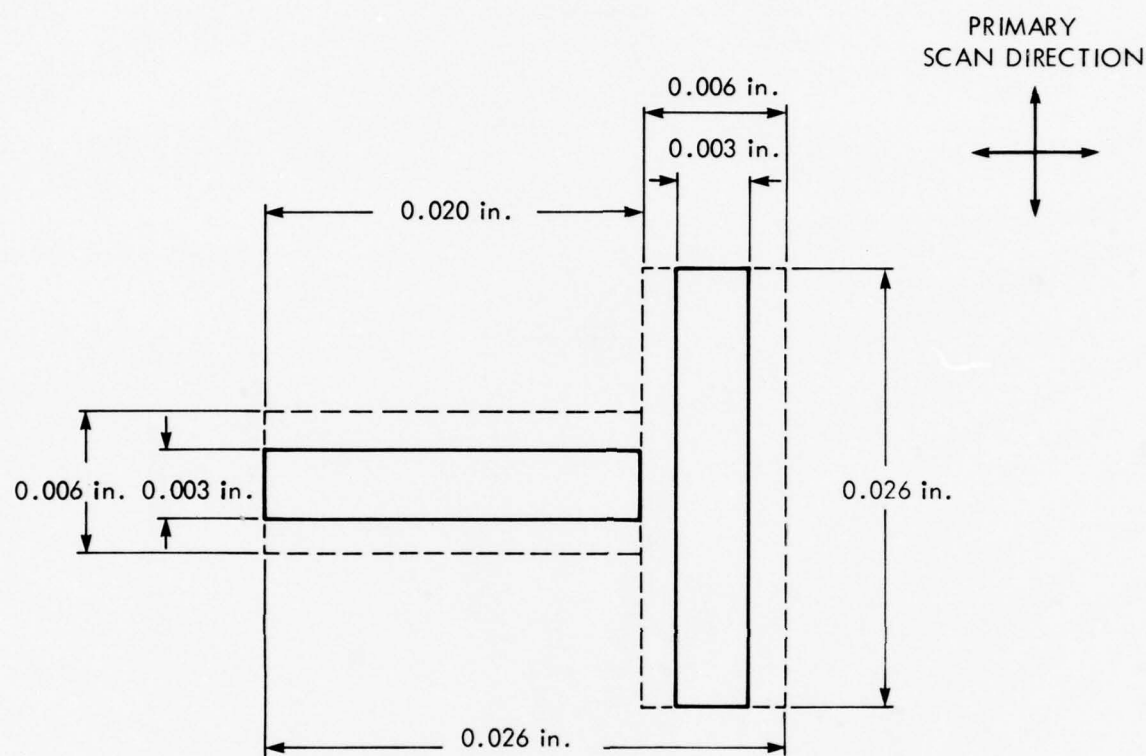


Figure 5.1 SPARAD INSTRUMENT



- 2 DETECTORS, 16-PACK MCSFET, 2-TIAs
- 100 Hz ELECTRONIC BANDWIDTH
- $4 \times 10^3$  DYNAMIC RANGE
- 10 K OPERATING TEMPERATURE
- 6 mil DETECTORS, MASKED TO 3 mils

Figure 5.2 SPARAD FOCAL PLANE

A two-element spectral-bandpass filter, containing germanium and Irtran II substrates, fulfills the SPARAD, out-of-band, spectral-rejection requirements. Filter specifications are predicted on operation at 20 K, and the wavelength of maximum transmission is 11.375 ( $\pm$  1%) micrometers. The half-power bandwidth is  $1.08 \pm 0.12$  micrometer. Short wavelength rejection between 10 micrometers and 0.9 micrometer will be 0.01%. Between 12.75 micrometers and 20 micrometers, the 0.01% out-of-band rejection can be held; however, between 20 and 25 micrometers, the filter spectral rejection will be limited to 0.1%. The above specifications on out-of-band rejection are maximum values, and HRC expected that the rejection would approach 0.001% for the wavelength intervals of 10 to 0.9 micrometers and 12.75 to 20 micrometers.

The closest angle to the earth that the radiometer ever approaches is about 2 degrees. The required earth rejection of  $10^{-13}$  prevents degradation of optical system sensitivity. Such rejection can be achieved with a 2-inch diffracting aperture and an oversized first field stop. The effective aperture is one inch. Performance data is summarized in Table 5.1.

Table 5.1  
SPARAD PERFORMANCE CHARACTERISTICS

Effective Aperture (diameter in inches)	1
Optical f-number	f/6
Spectral Bandwidth (micrometers)	10 to 12
Dynamic Range	$4 \times 10^3$
Filter Rejection (percent)	0.1
NER (watts/cm <sup>2</sup> sr)	$5 \times 10^{-8}$
Effective FOV (milliradians)	$4.36 \times 4.36$
Instantaneous FOV (milliradians)	$4.36 \times 0.5$
Chopper Frequency (Hz)	45
Earth Rejection (maximum)	$10^{-13}$
Housing Temperature (degrees K - maximum)	50

#### 5.2.2.2 Telescope

The optical system, shown in Figure 5.1, consists of an off-axis parabolic primary focusing on a shielded field stop. The energy at the field stop is then collimated by a secondary off-axis parabola in a set of relay optics. The collimated energy passes through another stop that removes the energy diffracted from the edge of the entrance aperture. The off-axis primary

mirror works with a simple diffraction mask in which tolerances and positioning are not critical (i.e., the diffraction pattern is circularly symmetric). The collimated energy from the diffraction mask is focused by two germanium lenses on the detectors. The first focus between the lenses provides a location for signal chopping sufficiently removed from the focal plane to prevent electromagnetic interference at the detector array.

The primary mirror is superpolished to a scatter coefficient of approximately one part in  $10^5$  per steradian for angles greater than one degree from the angle at which specular reflection occurs. The two parabolas, operating in a confocal configuration, provide high resolution over a wide field of view. When the aperture stop of this system is located in front of the primary mirror at a distance equal to the focal length, spherical aberration and astigmatism are reduced to zero. Spherical aberration is nullified by the basic parabolic shape and by the cancellation of the individual contributions of the two elements; astigmatism is nullified by the location of the aperture stop.

This design is an adaptation of the design used in the ELS and SPHIRIS telescopes. The off-axis configuration permits rear-mounting of all mirrors to a common structure, and all mirrors are made of aluminum with nickel-coated surfaces.

#### 5.2.2.3 In-Flight Calibrator

The in-flight calibrator consists of a flat plate with a heat-sink to the radiation shield. The calibrator operates at a temperature of 100 K and covers the entire field of view. A calibration signal is derived from chopping the plate radiation. The optical system will be calibrated in the same time frame as the SPHIRIS in-flight calibration.

#### 5.2.3 Electronics Design

SPARAD flight electronics fall into four functional groups:

- Signal
- Housekeeping
- Experiment Interface
- GSE

Each will be briefly described with reference to the simplified block diagram, Figure 5.3. Table 5.2 summarizes the main operating characteristics of the SPARAD electronics system.

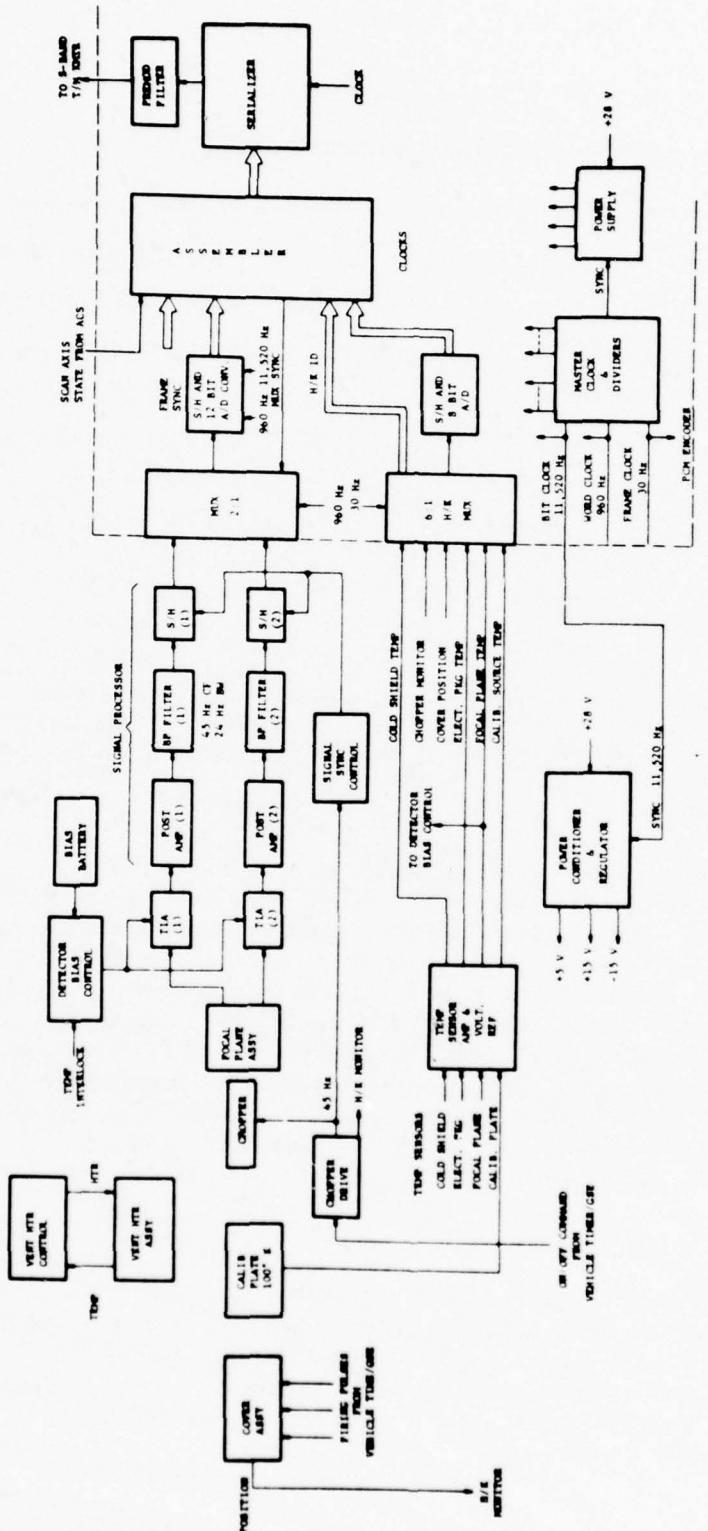


Figure 5.3 SPARAD FLIGHT ELECTRONICS, BLOCK DIAGRAM

Table 5.2  
SPARAD ELECTRICAL CHARACTERISTICS

Signal-Detector A	16-pack MOSFET
Signal-Detector B	16-pack MOSFET
Signal Bandwidth of Detector A	12 Hz
Signal Bandwidth of Detector B	1.8 Hz
Dynamic Range	$4 \times 10^3$
A/D Conversion	12 bits
PCM Bit Rate	11,520 Hz
PCM Word Rate	960 Hz
PCM Data-Frame Rate	30 Hz
Words per Frame	32 (see Note)

NOTE: Includes 15 data words from each detector channel.

#### 5.2.3.1 Signal Group

The chopper, a tuned fork, operates at a resonant frequency of 45 Hz. The modulated radiation is detected by the two-element detector array in the focal plane assembly. Each detector feeds a transimpedance preamplifier (TIA) and identical signal-processing channel. A detector bias control withholds bias voltages to the detectors and TIAs until the focal plane reaches cryogenic operating temperatures. A postamplifier follows the TIA, and a bandpass filter, centered at 45 Hz, follows the postamplifier. The filter bandwidth is 24 kHz with a rolloff equivalent to a 2-pole Butterworth. The signal is then demodulated from the 45-Hz carrier by a sample-and-hold circuit, where sampling is made to occur on the positive peaks of the carrier by the signal sync control. At this point, the IR signals are ready for digital conversion and telemetry.

#### 5.2.3.2 Housekeeping (H/K) Group

Housekeeping consists primarily of temperature monitoring. Voltages from temperature sensors located on the cold shield, focal plane, calibration plate, and electronic package are amplified, scaled, and commutated. Also commutated are the cover-position signal and a monitor from the chopper. Other housekeeping electronic items include a vent heater control similar to SPHIRIS and a modified power conditioner.

#### 5.2.3.3 Experiment Interface Group

The two IR signals from detectors A and B and six housekeeping outputs go to the PCM encoder. The IR signals are commutated and sampled at better than ten times the chopping frequency. Each sample is given a 12-bit A/D conversion. The H/K channels are commutated at the output frame rate and given 8-bit A/D conversion. The digital words and identification become assembled in the PCM encoder into a continuous, serial digital stream for modulation of the telemetry transmitter. In addition to the IR signals and H/K data, a logic level corresponding to the scan direction by the Attitude Control System (ACS) gets inserted once per output frame. The PCM encoder is constructed from standard building blocks. PCM data rates are low (see Table 5.2).

#### 5.2.3.4 GSE Group

The radiometer operates from a ground-support console in all ground-test and laboratory configurations and prior to launch in the flight configuration. This console monitors the performance of the SPARAD flight packages before launch disconnect. The simplified block diagram, see Figure 5.3, shows GSE functions for SPARAD. This console shares the PCM decommutator used on HIRIS and SPHIRIS. In lieu of a computer, the word/bit decoder strips off each IR-signal word, converts it back to analog, and makes it available for presentation on any external oscilloscope. The decoder also strips off the desired H/K word, converts it to analog, and displays its value on a digital panel meter. Appropriate lamps display ACS scan direction. Controls for commanding the radiometer are contained on the console. They consist of chopper, cover, and detector bias commands. The console contains a 28-V power supply for the radiometer during ground operation.

### 5.2.4 Vacuum and Cryogenic Design

It is necessary to create and critically control three aspects of the radiometer's internal environment: cleanliness, pressure evacuation, and low temperature. The cryogen storage tank and radiometer compartment are contained within a pressure vessel inside the helium dewar as shown in Figure 5.1. The pressure vessel provides a rigid structure to contain a high vacuum ( $10^{-4}$  Torr or better) during the ground-hold and flight periods. High vacuum reduces convective heat transfer and eliminates cryodeposits on critical components. The SPHIRIS vacuum pumping system evacuates the experiment pressure vessel during an actual or simulated countdown that requires many hours.

#### 5.2.4.1 Vacuum Door

The SPARAD instrument has a vacuum door mechanism, using pyrotechnic actuating devices that retain the gaseous products in an expanding bellows. Several designs that employ the pyrotechnic actuator and a spring-loaded escape-mechanism were analyzed. In these designs, the cover O-ring release goes

through a lifting motion before cover rotation through 180 degrees by the escape-mechanism. To close the vacuum chamber, a similar spring-driven mechanism returns the vacuum door to a position directly over the telescope aperture. Then a second pyrotechnic device produces thrust to achieve a vacuum O-ring seal with metal-to-metal contact between the door and dewar bearing surfaces. This design permits a door-opening time compatible with the SPHIRIS instrument and fits the limited space requirements dictated by the SPARAD instrument diameter.

#### 5.2.4.2 Cryogen Source

A two and one half liter tank of liquid helium provides cooling. This is sufficient to cool the instrument for a four-hour hold plus the mission flight time. The helium operates in its supercritical mode by use of a pressure valve. This eliminates the problems of thermal equilibrium and liquid loss often associated with vented liquid systems. The supercritical vapor maintains effective heat transfer by means of aluminum honeycomb contained within the tank. A heater, mounted on the exterior of the tank, converts the liquid to vapor.

#### 5.2.4.3 Conductive Cooling

Radiometer components are conductively cooled from the base of the helium tank. Heat straps maintain critical parts at their required operating temperatures. Because the system is exposed to cryogenic temperatures, material stability and predictable performance are vital. The structure spacing must match the optic change over the temperature excursion.

The mounting of the filter, chopper, and focal plane to the telescope is simplified by the fact that all components have the capability of operating at liquid helium temperatures. All internal telescope components can be mounted directly to the telescope structure without a thermally-insulated intermediate mount. The focal plane mounts to a high thermal-conductivity material which is heat sunk to the base of the telescope. At this location, the temperature of the telescope structure approaches the temperature of the cryogen.

#### 5.2.4.4 Dewar Construction

The dewar utilizes technology employed for similar rocket-borne instruments, such as SPHIRIS. This technology covers aluminum radiation shields and helium tanks supported by low-thermal-conductivity members. Structural members are designed to resist the environmental loads imposed by launch conditions while minimizing heat inflow. Multilayered cryogenic insulation (MLI) further reduces the heat leak to the radiometer and helium tank.

Servicing connections are mounted on the back end of the dewar with separate helium fill ports and vents. Other service connections include the dewar evacuation ports and valves and electrical connections to the tank liquid-level gauge and internal radiometer leads.

SECTION 6  
GROUND TEST AND CALIBRATION EQUIPMENT

The complement of equipment used for ground operations of the HIRIS provides for vacuum and cryogenic servicing, system operation, data collection, reduction, and analysis, test and calibration. Most of this equipment was developed under other contracts. The two major items developed under this contract, and described below, are the Low Background Calibration Facility (LBCF) and the Field Portable Monochromator.

6.1 LOW BACKGROUND CALIBRATION FACILITY

6.1.1 Background

Calibration and test of sensors of the type developed under this contract require the use of radiation sources and targets which can be operated in a low photon background environment. By low photon background is meant the photon flux level normally associated with helium cooled surfaces, at temperatures on the order of 30 K. Such a low background environment, in which radiation sources can be operated, requires a vacuum chamber, cooled shrouds, photon baffles, and appropriate target sources, optics and actuators. At the start of this contract cryo-vacuum technology for such a facility had been under development by Honeywell for some time and such a chamber had been built and tested. This facility possessed the capability of LWIR testing at vacuum levels of  $10^{-6}$  Torr, at adjustable background temperatures from 15 K to 300 K and the potential for inclusion of optical instrumentation within the controlled environment. Vacuum integrity and cryogenic systems operation for both the vented LN<sub>2</sub> radiation shield and the closed-cycle helium refrigeration unit (CTi model 1400 Refrigerator/Liquifier) had been demonstrated. Limited radiometric capability had been demonstrated at the existing stage of development.

This existing hardware was considered to have successfully demonstrated the cryo vacuum technology required for a calibration facility suitable for use with sensors to be developed under this contract. The radiometric characteristics and interfaces remained to be developed to be suitable for such sensors. Accordingly, objectives were established to expand the radiometric capabilities to provide the following:

- 1) A full-field blackbody calibration utilizing an extended source.
- 2) A scanned point source to determine field-of-view characteristics over the total field of the instrument under test.
- 3) Determination of the radiance noise level of the sensor (NESR).

- 4) Determination of the compound boresight angle for the SPIRE and other instruments.
- 5) Potential for inclusion of a spectral calibration capability.
- 6) Performance of the functions presented above for sensors with up to a 10-inch clear aperture.

#### 6.1.2 Tasks and Requirements

In order to achieve the stated design goals, HRC undertook chamber modifications, performed system tradeoffs, electrical and mechanical design, fabrication and test of the source assembly, collimating and scanning optics, boresight assembly and sensor-chamber interfaces resulting in a calibration facility with broad IR spectral range and low background (LHe temperature) capability.

The following tasks, related to the vacuum/cryogenic operation of the chamber, were performed to improve the chamber's capability to provide a high vacuum, low background, repeatably-positioned test bed:

- 1) Rework of the vacuum vessel to insure vacuum integrity and clean operation within the chamber environs.
- 2) Design and fabrication of a new photon-tight He-shroud with a modified support system to minimize mechanical shifts during chamber cooldown.
- 3) Fabrication of a new center-supported optical baseplate with provisions to allow for repeatable, radial expansion during thermal cycling without baseplate rotation.
- 4) Modifications to the cooling system within the chamber to permit greater flexibility and reduced system maintenance.

The tasks performed to generate the required radiant input source to the experiment under test were the following:

- 1) Modification to the existing blackbody and integrating sphere to provide a baseline radiance for the source assembly.
- 2) Provision for source divergence control to allow for point source and extended source calibrations.
- 3) Design and fabrication of radiance-control mechanisms to provide better than five orders of dynamic range control without affecting the source divergence.
- 4) Incorporation of spectral bandpass controls without affecting the dynamic range or divergence.
- 5) Design of mechanisms to allow maintenance of low background conditions during source operation.

The optical design and fabrication efforts as part of the chamber instrumentation included the following tasks:

- 1) Design and fabrication of an optical system to provide full field and point source operation for a wide range of test vehicles, while minimizing the required changes for these and laser source modes.
- 2) Design and fabrication of optical mounts to minimize thermally-induced distortions during chamber cooldown.
- 3) Incorporation of a scanned source capability through  $\pm$  2 degrees in two orthogonal directions with a direct positional readout.
- 4) Provision for adequate cooling of the optical assemblies to allow for low background operating conditions.

A technique was also devised and implemented to permit measurement of a sensor's boresight reference compound angle for those systems where the element is maintained at cryogenic temperatures. During the test phase of the program, an alternate scheme was generated for those sensors where the boresight element is at room ambient conditions.

The test phase of the program encompassed the following efforts:

- 1) Determination of the radiant characteristics of the source assembly components.
- 2) Measurement of the surface characteristics of the optical components including figure distortion at cryogenic temperatures and mirror scatter.
- 3) Collimation adjustment and field center definition for the chamber optical train at cryogenic temperatures.
- 4) Measurement of the offset characteristics of the boresight assembly at room and cryogenic temperatures.
- 5) System calibration using a known radiometric transfer standard.

All these efforts were performed to satisfy design and performance specifications established for the calibration of those instruments having characteristics similar to those listed in Table 6.1.

#### 6.1.3 Design and Engineering

Upon completion of the required chamber modification for improved vacuum operation and cryogen flow, source and optical components were designed and fabricated to insure a suitable test-bed with low-background operational properties. Figure 6.1 shows the resulting configuration. The paragraphs below describe relevant activities on the major items.

Table 6.1  
TEST SENSORS DESIGN PARAMETERS

	HIRIS	SPHIRIS	SPARAD	DUAL CVF UPPER LOWER BAND
Sensitivity	$2 \times 10^{-12}$ W/cm sr cm <sup>-1</sup>	$2 \times 10^{-12}$ W/cm sr cm <sup>-1</sup>	$5 \times 10^{-11}$ W/cm <sup>2</sup> sr	$10^6$ W/cm <sup>2</sup> sr μm <sup>-8</sup>
Dynamic Range	$2 \times 10^4$	$2 \times 10^4$	$5 \times 10^3$	$5 \times 10^3$
Clear Aperture (inch)				
IFOV (mr)	1.0	10.0	4.0	4.0
IFOV (mr)	4.5	4.37	4.37	17.45
Optics blur (mr)	1.0	$\leq 0.25$	0.25	$\geq 1.0$
System F#	1.0	1.0	2.0	3.0
Allowable Background Flux (ph/cm <sup>2</sup> s)	$10^{10} - 10^{11}$	$10^{10} - 10^{11}$	$10^{10} - 10^{11}$	$10^{16}$
Spectral Range (μm)	5-22	5-22	10-12	5-22 1-5
Spectral Resolution	$1 \text{ cm}^{-1}$	$1 \text{ cm}^{-1}$	$2 \mu\text{m}$	$0.34 \mu\text{m}$ 0.1 μm
Spectral Rejection	-	-	$10^5$	-

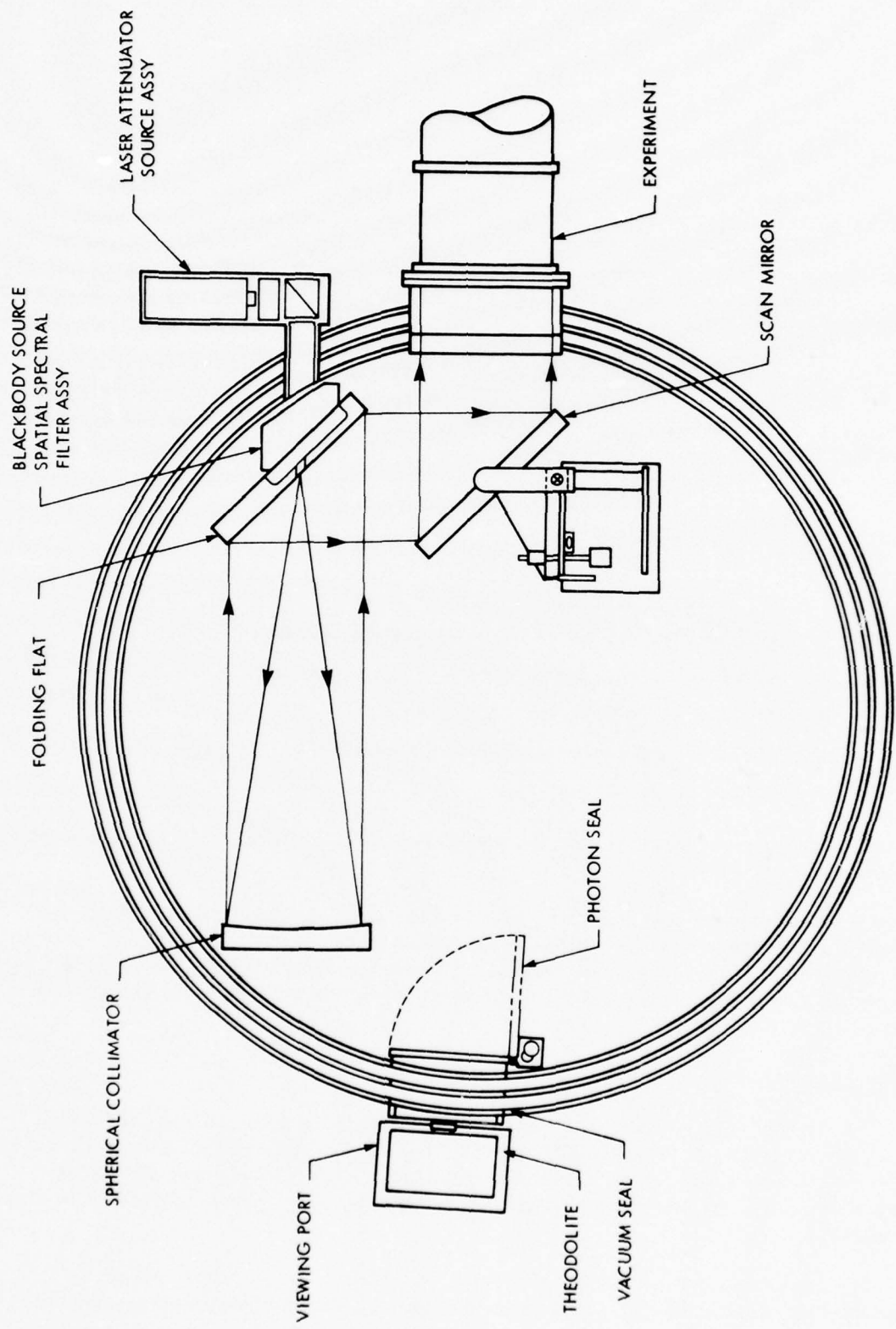


Figure 6.1 LBCF OPTICAL SYSTEM

### Chamber Modifications

The baseplate was designed to provide an optical mounting surface which could be actively cooled and moved repeatably with cryogenic cycling. A center-supporting mount with three posts in slip-grooves along the circumference permitted radial expansion without baseplate rotation during thermal cycling. Rapid uniform cooling is achieved with a cryogen path through the bulk material of the Blanchard ground optical mounting surface.

The inner helium shroud, the most immediate enclosure to the optical bed, was designed to provide the required low photon-flux background when enclosed within the LN<sub>2</sub> radiation shield. The photon-leakage through the shroud was found to be approximated by:

$$\frac{J_{\text{leak}}}{J_{\text{rad shield}}} \approx \frac{\rho^2 \pi D \Omega_1}{\pi DH + \frac{\pi}{2} D^2}$$

where

$\rho$  = reflectivity of inner walls at normal incidence

D = diameter of the shroud

h = leakage gap = 0.06 in.

$\Omega_1$  = field of the radiation shield accessible to the gap

H = Height of He shroud

For the geometry of the helium shroud, the leakage ratio was found to be less than one part in 10<sup>6</sup>.

In terms of radiant flux, should the outer chamber rise to 90 K, the photon flux within the inner shroud would remain less than  $5 \times 10^{-9}$  ph/cm<sup>-2</sup>s-sr, equivalent to a 30 K background emission. These levels represent compatible background fluxes for calibration of those instruments described in the previous section.

### Source Assembly

The source assembly of the LBCF consists of a temperature controlled blackbody radiator, an integrating sphere, selectable spectral filters, selectable apertures for controlling apparent angular size of the source, and separately selectable apertures for controlling the source assembly output radiance, as shown in Figure 6.2.

The radiator is a conical cavity blackbody, with a cone L/D of 4, painted with Catalac Black. Estimated emissivity, at 10.6 micrometers, exceeds

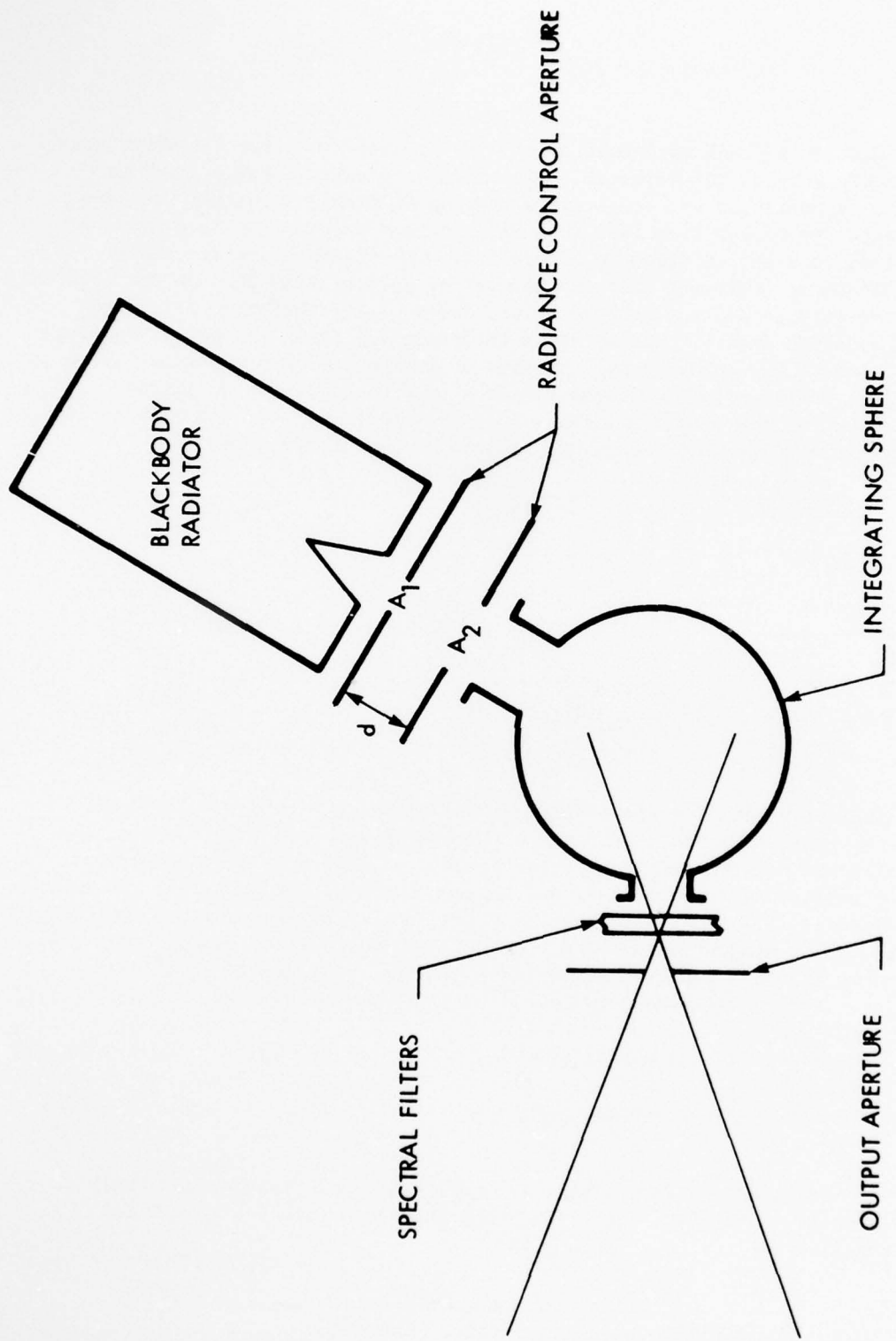


Figure 6.2 SOURCE ASSEMBLY BLOCK DIAGRAM

0.995 from reference 5. Temperature control is provided to  $\pm 0.1$  K over a range of 100 K to 400 K by an EOI adjustable blackbody controller using a platinum resistance thermometer as the temperature sensing element. Resulting radiance output uncertainty varies from less than 1% at longer wavelengths to a maximum of 10% at 1 micrometer, as shown in Figure 6.3. The blackbody output passes through a double aperture set into an integrating sphere, then through the spectral filter to the output aperture located at the focus of the chamber collimating optics. The double aperture set controls the radiance level; the output aperture is used to control the apparent angular size of the source, and the integrating sphere spatially decouples these apertures and provides a source of diffuse uniform radiance to the output aperture. Six attenuation levels are provided by the double aperture set/integrating sphere combination listed below:

<u>Aperture Position</u>	<u>Attenuation</u>
0	$1.3 \times 10^{-3}$
1	$4.6 \times 10^{-4}$
2	$6.2 \times 10^{-5}$
3	$2.7 \times 10^{-6}$
4	$2.6 \times 10^{-7}$
5	$1.6 \times 10^{-8}$

The integrating sphere configuration, shown in Figure 6.4, replaced an earlier version which had insufficient throughput and output uniformity. The configuration was constrained to meet the space available and other mechanical constraints imposed by the then existing source assembly configuration. To enhance output uniformity, the two reflectors and folded path were incorporated to provide 90 degrees angular separation between entrance and exit ports. Sphere walls were sandblasted to minimize specular reflections and then gold coated to enhance reflectivity. Sphere measured performance is given in Section 6.4.

Spectral filtering capability was provided at the exit of the integrating sphere by incorporating a filter wheel with one fixed 2.0 to 3.5-micrometer bandpass filter and locations for five other passbands to suit particular sensor requirements.

Two selectable output aperture sizes, 0.500 in. diameter and 0.020 in. diameter, provide an angular size given below when used with one of the two available collimators.

Source Angular Size		
Collimator	Aperture Diameter	
	0.5 in.	0.020 in.
Long Focus	13 mrad	0.5 mrad
Short Focus	56 mrad	2 mrad

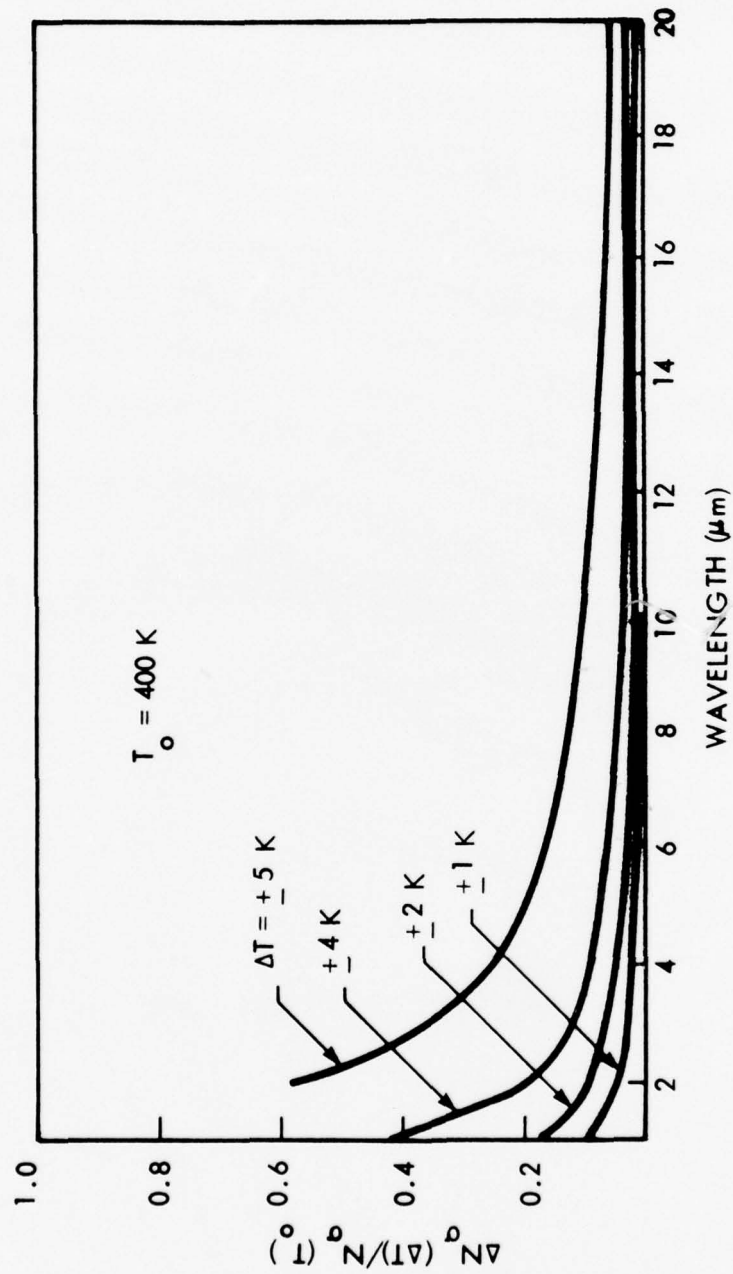


Figure 6.3 RADIANCE STABILITY VS TEMPERATURE STABILITY

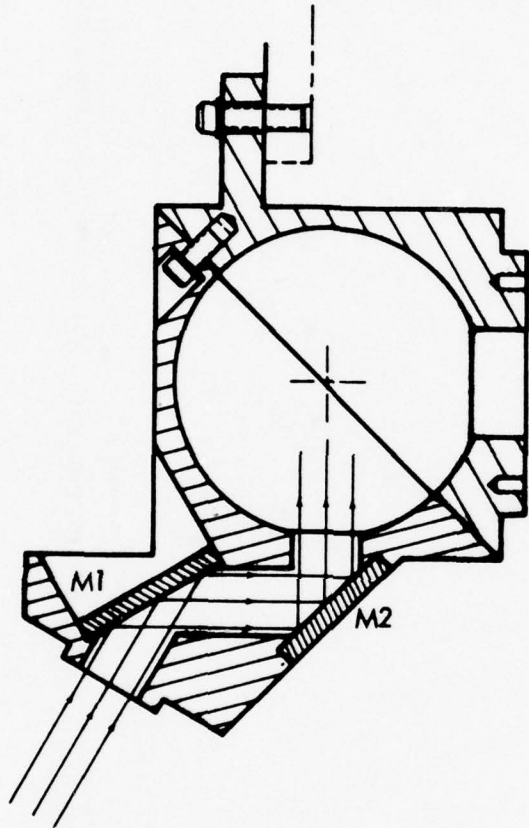


Figure 6.4 LBCF INTEGRATING SPHERE

These angular diameters do not include the effects of collimator aberrations which are dependent on mode of operation and which should be considered in any sensor measurements.

Both the aperture and spectral filter wheels can be selectively positioned with a scope display providing positional readout capability. The wheels are turned with a Kearfott-Singer stepper motor and driver, with  $T^L$  logic control being performed in conjunction with an LED-photodiode positioning device. MOSFET preamplifiers serve as a signal conditioner for the PD input to the control logic; the logic also controls the current drive for the LED.

Provision has also been made to allow for introduction of an external  $CO_2$ -laser as a narrowband spectral source with appropriate attenuation and background filtering. This operation would require removal of the existing wideband source assembly.

#### Optical Assemblies

The collimation optics were designed to provide high transmission, broadband operation which maintained suitable spotsizes over the full scan ranges and yet maximized flexibility for those combinations of sensor and source apertures required. In addition, in order to minimize the background radiation levels, low-scatter polished Dynasil quartz was used for the mirror substrates, with chromium and gold overcoats provided for high IR reflectivity.

The collimation system uses an on-axis spherical element with the source positioned behind a folding element with a source aperture in the center (see Figure 6.1). The various narrow-field sensors use portions of the 10.5-in. beam which avoids the central obscuration introduced by the fixed flat. The wide-field sensors use a 9-in. focal length collimator which is placed between the source and the 40-in. element. Its resultant beam diameter is 4.4 inches. The worst case collimation error from both source size and optical aberration exists for the case of a HIRIS-type point-source scan where the 45-mr FOV sensor is mapped with a 6-mr spot at the 2-degree field edge. On-axis, the error is approximately 4 mr.

All the optical elements are mounted to their supports with spring loads which keep them in contact with the mounting pads while minimizing stress introduced during cooldown. The collimators are center-mounted on a steel support-pin to allow for radial shrinkage, with a spring-balanced mount underneath the mirror to keep the load off the pin itself.

The last element in the optical train - a scanning flat - permits two-axis rotation which varies the beam angle over  $\pm 2$  degrees in each direction. Motion is provided by a four-phase stepper motor and controller circuitry. Current limiting capability has been introduced for cryogenic operation.

Position determination is obtained from a cryogenic ac LVDT transducer with excitation electronics. Direct arc-second readout is achieved with a 4-1/2 digit Ultra-Stable Transducer Readout with a built-in signal conditioner. An analog output signal is also available for recording purposes. Positioning repeatability of the mirror is  $\pm$  20 s with a total combined positional-readout accuracy of  $\pm$  25 s.

A backup system for mirror-position determination was implemented for use in the event of an LVDT-associated problem. A small flat was affixed to the back of the scan mirror which can be viewed from the observation port. Autocollimation through the port window with a DKM-3 theodolite permits a measure of mirror motion from a reference position to better than  $\pm$  2 s accuracy.

Two techniques were devised to achieve boresighting of a test sensor with respect to its reference mirror normal, one each for cases of warm and cryogenically-cooled sensor boresight elements. In the case of the latter, the theodolite autocollimates off the boresight mirror through the periscopic, flat and parallel-faced quartz rhomboid prisms which allow viewing under the scan-mirror assembly. A viewing port which mates to the boresight section of the sensor permits viewing of the element. This determines the direction of the cold boresight mirror. A transfer mirror allows the theodolite to view the scan mirror reference flat and determines the position of the sensor cold line-of-sight with respect to the plane of interface with the chamber, and the boresight element angle to this same interface. The difference between the two angles is the angle between the cold sensor LOS and the boresight mirror normal.

In the case of a warm boresight mirror this technique cannot be used since the viewing port to the mirror would introduce a 300 K leak into the chamber. As such, prior to sensor-chamber interface the angle between the boresight mirror and the plane of interface is measured with a theodolite. When the sensor is calibrated the angle between the interface plane and LOS is determined. Once again, the difference between these angles is the compound boresight angle.

In order to permit these theodolite measurements yet retain low-background conditions for calibration purposes, a high reflectivity door facing outside the chamber was introduced inside the chamber to close off the observation port from within. A phased split-winding reversible motor was used for this task. When closed, the door itself remains below 30 K despite adjoining the 300 K outside environment.

#### Thermometry

Throughout the chamber 30 Si temperature sensors are positioned to monitor the internal environment. These sensors are redundant 3-wire devices which provide  $\pm$  1 K accuracy from approximately 28 to 400 K, and  $\pm$  2 K below that level. Twenty-two of the sensors are on helium-cooled surfaces including optics, mounts and the baseplate while the other eight are on the LN<sub>2</sub> shields.

### Cleanliness

In order to maintain sensor cleanliness, the chamber is vacuumed and covered prior to sensor interface. The sensor is opened and attached to the chamber within the confines of a class 100 flow tent.

All active vacuum pumping on the sensor is achieved through the chamber to keep the flow direction out from the sensor and into the chamber. Thermal cycling is accomplished with the chamber always at a lower temperature than the sensor to insure cryo-pumping into the chamber only. The entire cryovac operation is monitored at all times to insure maintenance of these conditions.

#### 6.1.4 Test Program

The test phase of the LBCF program was divided into two parts: component/assembly performance evaluation and system alignment and test. The principal areas of the former were the source and optical assemblies.

### Source Assembly

Radiance characteristics of the source assembly can be no better than those of the blackbody source. Broadband measurements with a (Hg,Cd)Te detector were taken which showed the source radiance at 400 K to be within 5% of a calibrated laboratory blackbody. Also the source spatial uniformity was shown to be flat within 2% over the range of use in the assembly (see Figure 6.5).

Broadband, spatial and spectral performance characteristics were measured for the integrating sphere used in the assembly. Broadband sphere efficiency measurements indicated a power transmission through the sphere of approximately 1.4%, an order of magnitude below theoretical performance. The probable cause for this less-than-predicted performance was the reduced entrance cone-angle from the source into the sphere introduced by the long entrance enclosure. This was necessitated by the incompatibility of a 90-degree input-output angle for good sphere black walls to preclude direct input-output specular paths which could avoid the sphere surface. However, the resultant attenuation fell at a workable level.

The output spatial uniformity of the sphere was measured and shown to be flat within 14% over the worst-case field to the collimator (see Figure 6.6). Spectral data was taken using the AFGL monochromator source. Relative spectral response of the output over the 1.2 to 3.2-micrometer range remained within the measurement tolerance out to approximately 2.7 micrometers (see Figure 6.7). Beyond that point spectral purity degraded to about 84%; however, the presence of water vapor absorption in this region indicates the problem was likely caused by ineffectiveness of the dry-nitrogen purge on the sphere during the test.

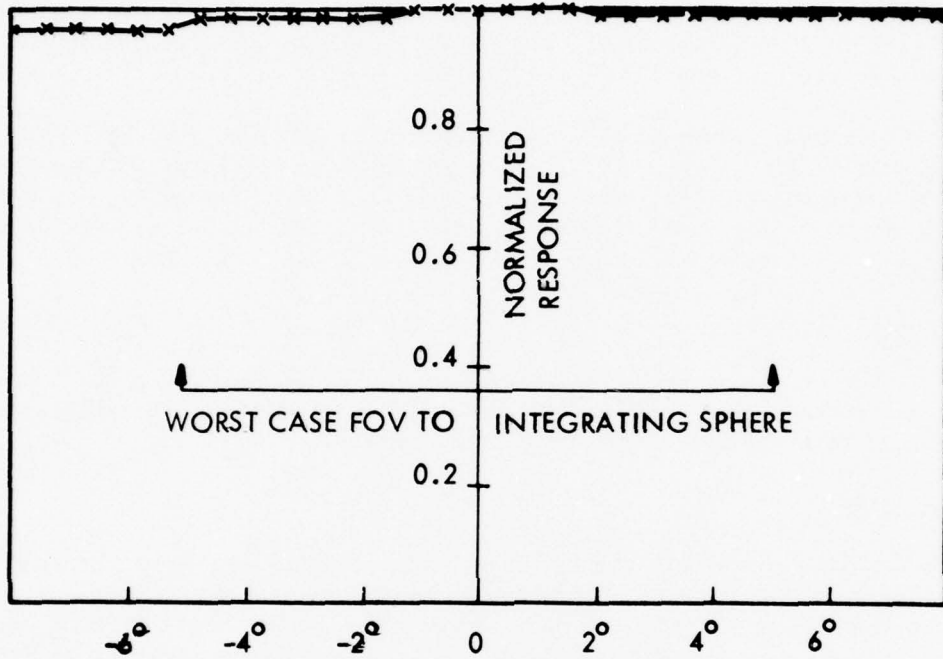


Figure 6.5 LBCF BLACKBODY SOURCE: OUTPUT SPATIAL UNIFORMITY

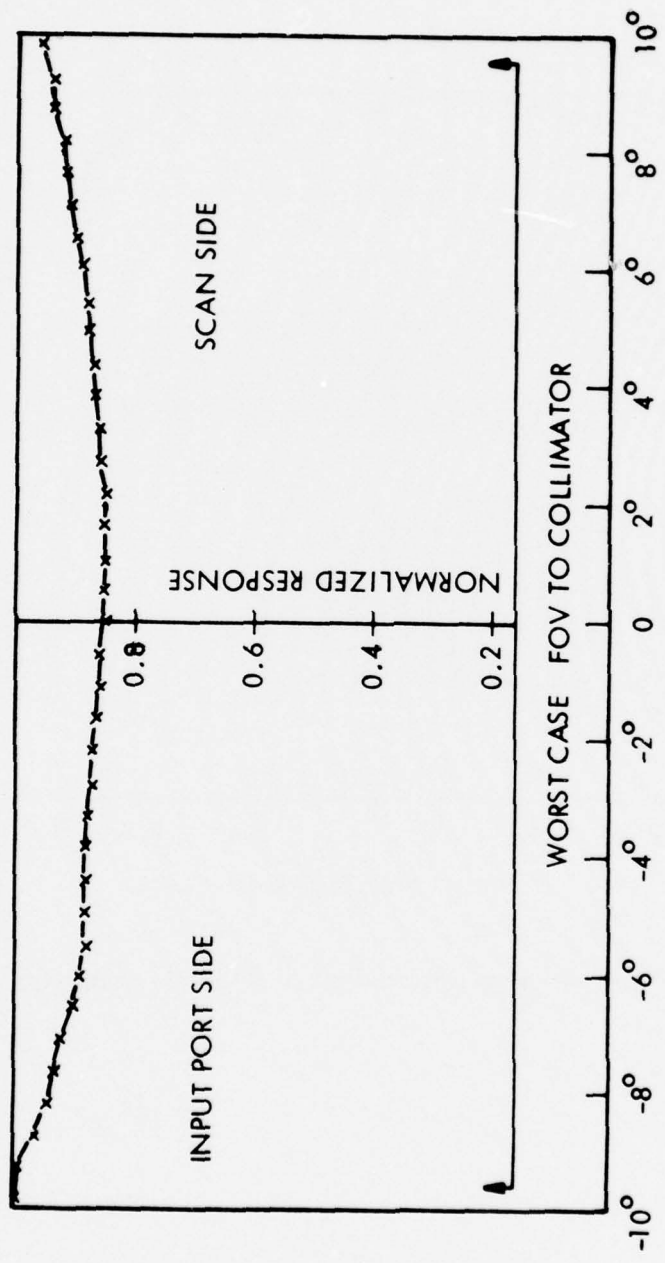


Figure 6.6 LBCF INTEGRATING SPHERE: OUTPUT SPATIAL UNIFORMITY

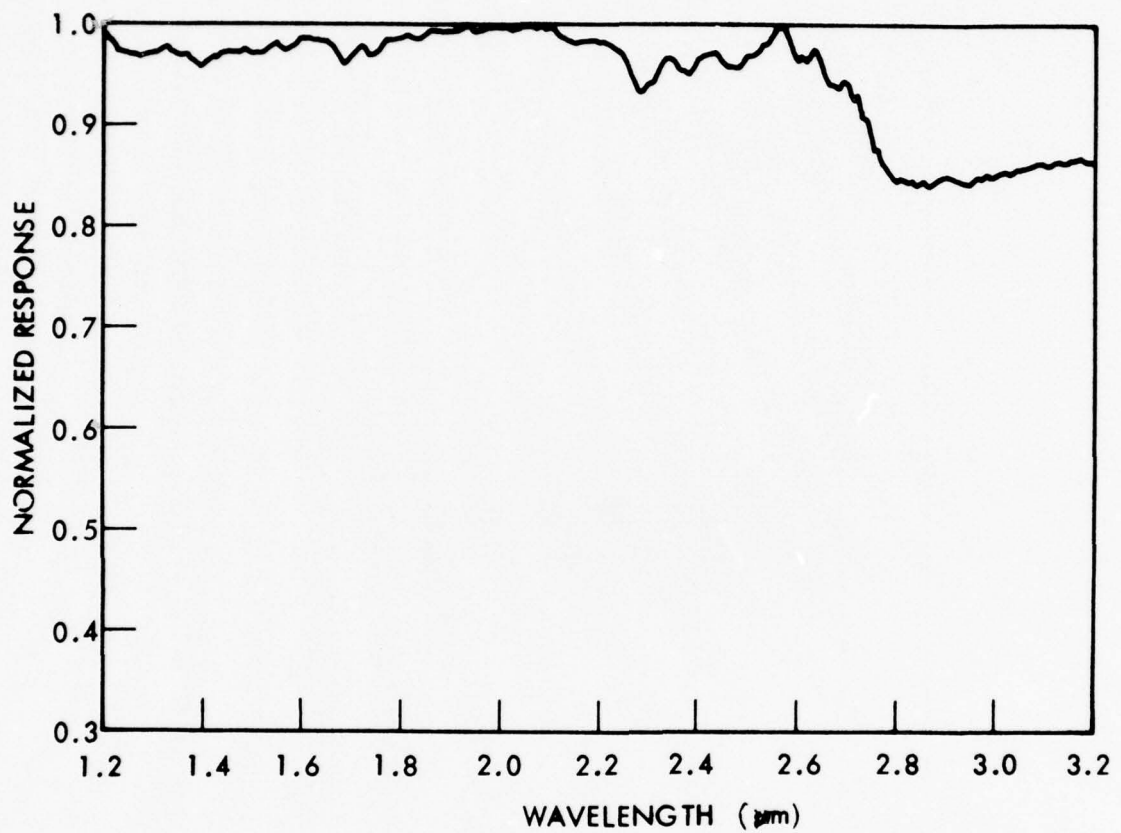


Figure 6.7 INTEGRATING SPHERE - SPECTRAL RESPONSE

One of the most important features of the source assembly is radiance control with source apertures at the input to the sphere. The linearity of broadband source radiance with input-aperture area was tested for the sphere-use configuration; results are given in Figure 6.8. The worst case nonlinearity occurred at those largest apertures which approximated the size of the input port. The vignetting due to the entrance enclosure was the cause of this effect; as a result actual transmission values for the source assembly were measured as part of the system calibration effort and are presented in the next section.

During assembly testing at helium temperatures all source functions were verified including initialization, positioning and readout of the aperture and filter wheels, activation of the flag for point-source operations and calibration of the blackbody controller.

#### Optics

Optical component testing was also performed both before and after mounting as well as at cryogenic temperatures. The optical figure was measured for all elements with a Laser Unequal Path Interferometer (LUPI) with the worst case distortion being a  $\lambda/2$  astigmatism at 0.6328 micrometer by the scan mirror. In the latter case additional interferograms were taken after mounting to insure maintenance of figure during mount-loading and the bolt-down operation.

In order to insure low-background operating conditions mirror scatter measurements were taken of those elements which would be the principal contributors to the sensor's aperture - the flat scan mirror because of its proximity to the sensor and the collimator due to the increased difficulty in substrate polishing and coating. Measurements of the Bi-directional Reflectance Distribution Function (BRDF) were performed at  $\lambda = 10.6$  micrometers and the 5-sample averages for each mirror are shown in Figure 6.9. These levels are better than those required for the performance of effective field-map measurements, allowing for approximately 6 orders of dynamic range for a wide-field sensor, such as the HIRIS.

Additional component testing was performed on the scan mirror assembly to verify positioning repeatability as well as calibrate the LVDT readout at cryogenic temperatures. This was accomplished using the theodolite at the observation port and verified achieving the repositioning-readout design goal of  $\pm 25$  s across the  $\pm 2$  degree two-axis scan.

Tests were also performed on the rhomboid prisms to demonstrate their accuracy in autocollimation for use in boresighting with respect to the sensor's reference mirror. The total autocollimation error introduced at cold temperatures through the use of the prisms was less than 10  $\text{''}$ .

Frequent testing was performed to maximize the chamber cooldown rate and temperature uniformity among elements. After sufficient cold-strapping, the lagging component, the scan mirror assembly, reached 14 K within 70 hours after

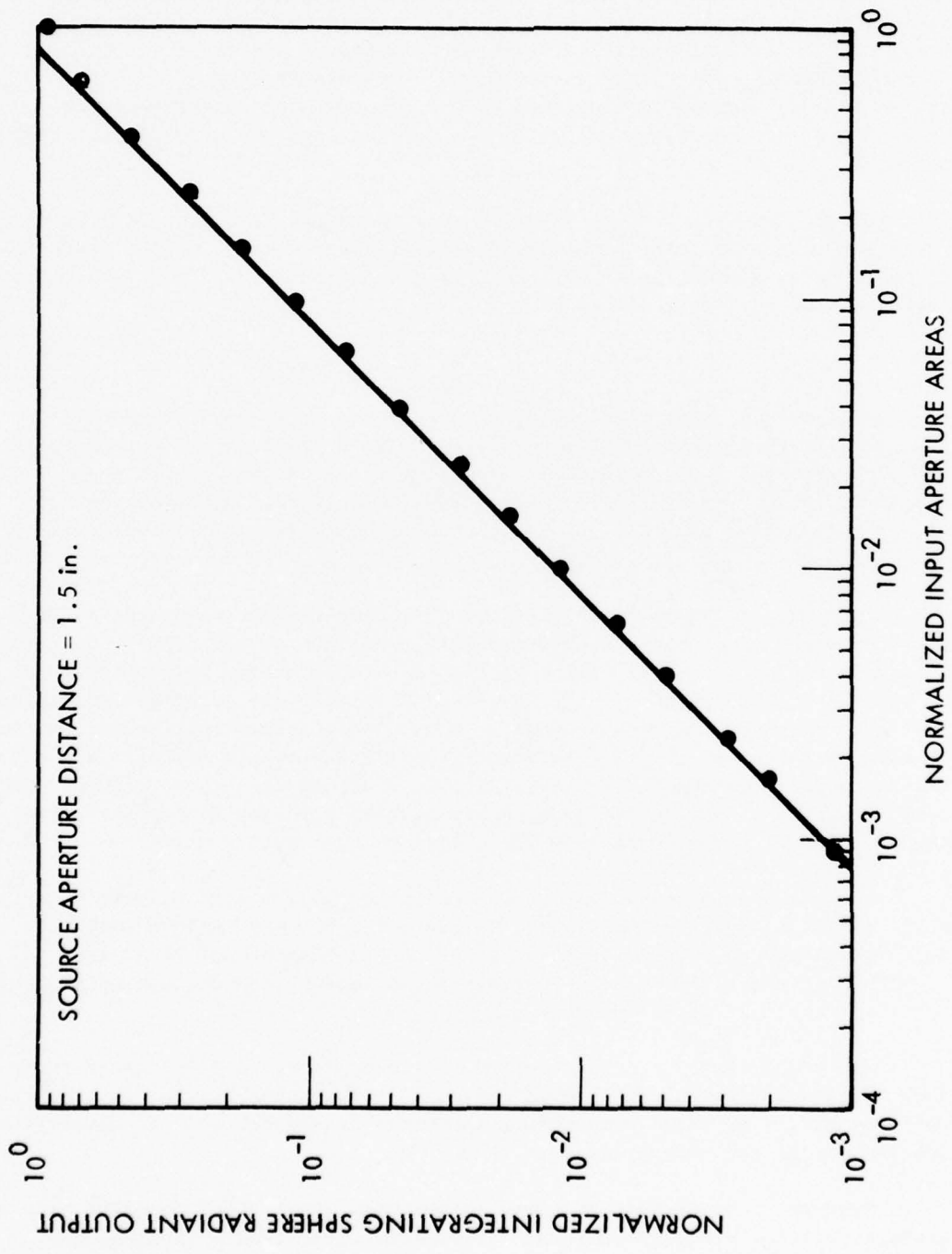


Figure 6.8 LBCF INTEGRATING SPHERE RADIANCE VS APERTURE SIZE

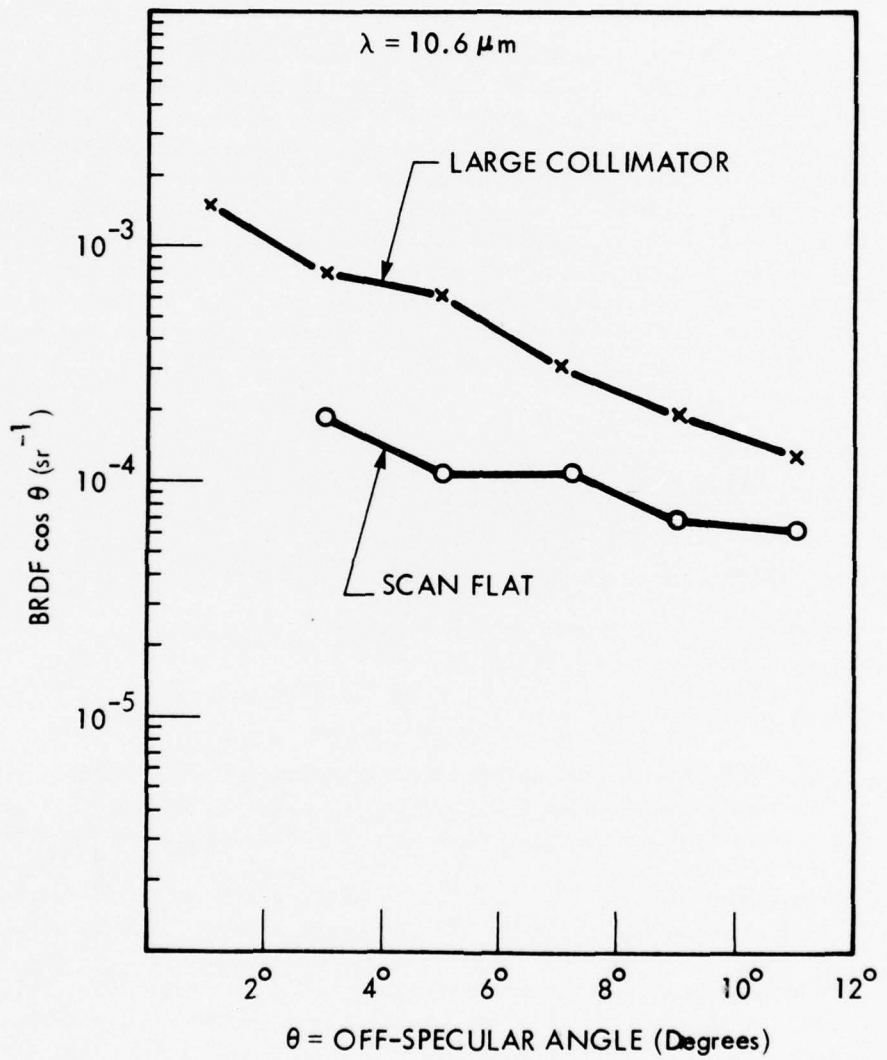


Figure 6.9 SCATTER PERFORMANCE OF LBCF MIRRORS

the inception of active cooling. All mirrors, their mounts and the baseplate ultimately reach approximately 10 K.

#### System Test

Once all the optical components were installed in the chamber the system had to be collimated for cryogenic operation and the reference direction determined for boresighting purposes. An existing star simulator was modified and adjusted for use as an alignment telescope. Focus measurement was accomplished at cryogenic temperatures using the test setup shown in Figure 6.10. A visible light source incorporated as part of the source assembly illuminated the flag-mounted pinhole in its activated position. The image of the pinhole formed in the telescope was viewed with a microscope eyepiece-objective combination. The difference between the cross-hairs-defined focal plane of the telescope and the image position  $b$ , was related to the required translation of the collimator for proper focusing,  $a$ :

$$a = \frac{f_c^2 b}{-f_t^2 + b(120 - f_c - f_t)}$$

where

$a$  = required movement of the collimator

$b$  = image distance from proper focus

$f_c$  = focal length of the collimator

$f_t$  = focal length of the telescope

The test configuration was sufficiently sensitive that a 0.001-in. displacement of the image represented a 0.0007-in. collimator adjustment. After final adjustment a verification thermal cycle was performed to insure repeatability.

The sensor-chamber interface utilized to define the nominal zero-direction was the sensor-to-chamber mounting plane. The perpendicular to this interface plane provides the nominal on-axis direction, with measurements of both the sensor line-of-sight and boresight-mirror normal referenced to this direction. During cryogenic alignment testing a flat/parallel window was attached to the sensor mounting plane with a fixture such that the combined error in determining the normal to the plane by autocollimating off the window surface was less than  $10 \text{ } \mu\text{rad}$ . This was performed with a DKM-3 theodolite which was then used as a telescope to position the output beam along this same direction to better than  $2 \text{ } \mu\text{rad}$ .

System level optical wavefront testing was performed under both room ambient and cryogenic operating conditions. With the optical system in its final configuration, LUPI interferograms were taken of the entire optical train. The laser source was relayed to the collimator's center of curvature from outside the

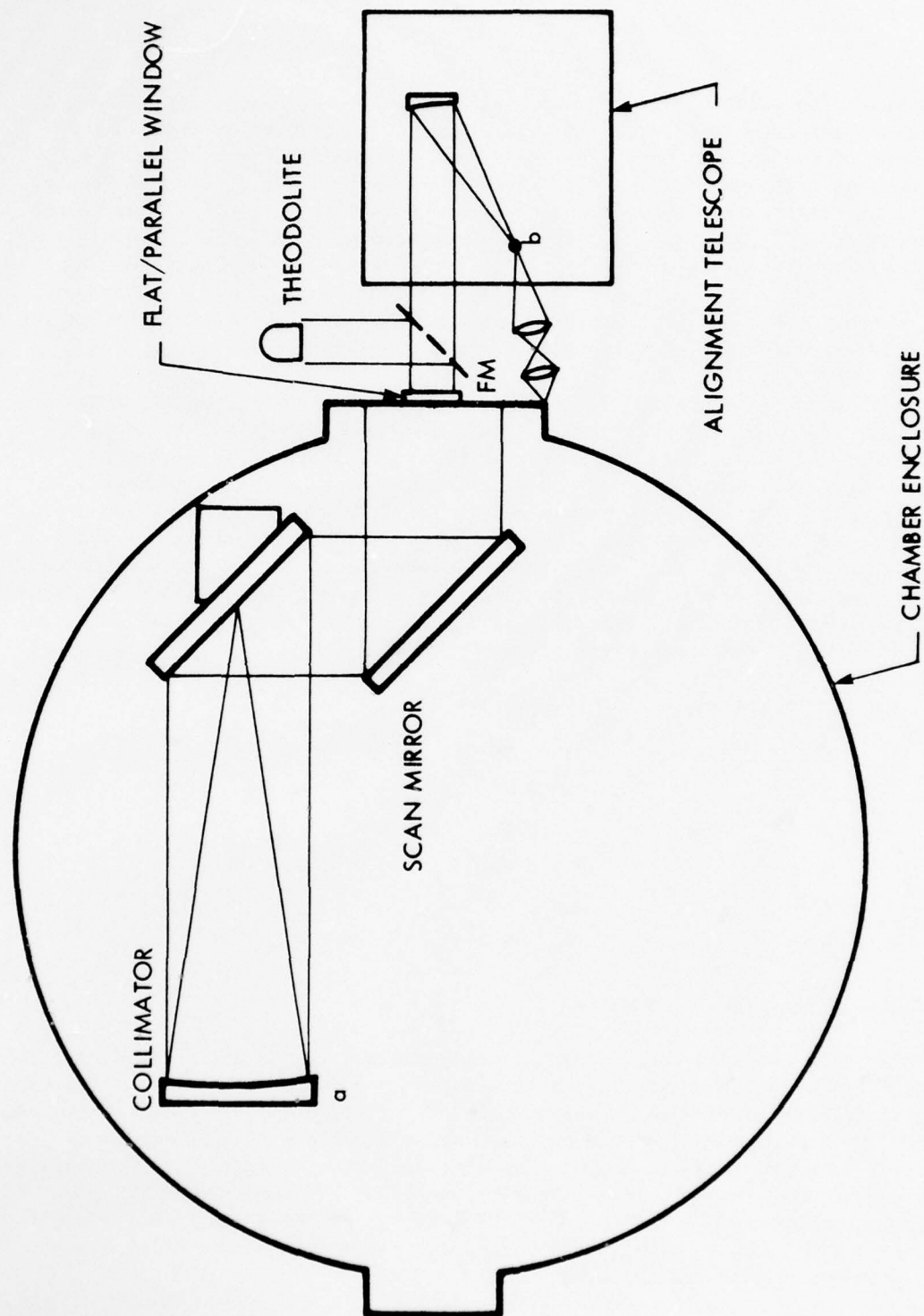


Figure 6.10 LBCF COLLIMATION/ALIGNMENT TECHNIQUE

chamber through the window. This permitted a measure of the system's performance as assembled over approximately 80% of the collimator's aperture as well as the effectiveness of the optical mounts in preventing cryogenic distortion. After final adjustment of the mounting screws, a wavefront distortion of  $5/4 \lambda$  irregular and  $\pm 3/4 \lambda$  cylindrical at  $\lambda = 0.6328$  micrometer was maintained for both warm and cryogenic conditions (see Figure 6.11). This represents diffraction-limited operation for those wavelengths in excess of approximately 3.7 micrometers.

After performance of these wavefront distortion tests, both the alignment and reference direction of the optical train were once again verified.

Radiometric performance verification for the chamber was accomplished using the HS-2 spectrometer, the installation shown in Figure 6.12. Field maps and radiance response data were achieved over the full spectral range of the instrument down to the sensor noise floor. The instrument uncovered a stray background radiance problem which was traced to leaks in the areas of the source, boresight and observation port assemblies. Improvements were incorporated which reduced the background radiance levels to the sensor noise floor, thus permitting sensor dynamic range measurements and extended range field-of-view maps. A typical map is shown in Figure 6.13. Calibration of the output radiance attenuation factor was also performed; results are given below:

<u>Aperture Position</u>	<u>Attenuation</u>
0	$1.3 \times 10^{-3}$
1	$4.6 \times 10^{-4}$
2	$6.2 \times 10^{-5}$
3	$2.7 \times 10^{-6}$
4	$2.6 \times 10^{-7}$
5	$1.6 \times 10^{-8}$

#### 6.1.5 Accomplishments and Results

The LBCF phase of the SPHIRIS program resulted in the optical/radiometric design and fabrication of a calibration testbed and its integration and verification with a modified existing cryogenic-vacuum chamber. Environmental system capabilities include  $10^{-6}$  Torr vacuum levels with optics, mounts and testbed temperatures of approximately 10 K providing in conjunction with radiation shielding, low-background operating conditions. Full-field sensitivity measurements with five-orders of dynamic range control without affecting source divergence, two-axis sensor field mapping over  $\pm 2$  degrees to within  $\pm 25$ 's accuracy and sensor boresighting capabilities to within  $\pm 35$ 's are included.

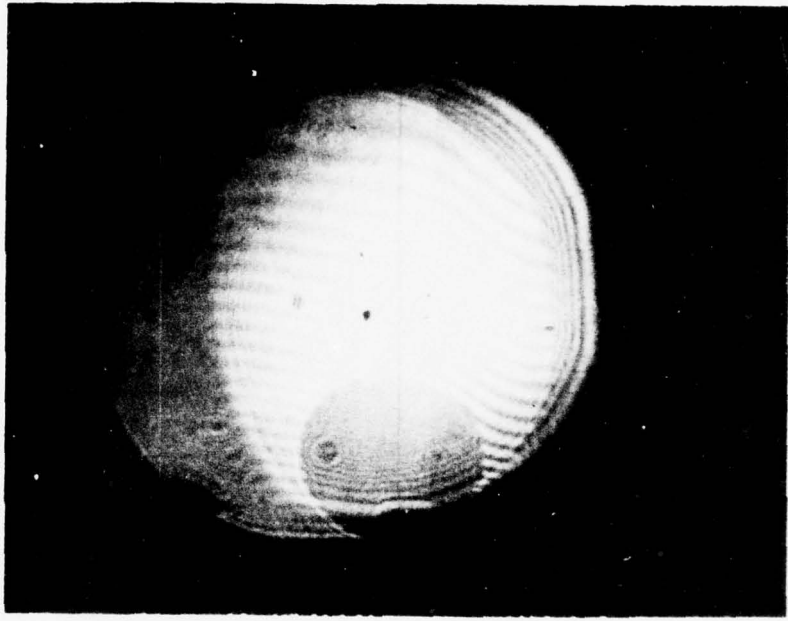
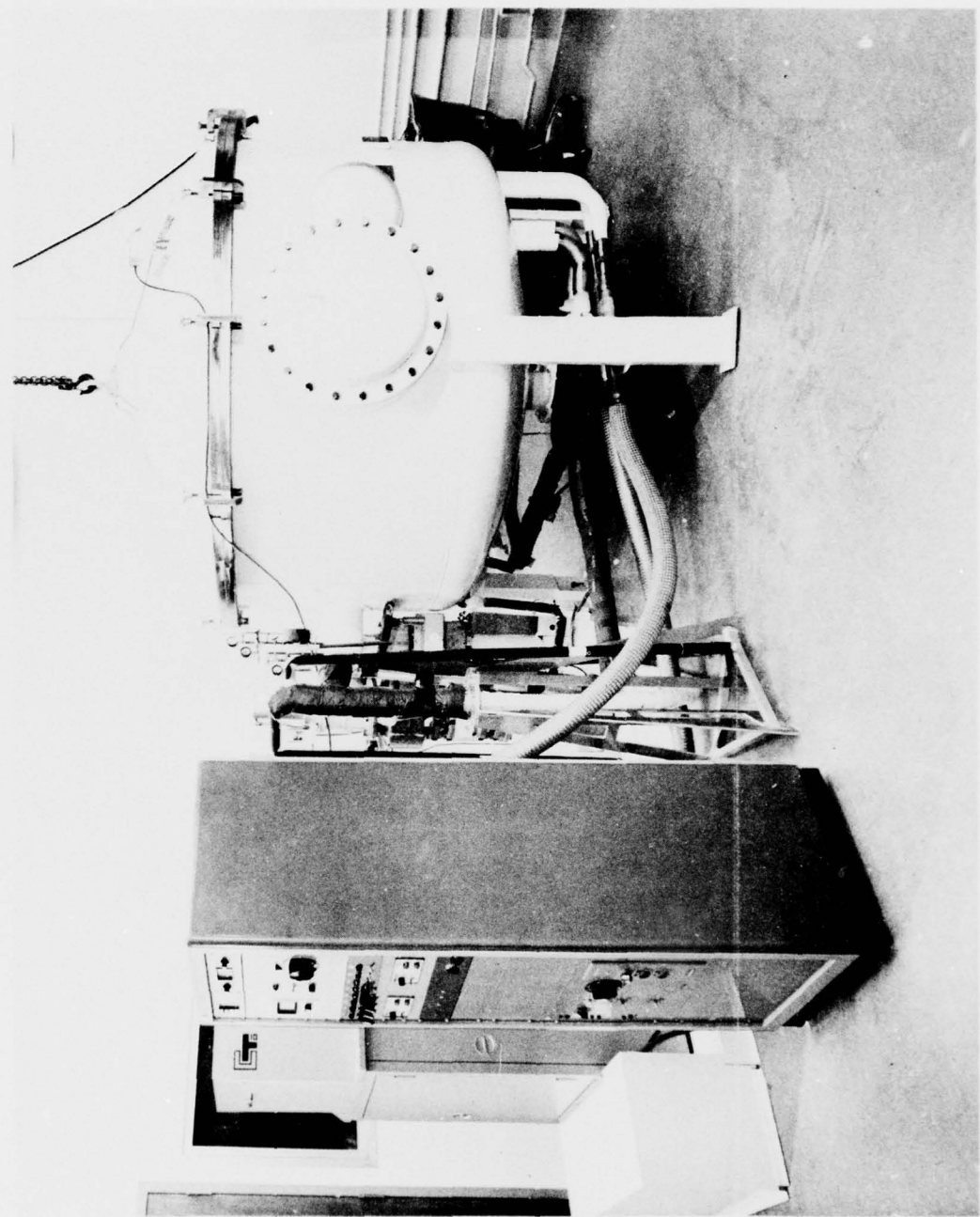


Figure 6.11 INTERFEROGRAM OF LBCF OPTICAL TRAIN AT CRYOGENIC TEMPERATURES

Figure 6.12 HS-2 SPECTROMETER INSTALLATION



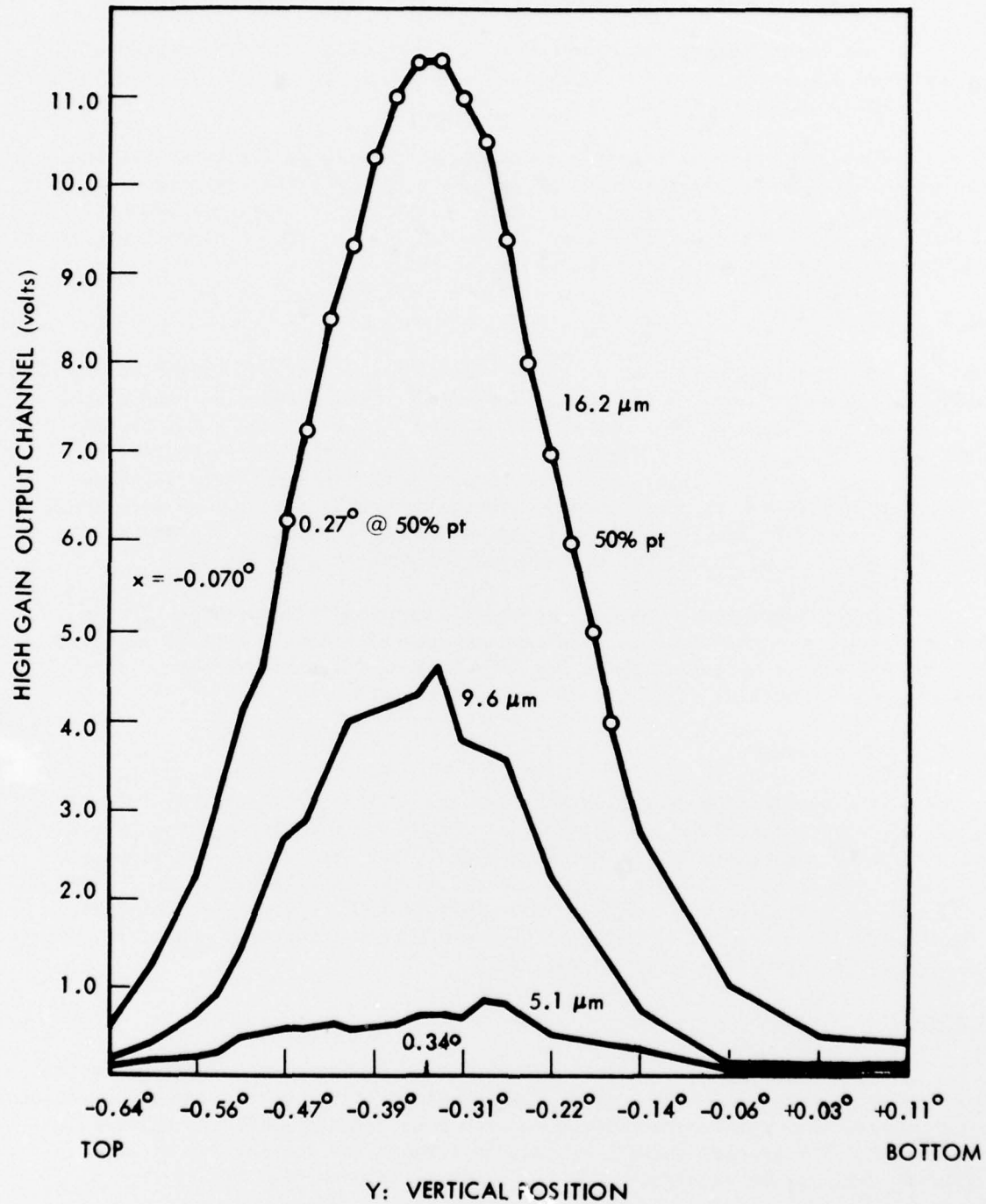


Figure 6.13 VERTICAL FIELD PROFILE

## 6.2 FIELD PORTABLE MONOCHROMATOR

The Field Portable Monochromator is a narrowband spectral source which may be tuned continuously over a wide wavelength range from UV to IR. The output energy level is constant at all times.

The wavelength of interest is shown on a front panel digital display. This wavelength can be selected manually by means of a digital keyboard -- or any wavelength range can be scanned automatically by use of the same keyboard to enter and store the upper and lower wavelength limits. The following paragraphs describe the major components of the monochromator.

### 6.2.1 Source

The spectral energy is obtained from either a tungsten Quartz Iodine lamp or a Xenon arc lamp. Both lamps are mounted in a water-cooled case which attaches to the inside of the main source module. Copper tubing connects the water-cooled housing to hose fittings on the outside of the source module. A pivoting mirror allows either lamp to be imaged on the monochromator entrance slit. This mirror is operated by two solenoids driven by the digital wavelength selection circuits. The Xenon lamp is used at wavelengths less than 450 nm and the tungsten lamp is used at all wavelengths greater than 450 nm.

A Pen Ray mercury lamp may be plugged into the hole provided in the bottom of the source module. In this case the pivoting mirror must be adjusted with the set screws to position the Pen Ray image on the entrance slit. This lamp is used for optical alignment of the monochromator.

### 6.2.2 Monochromator

The broadband spectral energy from the source is selectively filtered by two identical monochromators in cascade. These are 0.25 meter focal length, coma corrected asymmetric Czerny-Turner design. They are unique in that a lead screw and sine-drive mechanism is not employed for wavelength selection. Instead, both grating turntables are driven by worm gears which are geared to a single "three-phase dc motor." This motor is controlled by a calculator and drive circuit which provides linear wavelength scanning.

#### Gratings

The worm driven scanning turntable in each monochromator holds a motor driven grating turntable with four 2" x 2" gratings, thus, the wavelength calculator logic selects the appropriate grating in both monochromators for the wavelength of interest. The grating turrets are easily removed for loading any of six different gratings as required:

<u>Resolution, <math>\mu\text{m}/\text{mm}</math></u>	<u>Range, <math>\mu\text{m}</math></u>	<u>Lines/mm</u>
0.0016	0.250 to 0.600	2400
0.0033	0.400 to 1	1200
0.0066	1 to 2	600
0.0130	2 to 4	300
0.0260	4 to 8	150
0.0540	8 to 16	75

### Filters

At the entrance slit and intermediate slit are two identical motor driven filter wheels. Each contains any of six different long pass interference filters. The gratings are used in their first order and all other orders and strays are suppressed by the filters. The wavelength calculation logic selects the appropriate filter in both monochromators for the wavelength of interest. The filter wheels are easily removable for loading of any of seven different filters as required, with the wavelength coverage,  $\mu\text{m}$ , for each given below:

None	up	to	0.7
0.7	to	1.2	
1.2	to	2.1	
2.1	to	3.8	
3.8	to	6.2	
6.2	to	10.0	
10.0	to	16.0	

### Slits

The entrance slit of the first monochromator can be varied continuously from 0 to 0.128 inch width. This slit is electrically driven by the control chassis. The intermediate slit and the exit slit of the second monochromator have six preset widths. They are: 0.004", 0.008", 0.016", 0.032", 0.064", and 0.128". A knob on the rear of the monochromator allows selection of the intermediate slit; and a knob on top of the monochromator is used to select the exit slit width.

#### 6.2.3 Wavelength Control Chassis

The wavelength of output energy from the Spectral Signal Generator is selected by a digital keyboard on this chassis. A digital display indicates the true output wavelength and a number of other parameters. The instrument operates in either of two ways -- direct selection of a new wavelength or a continuous scan from one preselected wavelength to another.

Nine plug-in digital cards perform these functions. Six of these cards are used for scanning in a linear manner from one wavelength to another. The CLOCK, PB174 generates a series of pulses at a rate determined by the keyboard

slide switch. The WAVELENGTH GENERATOR, PB172 counts these pulses with a six decade counter and sends the BCD count information to two display drivers. PB169 converts this BCD count to 7 segment drive for the two right hand LSB digits. PB167 converts the count to 7 segment drive for the three left hand MSB digits. The count rate is always greater than is shown on the display; thus, 100,000 counts are 1.000 MICROMETER and 50,000 counts are 500.0 NANOMETERS.

While PB172 counts and displays the CLOCK pulses, the same pulses are counted by the SINE DRIVE PB171. This card has a 24-bit binary counter rather than a decade counter. The binary count is used for two purposes. First, each bit change generates a pulse out. Second, the binary count is used to address a read only memory with 32 different 8-bit numbers stored in it. These bits are added to the linear clock pulses to produce a nonlinear pulse rate for the scan drive motor. The system works as follows.

In the visible spectrum (for example) the total grating tilt ranges from  $0^{\circ}$  at 000.0 nm to  $39.2^{\circ}$  at 1.000  $\mu\text{m}$ . A clock count of 100,000 bits = 1.000 on the display. The scan angle below 200 nm is not used, so starting at 204.8 nm, and every 256 nm thereafter a new address is selected on a binary basis. At each address, the bits stored in the memory are added to the clock pulses as they are applied to the scan motor driver. Thus the angular tilt of the grating becomes progressively larger for each input pulse -- exactly duplicating the effect of a sine-drive mechanism in an ordinary monochromator. This is shown on the following partial list:

WAVELENGTH, $\mu\text{m}$	ANGLE	ADDRESS	Binary Count	PULSES ADDED
0.2048	$7.45^{\circ}$	0	2048	14
0.2304	$8.38^{\circ}$	1	2304	20
0.2560	$9.32^{\circ}$	2	2560	24
0.2816	$10.26^{\circ}$	3	2816	30
0.3072	$11.21^{\circ}$	4	3072	34
0.3328	$12.15^{\circ}$	5	3328	42
0.3584	$13.11^{\circ}$	6	3584	50
0.3840	$14.06^{\circ}$	7	3840	56
0.4096	$15.02^{\circ}$	8	4096	66
etc				
0.9984	$39.17^{\circ}$	31	9984	494
1.0240	$40.38^{\circ}$	32	10240	536

The stored pulses are not "dumped" into the motor at each new address, however. They are distributed evenly through the count from one address to another. When the instrument is scanned backward from a long wavelength to a short wavelength, they are subtracted evenly as well.

The mixed pulses are applied to the 3-phase DRIVER PB123. This card uses a divide by six counter and a digital-analog converter to generate three trapezoidal wave forms 120 degrees apart which are proportional to the input count. 360 pulses are required for one complete cycle, so the motor rotates in  $1^{\circ}$  steps, but it is not a stepping motor. At high speeds (3600 rpm), it may be seen with an oscilloscope to be a three-phase 60-Hz ac motor with trapezoidal drive wave forms rather than sine waves. At very low speeds (1 pulse per second) the motor may be seen to be more nearly a continuously rotating meter movement, where the permanent magnet armature is aligned with the vector sum of the three magnetic forces generated in the field coils. The term "three phase dc motor" has been coined to describe this motor and current.

Thus, to review the complete scan drive sequence: the clock (PB174) pulses are counted by the wavelength generator (PB172) which drives the display through the MSB driver (PB167) and LSB driver (PB169). Simultaneously, the clock pulses drive the scan motor through the sine converter (PB171) and 3-phase driver (PB123). In order to start all of the converters at the right number and synchronize the display with the scan drive, a reset pulse is generated by a combination of photo and magnetic pickups in the monochromator. These pickups are mechanically adjusted to coincide at  $26.4^{\circ}$  which corresponds to 100.0 nm - close to the blaze angle of the gratings. The reset pulse loads the correct binary number in the scan drive circuit and also loads the correct BCD number in the wavelength generator. This number is different for each grating.

<u>Lines/mm</u>	<u>Reset Wavelength, <math>\mu\text{m}</math></u>
2400	0.35
1200	0.70
600	1.400
300	2.800
150	5.600
75	11.20

Each time the monochromator scans through  $26.4^{\circ}$ , the reset pulse gets all of the counters in step. This operation is indicated on the digital display by flashing the  $\lambda$  CALIBRATION lamps. Normally this operation is not required after the initial setup when the instrument is first turned on. Therefore, a special circuit on the CALIBRATE card PB177 causes the instrument to "home" on 700.0 nm and calibrate itself automatically each time the power switch is turned on.

PB169 contains the program which monitors the wavelength display and chooses the appropriate filters and gratings. A BCD code is used with 1 to 6 for the filter and 1 to 4 for the gratings. These numbers are sent to the Output Control Chassis where they are displayed on the front panel and another card drives the selection motors in the monochromators until the correct gratings and filters are positioned. The grating number also is used to control the CLOCK and WAVELENGTH GENERATOR so that the correct scan rate and display wavelength is provided for the grating in use.

The keyboard controls the system through the ENTRY card PB170 and the SCAN CONTROL PB173. The ENTRY card converts the keyboard information into BCD words and commands. It addresses any one of three different storage registers as required for new commands.

When a new wavelength is punched in, the number is stored in the entry register of the WAVELENGTH GENERATOR PB173. Magnitude comparators on this card then determine whether the new number is larger or smaller than the wavelength in use. Also they determine whether it is within the range of the grating in use. If it is within the range, the SCAN CONTROL card runs the CLOCK either forward or reverse until the BCD counters on the WAVELENGTH GENERATOR have the same number as the entry storage register. Then the filter selector changes the filter if necessary, and the ENTRY lamp on the display goes out, indicating the cycle is complete.

When a new wavelength is selected outside of the range of the grating in use, the SCAN CONTROL card first runs the CLOCK in the correct direction to slew at high speed to the  $26.4^{\circ}$  calibration angle. There, it stops, changes to the correct grating for the new wavelength and loads the correct reset wavelength for this grating into the counters. Then the scan drive slews at high speed in the correct direction to reach the new wavelength. When the WAVELENGTH GENERATOR counters have the same number as the entry wavelength stored in the register, the CLOCK stops. The filter selector changes to the correct filter and the ENTRY lamp again goes indicating the cycle is complete.

All of the above steps are completed automatically by simply punching into the keyboard a complete wavelength number and pressing the NEW  $\lambda$  key. If an impossible number is selected by the operator, a program on PB170 stops the system and lights the OUT OF RANGE lamp on the display.

To scan from one preset wavelength to another (larger) wavelength, the keyboard ENTRY loads first one wavelength and then the other into storage registers on PB167. Then, whenever the LL RTN button is pressed, the system functions exactly as described earlier in seeking a new wavelength - except the lower limit register is used for comparison rather than the entry register.

The upper limit register is continually compared with the operating wavelength and a stop scan command is generated when they are equal. During scanning, the filter and grating selector monitors the true wavelength and stops the scan to change filters and gratings as required and then continues the scan. The new filters are simply indexed into position and the scan resumes. When the gratings are changed, however, they must be slewed to  $26.4^{\circ}$  where the counters are reset correctly - then they proceed to the correct angle to resume the scan. The SCAN CONTROL card PB173 establishes the correct sequence of operations for all modes of operation.

#### 6.2.4 Power Output Chassis

In order to maintain constant output energy, an internal reference detector is used to continuously monitor and control the exit slit energy. This is accomplished in the following way.

The energy from the source is chopped by a rotating opaque blade at the entrance slit. At the exit slit, a rotating mirror surfaced blade alternately directs the energy out the exit slit, or allows the energy to fall on the reference detector. The detector is a Reeder Thermocouple with 2 x 6-mm sensitive area.

The mirror blade chops the beam at 30 Hz and is phase-locked to the 7.5 Hz entrance shutter. The two chopper motors are 3-phase 400 $\text{v}$  ac motors with 64-bit optical encoders on their shafts.

The CHOPPER CONTROL card PB176 contains the oscillator and phase-lock circuitry which decodes the information from both motor shaft encoders and produces the correct dc voltage proportional to rpm for both motors.

These dc control voltages are fed to the CHOPPER DRIVE card PB175 which contains a 3-phase 400 $\text{v}$  oscillator and six power amplifiers to drive the three phases of both motors. The dc control voltage for each motor determines the amplitude of the three-phase drive waveforms for the chopper motor. The mirror blade dc control voltage controls the amplitude of the three-phase drive waveforms for the mirror blade motor.

The detector signal is basically a 7.5-Hz square wave modulated at 30 Hz. This is an extremely low level signal which is transformer coupled to a preamplifier in the monochromator and amplified 100,000 times before it is sent to the Output Control Chassis.

Here, the LOCK-IN-AMPLIFIER card PB178 amplifies the signal and converts it to dc proportional to output energy. The reference detector signal is displayed in MICROWATTS on the output meter on the front panel.

The detector dc signal is applied to both source power DRIVER card PB175. An increase in the detector signal causes the entrance slit width to decrease.

The detector dc signal is also applied to both source power supplies. An increase in the detector signal causes the lamp power to decrease.

The TUNGSTEN POWER card PB188 uses a simple phase delay triggered SCR circuit to apply full wave rectified line voltage to the 400-watt tungsten lamp. The raw dc voltage thus obtained has a large 120 $\text{v}$  ripple component which is removed by the lock-in amplifier tuned signal channel.

The XENON POWER card PB187 uses a high speed switching regulator with current feedback sensing to maintain constant current in the Xenon arc lamp. The current level is controlled by the detector signal and ranges between 1 and 6 amps.

Thus to review the output power control sequence; the entrance and exit choppers produce an output energy beam which is chopped at 7.5 Hz with 30 Hz ripple. This is detected by the internal detector, and amplified by a lock-in amplifier. The resultant dc signal voltage increases the source power and opens the entrance slit if the exit power falls below the level set by front panel controls. If the exit power level exceeds this preset level, the signal control voltage reduces the slit width and source power. In this way, the output power level remains constant at all wavelengths of interest.

The BCD 1 to 4 grating and BCD 1 to 6 filter selection codes from the Control Chassis are applied to the FILTER, GRATING CHANGE card PB168. A rotary switch on each filter wheel in the monochromator produces a BCD 1 to 6 code to indicate the filters in positions. Magnetic pickups on each grating turret in the monochromator produce a BCD 1 to 4 code to indicate the gratings in position. The control chassis codes are compared to the monochromator to operate the change motors until the selection codes agree with the actual codes.

The four change motors in the monochromator are brushless dc types. Two motors are driven by one SIEMANS DRIVER card PB117 and the remaining two motors are driven by the other identical card PB117.

In the AUTOMATIC CONTROL mode, the above operations are performed without the operator's attention. In the MANUAL CONTROL mode, the individual front panel controls may be used to set either source power, slit width and any grating or filter may be selected at will. The MODE CONTROL card PB179 in conjunction with the front panel pushbuttons determines the mode of operation.

#### 6.2.5 Power Supply

The RAW POWER PACK contains a 500-watt isolation transformer full wave rectifier, choke and electrolytic capacitor. It produces an unregulated 100 V at 6 A with a high degree of 120 $\text{v}$  ripple. This raw power is applied to the +75 V REGULATOR card PB182, which employs a high speed switching regulator to supply a constant +75 Vdc regardless of line voltage changes or load changes as the various motors switch on and off.

The constant +75 V is applied to the DC/AC INVERTER, card PB183 which contains a 20-kHz squarewave oscillator and power output transistor to drive the primary windings of the main power transformer. Since the frequency is very high, the transformer can be made very small.

The power transformer, full wave rectifiers, filter chokes and capacitors for all of the voltages used in the system are located on the AC/DC CONVERTER, card PB184.

#### REFERENCES

1. Air Force Geophysics Laboratory, "LWIR (7-24 micrometer) Measurements From The Launch of a Rocketborne Spectrometer Into an Aurora (1973)," Contract No. AFGL-TR-76-0274, 15 November 1976.
2. Honeywell Radiation Center, "Final Report on HIRIS (High Resolution Interferometer Spectrometer)", Contract No. DNA001-72-C-0193, 30 July 1975 (Unclassified).
3. Honeywell Radiation Center, "HIRIS Field Operations Procedures Manual," Contract No. DNA001-73-0164, August 1976 (Unclassified).
4. Optical Physics Technical Memorandum No. 2, "HIRIS Experiment," AFGL-OP-TM-02, 15 April 1976, A.T. Stair, Jr., James W. Rogers, and William R. Williamson.
5. Honeywell Aerospace Division, "Emittance Measurement Study Final Report," Contract No. NAS1-8447, June 1969 (Unclassified).

#### BIBLIOGRAPHY

1. Introduction to Fourier Spectroscopy by R.J. Bell, Academic Press, 1972.
2. Born and Wolf, pages 55 through 70.
3. Aspen International Conference on Fourier Spectroscopy (1970), edited by George A. Vanasse, A.T. Stair, Jr., Doran J. Baker, AFCRL-71-0019, Special Reports No. 114.

## GLOSSARY

<u>TERM</u>	<u>MEANING</u>
ACS	Attitude Control System (in payload)
A/D	Analog to Digital (converter)
AEDC	Arnold Engineering Development Center
AFGL	Air Force Geophysics Laboratory (formerly AFCRL = Air Force Cambridge Research Laboratory)
CDR	Critical Design Review
CVF	Circular Variable Filter (Utah State University)
DNA	Defense Nuclear Agency
DVM	Digital Voltmeter
ELS	Earth Limb Sensor (a forerunning program to SPHIRIS)
FOV	Field of View
GFE	Government Furnished Equipment
GSE	Ground Support Equipment
HAES	High Altitude Effects Simulation (a DNA program)
HIRIS	High Resolution Interferometer Spectrometer
H/K	Housekeeping
HRC	Honeywell Radiation Center
I/F	Interferometer
LBCF	Low-Background Calibration Facility
LED	Light Emitting Diode
LSB	Least Significant Bit
LWIR	Long-Wave Infrared
MLI	Multilayered Insulation
MSB	Most Significant Bit
NEFD	Noise Equivalent Flux Density
NER	Noise Equivalent Radiance
NESR	Noise Equivalent Spectral Radiance
NRZ-L	NonReturn to Zero Level

GLOSSARY (continued)

<u>TERM</u>	<u>MEANING</u>
PCM	Pulse Code Modulation
PLL	Phase-Lock Loop
SPARAD	Spatial Radiometer
SPHIRIS	Spatial High-Resolution Interferometer Spectrometer
SPIRE	Spatial Infrared Experiment
SWIR	Short-Wave Infrared
TIA	Transimpedance Amplifier
TTL	Transistor-to-Transistor Logic
VPS	Vacuum Pumping Station

PRECEDING PAGE NOT FILMED  
BLANK

DISTRIBUTION LIST

DEPARTMENT OF DEFENSE

Director  
Defense Advanced Rsch. Proj. Agency  
ATTN: LTC W. A. Whitaker  
ATTN: Strategic Technology Office  
ATTN: Nuclear Monitoring Research

Defense Documentation Center  
Cameron Station  
12 cy ATTN: TC

Director  
Defense Nuclear Agency  
ATTN: TISI Archives  
ATTN: RAAE, MAJ John Clark  
ATTN: RAEV, Harold C. Fitz, Jr.  
ATTN: DDST  
ATTN: RAAE, MAJ James W. Mayo  
2 cy ATTN: RAAE, Charles A. Blank  
3 cy ATTN: TITL, Tech. Library

Commander  
Field Command, Defense Nuclear Agency  
ATTN: FCPR

Chief  
Livermore Division, Fld. Command, DNA  
Lawrence Livermore Laboratory  
ATTN: FCPL

Under Sec'y of Def. for Rsch. & Engrg.  
ATTN: S&SS (OS)

DEPARTMENT OF ARMY

Commander/Director  
Atmospheric Sciences Laboratory  
ATTN: DELAS-AF-M, F. E. Niles  
ATTN: H. Ballard  
ATTN: DRSEL-BL-SY-S, D. Snider  
ATTN: R. Rosen

Director  
BMD Advanced Tech. Center  
ATTN: ATC-O, W. Davies  
ATTN: ATC-T, Melvin T. Capps

Commander  
Harry Diamond Laboratories  
2 cy ATTN: DELHD-NP, F. N. Wimenitz

Chief of Engineers  
ATTN: Fernand DePercin

Dep. Chief of Staff for Rsch. Dev. & Acq.  
ATTN: NCB Division  
ATTN: DAMA-CSZ-C  
ATTN: DAMA-WSZ-C

Deputy Chief of Staff for Ops. & Plans  
ATTN: DAMO-DDL, COL D. W. Einsel  
ATTN: DIV. of Chem. & Nuc. Ops.

DEPARTMENT OF ARMY (Continued)

Director  
U.S. Army Ballistic Research Labs.  
ATTN: Tech Lib., E. Baicy  
ATTN: John Mester  
ATTN: J. Heimerl  
ATTN: M. Kregl

Commander  
U.S. Army Electronics Command  
ATTN: DRSEL-PL-ENV, Hans A. Bomke  
ATTN: DRSEL  
ATTN: Stanley Kronenberg  
ATTN: DRSEL-TL-IR, E. T. Hunter  
ATTN: Inst. for Exploratory Rsch.  
ATTN: Weapons Effects Section  
ATTN: DRSEL-RD-P

Commander  
U.S. Army Foreign Science & Tech. Ctr.  
ATTN: Robert Jones

Commander  
U.S. Army Material Dev. & Rdns. Cmd.  
ATTN: DRXCD-TL  
ATTN: DRCCDC, J. S. Bender

Commander  
U.S. Army Missile Command  
ATTN: DRSMI-ABL  
ATTN: Chief, Doc. Section  
ATTN: DRSMI-XS, Chief Scientist

Commander  
U.S. Army Nuclear Agency  
ATTN: MONA-WE, J. Bereret

Chief  
U.S. Army Research Office  
ATTN: CRDARD-CCS, Hermann Robl  
ATTN: CRDARD-P, Robert Macu

DEPARTMENT OF NAVY

Chief of Naval Research  
ATTN: CODE 421, R. R. Junker  
ATTN: Code 461, Jacob Warner  
ATTN: Code 461, R. G. Joiner

Commanding Officer  
Naval Intelligence Support Center  
ATTN: Document Control  
ATTN: Code 40A, E. Blase

Commander  
Naval Ocean Systems Center  
ATTN: Code 2200, Verne E. Hildebrand  
ATTN: Code 2200, Ilan Rothmuller  
ATTN: Code 2200, Jurgen Richter  
ATTN: Code 2200, William F. Moler  
ATTN: Code 2200, Richard Pappert  
ATTN: Tech. Lib. for T. J. Keary  
ATTN: Code 2200, Herbert Hughes

DEPARTMENT OF NAVY (Continued)

Superintendent (Code 1424)  
Naval Postgraduate School  
ATTN: Code 2124, Tech. Reports Librarian

Director

Naval Research Laboratory  
ATTN: Douglas P. McNutt  
ATTN: Code 7701, Jack D. Brown  
ATTN: Code 7709, Wahab Ali  
ATTN: Code 7750, Darrell F. Strobel  
ATTN: Code 7700, Timothy P. Coffey  
ATTN: Code 7750, Paul Julenne  
ATTN: Code 2600, Tech. Lib.  
ATTN: Code 7127, Charles Y. Johnson  
ATTN: Code 7120, W. Neil Johnson  
ATTN: Code 7750, J. Davis  
ATTN: Code 7750, Klaus Hein  
ATTN: Code 7750, Joel Feddler  
ATTN: Code 2027, Tech. Lib.  
ATTN: Code 7750, S. L. Assakow  
ATTN: Code 7730, Edgar S. McClean

Officer-in-Charge

Naval Surface Weapons Center  
ATTN: Code WA501, Navy Nuc. Prgms. Off.  
ATTN: Code WX21, Tech. Lib.  
ATTN: D. J. Sand  
ATTN: L. Rudlin

Commander

Naval Weather Service Command  
Naval Weather Service Hqs.  
ATTN: Mr. Martin

DEPARTMENT OF THE AIR FORCE

AF Geophysics Laboratory, AFSC  
2 cy ATTN: OPR-1, R. Murphy  
2 cy ATTN: OPR-1, J. Kennedy  
5 cy ATTN: OPR, Alva T. Stair  
5 cy ATTN: LKB, Kenneth S. W. Champion  
5 cy ATTN: OPR, J. Ullwick

AF Weapons Laboratory, AFSC  
ATTN: CA  
ATTN: G. J. Fryer

2 cy ATTN: DYM  
5 cy ATTN: SUL  
5 cy ATTN: DYT  
5 cy ATTN: DYC

AFTAC

2 cy ATTN: Tech. Lib.  
5 cy ATTN: TD

Commander

ASD  
ATTN: ASD-YH-EX, Lt Col Robert Leverette

Hq. USAF

ATTN: DLS  
ATTN: DLCAW  
ATTN: DTL  
ATTN: DLXP  
ATTN: SDR  
ATTN: Tech. Lib.

SAMSO/AW

ATTN: AW

DEPARTMENT OF THE AIR FORCE (Continued)

SAMSO/SZ  
ATTN: SZJ, Major Lawrence Doan

DEPARTMENT OF ENERGY

Division of Military Application  
ATTN: Doc. Con. for Maj D. A. Haycock  
ATTN: Doc. Con. for Col T. Gross  
ATTN: Doc. Con. for David Slade  
ATTN: Doc. Con. for Donald I. Gale  
ATTN: Doc. Con. for F. S. Ross

Aero-Chem Research Laboratories, Inc.  
3 cy ATTN: A. Fontijn

Argonne National Laboratory  
Records Control

ATTN: Doc. Con. for A. C. Wahl  
ATTN: Doc. Con. for S. Gabelnick  
ATTN: Doc. Con. for J. Berkowitz  
ATTN: Doc. Con. for Lib. Svsc. Rpts. Sec.  
ATTN: Doc. Con. for Len Liebowitz  
ATTN: Doc. Con. for David W. Green  
ATTN: Doc. Con. for Gerald T. Reedy

Los Alamos Scientific Laboratory

ATTN: Doc. Con. for R. A. Jeffries  
ATTN: Doc. Con. for C. R. Mehl  
ATTN: Doc. Con. for G. Rood  
ATTN: Doc. Con. for H. V. Sego  
ATTN: Doc. Con. for D. Steinhaus  
ATTN: Doc. Con. for J. Judd  
ATTN: Doc. Con. for T. Bieniewski  
ATTN: Doc. Con. for J. M. Robrer  
ATTN: Doc. Con. for Martin Tierney  
ATTN: Doc. Con. for Marge Johnson  
ATTN: Doc. Con. for John S. Malik  
ATTN: Doc. Con. for William Maier  
ATTN: Doc. Con. for S. Rockwood  
ATTN: Doc. Con. for Donald Ken  
ATTN: Doc. Con. for W. D. Barfield  
ATTN: Doc. Con. for Reference Library  
ATTN: Doc. Con. for W. M. Hughes  
ATTN: Doc. Con. for E. W. Jones, Jr.  
ATTN: Doc. Con. for John Zinn  
ATTN: Doc. Con. for E. S. Bryant

Sandia Laboratories

ATTN: Doc. Con. for W. D. Brown  
ATTN: Doc. Con. for Org. 9220  
ATTN: Doc. Con. for Craig Hudson  
ATTN: Doc. Con. for J. C. Eckardt  
ATTN: Doc. Con. for C. W. Gwyn  
ATTN: Doc. Con. for D. A. Dahlgren  
ATTN: Doc. Con. for M. L. Kramm  
ATTN: Doc. Con. for T. Wright  
ATTN: Doc. Con. for Charles Williams  
ATTN: Doc. Con. for Sandia Rpt. Coll.  
ATTN: Doc. Con. for Document Division

University of California

Lawrence Livermore Laboratory

ATTN: G. R. Haugen  
ATTN: A. Kaufman  
ATTN: D. J. Wuebbles  
ATTN: J. F. Tinney  
ATTN: Julius Chang  
ATTN: Tech. Info. Dept.  
ATTN: W. H. Duewer

DEPARTMENT OF ENERGY (Continued)

Sandia Laboratories  
Livermore Laboratory  
ATTN: Doc. Con. for Thomas Cook

U.S. Energy Rsch. & Dev. Adm.  
Div. of Hqs. Services  
ATTN: Doc. Con. for D. Kohlstad  
ATTN: Doc. Con. for J. D. LaFleur  
ATTN: Doc. Con. for Class. Tech. Lib.  
ATTN: Doc. Con. for George Regos  
ATTN: Doc. Con. for Rpts. Section  
ATTN: Doc. Con. for R. Kandel  
ATTN: Doc. Con. for H. H. Kurzwek

OTHER GOVERNMENT AGENCY

Department of Commerce  
Office of Telecommunications  
ATTN: William F. Utlauf

DEPARTMENT OF DEFENSE CONTRACTORS

Aerodyne Research, Inc.  
ATTN: M. Camac  
ATTN: F. Bien

Aerospace Corporation  
ATTN: Harris Mayer  
ATTN: Thomas D. Taylor  
ATTN: R. D. Rawcliffe  
ATTN: R. Grove  
ATTN: R. J. McNeal

University of Denver  
Colorado Seminary  
ATTN: Sec. Officer for Mr. Van Zyl  
ATTN: Sec. Officer for David Murcrary

General Electric Company  
TEMPO-Center for Advanced Studies  
ATTN: Warren S. Knapp  
5 cy ATTN: DASIAIC, Art Feryok

General Research Corporation  
ATTN: John Ise, Jr.

Geophysical Institute  
University of Alaska  
ATTN: T. N. Davis  
y ATTN: Neal Brown

neywell Incorporated  
adiation Center  
ATTN: W. Williamson  
ATTN: Carl Bohne (HRC)  
ATTN: Lloyd Harkless (HRC)  
ATTN: Elton Dunbar

Institute for Defense Analyses  
ATTN: Hans Wolfhard  
ATTN: Ernest Bauer

DEPARTMENT OF DEFENSE CONTRACTORS (Continued)

Lockheed Missiles and Space Co., Inc.  
ATTN: Billy M. McCormac, Dept. 52-54  
ATTN: John B. Cladis, Dept. 52-12  
ATTN: J. B. Reagan, D/52-12  
ATTN: John Kumer  
ATTN: Martin Walt, Dept. 52-10  
ATTN: Richard G. Johnson, Dept. 52-12  
ATTN: Robert D. Sears, Dept. 52-14  
ATTN: Tom James

Mission Research Corporation  
ATTN: P. Fischer  
ATTN: D. Archer

Photometrics, Inc.  
ATTN: Irving L. Kofsky

Physical Dynamics, Inc.  
ATTN: Joseph B. Workman

Physical Sciences, Inc.  
ATTN: Kurt Wray

R & D Associates  
ATTN: Robert E. Lelevier  
ATTN: Forrest Gilmore

R & D Associates  
ATTN: Herbert J. Mitchell

Science Applications, Inc.  
ATTN: Daniel A. Hamlin

Space Data Corporation  
ATTN: Edward F. Allen

SRI International  
ATTN: M. Baron  
ATTN: Ray L. Leadabrand  
ATTN: Walter G. Chesnut

SRI International  
ATTN: Warren W. Berning

Technology International Corporation  
ATTN: W. P. Boquist

Utah State University  
ATTN: D. Burt  
ATTN: Kay Baker  
ATTN: C. Wyatt  
ATTN: Doran Baker

Visidyne, Inc.  
ATTN: L. Katz  
ATTN: William Reidy  
ATTN: Henry J. Smith  
ATTN: Charles Humphrey  
ATTN: J. W. Carpenter  
ATTN: T. C. Degges